

ARO ~ 21807.1-MS-CF  
Also a part of the Final Report

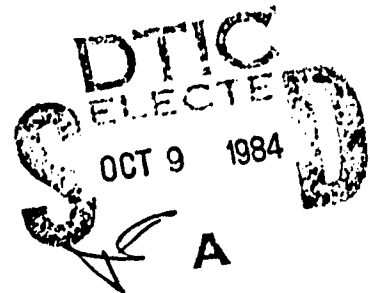
PROCEEDINGS OF THE SEVENTEENTH SYMPOSIUM  
ON  
ELECTROMAGNETIC WINDOWS

July 25-27, 1984

PART 2.

slb 1-22-85

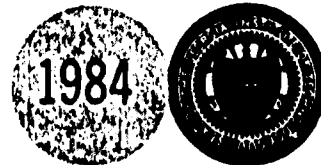
Edited by  
H. L. Bassett



AD-A149 125

**GEORGIA INSTITUTE OF TECHNOLOGY**

A Unit of the University System of Georgia  
Engineering Experiment Station  
Atlanta, Georgia 30332



DTIC FILE COPY

This document has been approved  
for public release and sale; its  
distribution is unlimited.

COMPONENT PART NOTICE

THIS PAPER IS A COMPONENT PART OF THE FOLLOWING COMPILATION REPORT:

(TITLE): Proceedings of the Symposium on Electromagnetic Windows (17th) Held at  
Georgia Institute of Technology, Engineering Experiment Station, Atlanta,  
Georgia on 25-27 July 1984. Part 2. See also Part 1, AD-A149 185.

(SOURCE): Georgia Institute of Technology, Atlanta, Engineering Experiment  
Station.

TO ORDER THE COMPLETE COMPILATION REPORT USE AD-A149 125 and AD-A149 185.

THE COMPONENT PART IS PROVIDED HERE TO ALLOW USERS ACCESS TO INDIVIDUALLY AUTHORED SECTIONS OF PROCEEDINGS, ANNALS, SYMPOSIA, ETC. HOWEVER, THE COMPONENT SHOULD BE CONSIDERED WITHIN THE CONTEXT OF THE OVERALL COMPILATION REPORT AND NOT AS A STAND-ALONE TECHNICAL REPORT.

THE FOLLOWING COMPONENT PART NUMBERS COMPRISE THE COMPILATION REPORT:

AD#:            TITLE:

FOREWORD

The Seventeenth Electromagnetic Window Symposium marks 29 years of regularly scheduled symposia on electromagnetic windows. The first seven symposia were held at Ohio State University. The Georgia Institute of Technology has hosted the symposium biennially since 1966, with the U. S. Air Force cohosting the symposia of 1966, 1968, and 1972.

The Steering Committee responsible for the team planning and coordination of the symposium consisted of the following individuals from the Georgia Institute of Technology, Engineering Experiment Station:

J. N. Harris, Chairman  
EMSL

H. L. Bassett  
RAIL

J. C. Handley  
EMSL

J. M. Newton  
EML

along with

D. J. Evans, AFWAL/AFML  
Wright-Patterson Air Force Base, Ohio

J. A. Fuller, Electromagnetic Sciences, Inc.  
Atlanta, Georgia

G. K. Huddleston, Martin-Marietta Aerospace  
Orlando, Florida

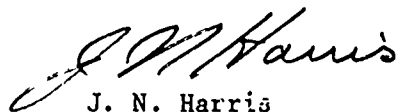
K. N. Letson, U. S. Army MICOM  
Huntsville, Alabama

W. Messick, NSWC/K-22  
White Oak, Maryland

In addition, G. H. Adams, Mercedes Edwards, and Elaine Nicholas of Continuing Education put forth significant efforts in the coordination of the meeting activities and mailing out of brochures.

Papers not received in time for publication will be available during the meeting from either the registration desk or the particular author.

For the Steering Committee



J. N. Harris  
Chairman



A-1

TABLE OF CONTENTS

	Page
1. Electromagnetic Analysis of Radomes by the Moment Method G. Tricoles, E. L. Rope and R. A. Hayward, General Dynamics Electronic Division . . . . .	1
2. A Computer Analysis of the RF Performance of a Ground-Mounted, Air-Supported Radome Milton B. Punnett, CHEMFAB/Birdair Div., and Edward B. Joy, Georgia Institute of Technology . . . . .	9
3. Comparison of Spherical Wave Ray Tracing and Exact Boundary Value Solutions for Spherical Radomes D. A. Bloom, P. L. Overfelt, and D. J. White, Michelson Laboratory . . . . .	17
4. Generalized Radome BSE Characterization Using Superposition Techniques Glenn Plimpton and Michael Cerullo, Raytheon Company . . . . .	27
5. A Subaperture Approach to the Calculation of Flashlobes Introduced by Airborne Radomes A. Hizal, Middle East Technical University R. W. Lyon and A. Cuthbertson, ERA Technology Ltd . . . . .	33
6. Near-Field Effects on Radome Boresight Errors G. K. Huddleston, Georgia Institute of Technology . . . . .	41
7. PWS Radome Analysis Including Reflections Edward B. Joy and Harold L. Rappaport Georgia Institute of Technology . . . . .	57
8. A Fast Ray Tracing Algorithm for Arbitrary Monotonically- Concave Three-Dimensional Radome Shapes Edward B. Joy, Georgia Institute of Technology David E. Ball, Harris Corporation/GASE . . . . .	59
9. Dual Band Radome Wall Design Bernard J. Crowe, Flight Systems, Inc. . . . .	61
10. Study of Laminated Dielectric Behavior at Microwave and Millimeter-Wave Frequencies D. J. White and C. N. Helmick, Jr., Michelson Laboratory, Naval Weapons Center . . . . .	67
11. Image Lobe Analysis for Large Radomes B. Pupko, D. Gordon, S. Starobinets Israel Aircraft Industries . . . . .	77
12. Hypersonic Radome Study R. J. Joachim, Raytheon Company . . . . .	85

(continued)



TABLE OF CONTENTS (Continued)

	Page
13. Supersonic Tactical Missile (STM) Radome Development Arthur J. Thompson, Brunswick Corporation . . . . .	87
14. Silicon Nitride Radome Development For Broadband High Temperature Applications James F. Schorsch and Gary E. Mller Boeing Aerospace Company . . . . .	97
15. A Millimeter Wave Apparatus for Free-Space Measurement of Dielectric Constants at High Temperature D. R. Gagnon and D. J. White Michelson Laboratory, Naval Weapons Center . . . . .	99
16. Automated Radome Testing Charles E. Moore and John B. Styron, Brunswick Corp. . . . .	105
17. Design and Calibration of a 35 GHz Dielectrometer J. Hanson and J. Brazel, General Electric Co. . . . .	115
18. Hot Radome Boresight Error Measurements C. S. Ward, M. Cerullo and G. Plimpton Raytheon Company . . . . .	125
19. Near-Field Testing To Investigate Radome Aberration Phenomena David G. Burks, Texas Instruments Inc. . . . .	133
20. A Broadband Kevlar Radome for Shipboard John B. Styron, and Robert S. Francisco Brunswick Corporation . . . . .	135
21. Fiber Reinforced Fused Silica for Hypersonic Radome Applications F. P. Meyer, G. D. Quinn and J. C. Walck U. S. Army Materials and Mechanics Research Center . . . . .	145
22. Pressureless Sintered Silicon Nitride as a Promising Candidate for Radome Materials M. Y. Hsieh, H. Mizuhara and P. W. Smith GTE - WESGO Division . . . . .	159
23. LL-100 - A New Polybutadiene G. Wayne Eastridge, Brunswick Corporation . . . . .	167
24. Broadband Thermoplastic Radomes Kurt Hollenbeck and Matt Rehrl Texas Instruments . . . . .	177

(continued)

TABLE OF CONTENTS (Concluded)

	Page
25. Progress on Transparent Yttria W. H. Rhodes and E. A. Trickett GTE Laboratories . . . . .	187
26. Development of a High Temperature Single Impact Rain Erosion Test Capability Kenneth N. Letson and Steven P. Risner US Army Missile Laboratory . . . . .	195
27. Infrared Material Optical Damage by Rain Alain Deom, George Gauffre and Daniel L. Balageas Office National d'Etudes et de Recherches Aerospatiales . . . . .	207
28. Rain Erosion Tests of Full-Size Slip-Cast Fused Silica Radomes at M3.5 and M4.8 R. K. Frazer, Johns Hopkins University . . . . .	215
29. Dual Mode Cooled Metallic Antenna Window Design Concept John W. Hidahl and E. L. Kessler Aerojet TechSystems Company . . . . .	217
30. A Radome for Air Traffic Control SSR Radar System Staff of Electronic Space Systems Corporation and ESSCO Collins Limited . . . . .	219
31. Development of the F-20 Nose Radome E. L. Cain and P. Tulyathan, Northrop . . . . .	225
32. High Radiant Flux Thermal Testing of Ceramic and Ablative Coatings for Hardening EHF Radomes K. A. Zimmerman and G. M. Briand, Harris Corp. J. A. Fuller, Georgia Tech . . . . .	235

ELECTROMAGNETIC ANALYSIS OF RADOMES BY THE MOMENT METHOD

G. Tricoles, E.L. Rope, and R. A. Hayward

General Dynamics Electronic Division  
P.O.Box 85227, San Diego, Ca 92138

AD-P004 351

INTRODUCTION

The electromagnetic performance of radomes is usually analyzed approximately by ray tracing, surface integration, or angular spectra. A significant approximation is that the radome is locally flat, and transmittance at a point is described by a set of flat sheets of infinite extent. This approximation is significant in the analysis of wave polarization dependence of boresight error, especially near the shadow of a tip where the surface normal direction varies rapidly because of circumferential curvature. The flat sheet approximation also omits guided waves and scattering by the discontinuity at the tip. The moment method also includes reflections, which influence antenna sidelobe calculations.

This paper describes calculations for hollow wedges; these are based on a theory of J. H. Richmond for hollow cylinders of arbitrary shape. The paper also gives a new theory for hollow cones and circular rings, and it compares computed and measured phase and intensity values for a cone and a ring.

THE MOMENT METHOD

J.H. Richmond developed a theory for scattering by hollow dielectric cylinders of arbitrary shape [1-2]. This theory is part of what is now called the moment method. The method involves solving an integral equation for the total field  $E^T$  where  $E^T$  is the sum of the incident field, that without a scatterer, and the scattered field  $E^S$ . In symbols

$$E^T = E^i + E^S; \quad (1)$$

these fields are vectors. They are derived from a vector potential  $A$  and a scalar potential  $\phi$ . For the scattered field,

$$E^S = i\omega A - \nabla'\phi \quad (2)$$

where  $i$  is  $\sqrt{-1}$ ,  $\omega$  is radian frequency, and time dependence is  $\exp(-i\omega t)$ . The prime means the gradient is taken at the observation point. The vector potential is

$$4\pi A = i\omega\rho_0\epsilon_0 \int (K-1)gE^T dv \quad (3)$$

where  $K$  is dielectric constant;  $g$  is  $r^{-1}\exp(ikr)$ ;  $k$  is  $2\pi/\lambda$ ;  $\lambda$  is wavelength,  $r$  is the distance between source and observation points. The scalar potential is

$$4\pi = - \int g \nabla \cdot (K-1) E^T dv \quad (4)$$

Equation 1 is an integral equation. It is changed to a set of simultaneous equations by decomposing the scatterer into cells small enough to justify assuming the field is constant in a cell. At the center of each cell

$$E_m^T - E_m^S = E_m^I$$

the index  $m$  ranges from 1 to  $N$ , the number of cells. Now  $E_m^S$  is a sum because all cells contribute to the field at a cell.

#### SCATTERING BY CYLINDERS AND HOLLOW WEDGES

Richmond considered cells that were infinitely long circular cylinders. With these cells, hollow cylinders, hollow wedges, and slabs can be analyzed. Richmond gave examples of farfield scattering calculations. We have evaluated nearfields for slabs and wedges according to Richmond's theory [3]. For example, Figure 1 shows the scattered field near a hollow, right angle wedge with dielectric constant 2.6; thickness was 0.25 inch; wavelength was 1.26 inch. The wave was incident on the symmetry axis, and polarization was perpendicular. The brightest regions are intensity maxima; dark regions are minima. The fringes on and near the slab are produced by interference of guided and free space waves.

#### SCATTERING BY DIELECTRIC RINGS

To generalize Richmonds' work we developed a theory for rings as in Figure 2 [4]. Rings of arbitrary length are decomposed into rings that have length approximately  $\lambda/6$ . Each ring is decomposed into angular sectors.

To test the theory we measured and calculated total fields near a ring of length 0.42 inch, diameter 1.25 inch, and dielectric constant 2.6 for linearly polarized waves with wavelength 1.26 inch. For axial incidence at distance  $\lambda/3$  behind the ring, Figure 3 shows the field for the H-plane, and Figure 4 is for the E-plane. The receiving antenna was a half-wave dipole. Two sets of calculated results are shown. One assumes the axial component of field  $E_z$  is zero;

the other does not make this assumption. For the calculations  $N$  was 64. It can be seen that agreement in the H-plane is good. The phase discrepancies are a fraction of a degree except near the peak value where they are about 30%; intensity discrepancies are small. For the E-plane the phase discrepancies are small except near the peak, where they are about 25%; intensity discrepancies are more than in the H-plane, but are at most 10%. The theory with  $E_z \neq 0$  is the more accurate.

Measurements and calculations also were done for the distance behind the ring  $0.83\lambda$ . The discrepancies were smaller for this larger distance.

### SCATTERING BY HOLLOW CONES

The field near a hollow cone was calculated and measured. The calculations were done by decomposing a cone into rings, of unequal radii, and then decomposing the rings into angular sectors. Figure 5 shows the dimensions. An experimental model was fabricated of rings with the same dimensions.

For a wave incident at angle  $14.9^\circ$  to the cone axis, Figure 6 shows measured and computed fields in the plane  $z$  equal 0.86 inch which is the plane of the ring next to the largest. Agreement is good.

### REFERENCES

1. J. H. Richmond, "Scattering by Dielectric Cylinders of Arbitrary Cross Section Shape", IEEE Trans., Vol AP-13, pp 334-342 (1965).
2. J. H. Richmond, "TE Wave Scattering by a Dielectric Cylinder of Arbitrary Cross Section Shape", IEEE Trans., Vol AP-14, pp 460-464 (1966).
3. G. Tricoles, E.L. Rope, and R.A. Hayward, "Wave Propagation Through Hollow Dielectric Shells", General Dynamics Electronics Report R-77-092-5, Nov. 1978, Final report for Contract N00019-77-C-0303.
4. G. Tricoles, E.L. Rope, and R.A. Hayward, "Electromagnetic Waves Near Dielectric Structures", General Dynamics Electronics Division Report R-83-047, Feb. 1983, Final Report for Contract N00019-81-C-0389.

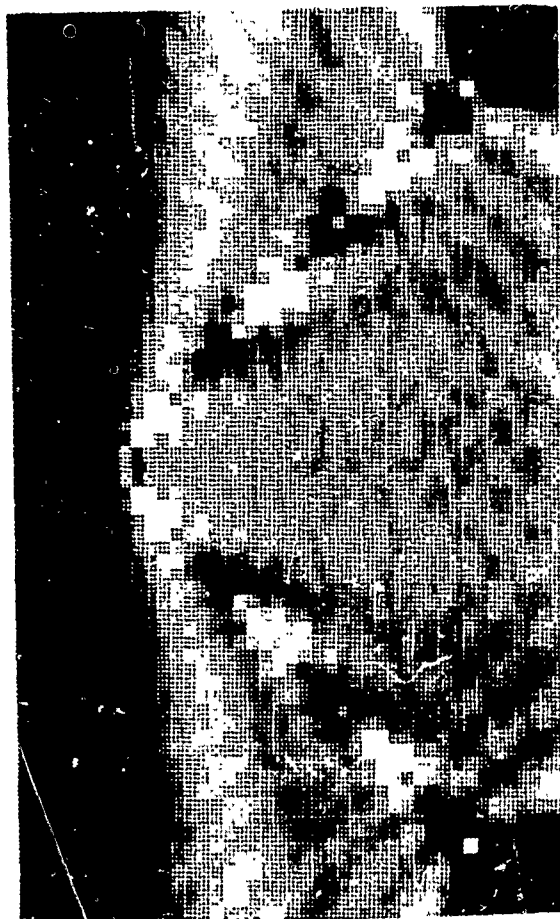
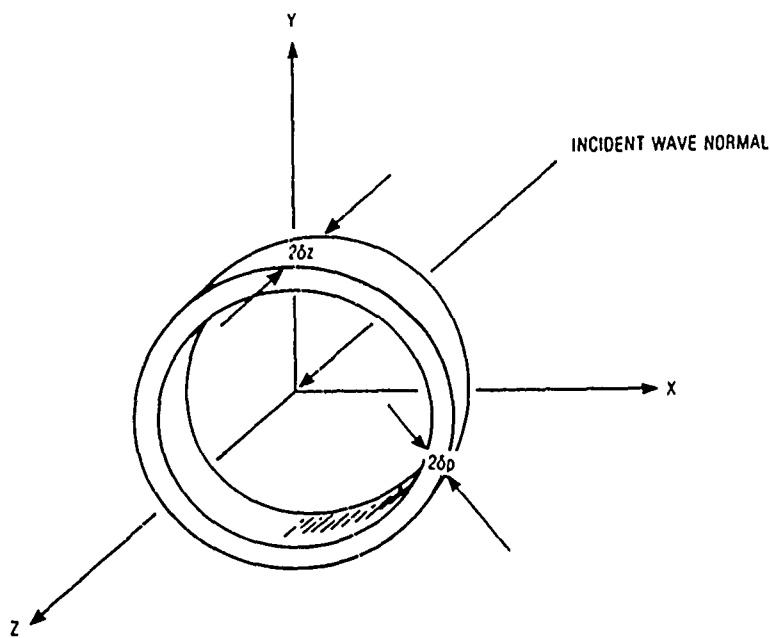
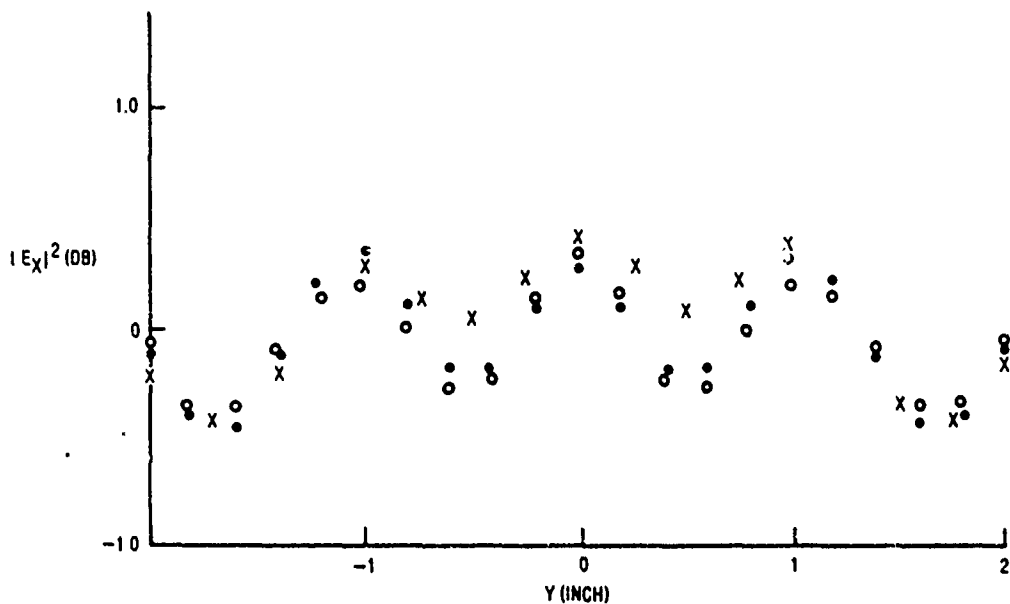
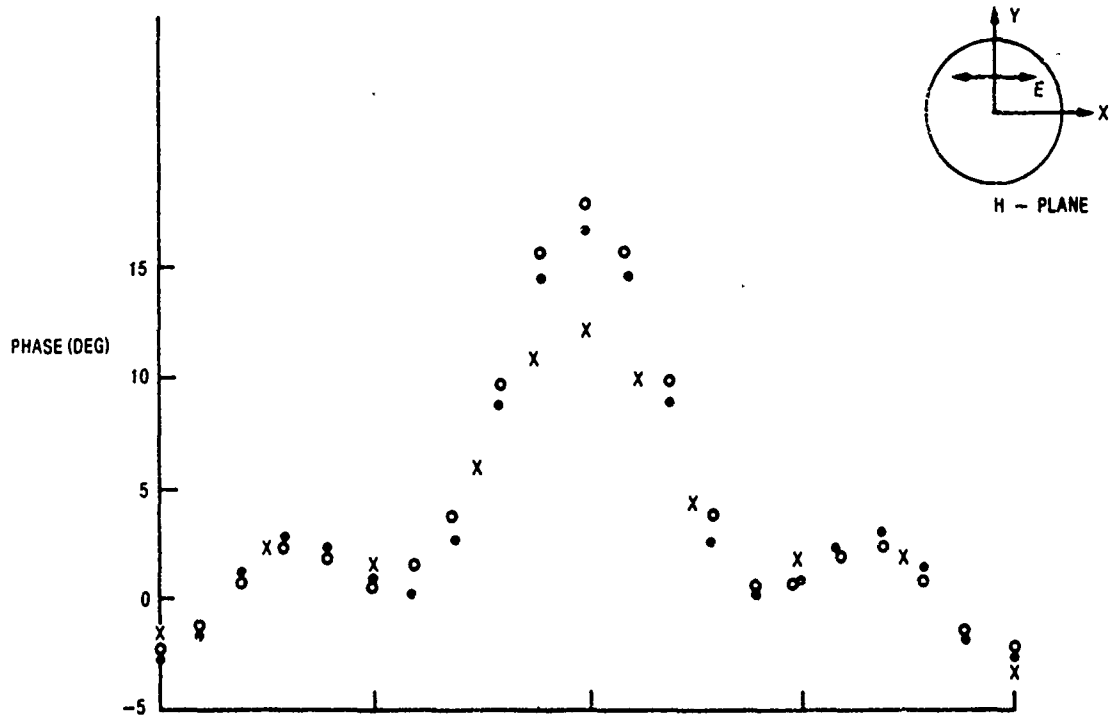


Figure 1. Computed scattered field near a hollow wedge for incident on symmetry plane. Brightest regions corresponds to highest intensities.



ADR002

Figure 2. Dielectric Ring and Co-Ordinate System



AML217A

Figure 3. H-plane total  $\lambda/3$  field behind 0.42 inch long dielectric ring. Measure (x). Calculated:  $E_z=0$  (o);  $E_z \neq 0$  (●).

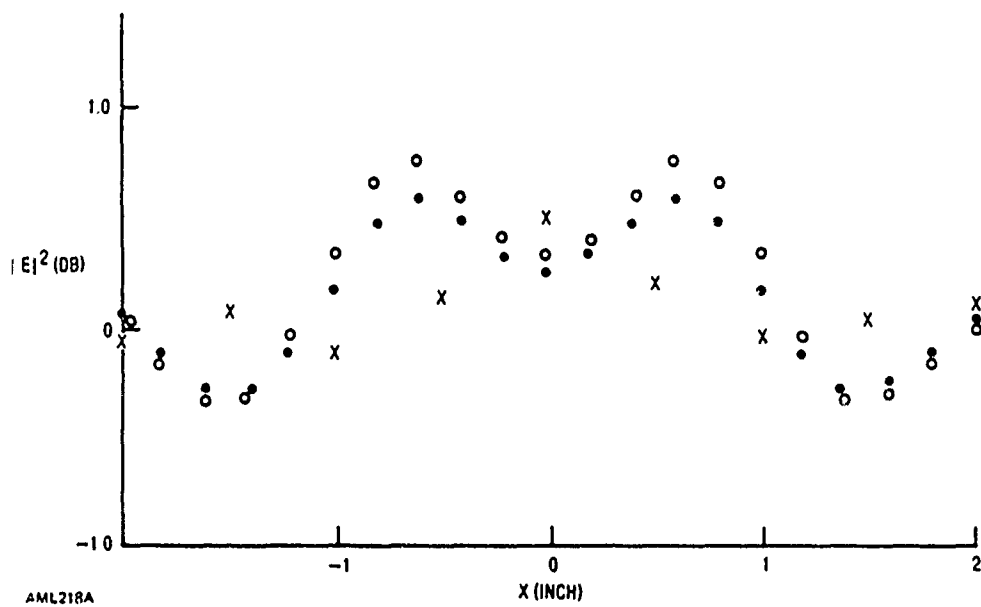
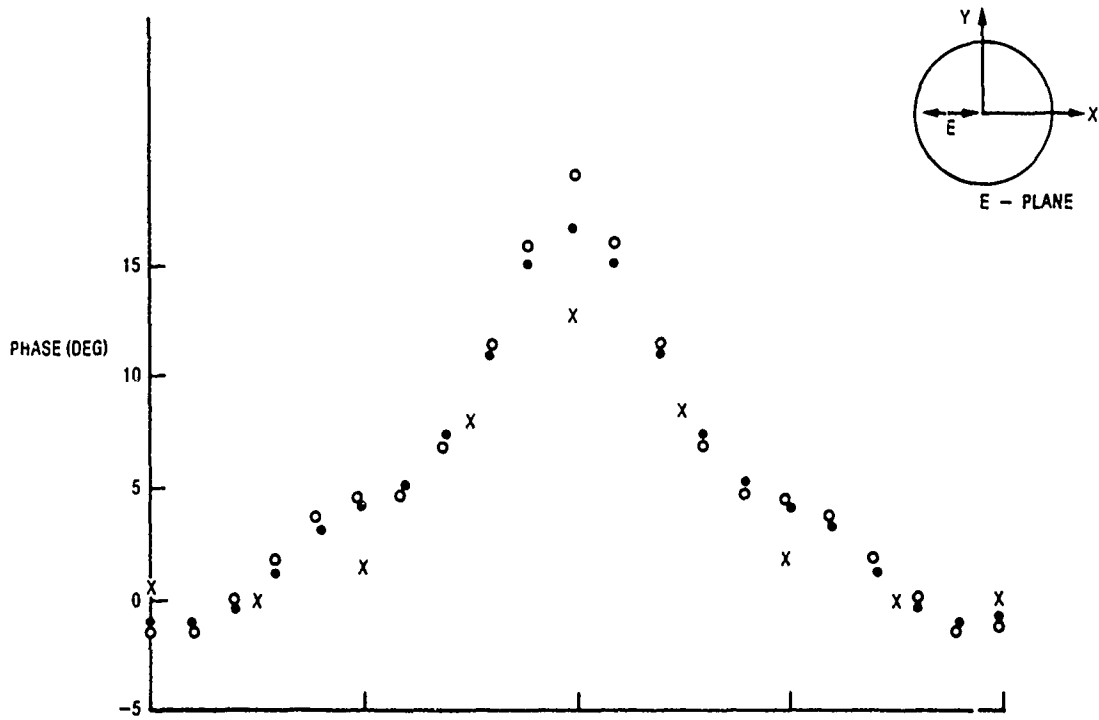


Figure 4. E-plane total  $\lambda/3$  field behind 0.42 inch long dielectric ring. Measured (x). Calculated:  $E_z = 0$  (o);  $E_z \neq 0$  (•).



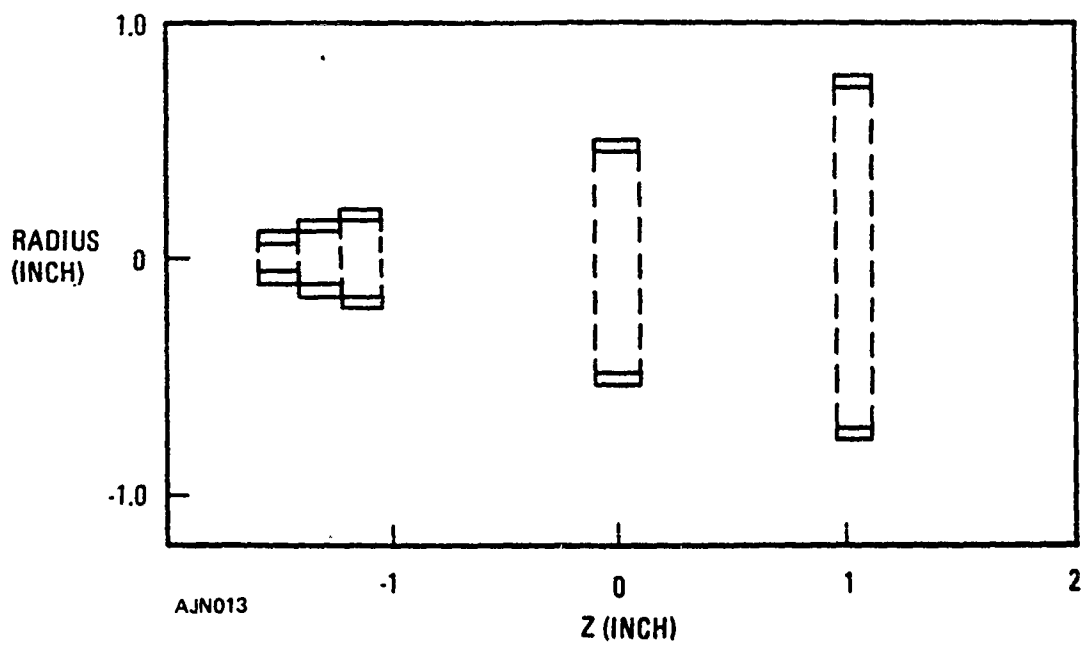
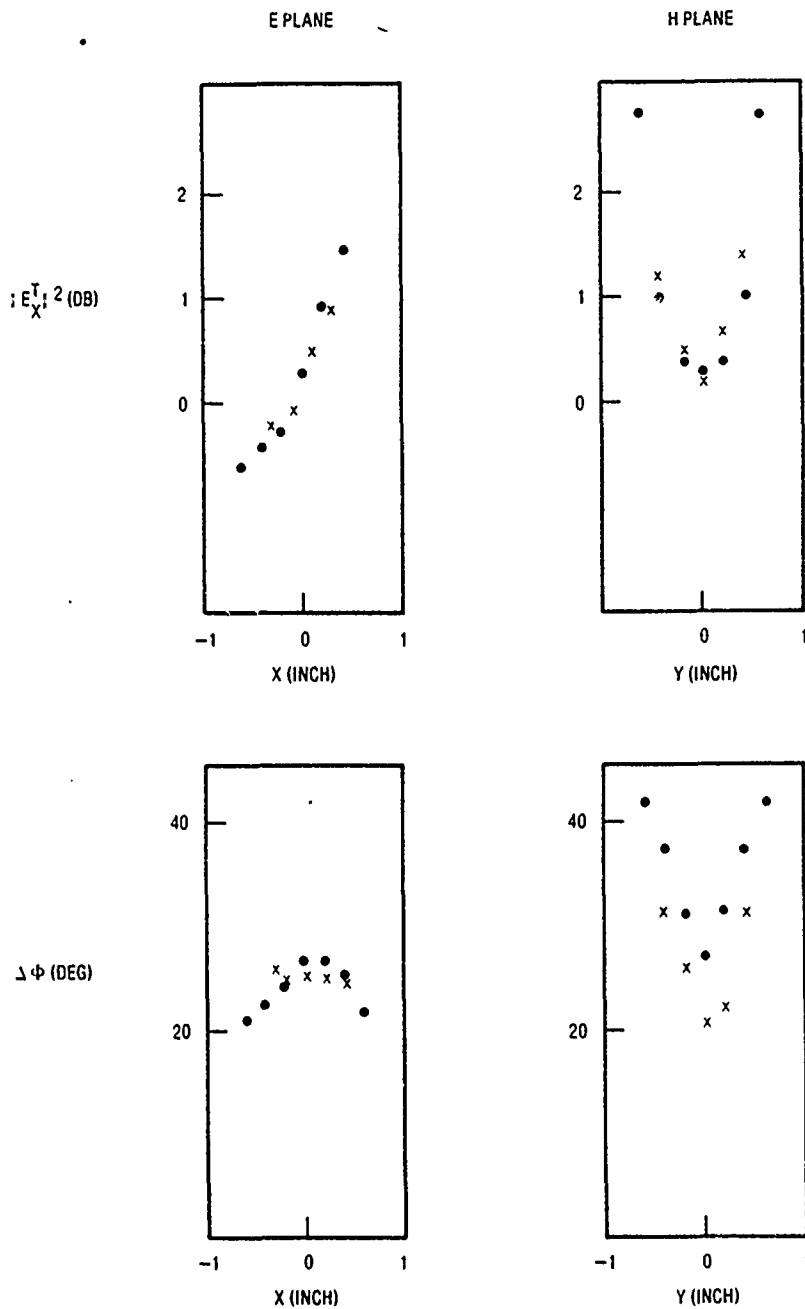


Figure 5. Hollow. Cone. Configuration. Although the figure shows 5 rings, experiments and calculations used either 13 or 15 rings.



AJN045

Figure 6. Field inside 13 ring cone. The field is in the plane of the second largest ring, at  $z$  equal 0.86 inch of Figure 5. The incident plane wave normal was at  $14.9^\circ$  to the cone axis. The field was horizontally polarized, in the plane of the cone axis and wave normal. Ring thickness were 0.065. Wavelength, 1.26 inch. Measured (x). Calculated:  $E_z = \emptyset$  (●).

A COMPUTER ANALYSIS OF THE RF PERFORMANCE OF A  
GROUND-MOUNTED, AIR-SUPPORTED RADOME

by

Milton B. Punnett (1) and Edward B. Joy (2)

AD-P004 352

I. INTRODUCTION

Several reports and actual operating experience have highlighted the degradation of RF Performance which can occur when SSR or IFF antenna are mounted above primary search antennae within metal space frame or dielectric space frame radomes. These effects are usually attributed to both the high incidence angles and sensitivity of the low gain antennae to sidelobe changes due to scattered energy. Although it has been widely accepted that thin membrane radomes would provide superior performance for this application, there has been little supporting documentation.

A plane-wave-spectrum (PWS) computer-based radome analysis was conducted to assess the performance of a specific air-supported radome for the SSR application. In conducting the analysis a mathematical model of a modern SSR antenna was combined with a model of an existing Birdair radome design (3). The PWS algorithm was used to represent the aperture fields of the SSR antenna as a finite collection of plane waves. Each plane wave is represented as a finite collection of parallel rays. The number of rays for this analysis exceeded one million. Each ray is traced from its aperture origin to its intersection point with the three-dimensional radome where it is modified in amplitude, phase and polarization due to the local radome wall properties. The radome model includes both the shaped membrane panels and the individual lap joints in their real life size and distribution. The electrical and physical properties of the panels and joints are specified independently using material characteristics based on laboratory measurements made at several different facilities. Both near field distributions and far field patterns are calculated. (The near field distributions are of interest as they show the detailed amplitude and phase effects of the lap joints.)

- (1) CHEMFAB/Birdair Division, Buffalo, New York.
- (2) School of Electrical Engineering, Georgia Institute of Technology, Atlanta, Georgia.
- (3) The work reported in this paper was performed with the cooperation of Raytheon-Canada.

## II. ANALYSIS (input) CONDITIONS

The following conditions and methods were used in the analysis.

1. A planar near field distribution was synthesized for the SSR planar array antenna. The aperture of the SSR is 26.5 feet wide by 5 feet 1 inch high. The aperture face is vertical and contains the vertical centerline of the radome. The lower edge of the aperture is 96 inches above the horizontal center of the radome and the top edge is 157 inches above the horizontal center. The frequency used in the analysis was 1060 MHz. The SSR antenna was modeled as a monopulse antenna with both a sum mode and an azimuth difference mode. Both modes were vertically polarized. The sum mode was characterized as having a gain of 28 db and 3 db beamwidth of 2.4 degrees in azimuth with main beam tilted upward 7.5 degrees from the horizontal. First sidelobe level in azimuth plane was approximately 25 db below the peak of the main beam. The azimuth difference mode was characterized by a 41 db null depth and a 25 db first sidelobe level with respect to the sum mode main beam peak. The resultant antenna patterns are included in plots as "without radome" in Figures 2 and 3.
2. The SSR antenna gimbal system was synthesized. The antenna is gimballed in azimuth only and the azimuth rotation center is located on the vertical centerline of the radome.
3. The Birdair radome was characterized as shown in Figure 1. The radome has a spherical shape with a diameter of 55 feet. The center is located 19.45 feet above the mounting plane. The radome is composed of 40 main spherical gore panels of equal size assembled with 2.50 inch double thickness lap joints. There is a "step down" lap joint for the crown region occurring at a diameter of 27.50 feet. The number of panels is reduced by 50% (i.e. 20 panels) above "step down". The panel material, Birdair Specification 2D8H40, is characterized as having a thickness of 0.040 inches, a dielectric constant of 3.2 and a loss tangent of 0.01.
4. The computer analysis was conducted using the facilities at Georgia Institute of Technology. The plane wave spectrum, equivalent aperture, transmitting formulation computer algorithm was used to analyze 19 azimuth rotation positions of the SSR antenna. The positions were in 0.5 degree increments from 0 to 9 degrees in azimuth. An azimuth scan angle of 9 degrees corresponds to the repeatable spacing of the radome panels. The analysis was conducted for a single frequency for both the sum mode and azimuth difference mode.

### III. RESULTS

The computer results are presented in a series of 34 plots and graphs. Of these, several representative three-dimensional and planar patterns are included as Figures 2-5. These figures illustrate comparative far field patterns both with and without the radome. Figures 7, 8 and 9 illustrate the effect upon null depth, boresight error and gain loss as the antenna sweeps in azimuth. The results repeat every 9 degrees due to the radome seam distribution. Figure 6 is of interest as it was used to verify the mathematical model, and in testing the correctness of that model. It shows a single component of the spectral analysis. The position and effect of the radome seams and panel step down is readily apparent.

Although the plots graphically illustrate the performance, it is obvious that the comparative effects to be examined are extremely minute. They would be very difficult to measure in an experimental setup. In fact, some values are so low as to approach or be below the "noise" level of the mathematical algorithm. Because of the low levels under real life conditions, more severe inputs (such as a 40 GHz signal) were introduced during the course of the study to verify that the program was indeed operating properly.

A listing of the key factors are tabulated in Table 1. Again, it should be noted that several of the values approach the noise limits of the algorithm and due consideration should be made in the interpretation.

### IV. CONCLUSIONS

The results verify what heretofore had been presumed; the thin membrane, air-supported radome has very little effect upon the performance of the SSR antenna even though it is mounted above the radome center. In comparison to other type radomes, the results (such as a cross-polarization ratio below -120 db and 0.02 db change in sidelobe level) are especially enlightening. It is readily apparent, from this view point, that the air-supported radome is ideally suited for such an application.

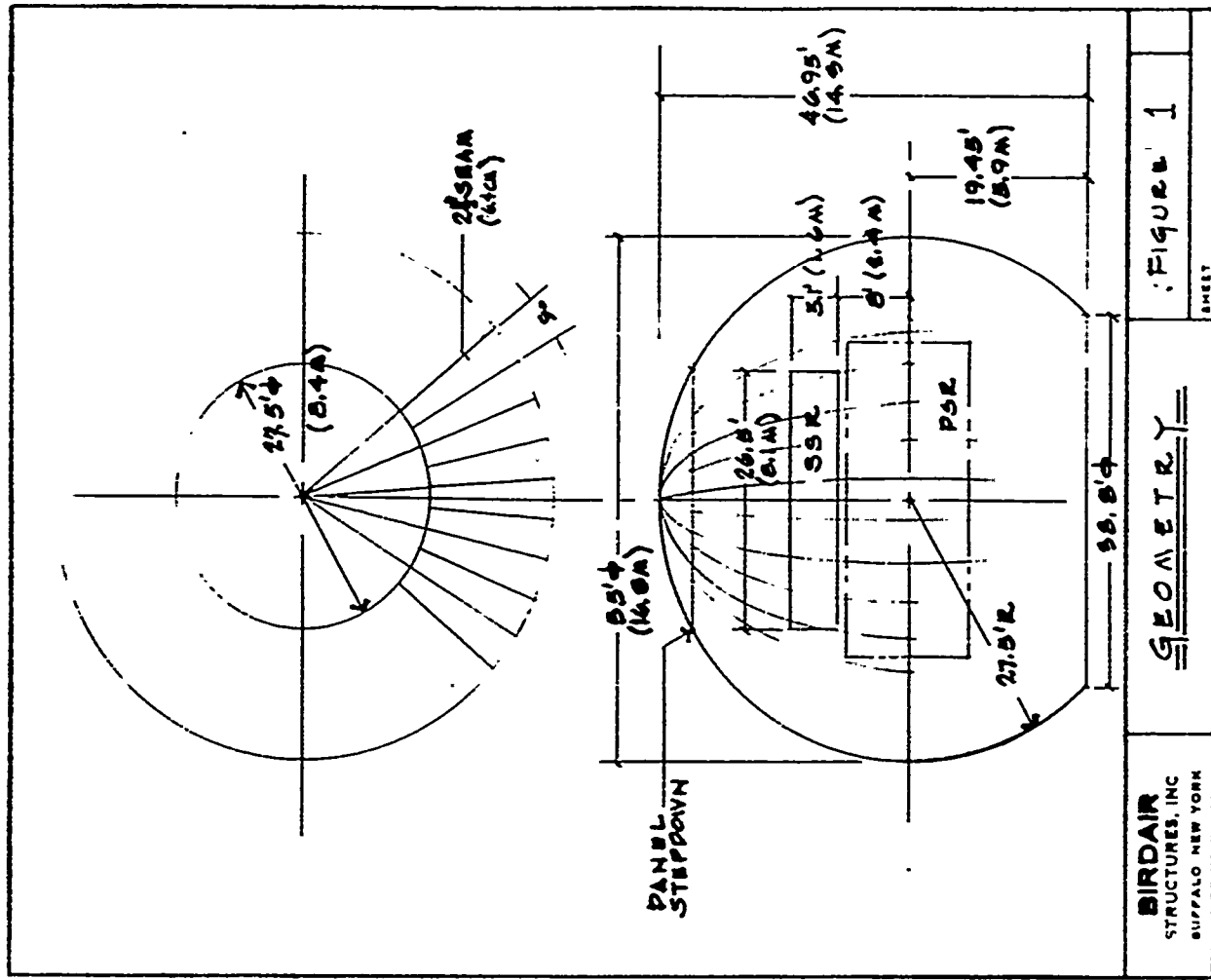
### REFERENCES:

1. "Effects of Dielectric Space Frame Radomes on SLS/SSR Antenna Pattern", J. Whelpton and D. W. Halayko, Fourth International Conference on Electromagnetic Windows, 1981.
2. "Comparison of Radome Electrical Analysis Techniques", E. B. Joy, R.E. Wilson, D. E. Ball, and S. D. James.
3. "Final Report on ASR-803 Radome Study", J. Whelpton, performed under DDS Contract OPB79-00247 for the Radar and Automation Division of Telecommunications and Electronic Branch, Transport, Canada.
4. "Radome Effects on the Performance of Ground Mapping Radar: Theory", E. B. Joy and G. K. Huddleston.

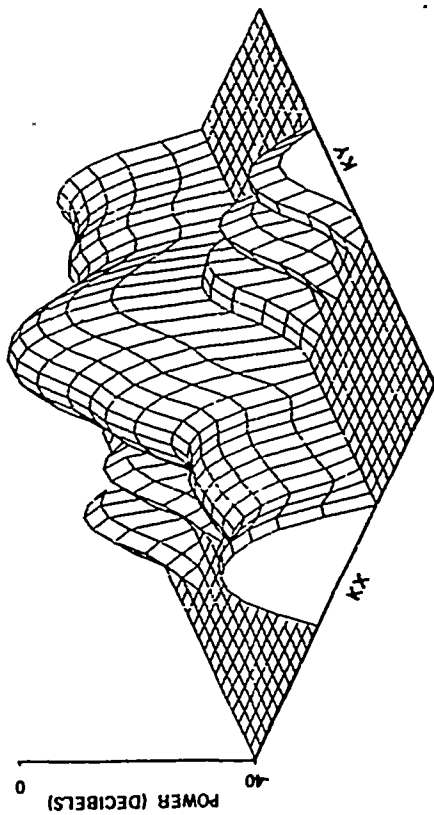
Table 1

SUMMARY OF RF PERFORMANCE

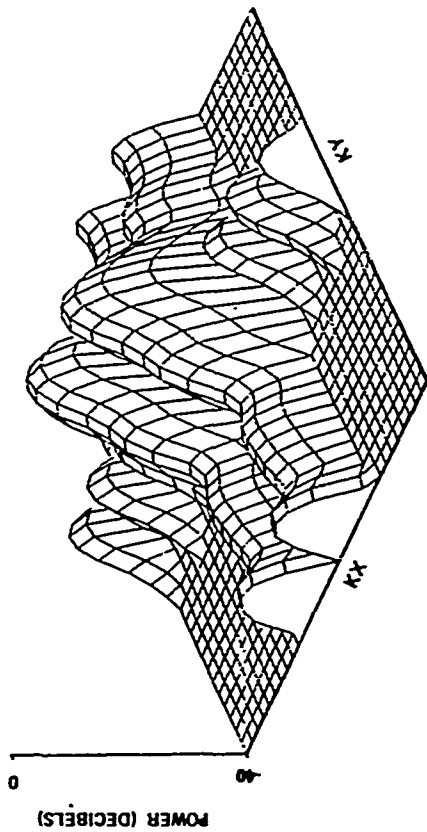
1. Radome Loss = 0.007 db total (reflection and attenuation)
2. Cross-Polarization Ratio = below -120 db.
3. Boresight Error (beam deflection) = approximately .001 milliradians
4. Boresight Error Slope (beam deflection rate) = 0.0001%
5. Change in sum mode 25 db sidelobe level = 0.02 db
6. Change in difference mode 25 db sidelobe level = 0.02 db
7. Change in difference pattern null depth = 0.25 db at 41 db down.



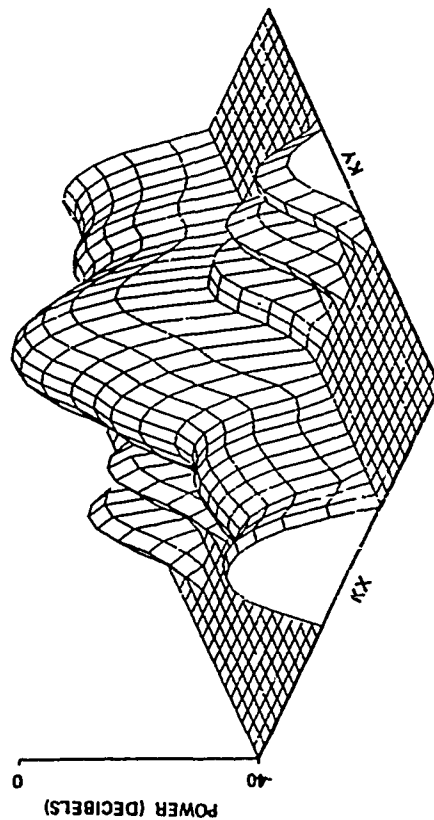
SSR SUM MODE FAR FIELD PATTERN WITHOUT BIRDAIR RADOME



SSR DIFFERENCE MODE FAR FIELD PATTERN WITHOUT BIRDAIR RADOME



SSR SUM MODE FAR FIELD PATTERN WITH BIRDAIR RADOME (0° SCAN)



SSR DIFFERENCE MODE FAR FIELD PATTERN WITH BIRDAIR RADOME (0° SCAN)

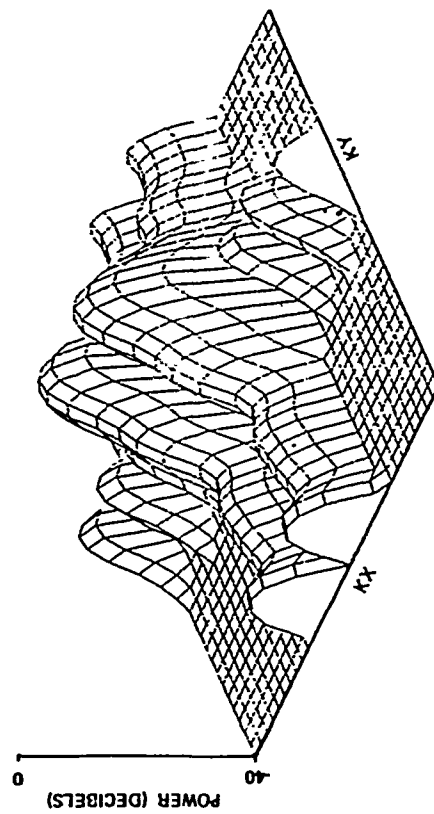
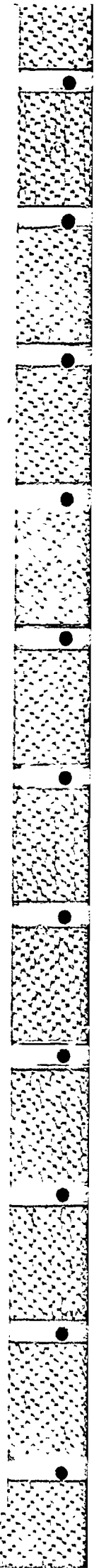
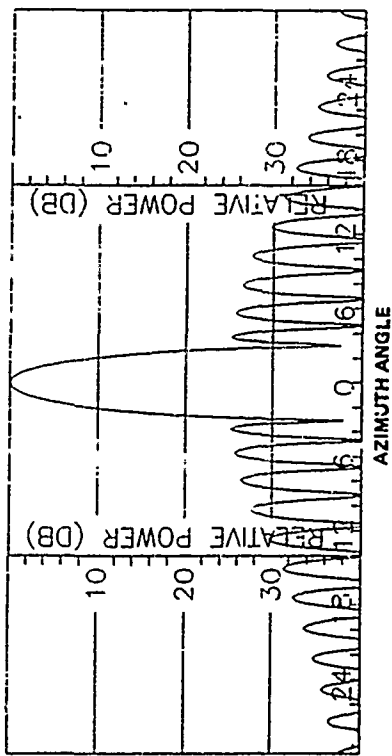


FIGURE 2

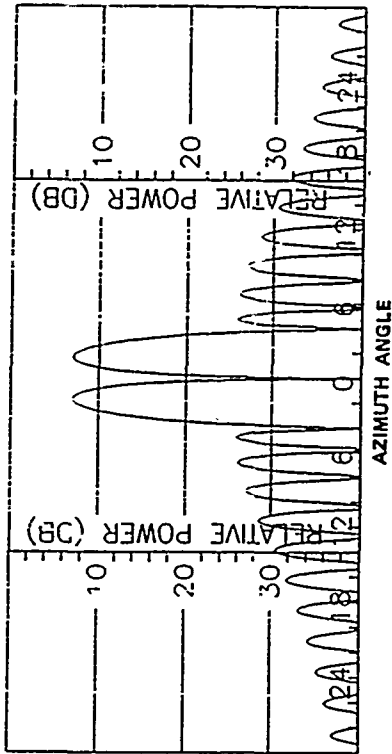
FIGURE 3



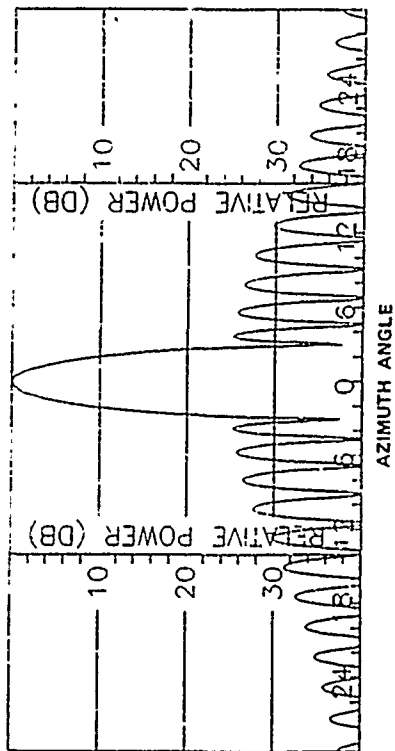
SSR SUM MODE FAR FIELD PATTERN WITHOUT BIRDAIR RADOME



SSR DIFFERENCE MODE FAR FIELD PATTERN WITHOUT BIRDAIR RADOME



SSR SUM MODE FAR FIELD PATTERN WITH BIRDAIR RADOME (0° SCAN)



SSR DIFFERENCE MODE FAR FIELD PATTERN WITH BIRDAIR RADOME (0° SCAN)

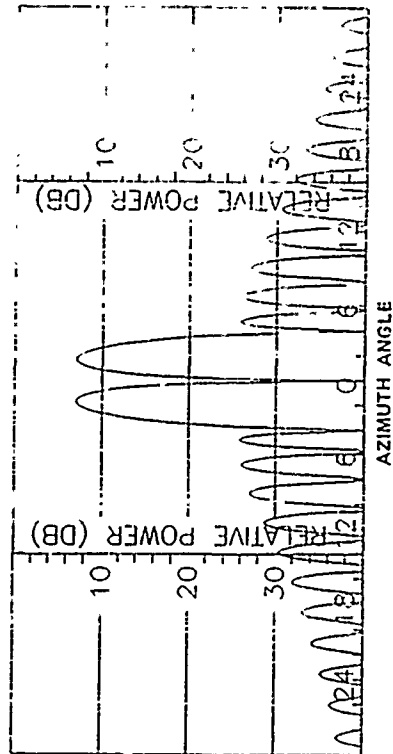
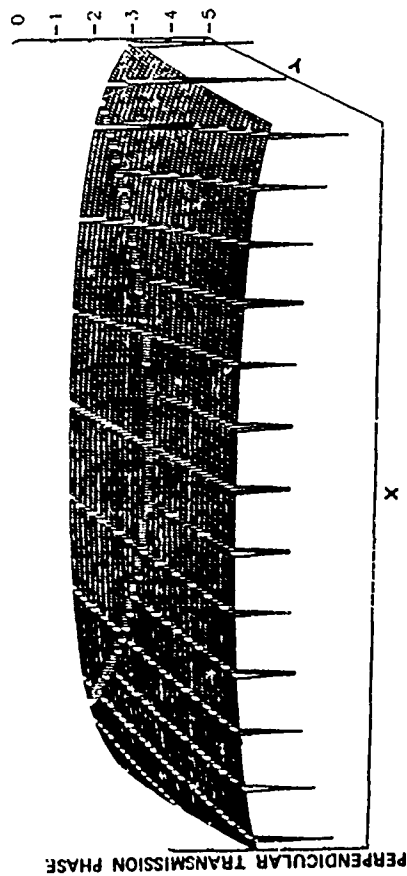


FIGURE 4

FIGURE 5

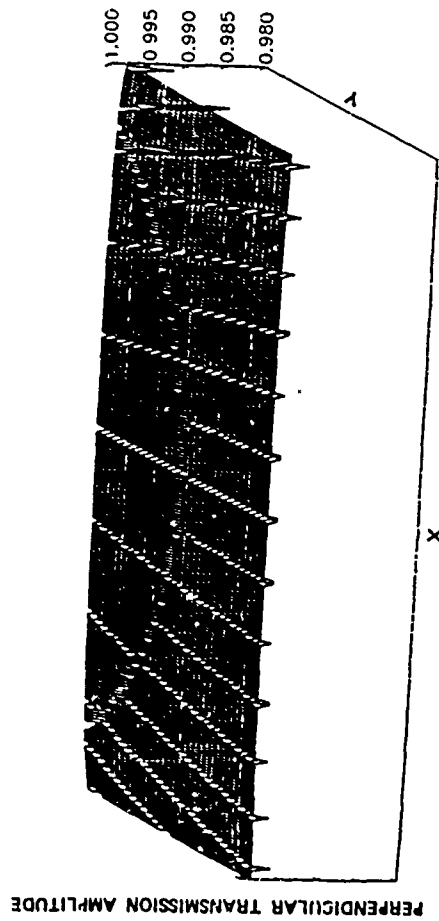


PLANE WAVE TRANSMISSION THROUGH BIRDAIR RADOME



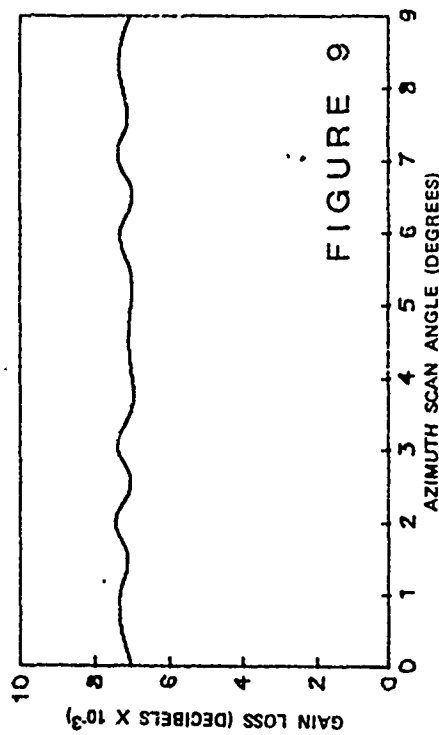
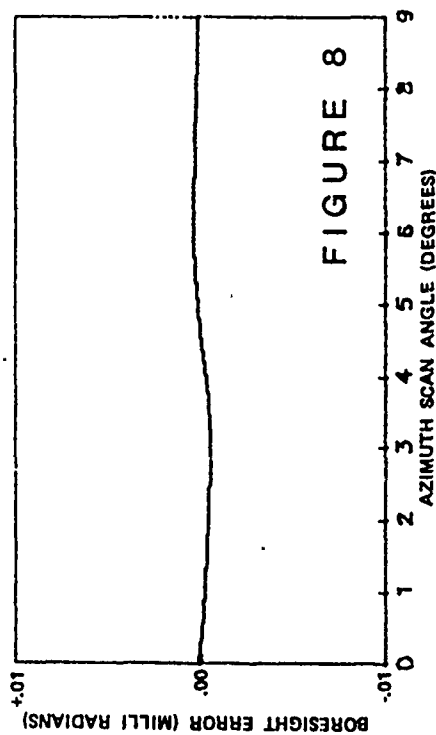
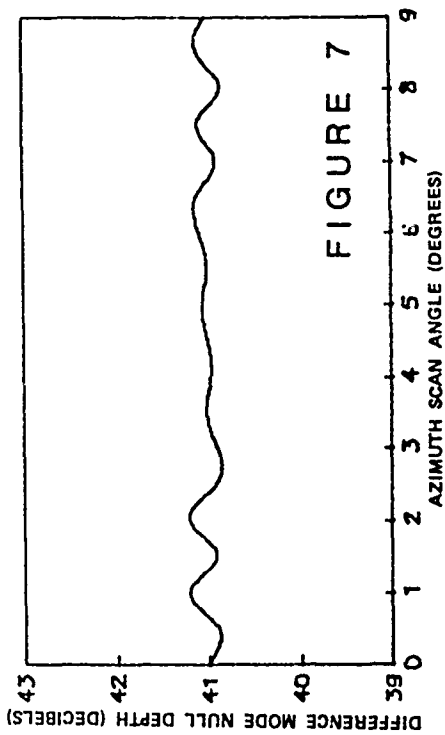
AZIMUTH = 0° ELEVATION = 23°

PLANE WAVE TRANSMISSION THROUGH BIRDAIR RADOME



AZIMUTH = 0° ELEVATION = 23°

FIGURE 6



Mr. Milton B. Punnett received a B.S.M.E. Degree from Purdue University and a Master of Science Degree from Cornell University. He has held engineering positions with Cornell Aeronautical Laboratory, United Aircraft Corporation, Moog, Inc, and is presently Manager of Engineering Development at Birdair Structures, Division of CHEMFAB in Buffalo, New York. Since joining Birdair at its founding in 1956, Mr. Punnett has acted as project engineer on a great number of fabric structure programs, including radomes ranging in size from 8' to 210' diameter. He is the author of several technical papers relating to radome design and performance. Mr. Punnett is a licensed Professional Engineer, an Associate of Sigma XI Research Society, The IEEE, The Air Force Association, and currently is an officer in the Niagara Frontier Association of Research and Development Directors.

Dr. Edward B. Joy received the B.S.E.F., M.S.E.E., and Ph. D. Degrees in Electrical Engineering from the Georgia Institute of Technology. He is currently Professor of Electrical Engineering at Georgia Institute of Technology, and has published over 60 technical papers and research reports. Dr. Joy is also a consultant to several U.S. and N.A.T.O. companies. His areas of interest are electromagnetic near field analysis and measurement, radome analysis and design, and antenna design. Dr. Joy is a Senior Member of the Antennae and Propagation Society of the IEEE, and a member of U.R.S.I. - Commission A, Sigma XI, and Eta Kappa Nu.

Comparison of Spherical Wave Ray Tracing and  
Exact Boundary Value Solutions for Spherical Radomes

D. A. Bloom, P. L. Overfelt, and D. J. White

Michelson Laboratory, Physics Division  
Naval Weapons Center, China Lake, California 93555

AD-P004 353

INTRODUCTION

Much radome analysis is based on plane wave ray tracing techniques which combine conceptual simplicity with reasonable accuracy. As increasing demands on the performance of airborne antennas necessitate more accurate methods of analysis for the enclosing radome, an exact idea of the limits of applicability of the ray-optical approximation becomes more critical. In an effort to contribute to this subject, we have taken a single layer spherical radome excited by a dipole source oriented parallel to the z-axis (see Fig. 1) and computed its transmitted electric and magnetic fields using a spherical wave ray tracing technique [1,2] and also by solving the electromagnetic boundary value problem exactly [3,4]. The exact solution is used as a standard against which the ray tracing approximation can be compared.

In this paper, we compare the field patterns of the two solutions by varying the dipole offset distance, the observation point position, wall thickness, dielectric constant, wavelength, and curvature. Parameter values and the compared field patterns are examined in terms of the theory, and conclusions are drawn as to which parameters affect agreement most strongly.

THEORY

A. Electric Fields

The total transmitted electric field as derived from the boundary value approach is given by

$$\vec{E} = \left\{ \sum_{n=1}^{\infty} T_n A_n \frac{n(n+1)}{k_o r} h_n^{(1)}(k_o r) P_n(\cos\theta) \hat{r} + \frac{1}{k_o r} \frac{\partial}{\partial r} \left[ r h_n^{(1)}(k_o r) \right] P_n^1(\cos\theta) \hat{\theta} \right\}, \quad (1)$$

where  $T_n$  is the "exact" transmission coefficient of an  $n^{\text{th}}$  order spherical wave of transverse magnetic type,  $h_n^{(1)}$  is the spherical Hankel function of the first kind,  $P_n$  and  $P_n^1$  are Legendre and associated Legendre functions,  $r, \theta, \phi$  are the usual spherical coordinates, and

$$A_n = \frac{ik_o^2 P}{4\pi\epsilon_o d} (2n+1) j_n(k_o d) \quad , \quad (2)$$

which characterizes the incident field of the source [3,4] as a sum of spherical waves.

The corresponding ray-optical electric field is given by (see Fig. 1)

$$\vec{E} = (DF) \begin{bmatrix} T_{\perp} E_{\perp}^i \\ T_{\parallel} E_{\parallel}^i \end{bmatrix} e^{ik_o(\sqrt{\epsilon} b + c)} \quad , \quad (3)$$

where DF is a spherical divergence factor,  $T_{\perp}$  and  $T_{\parallel}$  are the products of the usual transmission coefficients at each interface, and  $E_{\perp}^i$ ,  $E_{\parallel}^i$  are the incident field's for both polarizations [1,2]. The transmitted magnetic fields are of course found by Maxwell's curl equations.

Assuming parallel polarization, the incident ray-optical field has the form

$$\vec{E}_{\parallel}^i (r, \theta, \phi = 90^\circ) = \frac{e^{ik_o r}}{r/\lambda_o} \sin\theta \hat{\theta} \quad (4)$$

which is then modified by transmission through the dielectric layer and by the divergence factor which accounts for wave front and radome curvature. To compare Eq. (3) (with (4) substituted in) with Eq. (1), we take the first two terms of the  $\hat{\theta}$ -component of the  $\vec{E}$  field (the  $\hat{r}$ -component is dominated in the far-field in any case), and writing the Hankel functions in exponential form we have

$$\begin{aligned} E_{\theta} = & e^{ik_o r} \left[ \frac{i}{k_o r} + \frac{1}{(k_o r)^2} - \frac{i}{(k_o r)^3} \right] T_1 A_1 \sin\theta \\ & + e^{ik_o r} \left[ -\frac{1}{k_o r} + \frac{3i}{(k_o r)^2} + \frac{(6-6i)}{(k_o r)^3} \right] T_2 A_2 3\cos\theta \sin\theta \\ & + \dots \quad . \quad (5) \end{aligned}$$

Thus for  $k_o r \gg 1$  (i.e, the asymptotic regime), the ray-optical solution is simply the first-order term in  $1/k_o r$  of the exact series expression for the electric field.

The  $T_n A_n$  factor controls the rate of convergence of this series and when  $T_1 A_1$  is relatively large (i.e., close to 1) and  $T_2 A_2 \dots T_n A_n$  fall off rapidly, the ray tracing and exact field patterns match very well. This occurs when (1) the dipole offset distance is small in terms of a wavelength forcing  $A_n$  to decrease with  $n$  or when (2) particular combinations of the dielectric constant and wall thickness force  $T_n$  to decrease rapidly with  $n$ .

### B. Transmission Coefficients

The ray tracing model incorporates two different transmission coefficients. The first is the product of the standard Fresnel coefficients at each interface of the spherical shell which is used in refs. 1 and 2. It assumes a single ray path and does not account for multiple reflections. Its form is given in ref. 1, Eqs. (4a, b). The second coefficient is a flat panel coefficient which includes an extra phase shift due to the fact that point 2 (see Fig. 1) is not taken along the normal from point 1 and also accounts for multiple reflections. Its form is

$$T_k = \frac{(1-r_k^2)e^{-i\beta t} e^{-i\beta_o \ell}}{1-r_k^2 e^{-i2\beta t}}, \quad k = 1, \parallel, \quad (6)$$

where  $r_k$  are the interface reflection coefficients for each polarization,  $t$  is the shell thickness,  $\ell$  is the extra distance traveled due to noncoincident normals,  $\beta_o = 2\pi/\lambda_o = k_o$ , and  $\beta = \beta_o \sqrt{\epsilon - \sin^2 \phi}$ , where  $\phi$  is the incidence angle for each ray.

### CONCLUSIONS

The source offset distance and index of refraction (dielectric constant) are the parameters which most strongly affect a good match between the exact and ray-optical fields (see Figs. 2 and 3). Surprisingly, decreasing the radome curvature/increasing the observation point radius does not necessarily cause the exact solution to approach the ray tracing solution in the limit of large  $r$ . For large dielectric constants or certain combinations of dipole offset distance and wall thickness, the two solutions never match well regardless of how large the radome curvature is allowed to become, as shown in Fig. 4.

Comparison of the computed exact solutions with the experimental plots given in ref. 3 shows excellent agreement at x-band frequencies (see Fig. 5).

Finally, a comparison of the ray-optical fields using the two different transmission coefficients is shown in Fig. 6 and simply confirms the fact that multiple reflections and the exact point of application of the transmission coefficient along an interface are relatively unimportant effects in computing field magnitudes even for extreme values of the controlling parameters.

As a general observation, the ray-optical solution provides an envelope which contains the field pattern of the exact solution but causes fine structure effects to be lost. We are hopeful that the information gained from the spherical radome can be applied to more typical though nonseparable radome shapes.

Further results will be presented.

## REFERENCES

- [1] S. W. Lee, M. S. Sheshadri, V. Jamnejaid, and R. Mittra, "Wave Transmission Through a Spherical Dielectric Shell," Vol. AP-30, No. 3, May 1982, pp. 373-380.
- [2] S. W. Lee, V. Jamnejaid, M. S. Sheshadri, and R. Mittra, "Analysis of Antenna Radomes by Ray Techniques," Naval Air Systems Command, *Research Program Review in Electronics*, May 1980, pp. 124-155.
- [3] C. T. Tai and R. I. Barnett, "Characteristics of Large Spherical Radomes" (Antenna Laboratory, Ohio State University), in *Proceedings of O.S.U.-W.A.D.C. Radome Symposium*, Vol. I, June 1955, pp. 77-93.
- [4] T. Tice and J. Adney, "Transmission Through a Dielectric Spherical Shell," Report 531-3, Contract AF33 (616)-277, Antenna Laboratory, Ohio State University, August 1953.

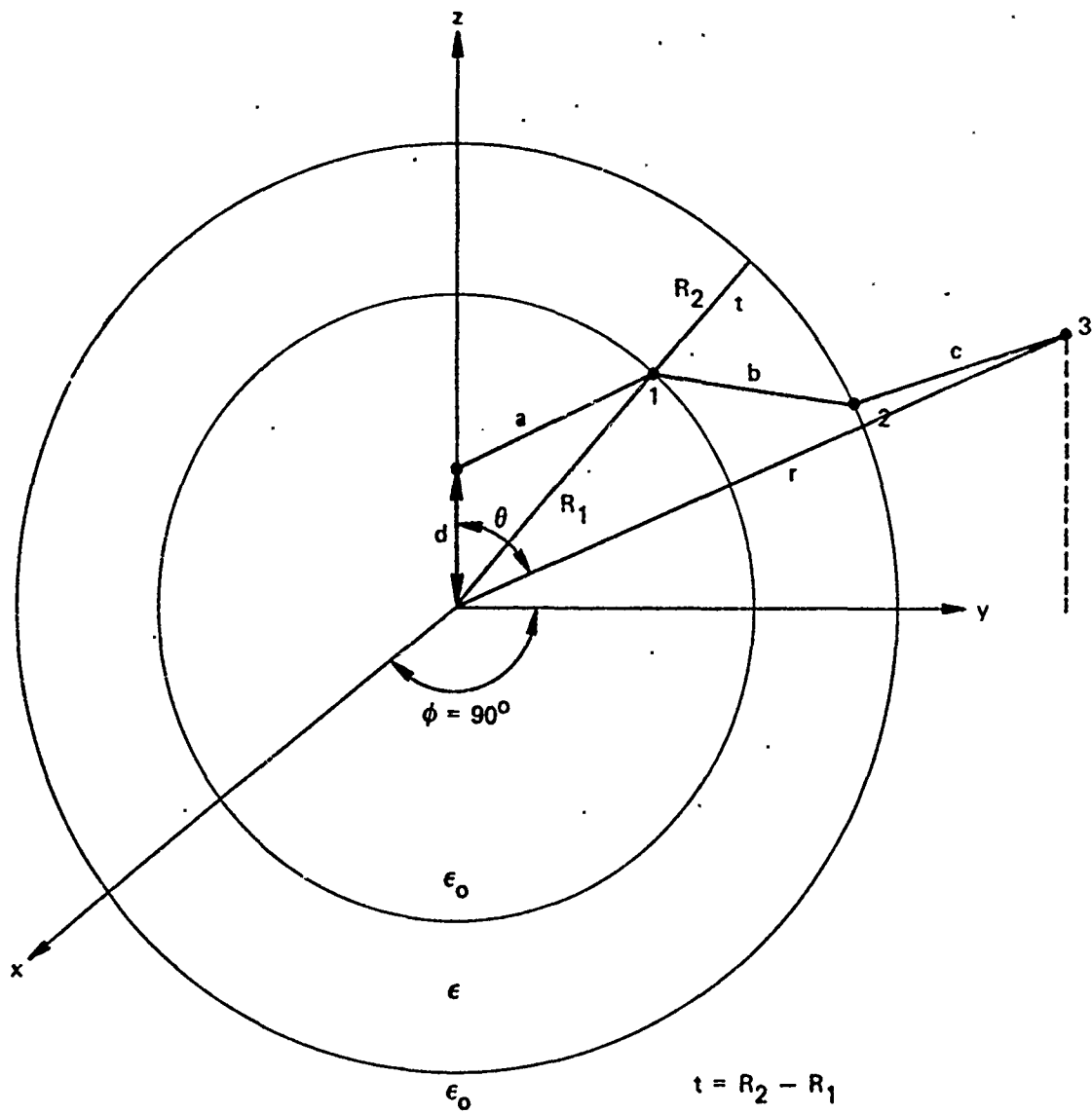


FIGURE 1. Spherical Radome Coordinates

SPHERICAL RADOME

INNER RAD.=11.81  
OUTTER RAD.=12.70  
INDEX IS 1.500  
DIPOLE OFFSET= .200  
OBSERVATION RAD.=13.00  
WAVELENGTH=1.181

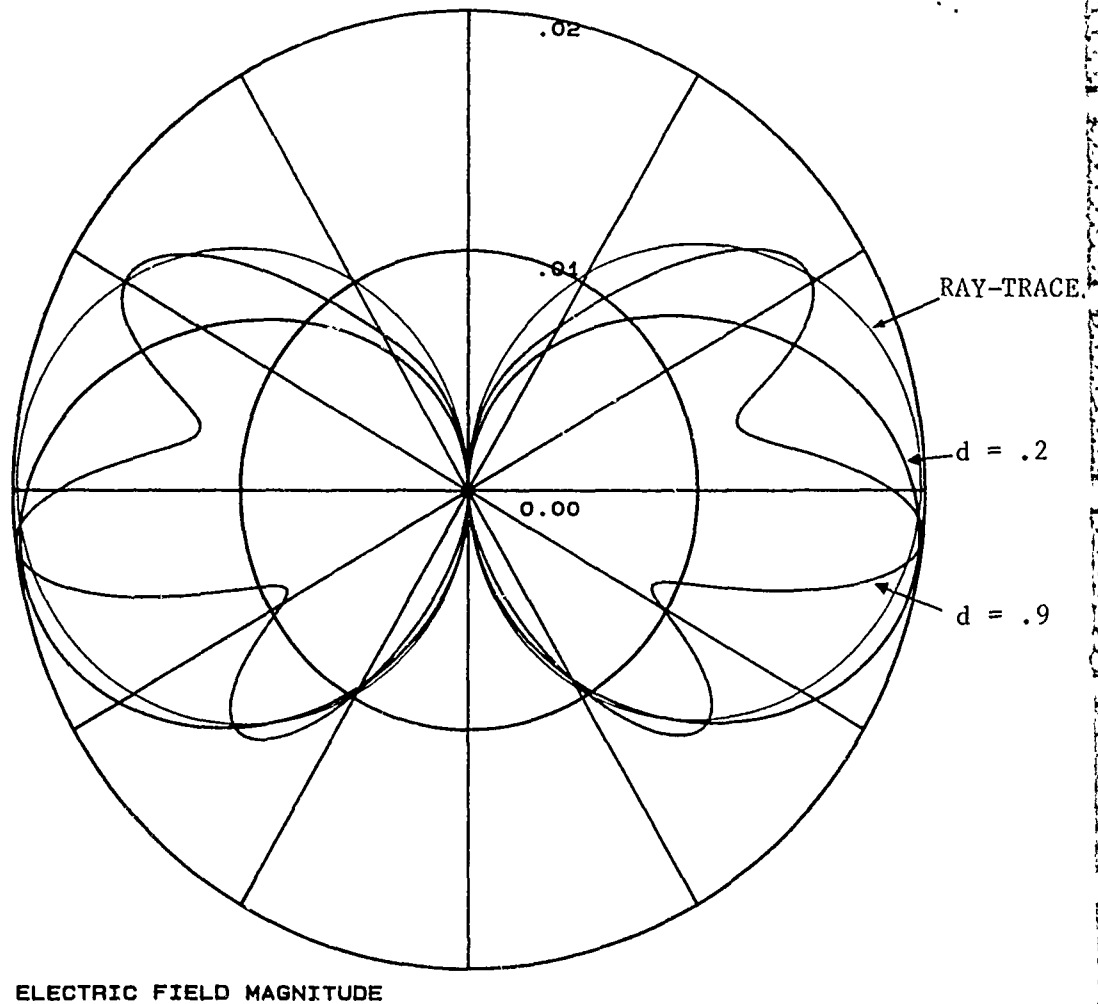
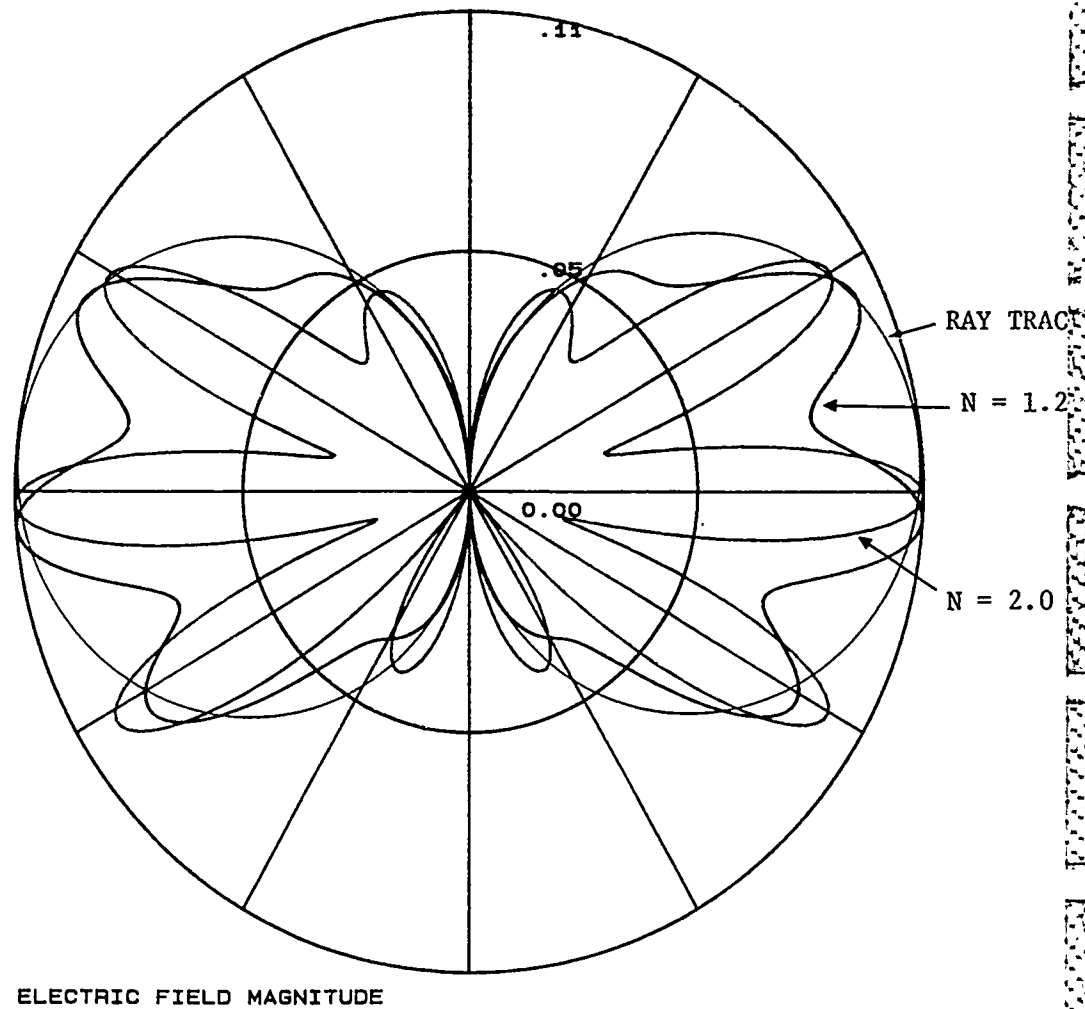


FIGURE 2. Effect of Increasing Dipole Offset Distance



SPHERICAL RADOME

INNER RAD.=23.82  
OUTTER RAD.=24.21  
INDEX IS 1.200  
DIPOLE OFFSET=1.181  
OBSERVATION RAD.=25.00  
WAVELENGTH=1.181

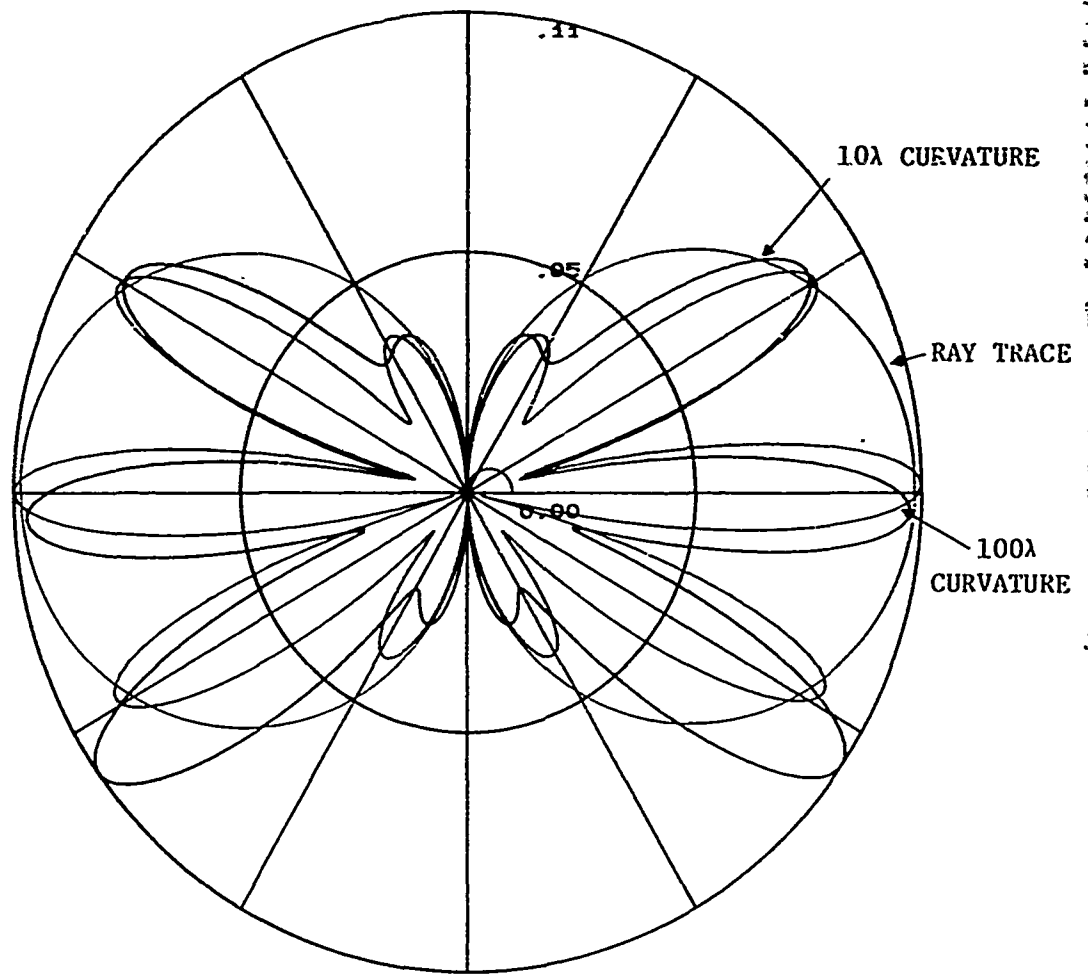


ELECTRIC FIELD MAGNITUDE

FIGURE 3. Effect of Increasing Index of Refraction

SPHERICAL RADOME

INNER RAD.=11.81  
OUTTER RAD.=12.40  
INDEX IS 4.000  
DIPOLE OFFSET=1.181  
OBSERVATION RAD.=25.00  
WAVELENGTH=1.181



ELECTRIC FIELD MAGNITUDE

FIGURE 4. Effect of Decreasing Curvature

SPHERICAL RADOME

INNER RAD.=8.00

WAVELENGTH=1.18

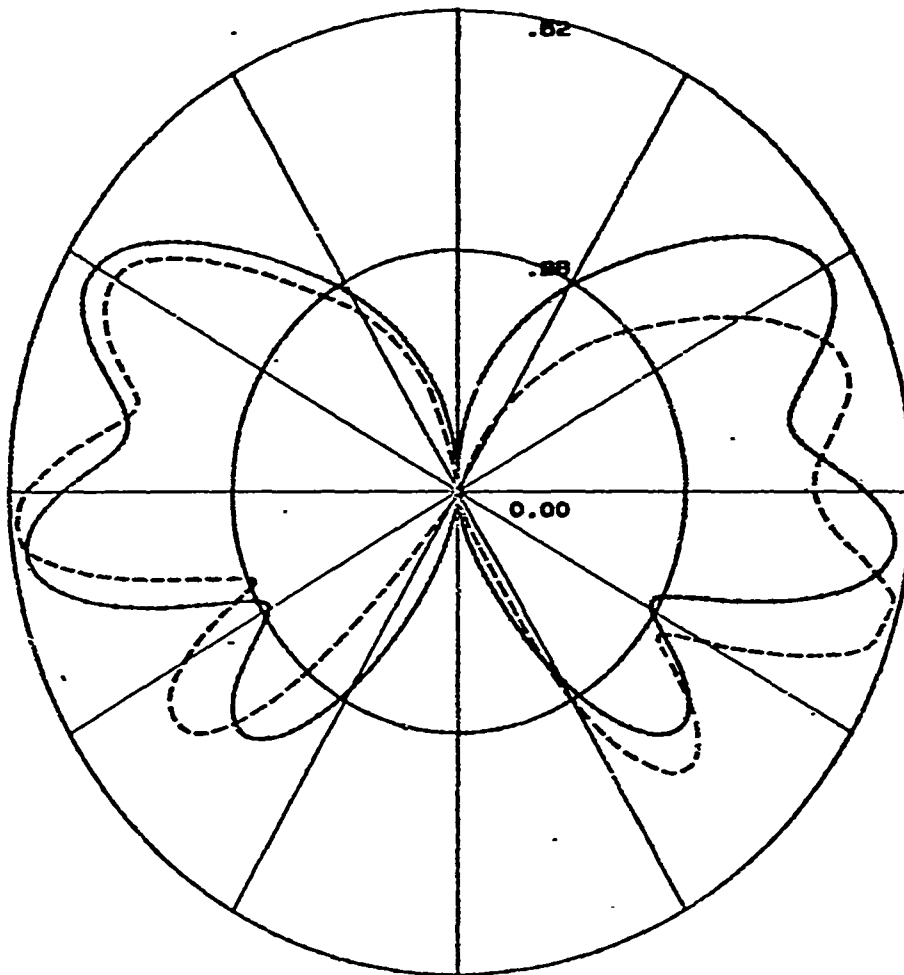
OUTTER RAD.=8.88

INDEX IS 1.28

DIPOLE OFFSET= .84

OBSERVATION RAD.=7.00

— Computed Exact Solution  
- - - Experimental Exact Solution [3]

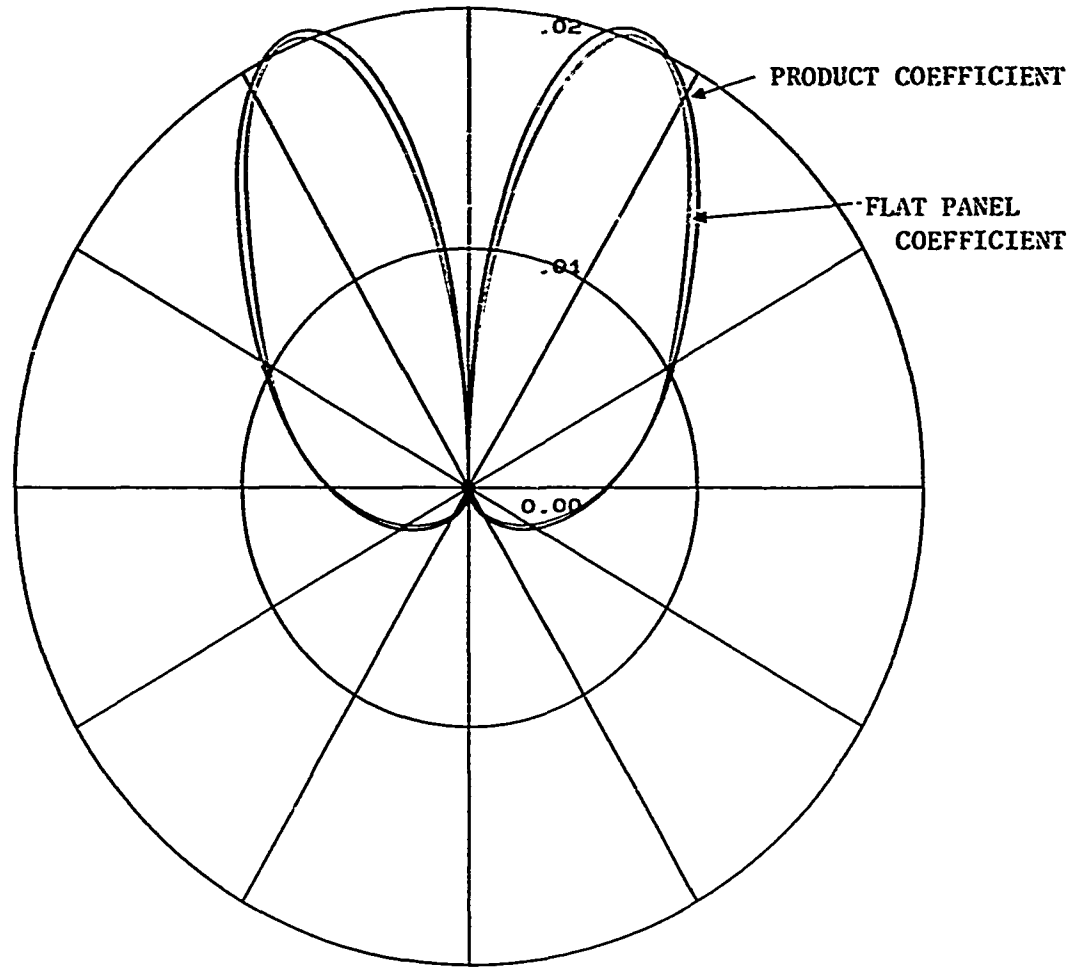


THIS GRAPH IS A POLAR PLOT OF THE MAGNITUDE  
OF THE E-FIELD AT AN OBSERVATION RADIUS.

FIGURE 5. Comparison of Experimental and Computed Exact  
Solutions

SPHERICAL RADOME

INNER RAD.-11.81  
OUTTER RAD.-14.17  
INDEX IS 3.000  
DIPOLE OFFSET-10.62  
OBSERVATION RAD.-15.00  
WAVELENGTH-1.181



ELECTRIC FIELD MAGNITUDE

FIGURE 6. Comparison of Product and Flat Panel Transmission Coefficients

GENERALIZED RADOME BSE CHARACTERIZATION  
USING SUPERPOSITION TECHNIQUES

Glenn Plimpton and Michael Cerullo  
Raytheon Company, Missile Systems Division  
Bedford, Massachusetts 01730

AD-P004 354

INTRODUCTION

Measurement of radome boresight error response to both polarization and gimbal angle variations can result in excessively long measurement times if a large number of incident polarizations are to be tested. Instead, by measuring the antenna radome system response to two orthogonal polarizations, and by using electro-magnetic superposition, it is possible to completely characterize the antenna/radome BSE response as a function of any arbitrary incident polarization.

Agreement between calculated and measured BSE for multiple linear incident polarization states is excellent. The method can also be applied to obtain multiple polarization antenna patterns in the presence of a radome.

This paper will focus on the details of implementing the generalized radome BSE characterization in the Bedford Automated Test Facility and will compare measured and superpositioned data.

A significant cost and time saving results from the use of superposition methods in radome testing.

ANALYSIS

Polarization Considerations in BSE Measurements and Calculations

Radome boresight error (BSE) contains the following constituent specifications,

- 1) Incident field polarization,  $\underline{E}_i = E_x \hat{x} + E_y \hat{y}$
- 2) Seeker antenna polarization,  $\underline{P} = P_x \hat{x} + P_y \hat{y}$

and

- 3) Radome complex transfer function,  $\underline{X}$

where 3) has finite cross coupling terms that permit the seeker to respond to an incident polarization spatially orthogonal to the seeker nominal polarization, and in general  $E_x$ ,  $E_y$ ,  $P_x$ ,  $P_y$  are complex quantities. For nominal vertically linearly polarized missile systems  $E_y = P_y = 1$  and  $E_x = P_x = 0$ .

The radome transfer matrix consists of elements  $X_{ij}$  which are responses (in the presence of the radome) in the  $i$ -polarized channel for  $j$ -polarization incident on the radome (receive formulation of radome problem assumed).  $X_{ij}$

for each complex gimbal angle are given analytically by the reaction integral equation (Reference 1) or can be measured with orthogonally polarized transmit antennas ( $E_y = 1, E_x = 0$  and  $E_y = 0, E_x = 1$ ).

Finally, the response  $V$  for arbitrary incident and antenna polarization is given by,

$$V = S_x P_x + S_y P_y$$

where

$$\begin{pmatrix} S_x \\ S_y \end{pmatrix} = \underline{X} \begin{pmatrix} E_x \\ E_y \end{pmatrix}$$

and the monopulse BSE may be derived from the delta over sum voltages, the monopulse sensitivity (co-pol), and the polarization dependent antenna null shift. True BSE would include a polarization dependent monopulse sensitivity as well.

### Test Station Application

From a measurement point of view the radome transfer matrix,  $\underline{X}$ , can be obtained by measuring antenna responses, in the presence of the radome, for two orthogonal linear transmit signals. In order to avoid receiver instabilities associated with large noise to signal ratios for the cross channel state (e.g.,  $E_x = 1$  and  $P_x = 0$  conditions) the orthogonal states chosen are

$$E_{x_0} = \pm 0.707$$

$$E_{y_0} = 0.707$$

for a typical

$$P_x = 0$$

$$P_y = 1$$

antenna. In this instance the radome transfer matrix  $\underline{X}$  becomes,

$$\underline{X} = \underline{T} \underline{X}' \underline{T}^{-1}$$

where,

$$\underline{T} = \text{coordinate transform for } 45^\circ \text{ axis rotation}$$

and

$$\underline{X}' = \text{measured antenna responses in the presence of the radome.}$$

A secondary potential problem to superposition measurements common to some (phase meter range  $\pm \pi$ ) automated test equipment is a nearly  $2\pi$  radians phase transition experienced in an antenna channel ( $\Delta$  pitch,  $\Delta$  yaw, or  $\Sigma$ ) voltage measurement which is computer sampled. If the computer samples voltage during phase transitions (during gimbaling) and computes BSE,

$$\text{BSE} = \text{Real} \left\{ \begin{array}{l} V_{\Delta}/V_{\Sigma} \\ S_{\Delta}/S_{\Sigma} \end{array} \right\}$$

where

$S_{\Delta}, S_{\Sigma}$  = monopulse sensitivities

a BSE as shown in Figure (1) could result. The probability of these transitions occurring increases when the antenna is receiving out of its nominal polarization plane. Retesting with  $\pi$  radians phase shift will relocate the indeterminate phase points in gimbal space. It is then possible to piece together the correctly sampled curve portions to define BSE over the desired gimbal angle range (see Figure (2)). This time-consuming retest process has been practically eliminated using a specially developed "deglitching" computer program.

The new approach operates directly on the antenna port voltages. First, voltage arguments (phases) are differentiated twice with respect to gimbal angle. Then, based on  $\partial^2\phi/\partial G^2$ , voltage points are retained or deleted. Next, gaps between retained voltage points are filled by fitting a complex third order polynomial to adjacent point pairs (Lagrange interpolation formulas). The method can be generalized to any order polynomial should future data indicate that further refinement is necessary.

#### MEASURED DATA

##### Data Sets

Global (off-axis, 32 cuts) BSE data were taken on an X-band radome of fineness ratio 2.50 for two conditions

- 1)  $\pm 45^\circ$  plane basis data, i.e.,  $E_x = \pm 0.707, E_y = 0.707$
- and
- 2) linear BSE for polarization angles ( $\alpha$ ) zero to  $87^\circ$

For comparison with data set (2) the data in set (1) were combined or superimposed, using the techniques outlined in section 2.1. The comparison plots are given in Figure 3. Good agreement exists between the measured and synthesized BSE multiple polarization data sets.

##### Data Reduction

The multiple polarization equations used to reduce test station data can be expressed in the following summary form for a y-polarized linear antenna:

$$V = aV_{x-pol} + bV_{co-pol}$$

where

$$V_{x-pol} = X_{21}, \quad a = E_x$$

$$V_{co-pol} = X_{22}, \quad b = E_y$$

and the complex coefficients  $a$ ,  $b$  define any linear, circular or elliptic polarization state using standard (Gamma) formulations (Reference 2).

#### CONCLUSION

A general method of calculating multiple polarization BSE data based on only two measurements has been developed. Comparison between superimposed orthogonal measured data and measured linear multiple polarization BSE confirms the applicability of the method from a radome test and evaluation viewpoint. The intended use of the characterization technique is to economize testing time required to characterize the polarization dependence of BSE.

#### ACKNOWLEDGEMENTS

The authors acknowledge the help of M. Fassett, who supervised the development project and suggested the use of tilted measurement basis axis, of K. Siwiak, who suggested the superposition applicability, and of D.K. Allen and A.J. LaCroix, who performed the radome measurements.

#### REFERENCES

1. D.G. Burks, E.R. Graf, M.D. Fahey, "Effects of Incident Polarization on Radome - Induced BSE", Proc. Fifteenth Symp. Electromagnetic Windows, Georgia Inst. of Tech, pp. 1-5, June 1980.
2. J.D. Jackson, Classical Electrodynamics, Wiley & Sons, N.Y., 1975, pp. 273-278.



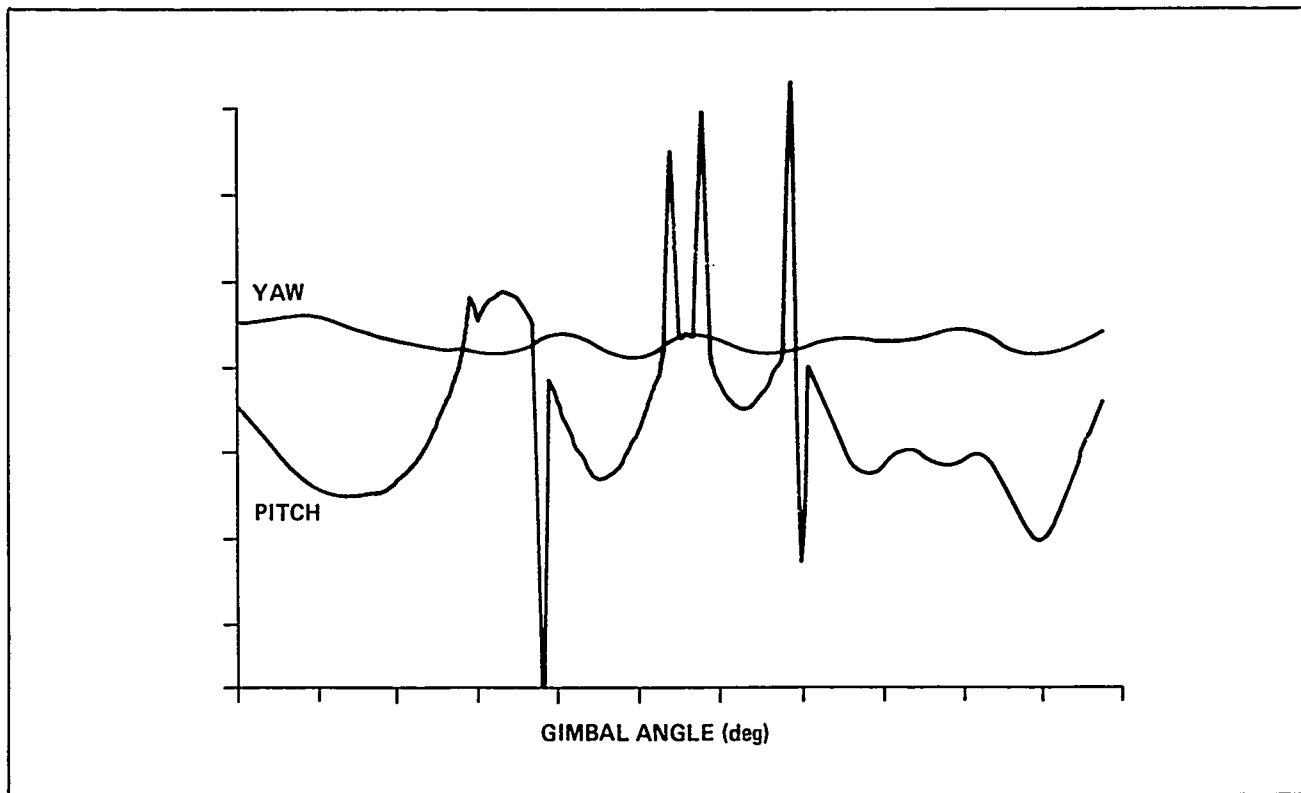


Figure 1. BSE vs Gimbal Angle without Computer Sampled Voltage Phase Corrections

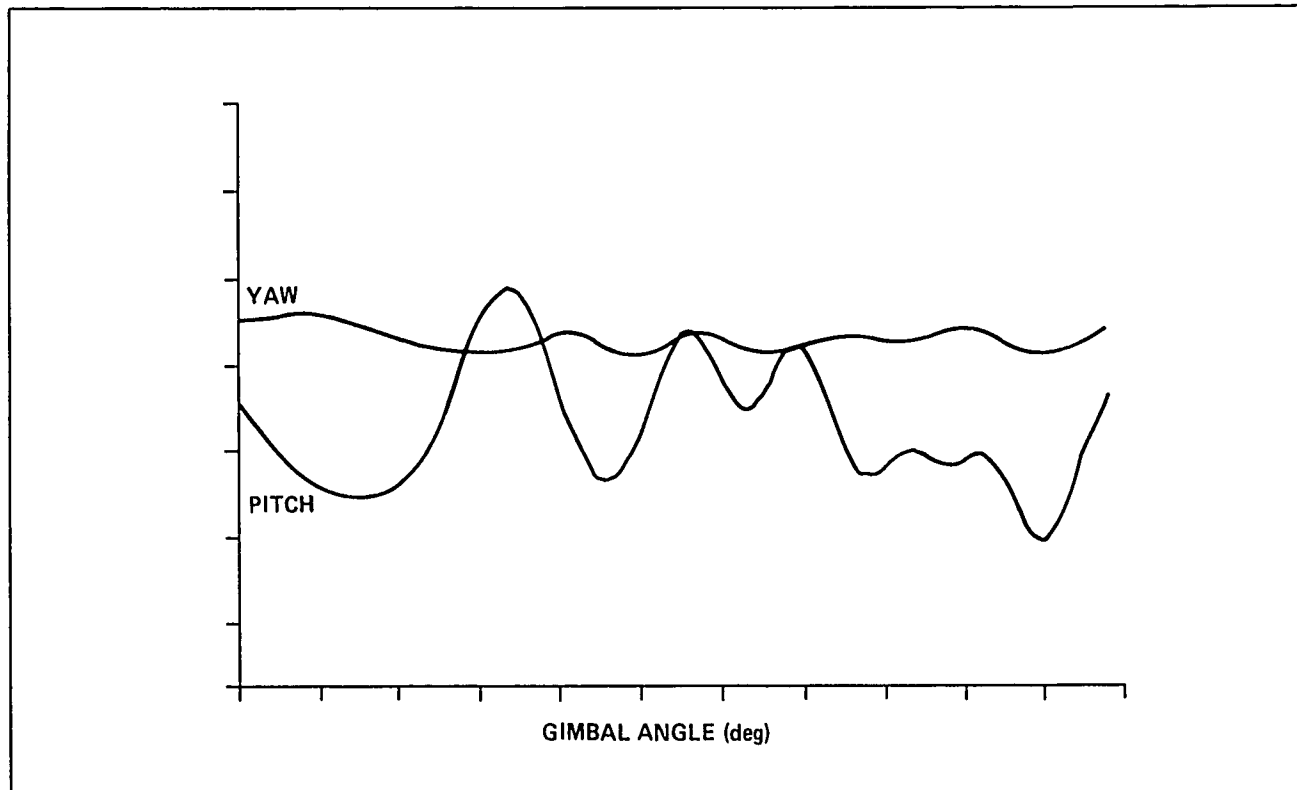


Figure 2. BSE vs Gimbal Angle with Computer Sampled Voltage Phase Corrections

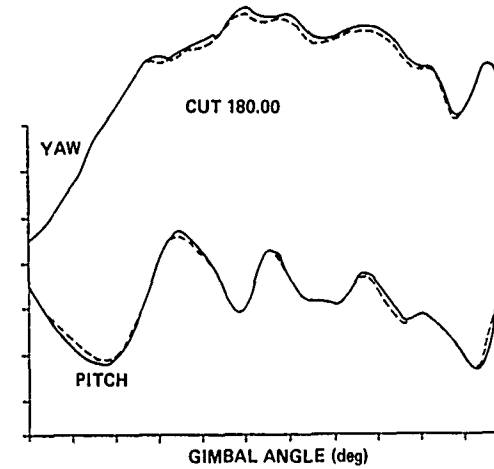
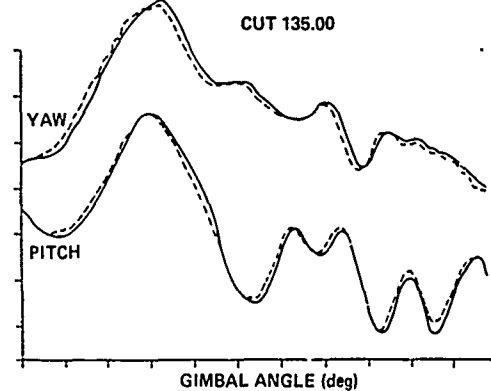
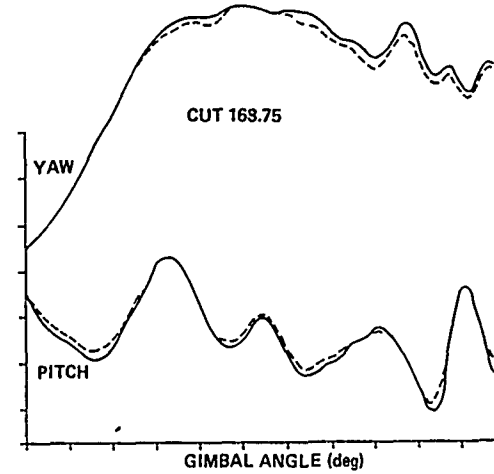
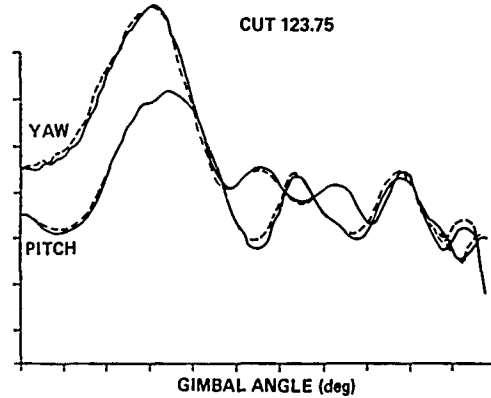
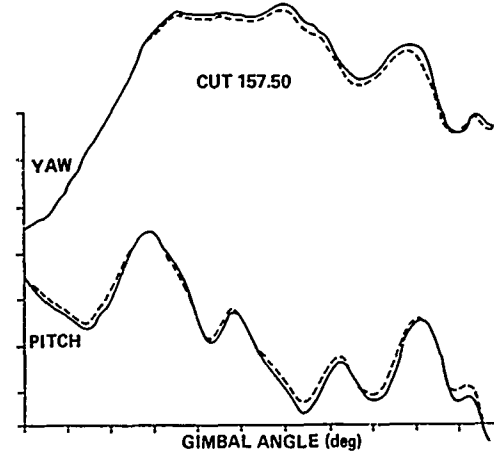
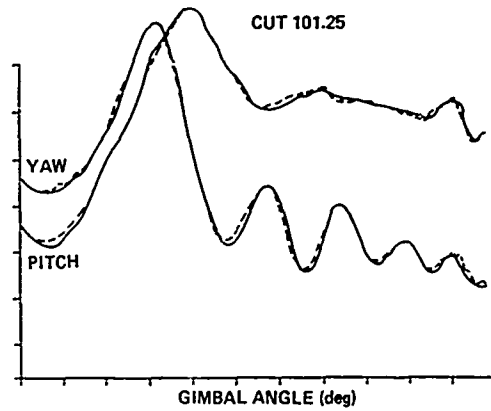
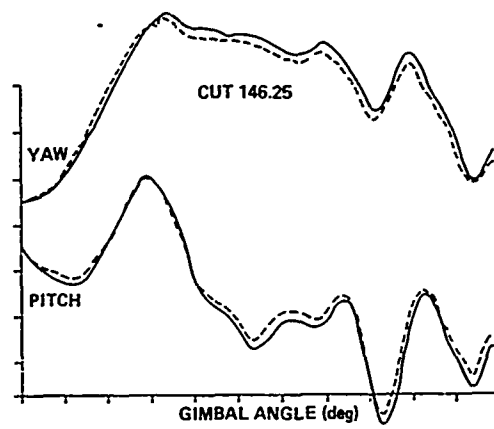
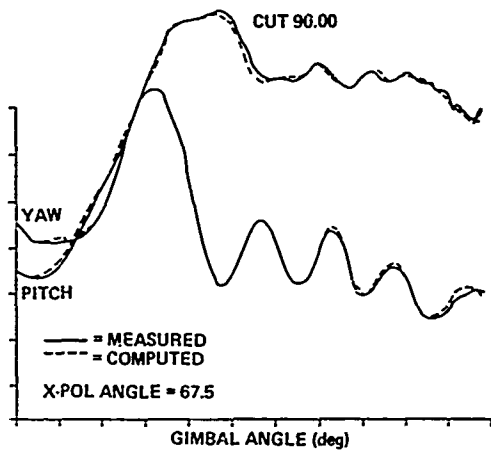


Figure 3. Computed and Measured Cross-polarization BSE Data

→

A SUBAPERTURE APPROACH TO THE CALCULATION OF  
FLASHLOBES INTRODUCED BY AIRBORNE RADOMES

A Hizal\*, R W Lyon\*\* and A Cuthbertson\*\*

\* Middle East Technical University, Ankara, Turkey.

\*\* ERA Technology Ltd., Leatherhead, Surrey, UK.

AD-P004 355

1 INTRODUCTION

In airborne radomes a considerable effort has been devoted to the calculation of boresight errors but little attention has been given to the computation of flashlobes. These are caused by reflections from the radome wall and generally appear at angles well away from the boresight of the enclosed antenna (Ref:1). In certain circumstances they can seriously compromise the sidelobe suppression of the overall system.

To date most flashlobe calculations have been performed by using a simple ray tracing approach which gives their approximate amplitude and direction but yields little additional data regarding their shape (Ref.2).

This paper describes an efficient method for flashlobe prediction which gives more detailed information and can be used in an optimisation of radome shape and wall build. The technique is based on the subaperture method which has already been successfully used to predict other bulk radome effects (Ref:3).

Theoretical predictions of the flashlobe level are presented for a circular horn enclosed by a radome with each at two different nose shapes. Measured results are also presented and are shown to be in good agreement.

## 2 DISCUSSION OF THEORY

In calculating the angular position and the pattern of the flashlobes in airborne radomes, the ray tracing technique is attractive because of its simplicity in the formulation. The antenna aperture can be subdivided into rectangular subapertures, small enough so that each subaperture illuminates the radome by its far-field. The flashlobe field due to a subaperture can be calculated by tracing a ray from a point  $O_s$  within the subaperture to a far-field point  $Q$  through the reflection and the transmission points  $P_1$  and  $P^*$ , respectively. First, the rays will be geometrically traced from a chosen far-field point  $Q$  via a set of chosen reflection points  $P_1$ 's on the radome surface  $S$  to the hit points  $O_s$  within the subapertures. For a given  $Q$  and a set of  $P_1$ 's on  $S$ , all or some of the subapertures will be hit, which are considered to be the contributing subapertures to the field at  $Q$ . The resulting total flashlobe field at  $Q$  is the sum of the fields due to the rays traced back from each  $O_s$  to  $Q$  via the points  $P_1$  and  $P^*$  (see Fig.1).

The plane of reflection is formed by  $\vec{r}_1$  and  $\hat{n}_1$  while the plane of transmission is formed by  $\vec{r}_2$  and  $\hat{n}$ . The two planes are generally non-parallel. The point  $P^*$  can be found analytically by solving a quadratic equation.

Assuming that the subaperture fields are uniform and equal to the aperture field at  $O_{ij}$  i.e.  $E_{ij,x}^a$  and  $E_{ij,y}^a$ , the field on the incident ray  $\vec{r}_1$  can be written as

$$E_{ij,x} = U \cos \theta_1 E_{ij,x}^a$$

$$E_{ij,y} = U \cos \theta_1 E_{ij,y}^a$$

$$E_{ij,z} = -U \sin \theta_1 (E_{ij,x}^a \cos \theta_1 + E_{ij,y}^a \sin \theta_1)$$

$$U = \frac{j k_0 e^{-jk_0 r_1}}{2 \pi r_1} \exp(-jk_{x_1} \cdot \Delta x - jk_{y_1} \cdot \Delta y) a b_i \operatorname{sinc} \left( k_{x_1} \cdot \frac{a}{2} \right) \operatorname{sinc} \left( k_{y_1} \cdot \frac{b_i}{2} \right)$$

where  $\theta_1$  and  $\phi_1$  are the spherical angles along  $\vec{r}_1$ ,  $\Delta x = x_s - x_i$ ,  $\Delta y = y_s - y_{ij}$ ,  $a$  and  $b_i$  are the dimensions of subaperture,  $k_{x_1} = k_0 \sin \theta_1 \cos \phi_1$ ,

$k_{y_1} = k_0 \sin \theta_1 \sin \phi_1$  and  $\operatorname{sinc}(x) = (\sin x)/x$ .

The field along the reflected ray can be found by using the principle of geometrical optics as illustrated in Fig.2. The radome will be considered to be a planar slab, possibly stratified along  $\hat{n}_1$ . The reflection coefficients for // and  $\perp$  polarisations are used for these two components of the incident field. The resultant reflected field is then again decomposed into // and  $\perp$  components with respect to the plane of transmission ( $\hat{x}_2, \hat{n}$ ) and the transmitted field at Q, is calculated by using the transmission coefficients for the two polarizations for a planar slab at P, which is also stratified along  $\hat{n}$ . The calculations involve coordinate transformations of the unit vectors and the coordinates from the antenna coordinates (x, y, z) to the radome coordinates (x', y', z') and vice versa. The coordinates of P is found by solving the problem of intersection of the line  $P_1Q$  by the radome, which is analytically possible for a quadric surface. The radome is assumed to be rotated about  $y = y'$  axis by an angle  $\alpha = \cos^{-1}(z, z')$ . The antenna aperture center O is reached by moving from O', the center of radome, by  $z_r$  along  $z'$  and then by  $z_o$  along  $z$ . When a large number of reflection points  $P_1$ 's are chosen, some subapertures are hit more than once due to adjacent reflection points. Such multiple hits are rejected in the algorithm by using a suitable criteria. On the other hand for curved radomes such as an ogive, multiple hits of subapertures for a given point Q are expected because of the focusing effect of the surface. The true multiple hits are sensed by noticing that they occur due to sufficiently remote reflection points  $P_1$ 's.

The reflection and transmission coefficients of the slab for the // polarization can be expressed by

$$R_{//} = (\phi_{22} + c\phi_{21} - \phi_{11} - \phi_{12}/c) / (\phi_{22} + c\phi_{21} + \phi_{11} + \phi_{12}/c)$$

$$T_{//} = 2 \exp(jk_o d c) / (\phi_{22} + c\phi_{21} + \phi_{11} + \phi_{12}/c)$$

where  $c = \cos\beta$  for reflection and  $c = \cos\psi$  for transmission,  $d$  is the total thickness of the slab and  $\phi_{ij}$ 's are the matrix elements of the total transition matrix  $\phi_n^T$  for an  $n$ -layer slab. It is known that  $\phi_n^T = \phi_n \phi_{n-1}^T$  where  $\phi_n$  is the transition matrix of the  $n^{\text{th}}$  layer whose elements are given by  $\phi_{n,12}(//) = jZ_n \sin\Gamma_n$ ,  $\phi_{n,21}(//) = (j/Z_n) \sin\Gamma_n$ ,  $\phi_{n,11}(//) = \phi_{n,22}(//) = \cos\Gamma_n$ . Where  $\Gamma_n = (\epsilon_{rn} - s^2)^{1/2} k_o d_n$ ,  $Z_n = (\epsilon_{rn} - s^2)^{1/2} / \epsilon_{rn}$ ,  $Y_n = (\epsilon_{rn} - s^2)^{1/2}$ ,  $s = \sin\beta$  (or  $\sin\psi$ ). For the  $\perp$  polarization, in the above formulae one should replace all  $\phi_{ij}(//)$  by  $(-1)^{i+j} \phi_{ji}(\perp)$  and  $Z_n$  by  $Y_n$  in the expression of  $\phi_{n,ij}$ ;  $i \neq j$ . The thickness  $d_n$  and the relative complex permittivity  $\epsilon_{rn}$  of each layer should be specified.

### 3 DISCUSSION OF RESULTS

In order to test this theory a solid GRP radome with exchangeable round and pointed ends was manufactured. The test antenna used was a circular horn with a diameter of  $20 \lambda_0$  and fitted with a phase correction lens. In all the results presented in this paper the antenna was vertically polarised and the results measured in the horizontal plane.

The measured radiation pattern of the horn alone is given in Fig.3 together with the pattern predicted using the subaperture method (Ref.3). In this computation it was assumed that the horn was radiating in the  $TE_{11}$  mode and that a residual  $110^\circ$  quadratic phase error across the aperture remained uncorrected.

In Fig.4 the measured far field pattern of the horn with pointed radome together with the theoretically predicted flashlobe is illustrated. It is evident that the theory predicts both the angle and shape of the flashlobe accurately. In Fig.5 the theoretical and experimental results for the radome/horn configuration with a round nose are presented. The theory predicts a reduction of the peak flashlobe level and this is confirmed experimentally.

#### ACKNOWLEDGEMENT

This work has been carried out with the support of the Procurement Executive, Ministry of Defence, UK.

#### REFERENCES

1. Cary, R H J: 'Radomes', Ch.4 of The Handbook of Antenna Design', ed. Rudge, A W; Milne, K; Olver, A D and Knight, P, published by Peregrinus, 1983, pp.458-552.
2. Scorer, M: 'The calculation of radome induced sidelobes', RADAR-77, 25-28 October 1977, pp.414-418.
3. Hizal, A; Adatia, N and Gupta, S: 'Depolarisation properties of airborne radomes', Proc. Military Microwave Conference, London, UK, pp.493-499.

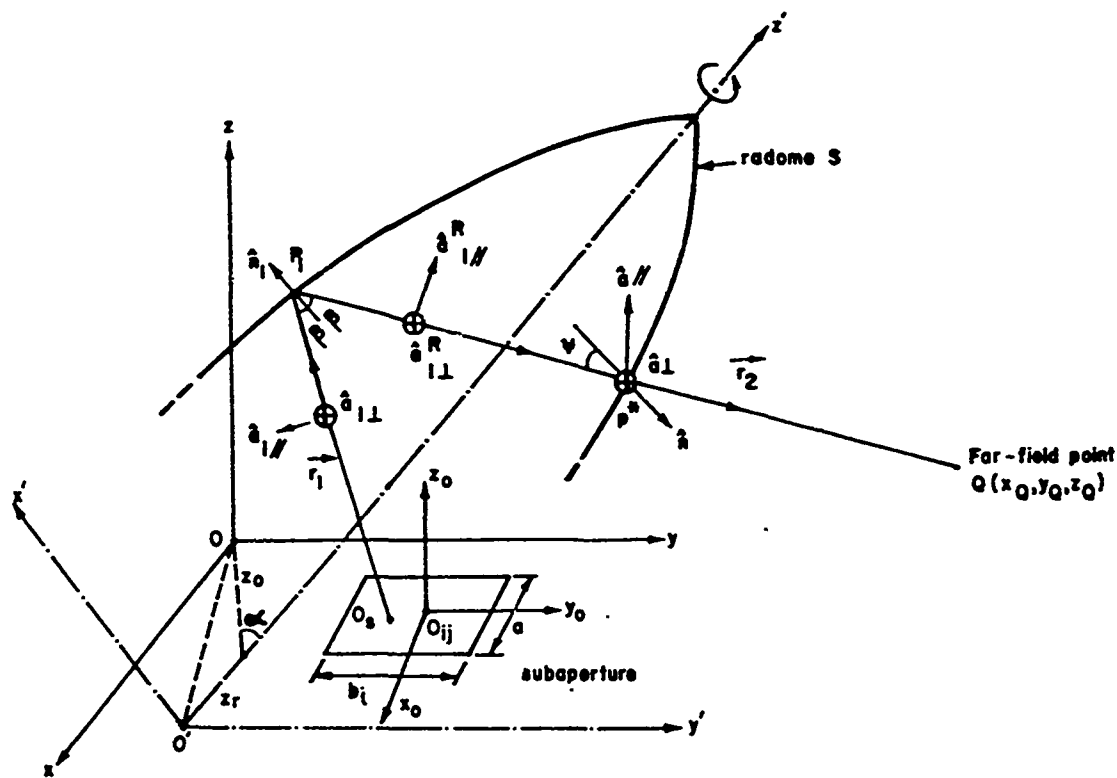


Fig. 1 Geometry of the radome and the ray tracing for flashlobe.

- $\vec{r}_1 \equiv \vec{O_s P_1}$  = incident ray for reflection,
- $\vec{P_1 P^*}$  = incident ray for transmission
- $\vec{P^* Q}$  = transmitted ray ( $\vec{r}_2 \equiv \vec{P_1 Q}$ )
- $O_{ij}$  = subaperture center point
- $O_s$  = Hit point of subaperture by a ray traced from Q via chosen reflection point  $P_1$ .

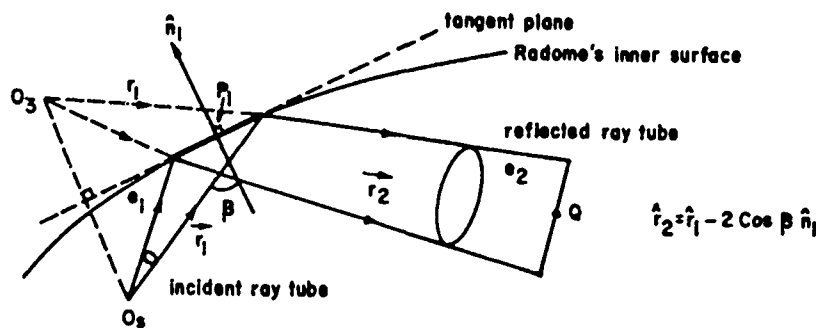


Fig. 2 Reflection geometry of the incident ray. The reflected wave function is  $e_2 = e_1 r_1 \exp(-jk_0 r_2) / (r_1 + r_2)$ .

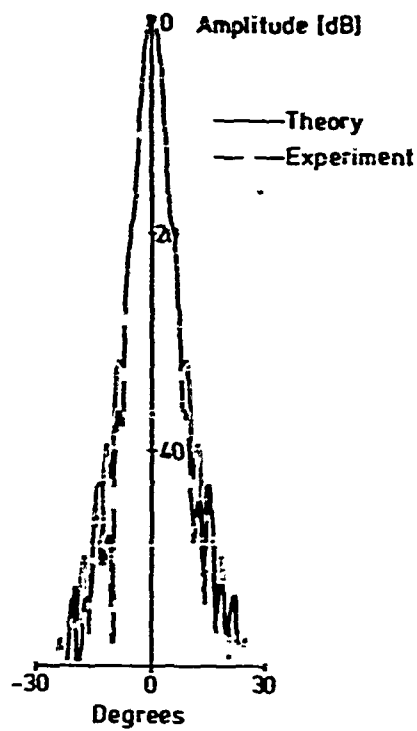


Fig.3: Radiation pattern of horn

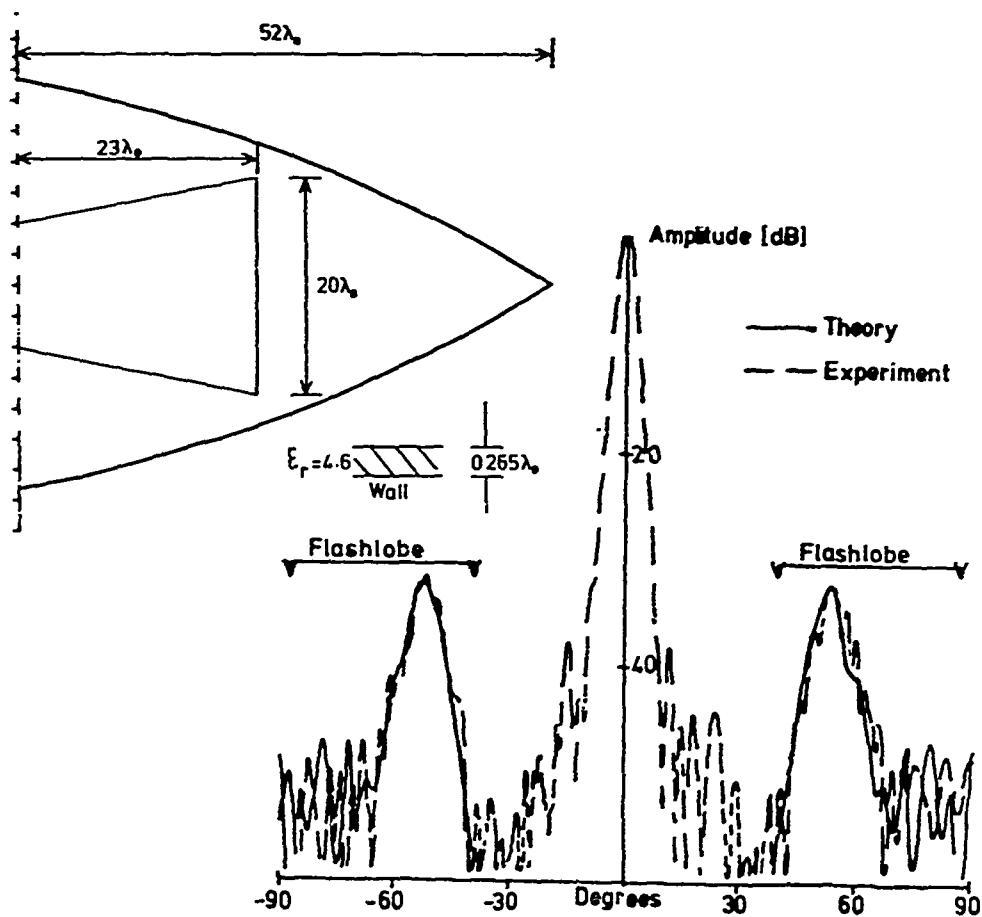


Fig.4: Flashlobe due to pointed radome



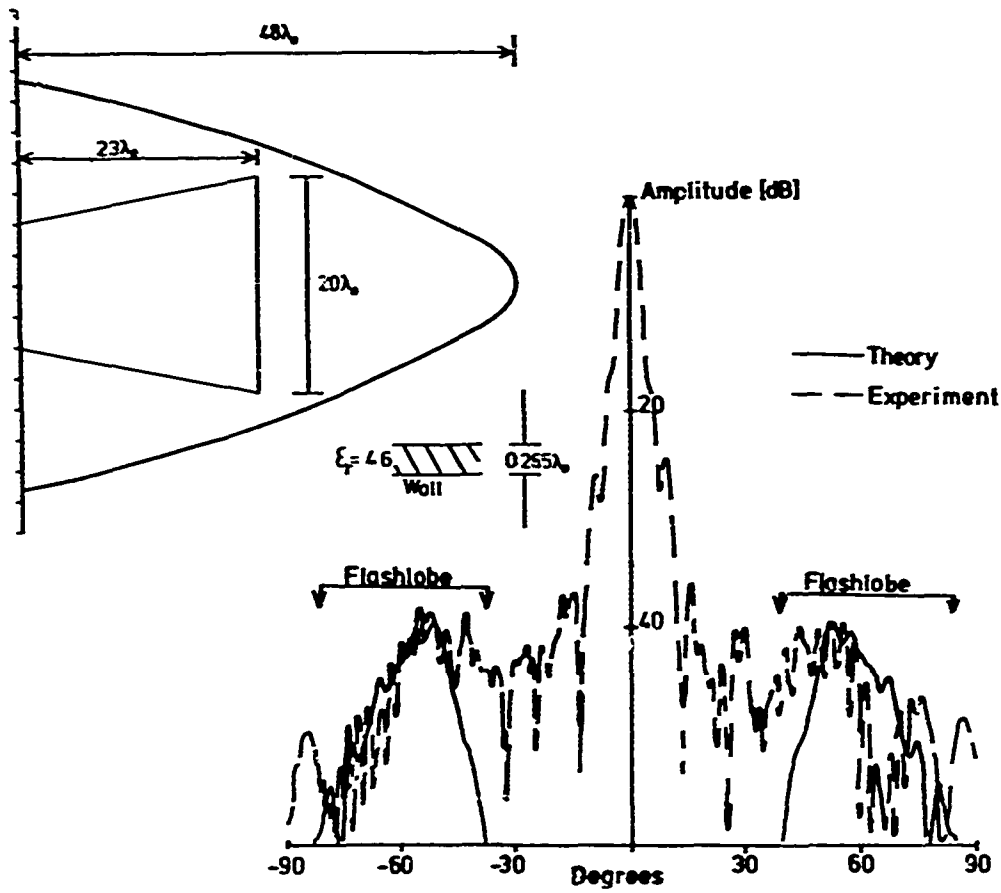
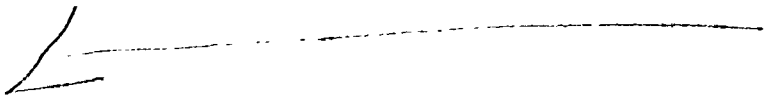


Fig.5: Flashlobe due to round nosed radome



G K. Huddleston  
 School of Electrical Engineering  
 Georgia Institute of Technology  
 Atlanta, Georgia 30332

AD-P004 356

### Introduction

A computer-aided simulation of a boresight error measurement procedure and facility was carried out to quantify the effects of separation distance and wave reflections from anechoic chamber boundaries on radome-induced boresight errors using two BSE algorithms.

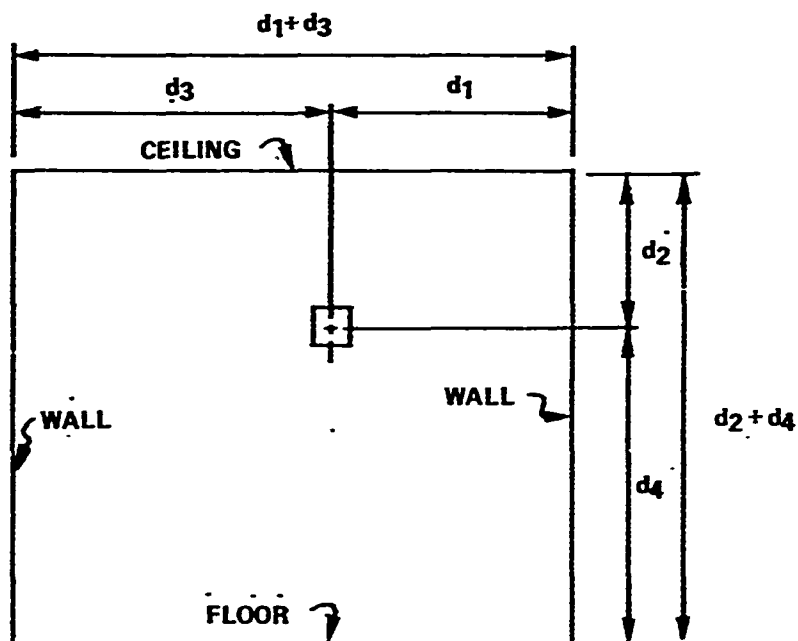
The 3-D radome analysis program described earlier [1] was modified to include near-field and reflection effects as illustrated in Figure 1. Waves emanate from the source antenna in the directions indicated by the rays (one arrowhead). These direct rays impinge on the radome as shown. Note that the angles of incidence on the radome wall for these rays are different than those of a true plane wave (horizontal rays).

Some of the rays emanating from the source antenna strike the walls, floor, and ceiling of the chamber and are reflected onto the radome. These reflections can be conveniently included using image sources, one for each boundary of the chamber (4 total). Each image is mirrored into the associated boundary and is given strength  $E'$  with respect to the actual source strength  $E_0$  according to

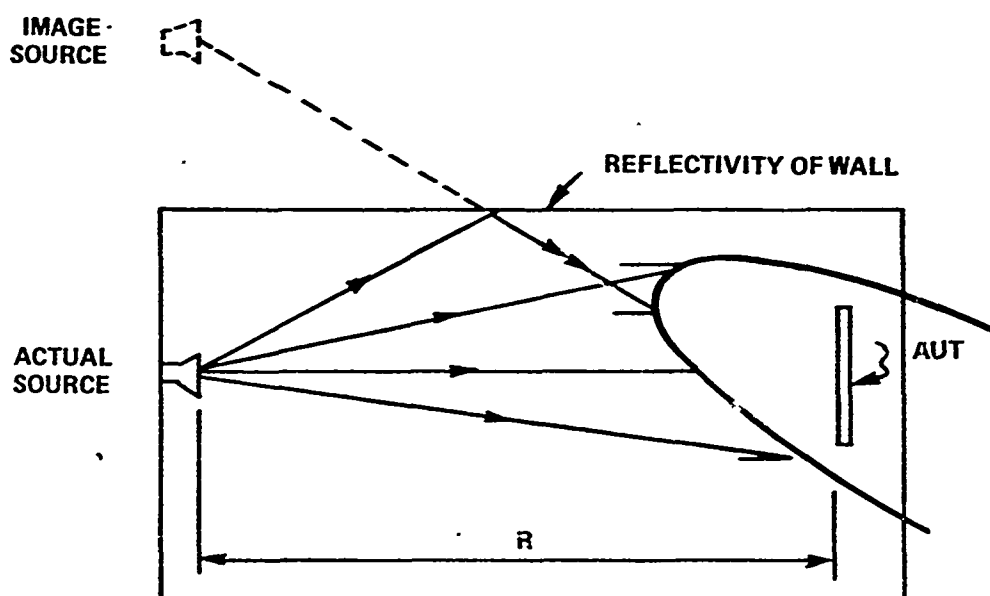
$$\frac{E'}{E_0} = 10^{(-R_{dB}/20)} \quad (1)$$

where  $R_{dB}$  is the reflectivity of the chamber wall in decibels. The reflectivity is assumed to be independent of incidence angle.

PREVIOUS PAGE  
IS BLANK



(a) VIEW OF SOURCE ANTENNA AT FAR END OF CHAMBER.



(b) TOP VIEW OF CHAMBER SHOWING ONE IMAGE SOURCE.

FIGURE 1. GEOMETRY OF BORESIGHT ERROR MEASUREMENT SIMULATION.

## BSE Algorithms

Three BSE measurement procedures or algorithms were simulated: null seeker, 1-point method, and 2-point method. In the null seeker method, the computation is done such that the source is moved around until nulls are obtained in each  $\Delta/\epsilon$  signal channel of the monopulse antenna. The direction to the source when it is in the null position is defined as the boresight error.

Figure 2 shows tracking functions computed for the radome/antenna combination under test, where the tracking functions in elevation and azimuth are defined by

$$f_{EL} \stackrel{\Delta}{=} \text{Im} \left\{ \frac{\Delta_{EL}}{\int} \right\} \quad (2a)$$

$$f_{AZ} \stackrel{\Delta}{=} \text{Im} \left\{ \frac{\Delta_{AZ}}{\int} \right\} \quad (2b)$$

Four computed tracking functions are shown in Figure 2 as indicated on each graph. The tracking functions are graphed versus the angle  $\theta$  from boresight in a diagonal plane defined by  $x_A = y_A$  in antenna coordinates. Without the radome,  $f_{EL}$  and  $f_{AZ}$  are almost identical so that only one solid graph is shown for both functions. When the radome is placed over the antenna and aligned with the true antenna boresight (Pitch =  $0^\circ$ , Yaw =  $0^\circ$ ), the tracking functions are slightly different as indicated by the AZ( $0^\circ, 0^\circ$ ) and EL( $0^\circ, 0^\circ$ ) graphs. Note also that the slopes of these functions (monopulse error slope MES) are different but are approximately equal to the MES of the antenna without the radome. Finally, the offset dash graph EL( $6^\circ, 0^\circ$ ) of Figure 2 shows the elevation tracking function when the radome is pitched up by  $6^\circ$ ;  $f_{AZ}$  is essentially the same as for the ( $0^\circ, 0^\circ$ ) case.

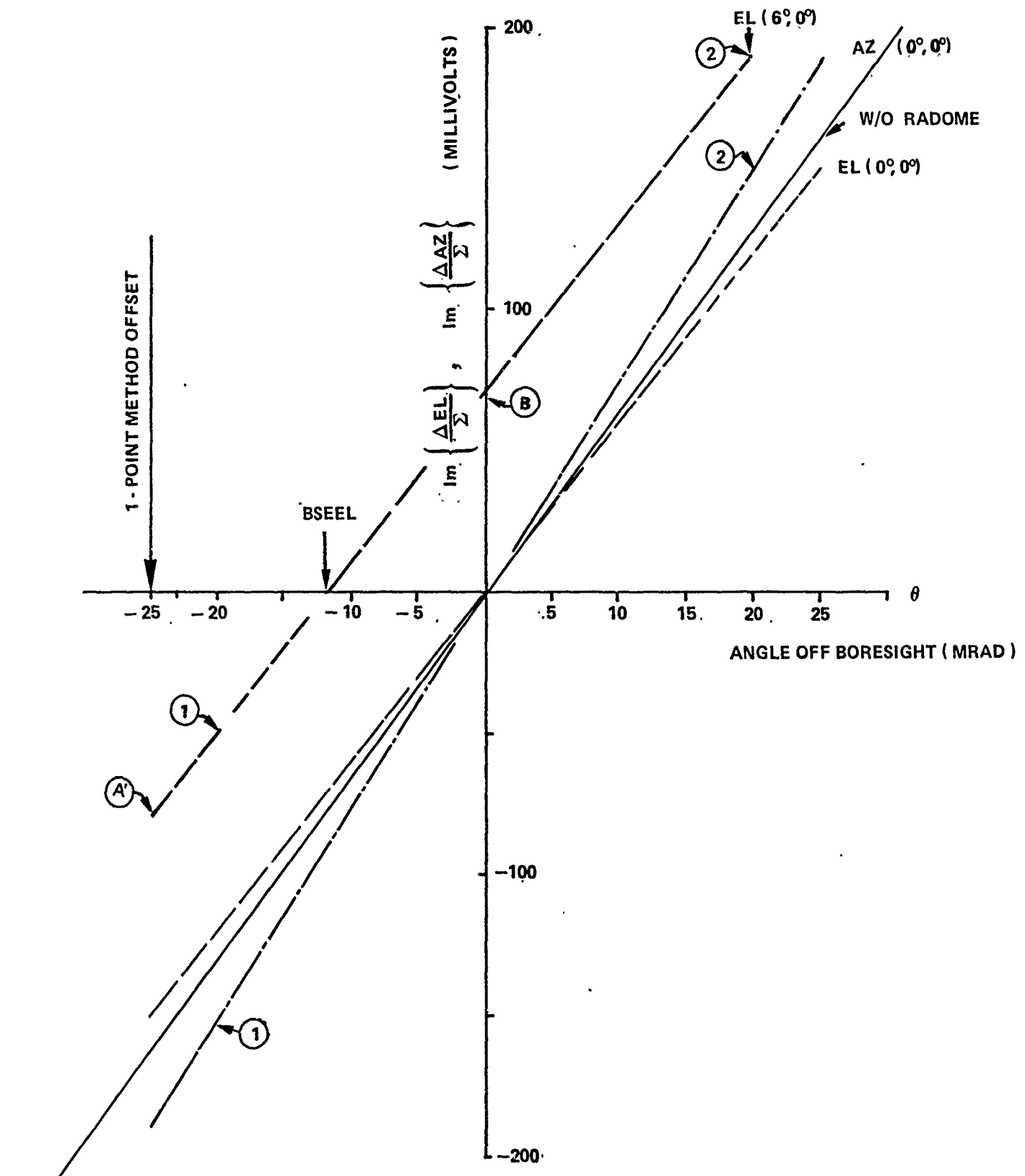


FIGURE 2. TRACKING FUNCTIONS IN ELEVATION (---) AND AZIMUTH (— · —) PLANES WITH AND WITHOUT (—) RADOME FOR (0,0) ORIENTATION.

The BSE algorithms can be explained using the EL(6°,0°) graph of Figure 2. The null seeker algorithm finds the zero-crossing of the tracking functions  $f_{EL}$  and  $f_{AZ}$ :  $f_{EL} = 0$  at -11.5 mrad;  $f_{AZ} = 0$  at 0 mrad in Figure 2. The 2-point method uses the values of each tracking function computed at only two points at  $\pm 20$  mrad to generate a linear estimate of each tracking function, and, hence, an estimate of where the zero crossings occur.

The 1-point method uses the single value of each tracking function as measured when the target is located on the true boresight of the antenna. This single value (Point B in Figure 2), combined with the MES, yields the following linear tracking model

$$f_{EL} = \text{MES}_{EL} \theta_{EL} + B_{EL} \quad (3)$$

where the ordinate intercept  $B_{EL}$  is given in terms of the measured tracking function at the known angle  $\theta = 0$  mrad by

$$B_{EL} = f_{EL} (\text{@ Boresight}) \quad (4)$$

The zero-crossing, or  $\text{BSE}_{EL}$ , is then obtained by setting Eqn. (3) equal to zero and solving for  $\theta_{EL}$ ; i.e.,

$$\theta_{EL} = \frac{f_{EL} (\text{@ Boresight})}{\text{MES}_{EL}} = \text{BSE}_{EL} \quad (5)$$

A similar treatment holds for the azimuth tracking function.

In the 1-point method, the monopulse error slope that should correctly be used is the slope of the tracking function for that particular radome orientation. In practice, the true slope is not used; instead, the MES of the

antenna without the radome is used in Eqn. (5). The significance of this source of error is investigated in the following presentation of the BSE measurement simulation.

### Simulation Results

Three medium-size antenna radome combinations having the parameters shown in Table 1 were used in the simulation. Radome 1 is the tangent ogive alumina radome described earlier by Siwiak, et al. [2] for which measured BSE data are available and indicated on the following figures for reference. The radome parameters include dielectric constant  $\epsilon_r$ , radome base diameter  $D_{OS}$ , radome length  $L_{OS}$ , aperture offset  $R_A$  from gimbal point, distance  $R_R$  along radome axis of symmetry from base of radome to antenna gimbal point, distance  $L_1 = L_{OS} - (R_A + R_R)$  of aperture to radome tip, antenna diameter  $D$ , and uniform radome wall thickness  $d_{wall}$ . All three radomes have the tangent ogive shape. Radomes 1 and 2 are alumina radomes and differ only in fineness ratio. Radome 3 is a fused silica radome and differs primarily in placement of the antenna and wall thickness.

The effects of distance (no reflections) on predicted boresight errors in the pitch plane for the null seeker and 1-point algorithms are shown in Figure 3 for Radome 1. The radome shape and sum channel antenna patterns are indicated at the top of the figure: the lower half of the pattern is for the elevation plane of the vertically polarized antenna; the upper half is for the azimuth plane. In Figure 3(a), curves 2-3 and 4-5 show that the null seeker and 1-point algorithms yield identical results at both large ( $16L_1^2/\lambda$ ) distance of separation and small ( $4D^2/\lambda$ ) separation when no reflections from chamber boundaries are considered. This agreement between the algorithms was found to hold very closely for other conditions; hence,

Table 1. Radome Parameters Used in Boresight Error Measurement Stimulation

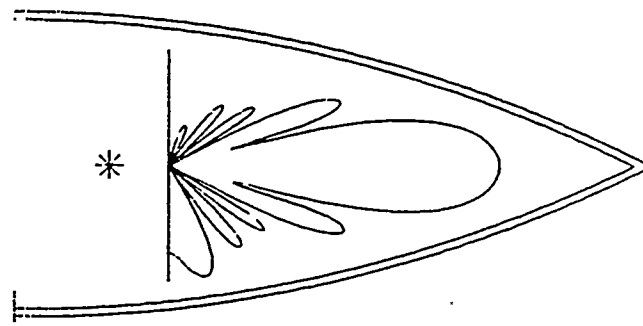
Radome <u>ID</u>	$\epsilon_r$	$\frac{D_{OS}}{\lambda}$	$\frac{L_{OS}}{\lambda}$	$\frac{R_A}{\lambda}$	$\frac{R_R}{\lambda}$	$\frac{L_1}{\lambda}$	$\frac{D_{AP}}{\lambda}$	$\frac{d_{wall}}{\lambda}$
1	9.30	6.81	14.87	1.40	2.21	11.26	5.16	.17553
2	9.30	6.81	20.44	1.40	2.21	11.26	5.16	.17807
3	3.33	6.78	20.34	.77	4.96	14.60	5.51	.32111

Chamber Dimensions (Figure 1):

$$d_1 = 25.81\lambda \quad d_3 = 26.13\lambda$$

$$d_2 = 50.30\lambda \quad d_4 = 49.43\lambda$$



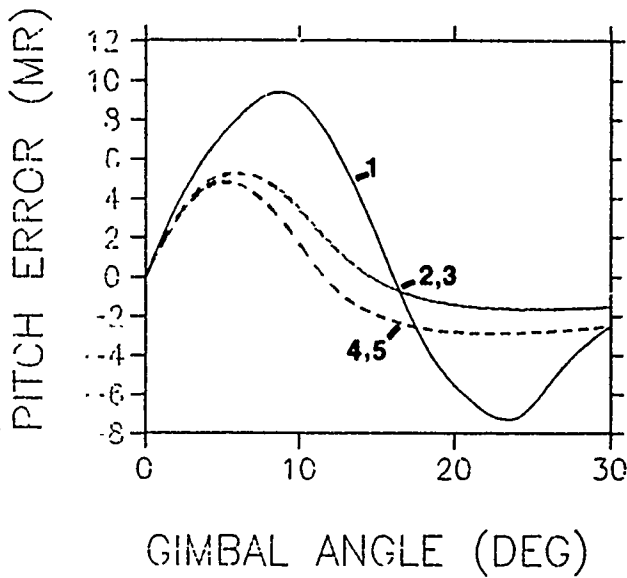


LEGEND

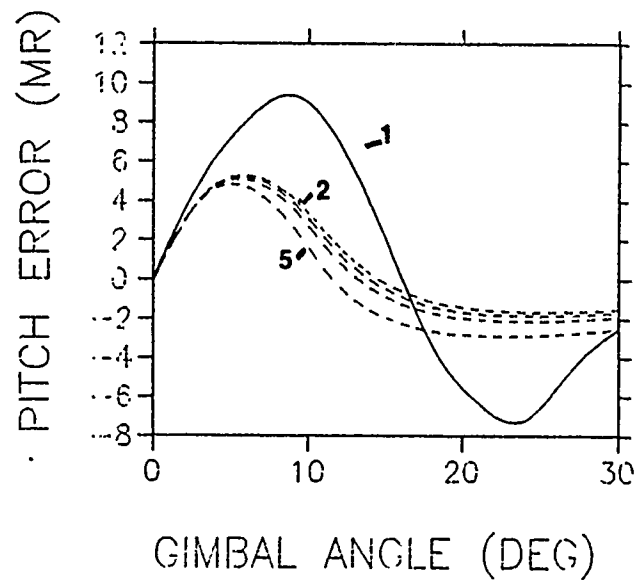
MEAS.	
1	$16L_1^2/\lambda$ NS
2	$16L_1^2/\lambda$ 1P
3	$4D^2/\lambda$ NS
4	$4D^2/\lambda$ 1P
5	

LEGEND

MEAS.	
1	$16L_1^2/\lambda$ 1P
2	$4L_1^2/\lambda$
3	$2L_1^2/\lambda$
4	$4D^2/\lambda$
5	



(a) Comparison of algorithms.



(b) Effects of distance on 1-point algorithm.

Figure 3. Effects of Distance on Predicted Boresight Errors in Pitch Plane for Radome 1 Using Null Seeker and 1-Point Algorithms.

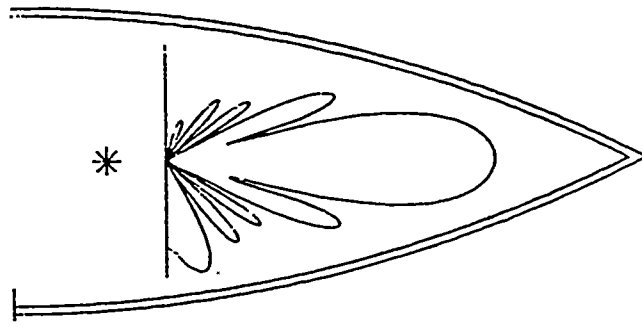
only the 1-point results are presented in subsequent data.

The distance of separation  $R = 16L_1^2/\lambda$  was chosen to simulate  $R = \infty$ . The distance  $R = 4D^2/\lambda$  corresponds to the generally accepted minimum distance recommended for measuring antenna patterns, where  $D$  is the antenna aperture diameter. The effects of these and other distances on the 1-point BSE predictions are shown in Figure 3(b). From curves 2-3, it is seen that a maximum error in BSE of approximately 0.5 mrad occurs when  $R = 4L_1^2/\lambda$ , or a 10% error. If the distance is reduced to  $4D^2/\lambda$ , curve 5 indicates a maximum error of 1.5 mrad, or 30%. Similar results are obtained in the yaw plane as shown in Figure 4(a).

The measured data for Radome 1 as reported earlier by Siwiak are also shown in Figures 3 and 4 for reference. The simulation results agree with the general trends of the measured data, but good agreement cannot be claimed. Efforts are underway to correct the deficiencies in the radome analysis method used: (1) an algorithm for computing transmission coefficients for curved radome walls is being developed; (2) the reaction of first-order scattered fields is being included.

The predicted effects of chamber reflections on the 1-point BSE algorithm for Radome 1 are shown in Figure 4(b) for separation distance  $4D^2/\lambda$ . It is seen that reflectivities less than -30dB result in BSE errors of less than 0.5 mrad with respect to the no-reflections case at the same distance.

The effect of separation distance on BSE is more pronounced for a more streamlined radome as shown by the data in Figure 5(a) for Radomes 1 and 2. Radome 1 has a fineness ratio of  $L/D = 2.18$ . Radome 2 has a fineness ratio of  $L/D = 3.00$  as indicated in the legend. Predicted gain data are also presented in Figure 5.

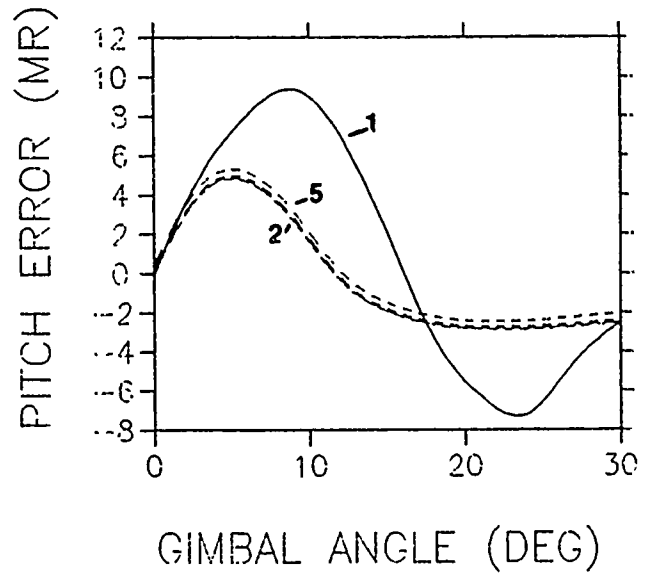
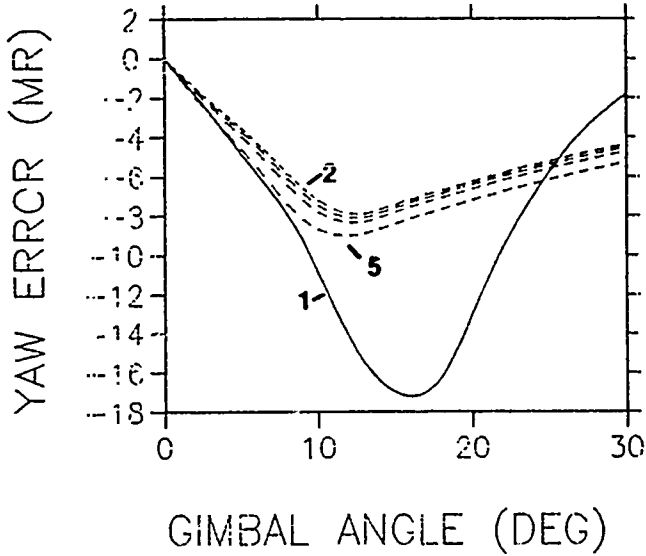


LEGEND  
MEAS.

1	$16 L_1^2/\lambda$	1P
2	$4L_1^2/\lambda$	
3	$2L_1^2/\lambda$	
4	$4D^2/\lambda$	
5		

LEGEND  
MEAS.

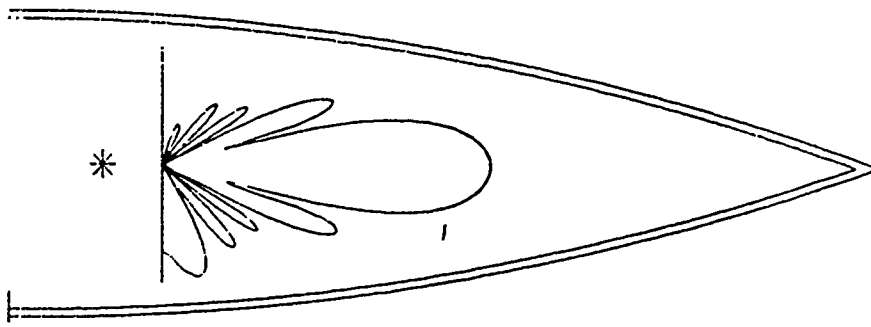
1	-100 DB
2	-50 DB
3	-40 DB
4	-30 DB
5	



(a) Effects of distance on yaw error.

(b) Effects of reflections on pitch error.

Figure 4. Effects of Distance and Reflections on Predicted Boresight Errors for Radome 1 Using 1-Point Algorithm.



LEGEND

1	MEAS.	2.18
2	$16L_1^2/\lambda$	2.18
3	$4D^2/\lambda$	2.18
4	$16L_1^2/\lambda$	3.00
5	$4D^2/\lambda$	3.00

LEGEND

1	$16L_1^2/\lambda$	2.18
2	$4D^2/\lambda$	2.18
3	$16L_1^2/\lambda$	3.00
4	$4D^2/\lambda$	3.00
5		

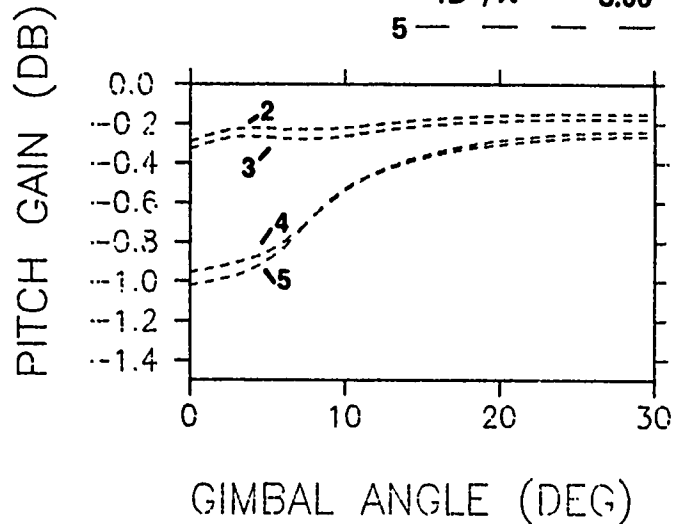
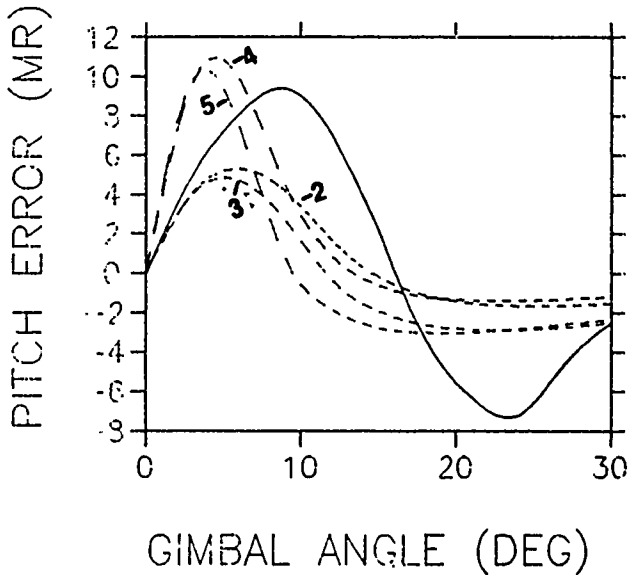


Figure 5. Effects of Distance and Fineness Ratio on Predicted Boresight Errors and Gain for Radome 1 ( $L/D = 2.18$ ) and Radome 2 ( $L/D = 3.00$ ) Using 1-Point Algorithm.

The effects of separation distance can be more pronounced if the radome parameters are modified slightly as shown in Figure 6 for Radome 3. This radome also has a fineness ratio of  $L/D = 3$ , but differs from Radome 2 in the placement of the antenna and in the dielectric constant of the radome wall. Data for  $R = 2D^2/\lambda$  are also shown and indicate the large error produced in BSE by this small separation distance;  $2D^2/\lambda$  is sometimes advocated as the absolutely minimum distance at which far-field antenna patterns can be measured with good results.

The effects of severe chamber reflections on BSE in pitch and yaw planes for the null seeker and 1-point algorithms are shown in Figure 7. The null seeker algorithm is more sensitive to reflections than is the 1-point algorithm.

#### Conclusions and Recommendations

It is concluded that the 1-point and null seeker BSE algorithms for computing radome-induced boresight errors yield essentially identical results regardless of separation distance  $R$  between the target and radome under test -- when reflections from chamber boundaries are less than -30dB. Effects of  $R$  on BSE are more pronounced for higher fineness ratios. The null seeker algorithm is more sensitive to severe reflections than the 1-point algorithm. The predicted sensitivities of BSE computation to the measurement environment makes one wonder how BSE measurement accuracies of +0.1 milliradian can be achieved in practice.

It is recommended that BSE measurements be made using the 1-point algorithm at a separation distance  $R > 4L_1^2/\lambda$ . The reflectivity of chamber boundaries should be less than -30dB. When measured BSE data are used to validate a radome analysis method, and it is not possible to obtain the recommended separation distance, then the computation of BSE should include distance effects.

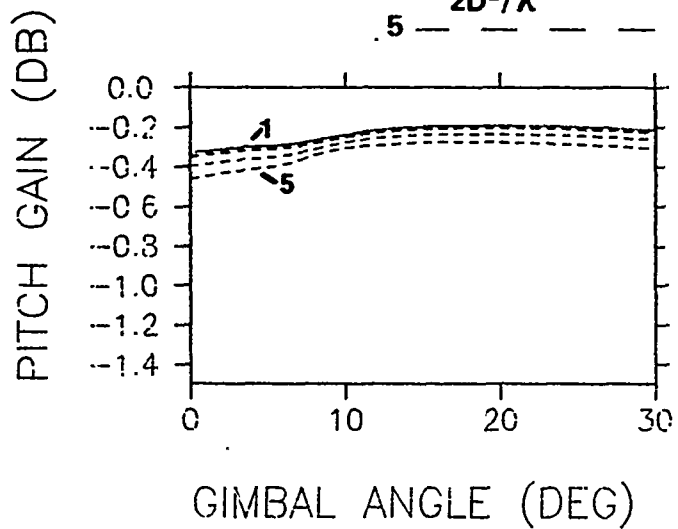
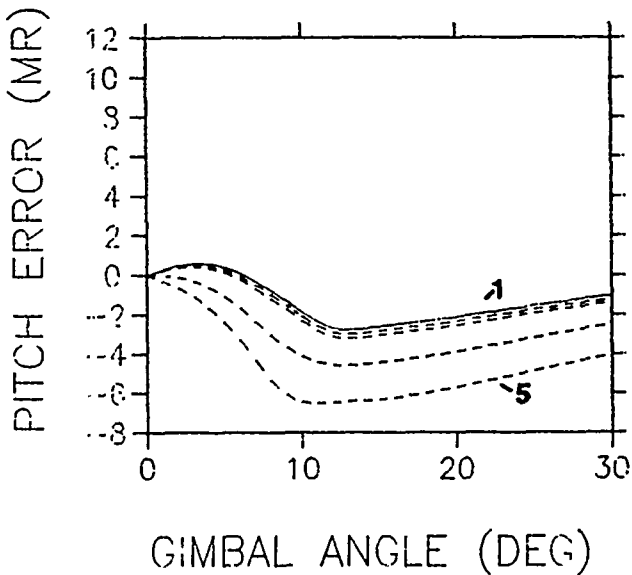
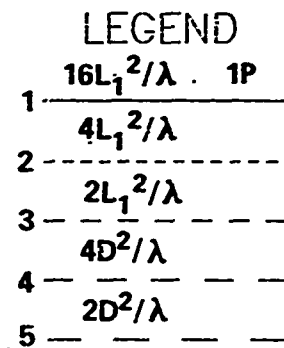
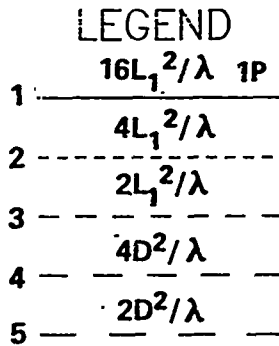
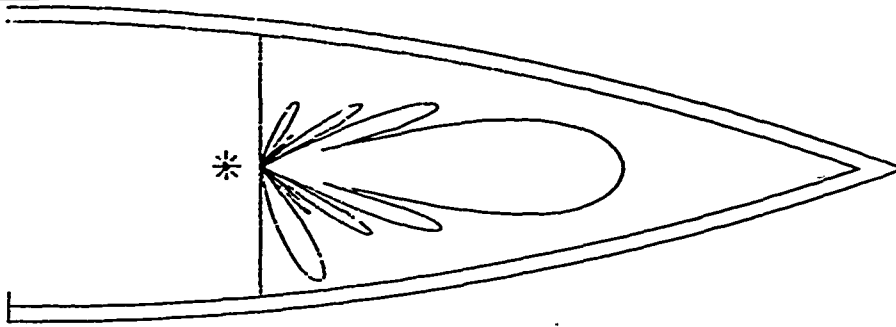


Figure 6. Effects of Distance on Predicted Boresight Errors and Gain for Radome 3 Using 1-Point Algorithm.

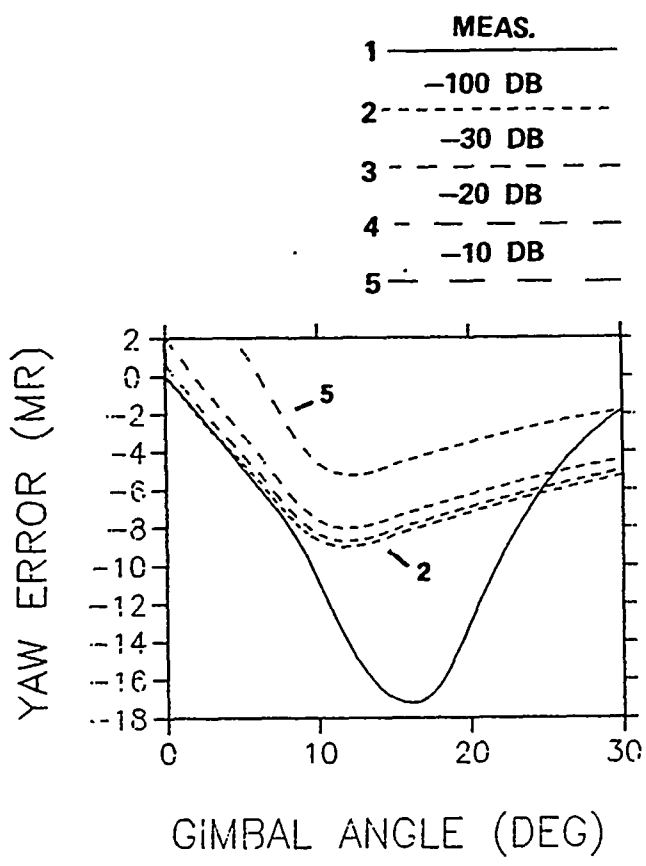
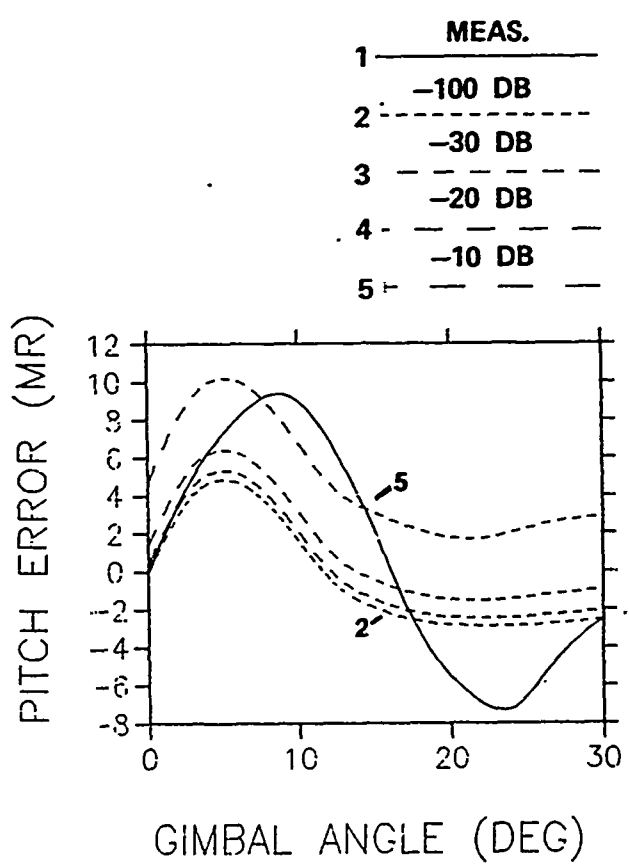
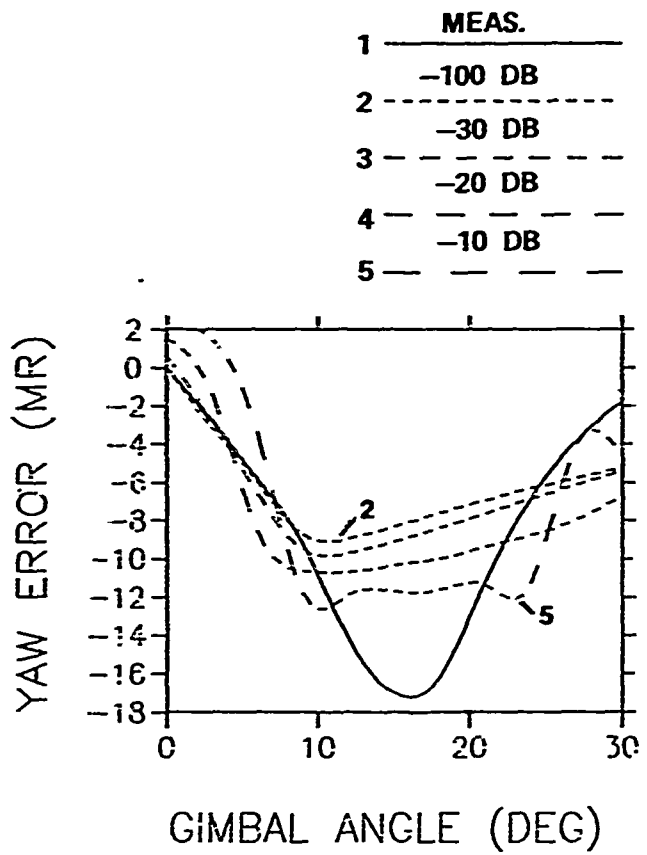
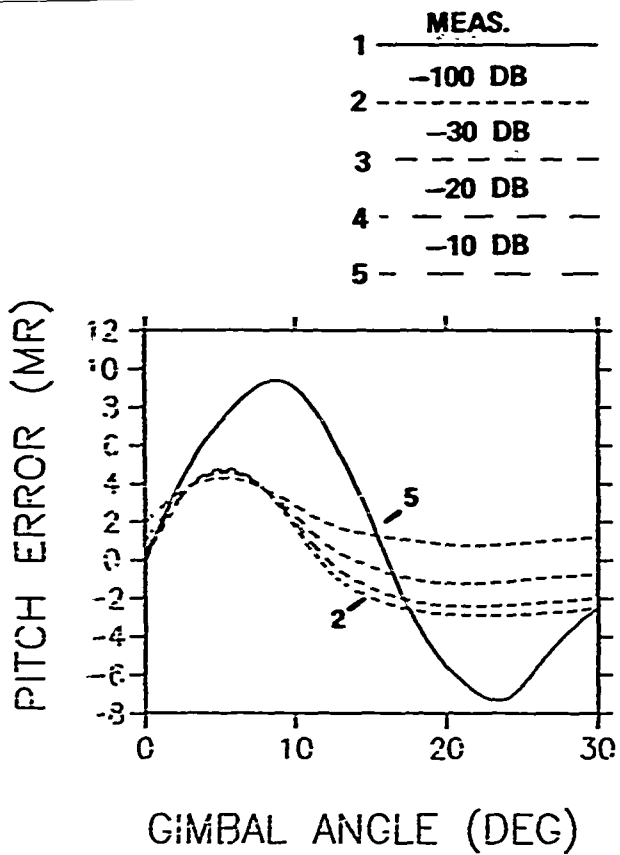
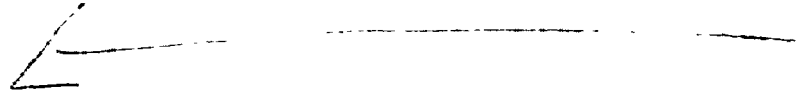


Figure 7. Effects of Severe Reflections on Predicted Boresight Errors for Radome 1 Using Null Seeker (Upper) and 1-Point (Lower) Algorithms.

**REFERENCES**

1. G. K. Huddleston, H. L. Bassett, and J. M. Newton, "Computer Aided Radome Analysis Based on Geometrical Optics and Lorentz Reciprocity," Final Report on AFOSR-77-3469, Vol. 2 of 4, February 1980.
2. K. Siwiak, T. B. Dowling, and L. R. Lewis, "Boresight Errors Induced by Missile Radomes," IEEE Trans., AP-27, No. 6, pp. 832-841, November 1979.





by

Edward B. Joy and Harold L. Rappaport

School of Electrical Engineering  
Georgia Institute of Technology  
Atlanta, Georgia 30332-0250

### Abstract

This paper reports on the work undertaken to include single order reflections into the equivalent-aperture, plane-wave-spectrum (PWS) radome analysis technique. The method used to add reflected plane wave rays to the equivalent aperture field is presented along with the key ray tracing equations for the reflected rays.

High fineness ratio radome shapes are shown to produce image lobes due to first order reflections. This image lobe can be distinct from the main beam or merge with the main beam to cause main beam distortion, high side-lobe levels and boresight error. Results are presented for a conical radome with 2.5 fineness ratio, dielectric constant of 5.5 and loss tangent of 0.00033 for two antenna types.

PREVIOUS PAGE  
IS BLANK



\* This work supported in part by The Joint Services Electronics Program

Monotonically-Concave Three-Dimensional Radome Shapes\*

by

Edward B. Joy

David E. Ball

School of Electrical Engineering  
Georgia Institute of Technology  
Atlanta, Georgia 30332-0250

Harris Corporation/GASE  
Melbourne, Florida 32902

Abstract

This paper reports on research conducted to increase the speed of ray intersection calculation with three-dimensional radome shapes. The radome inner or outer surface is specified as cylindrical radius values for a number ( $N_r$ ) of equally spaced cylindrical theta values for a number ( $N_\theta$ ) of constant station (axial position) values. This method of radome shape specification is typical of radome shape data available to the radome analyst.

The technique developed is an iterative algorithm that locally approximates the radome surface as a cone, tangent to the radome surface. The fineness ratio and the location of the cone axis are iteratively varied such that the intersection point of the ray and the cone equals the intersection point of the ray and the radome surface.

An estimate is made of the  $z$  (longitudinal) value and  $\theta$  value of the intersection point of the ray and the radome. A cone, tangent to the radome surface, is fitted to the radome surface at the estimated intersection point. The ray is traced to the cone using a fast closed-form solution. The cylindrical  $r$  value of the cone intersection point at the coordinate  $(z, \theta)$  is compared to the  $r$  value of the radome surface at the same  $(z, \theta)$  values. Based on this difference, a new cone is fitted to the radome surface and the process is repeated to convergence. Convergence is always possible for monotonically concave radome shapes. Typically 5 to 7 iterations are required for a one percent resultant error in radius.

Results are presented for several highly asymmetric radome shapes.

\* This work was sponsored in part by The Joint Services Electronics Program



## DUAL BAND RADOME WALL DESIGN

Bernard J. Crowe

Flight Systems, Inc.  
1901 Dove Street  
Newport Beach, CA 92660

INTRODUCTION

Radomes for currently-deployed air launched tactical missiles are typically designed to operate at a single frequency or narrow range of frequencies, and occasionally over a wider band of contiguous frequencies spanning an octave or slightly more. Requirements to operate against an extended threat suite, and/or to negate probable countermeasures tactics, indicate a need for future systems to encompass a multi-mode capability. Such systems will combine operations in two or more discrete segments of the electromagnetic spectrum in an integrated seeker unit. Possible mechanizations include combinations of RF/IR, IR/UV, passive RF/active RF, and microwave/millimeter wave bands. Multimode systems such as these will naturally require a matching capability from the radome.

A high-speed, streamlined radome presents a difficult enough design problem even for single-frequency applications; when it is required to provide clean transmission in two discrete bands, the difficulty is greatly increased. The conflict between the requirements of low aerodynamic drag, adequate structural integrity, and good electrical performance is brought even more sharply into focus, and the design tradeoffs and resulting compromise configuration must be approached with extreme care.

The first essential step in the process is necessarily the selection of a material or combination of materials, and appropriate thicknesses for each of them, which will result in adequate transmission of electromagnetic energy at the desired frequencies over the anticipated range of incidence angles. This is not the most difficult design task; the design of the radome shape and tailoring the wall thickness profile is expected to be more critical, as is the integration of a dual-mode seeker in a co-aperture or co-axial configuration. Nevertheless, the design cannot proceed without the prior selection of a suitable radome wall configuration.

Because of the increased complexity of these walls, a far greater range of feasible

solutions than usual will be possible, and optimum designs will be more difficult to determine. Even if the radome design task is initiated early, in parallel with the seeker design, a significant tradeoff study will be necessary to identify the best materials combinations and wall configuration for the intended application.

The groundwork for this effort can be accomplished in a timely manner, through a preliminary evaluation of suitable materials matched to projected electrical requirements. Computer analysis can permit the identification of promising wall configurations, exhibiting desirable electrical properties in physically realizable thickness combinations. This paper describes two dual-band walls designed in this manner.

SPECIFIC DESIGNS

As the number of layers in the radome wall is increased, the magnitude of the design task grows considerably, and some means of computer-assisted design becomes necessary. Even for walls of only two or three layers, the examination of possible combinations of material types and thicknesses is greatly facilitated by automated codes to characterize the transmission of the candidate wall configuration as a function of thickness, frequency, incidence angle, and polarization. The plotted data in the following figures was generated by one such code, Flight Systems, Inc., WALLTX flat plate analysis simulation, which has been used to develop conceptual radome wall designs for a number of applications. Included among these are walls designed to support discrete dual-band operation. Examples of two such designs are described in the following paragraphs.

Alumina Dual Band Radome Wall Design

Figure 1 is a cross section through a ceramic three-layer wall designed for a generic X-band/Ku-band application. The materials represented in this design are alumina (the skins), and a proprietary ceramic foam material, Cerez, manufactured by Omohundro Company. This wall configuration was one of nine developed under U.S.

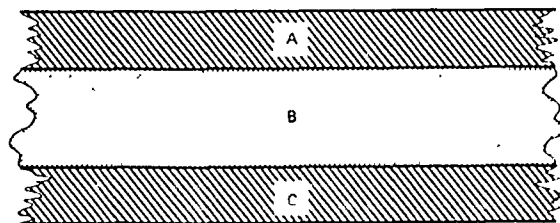
PREVIOUS PAGE  
IS BLANK



Navy contract number N00123-79-C-1042 in 1981. The selected materials were at that time under evaluation at the Naval Weapons Center, China Lake.

Several physical configurations of the symmetric three-layer wall were examined using the WALLTX analysis and design simulation, which allows the thickness of one or more layers to be varied at a given frequency to determine the optimum thickness. Fixing first one layer, then the other(s), and observing the transmission at the two frequencies of interest, the program may be used in an iterative fashion to arrive at a desired configuration such as that shown in Figure 1.

This wall is a rather unusual combination of thick skins on a thin core, and the resulting 57.5/100/57.5 configuration has a well-defined resonance at 10 GHz, plus two useful passbands at about 30 and 36 GHz (Figure 2). The phase grouping is unusually tight at the 10 GHz resonance, and on the basis of detailed analysis in the 5-15 GHz regime, would appear to offer the potential of performance at least equal to, if not in excess of, a 10 GHz-tuned half-wave wall. The transmission summary in Figure 2 shows the transmission coefficient for both parallel and perpendicular polarization at a single incidence angle in each plot. The broken line curve is the zero-incidence transmission coefficient, for reference. The curves show that the wall maintains transmission better than 75 to 80 percent at



SECTION THROUGH RADOME WALL

LAYER NO	MATERIAL TYPE	DIELECTRIC CONST	LOSS TANGENT	THICKNESS (MILS)
A	Alumina	9.50	0.0002	57.5
B	Cerez	2.41	0.0024	100.0
C	Alumina	9.50	0.0002	57.5

Figure 1. Alumina/Cerez Dual Band Radome Wall Configuration

both 10 GHz and 36 GHz out to 80 degrees incidence angle. Although the high passband frequency is a little higher than the desired 35 GHz value, the resonance could be adjusted to this value through small changes in wall thickness.

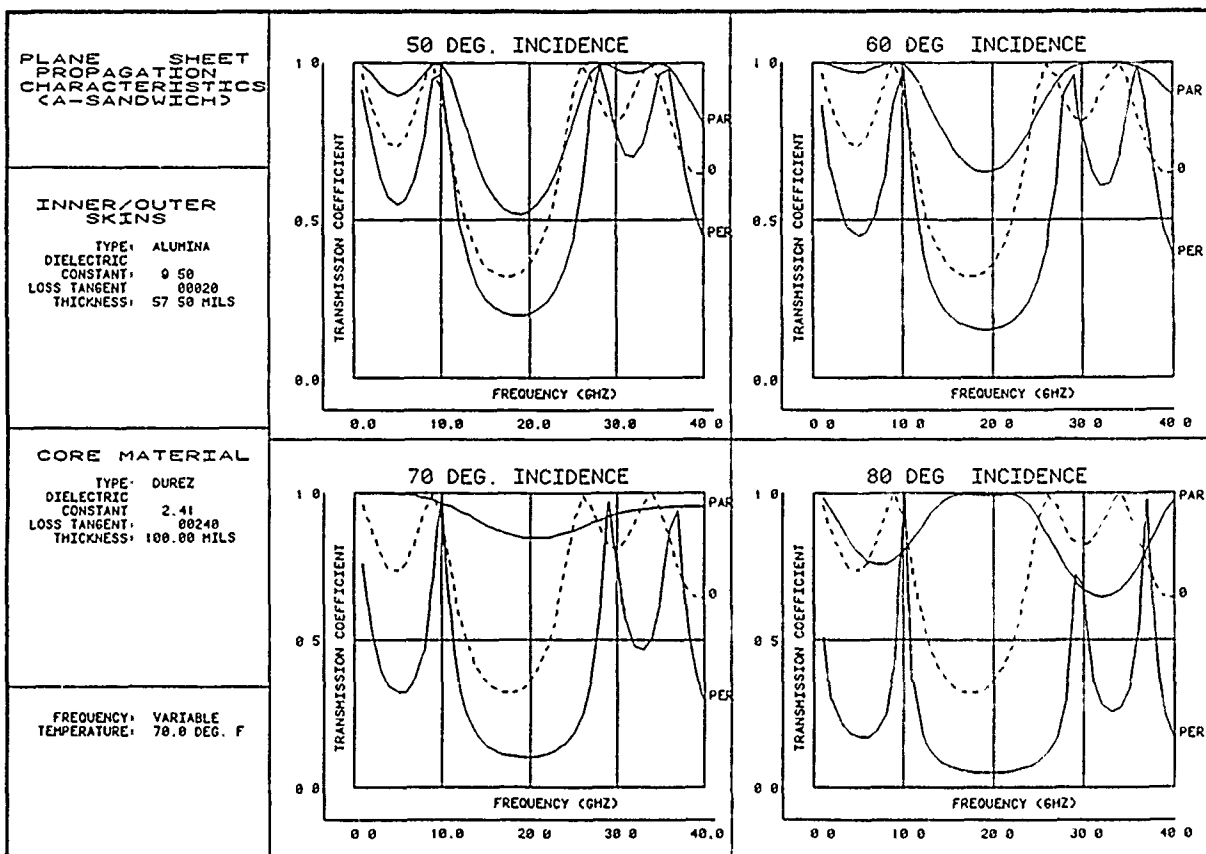
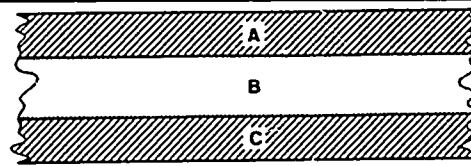


Figure 2. Transmission Summary, 0-40 GHz, Alumina/Cerez Wall

Silicon Nitride Dual Band Radome Wall Design

The "transportability" of this design was shown in a subsequent analysis task in which the radome wall was redesigned for a specific application using silicon nitride (Figure 3), a material with good thermal shock resistance and a low susceptibility to rain damage. Various forms of this material have been considered for high speed missile radome applications by both the Air Force and the Navy. By controlling the density of the material during manufacture, the dielectric constant of silicon nitride may be tailored to a specific requirement. The design illustrated in Figure 3 uses a moderate-to-high density reaction bonded formulation (with good rain erosion resistance) for the skins (Ref. 1), and an extremely low density core made by baking out inclusions introduced during the initial manufacture to produce a silicon nitride foam (Ref. 2) of low dielectric constant.



SECTION THROUGH RADOME WALL

LAYER NO	MATERIAL TYPE	DENSITY (GM/CM <sup>3</sup> )	DIELECTRIC CONST	LOSS TANGENT	THICKNESS (INS)
A	Reaction-Bonded Silicon Nitride	3.025	7.60	.0003	.069
B	Silicon Nitride Foam	0.69	1.93	.0003	.090
C	Reaction-Bonded Silicon Nitride	3.025	7.60	.0003	.069

Figure 3. Silicon Nitride Dual Band Radome Wall Configuration

The resulting 69/90/69 wall configuration has thicker skins but a slightly thinner core than the alumina version, and the overall thickness of 0.228 inches is comparable with a conventional single-mode X-band wall. The electrical performance of this wall is very similar to that of the Alumina/Cerez wall, as Figure 4 shows. The wall exhibits peak transmission windows at 10.5, 30, and 36 GHz as before, and though the resonance peaks are not quite so strong at the high incidence angles, they are adequate for low-loss transmission over bandwidths of

500 MHz, as shown in the two following figures.

Figure 5 details the electrical performance of the wall over the frequency range 9.5 to 10.5 GHz. The upper left plot shows the phase difference for incidence angles up to 85 degrees; the other three plots are similar to those in Figure 2 and depict parallel and perpendicular transmission coefficients at 60, 70, and 80 degrees incidence respectively. These latter plots show that the transmission of

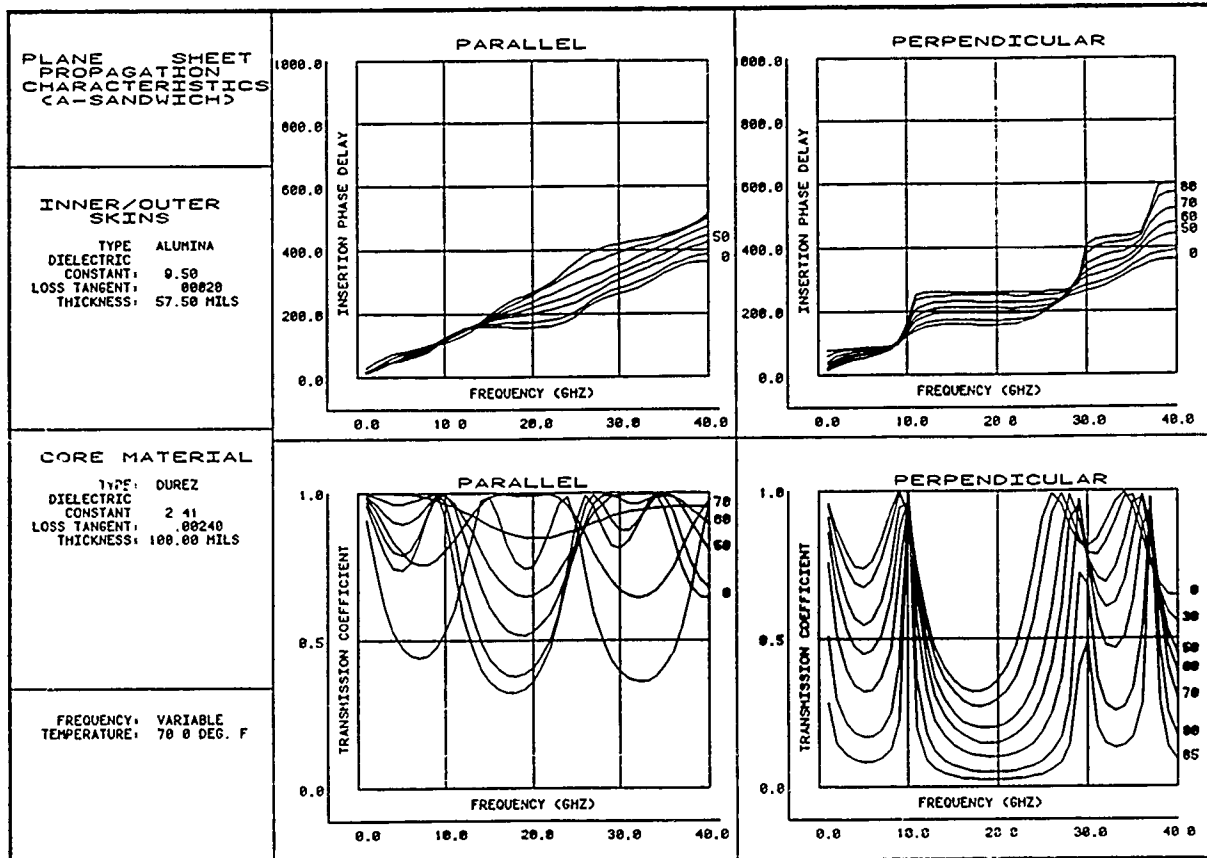


Figure 4. Electrical Performance, Silicon Nitride Dual-Band

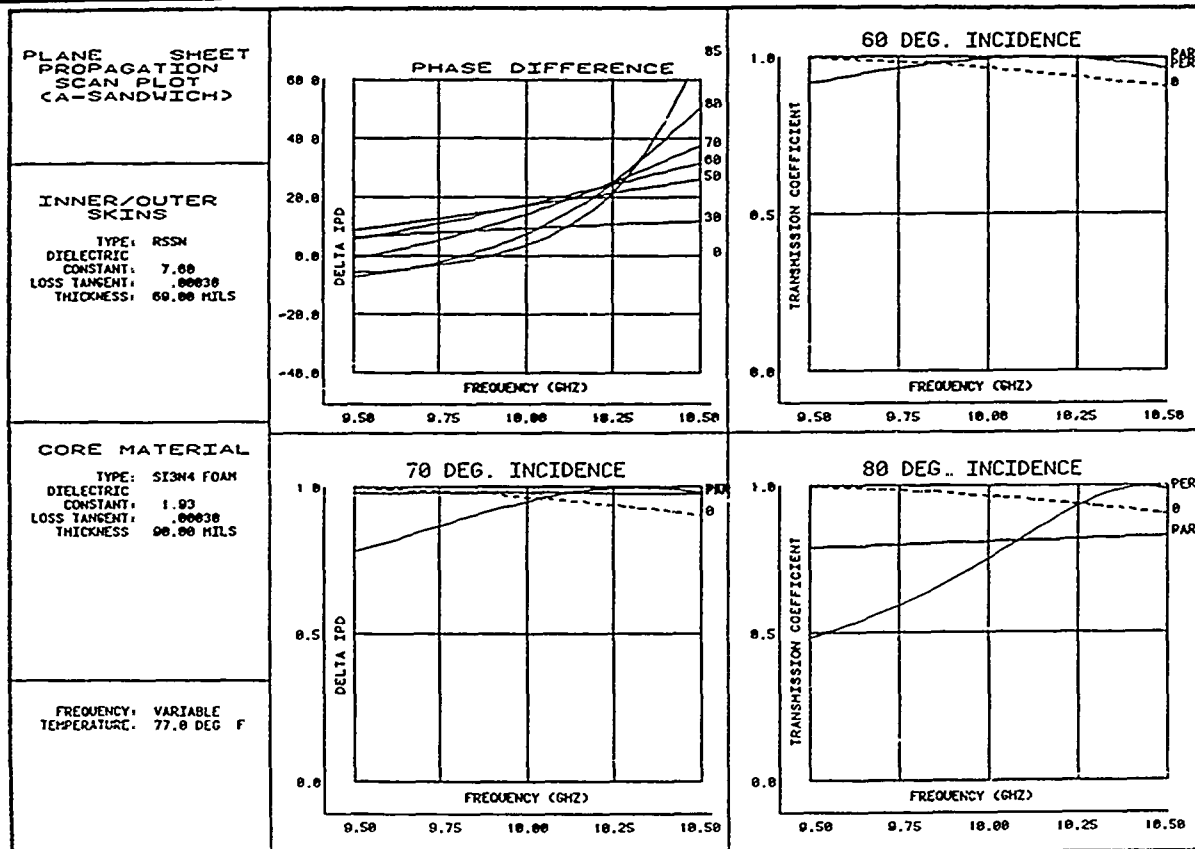


Figure 5. Performance Detail at 10 GHz, Silicon Nitride Dual Band Wall

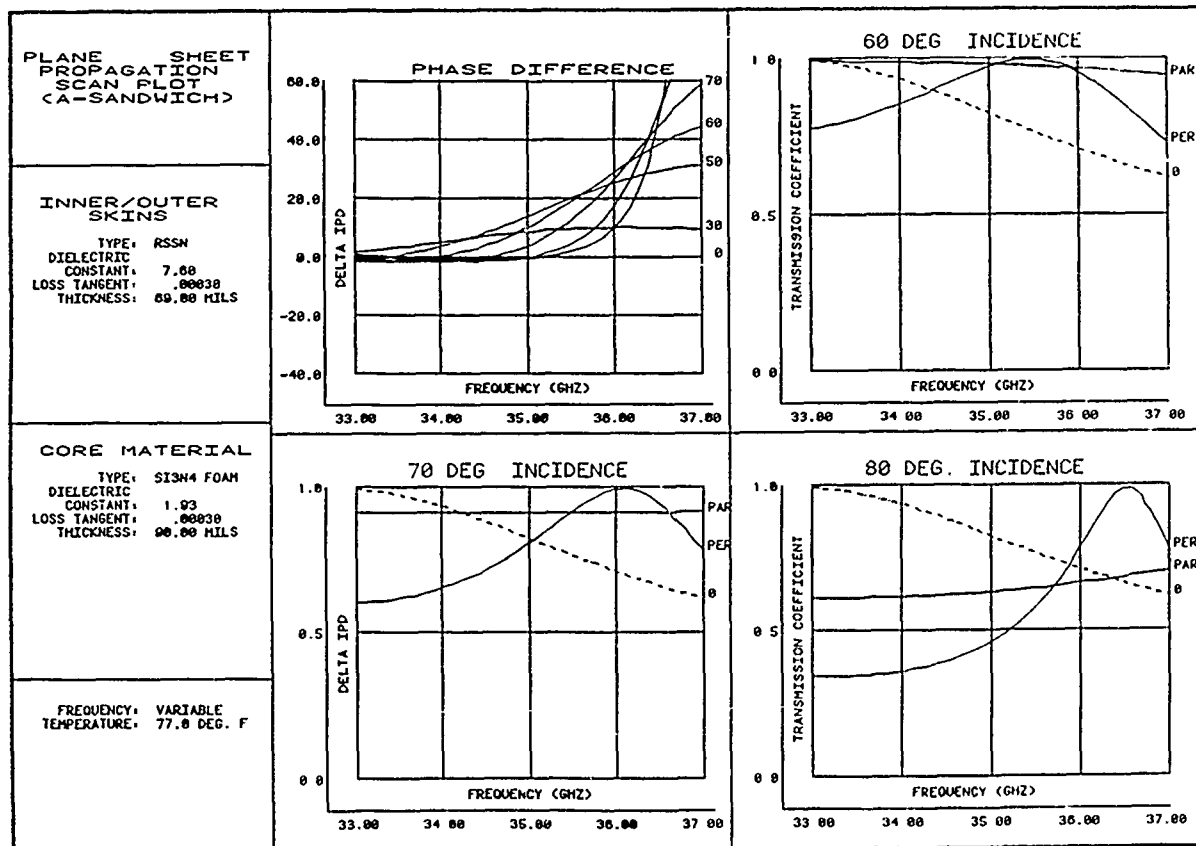


Figure 6. Performance Detail at 35 GHz, Silicon Nitride Dual Band Wall

the wall is excellent up to 70+ degrees incidence across the 9.75 to 10.25 GHz band, and is maintained well even at 80 degrees. The phase difference values over this frequency range lie within a band of values from -10 to +30 degrees, performance consistent with the attainment of low boresight errors and error slopes.

At 35 GHz the performance, though not quite as good as at 10 GHz, is still quite impressive (Figure 6). Transmission is maintained well to 70 degrees incidence, but is beginning to degrade badly at 80. The phase difference also holds up well out to 35.6 GHz for incidence angles of 70 degrees or lower. A full-aperture seeker at this frequency would be expected to suffer about 1 dB of loss (one way), and to introduce moderate guidance errors in a proportionally guided missile. If the high frequency aperture could be reduced, however, the range of incidence angles experienced would be limited and an overall performance might be attained suitable for high quality end-game guidance. With further refinement the design would be expected to yield improvement in both bands. It exhibits a useful characteristic at frequencies other than the design passbands; it transmits very little energy at these other frequencies (Figure 4), and would therefore make a contribution to a system designed for low-observable operation. The design in general certainly merits further investigation.

## CONCLUSIONS

The two radome wall designs presented in this paper were derived inexpensively using computer-aided analysis techniques. Useful performance potential is predicted in configurations employing a variety of materials, and novel wall configurations were developed which may find application in multi-band seeker applications as well as systems benefiting from stealthy operation.

The author believes that the computer-aided design technique for conceptualizing and screening wall configurations in this way can make a significant and useful contribution to the radome design process by identifying workable configurations in advance of system-specific requirements, thereby reducing the lead time required for design solutions and assisting the weapons system procurement process.

## REFERENCES

1. J. Barta and M. Manela, "Preparation and Properties of Silicon Nitride for Radome Applications", Proc. 16th Symposium on Electromagnetic Windows, G.I.T., June 1982.
2. F.H. Simpson and J. Verzemnieks, "Controlled Density Silicon Nitride Material", Proc. 16th Symposium on Electromagnetic Windows, G.I.T., June 1982.

# STUDY OF LAMINATED DIELECTRIC BEHAVIOR AT MICROWAVE AND MILLIMETER-WAVE FREQUENCIES

D. J. White and C. N. Helmick Jr.

Physics Division, Research Department (Code 3814)  
Michelson Laboratory  
Naval Weapons Center, China Lake, CA 93555

## AD-P004 358

### INTRODUCTION

Dielectrics composed of layers of different dielectric constant have radome applications. A laminated or layered structure can be used to improve mechanical and thermal properties, while a certain amount of dielectric-constant tailoring can be done by varying the layer permittivities and their relative thicknesses.

Such a multilayer system (sometimes called an artificial dielectric) is basically uniaxially anisotropic with the optic axis perpendicular to the planes of lamination, although this anisotropy may not be large, depending on the layer permittivities and thicknesses. In any case, the equivalent static dielectric constants for a laminated structure are readily calculated, provided the layer constants and thicknesses are known, by use of a model involving parallel and series capacitances.

Modeling laminated structures as a single uniaxial dielectric sheet works well, even at large angles of incidence, provided the wave frequency is low enough that the individual layer thicknesses are small with respect to the wavelength in each material. For millimeter waves this condition may no longer be met, and very large differences in complex transmission coefficient may be found between the actual multilayer panel and its single-layer "equivalent" model. A multilayer radome wall may even appear much like a dielectric mirror in certain wavelength regions.

In this paper we explore the range of validity of the artificial-dielectric model by comparing its computed results with those obtained from an N-layer flat-panel computer program for a number of specific multilayer dielectric structures.

### THEORY

Consider a flat wall consisting of alternating layers having different dielectric constants and uniform thicknesses. By modeling the structure as  $N$  ( $=N_1 + N_2$ ) series capacitors for the electric field perpendicular to the plane of the layers and as  $N$  parallel capacitors for the electric field parallel to the plane, the uniaxial dielectric constants (relative permittivities) in the long-wavelength limit can be found:

$$\epsilon_x = (N_1 d_1 \epsilon_1 + N_2 d_2 \epsilon_2) / d \quad , \quad (1a)$$

$$\epsilon_z = \epsilon_1 \epsilon_2 d / (N_1 d_1 \epsilon_2 + N_2 d_2 \epsilon_1) \quad , \quad (1b)$$

where  $N_i$ ,  $d_i$  and  $\epsilon_i$  are the number of layers, layer thickness, and dielectric constant of material species  $i$  ( $i = 1, 2$  for a two-component repetitive system).  $\epsilon_x$  is the dielectric constant in the plane parallel to the surface, and  $\epsilon_z$  is the dielectric constant along the surface normal (optic axis). The total thickness  $d$  is  $N_1 d_1 + N_2 d_2$ . The volume fraction of species  $i$  is  $N_i d_i / d$ . The permittivities may be complex. By "long-wavelength limit" is meant the assumption that  $d_i \sqrt{\epsilon_i} \ll \lambda_0$  (vacuum wavelength) for each  $i$ .

PREVIOUS PAGE  
IS BLANK



These equations can easily be extended to more complicated situations, e.g. where more dielectric species are involved or the layer thicknesses are non-repetitive, etc. The next step in complexity would be a three-component repetitive structure, as might arise when a glue layer is introduced to bond two of the dielectric materials together. The equivalent uniaxial dielectric constants for this case are:

$$\epsilon_x = (N_1 d_1 \epsilon_1 + N_2 d_2 \epsilon_2 + N_3 d_3 \epsilon_3) / d \quad , \quad (2a)$$

$$\epsilon_z = \epsilon_1 \epsilon_2 \epsilon_3 d / (N_1 d_1 \epsilon_2 \epsilon_3 + N_2 d_2 \epsilon_1 \epsilon_3 + N_3 d_3 \epsilon_1 \epsilon_2) \quad . \quad (2b)$$

Such equations are commonly written in terms of the volume fractions  $N_i d_i / d$ , which may represent the extent of the data actually available in practice, or even in terms of mass fractions.

We next proceed to the complex boundary reflection coefficients for the uniaxial anisotropic dielectric layer, which were derived previously.<sup>1</sup> Following established optical convention, we here denote the two basic polarizations of the incident plane wave as *s* and *p*, where *s* (German *senkrecht* = perpendicular) means the **E**-vector is perpendicular to the plane of incidence (i.e., **E** is parallel to the surface plane) and *p* (*parallel*) means **E** is parallel to the plane of incidence (i.e., **H** is parallel to the surface plane). The boundary reflection coefficients can be written:

$$r_s = (\cos\theta - k_s/k_0) / (\cos\theta + k_s/k_0) \quad , \quad (3a)$$

$$r_p = (k_p/k_0 - \epsilon_x \cos\theta) / (k_p/k_0 + \epsilon_x \cos\theta) \quad , \quad (3b)$$

where  $\theta$  is the angle of incidence, and the two wave numbers in the dielectric ( $k_s$  and  $k_p$ ) are given by

$$k_s/k_0 = [\epsilon_x - \sin^2\theta]^{\frac{1}{2}} \quad , \quad (4a)$$

$$k_p/k_0 = [(\epsilon_x/\epsilon_z)(\epsilon_z - \sin^2\theta)]^{\frac{1}{2}} \quad , \quad (4b)$$

and the vacuum wave number is

$$k_0 = 2\pi/\lambda_0 = 2\pi f/c \quad (4c)$$

The overall single-layer complex transmission coefficients are then

$$T_x = (1 - r_x^2) \exp(-jk_x d) / [1 - r_x^2 \exp(-j2k_x d)] \quad , \quad x = s, p \quad . \quad (5)$$

Note that  $\epsilon_z$  appears only in the case of *p* polarization; only  $\epsilon_x$  (the weighted mean value of the  $\epsilon_i$ ) is used for *s* polarization. Thus a further simplification of the one-layer representation of a laminate is to consider it to be isotropic with  $\epsilon = \epsilon_x$ . This leads to no change in the case of *s* polarization; and it will turn out to be seen later that in many cases (where  $\epsilon_z$  is not much different from  $\epsilon_x$ ), the isotropic model departs only mildly from the uniaxial model for many frequencies and angles of incidence.

## THE PROBLEM

Programs to calculate the N-layer flat-panel complex transmission coefficients

are fairly common, and such a program can be used instead of (or compared with) the "equivalent" single dielectric sheet model. The N-layer computation is exact within the usual limits of plane waves and semi-infinite sheets. However, in the real world, one may be given a laminated material to characterize, and it is not always practical to disassemble the composite structure to determine precise sheet thicknesses or composition empirically, nor are such details often supplied *a priori*. One may have to settle for taking a laminated dielectric sample, placing it in a microwave test setup, and determining the effective dielectric constants  $\epsilon_x$  and  $\epsilon_z$  at one or a few frequencies, or at best over a comparatively limited frequency range. The question then becomes one of how valid are such measured "average" dielectric constants—the issue that this paper is attempting to address.

The approximation involved in equations (1) and (2) clearly involves making each layer "thin" with respect to a wavelength in the layer. As the frequency of operation is increased, this thinness criterion is increasingly violated. At 100 GHz a .010-inch thick layer of dielectric constant six is just over one-fifth wavelength thick; and while the concept of "thin with respect to. . ." is not well defined, it seems likely that this situation does not meet this stipulation.

## APPROACH

We have developed computer programs in house for calculating the flat-panel transmission and reflection coefficients of single or multiple dielectric layers, isotropic or uniaxially anisotropic. These programs have been employed to compute the complete transmission coefficients for representative laminates, comparing them with the coefficients obtained for the corresponding single-layer artificial-dielectric models, considering both the uniaxial model (given by equations (1) or (2) or generalizations thereof) and the further simplified isotropic model (using  $\epsilon = \epsilon_x$ ). Emphasis has been on examining the magnitude of the complex transmission coefficient,  $|T|$ , though other quantities may also be obtained, such as transmission phase, insertion phase delay, and reflection magnitude and phase (both forward and reverse directions). Total wall thicknesses have been in the neighborhood of 1 cm, typical of many radomes. Parameters studied were: frequency (typically 1 to 100 GHz or subdomains thereof), angle of incidence, polarization, dielectric constants, relative thicknesses, and the number and ordering of constituent layers.

## RESULTS

Space limitations permit inclusion only of a few of the many plots produced in exploring the effects of varying the above-listed parameters. These figures have been selected to illustrate *some* of the trends observed in the study. Figures 1-6 are all for two-component laminates having a total thickness of 1 cm, with transmission magnitude displayed over 1-100 GHz. (Current frequency resolution is limited to 100 points across the frequency span, meaning 1-GHz increments in these plots, so truncation of sharp peaks and dips is evident in some cases). The dielectric constant of the first dielectric species was set equal to 2 in all illustrated cases, with the second dielectric constant set equal to 4 in all but Figure 4, where it was set equal to 7 to illustrate the effect of a greater difference in dielectric constants. For clarity, loss tangents were set equal to zero throughout, though finite losses could easily have been included if desired. Thickness ratios of the two components,  $d_1:d_2$ , were set at 1:1 in Figures 1-4 and 3:1 in Figure 5 (to illustrate the effect of unequal, but repetitive, thicknesses). In Figure 6 the thicknesses were varied in an arbitrary, nonrepeating manner (though the dielectric constants alternated regularly) to illustrate the effect of nonrepetitive thicknesses. Figures 1-5 each show three curves: (a) 16-layer laminate [broken line], (b) analogous 6-layer laminate (same

$\epsilon_1$  and  $d_1:d_2$  [heavy dotted line], and (c) corresponding uniaxial single-layer model [light solid line], with dielectric constants obtained from equation (1). In Figure 6, the nonrepetitive case, there is no unique 6-layer analog, so only the 16-layer laminate and single-layer model [obtained through a generalization of equation (1)] are displayed. Figures 1-3 illustrate the same structure for three different choices of incidence angle and polarization ( $0^\circ$ ,  $45^\circ:s$ ,  $45^\circ:p$ ), while Figures 4-6 illustrate three additional structures all at the same incidence angle and polarization ( $45^\circ:s$ ).

## DISCUSSION

Several trends are evident from the plots generated, not all of which are illustrated by the figures reproduced here:

1. For a given overall wall thickness, the larger the number of layers (i.e., the thinner they are), the greater is the range of validity of the one-layer model. Inclusion of uniaxial anisotropy in the artificial-dielectric model, as in equations (1) and (2), extends the frequency range of the model's validity, especially for parallel (p) polarization and high angles of incidence. Even so, the model begins to break down when any of the layer thicknesses approach  $\lambda/10$  in the respective material.

2. One or more frequency bands may occur in the 20-100 GHz region where the laminate exhibits very high reflectivity (much like a dielectric mirror), a behavior not at all predicted by the single-layer artificial-dielectric model. For a small number of layers (e.g., 6) the transmission dips are less pronounced but more numerous; for a large number of layers (e.g., 16) the transmission dips (reflection peaks) are less numerous in a given frequency interval but more intense. As one increases the angle of incidence from  $0^\circ$  for a given laminate, the reflection peaks become more intense for the s polarization; for the p polarization they become less intense, but do not disappear even as Brewster's angle for the single-layer model is approached.

3. Reflection peaks are enhanced by (a) increasing the total number of layers, (b) increasing the difference between the two dielectric constants, and/or (c) varying the thickness ratio  $d_1:d_2$  away from 1:1 (i.e., making one component significantly thicker than the other). The transmission dips do not disappear when the thicknesses are varied in nonrepetitive fashion, as in Figure 6, but the spectrum can in such cases become more irregular.

## CONCLUSION

Given the construction details of a multilayer laminate, one can accurately and unambiguously compute the complex transmission and reflection coefficients. Going in the other direction, however, is not so clear-cut. Given experimental dielectric measurements on a composite material for which the details are lacking or incomplete, one finds the artificial-dielectric model is insufficient to characterize the material completely and unambiguously at high frequencies. In typical cases (wall thickness around 0.4 inch), "anomalous" behavior (mild or strong reflection bands) may occur as low as 20 GHz.

## REFERENCE

1. D. J. White and D. J. Banks, "Plane Wave Transmission and Reflection Coefficients for Anisotropic Sheets of Radome Materials," *Proc. 16th Symp. on Electromagnetic Windows*, 9-11 June 1982 (Georgia Inst. of Technology, Atlanta, Georgia, 1982), pp. 7-12.

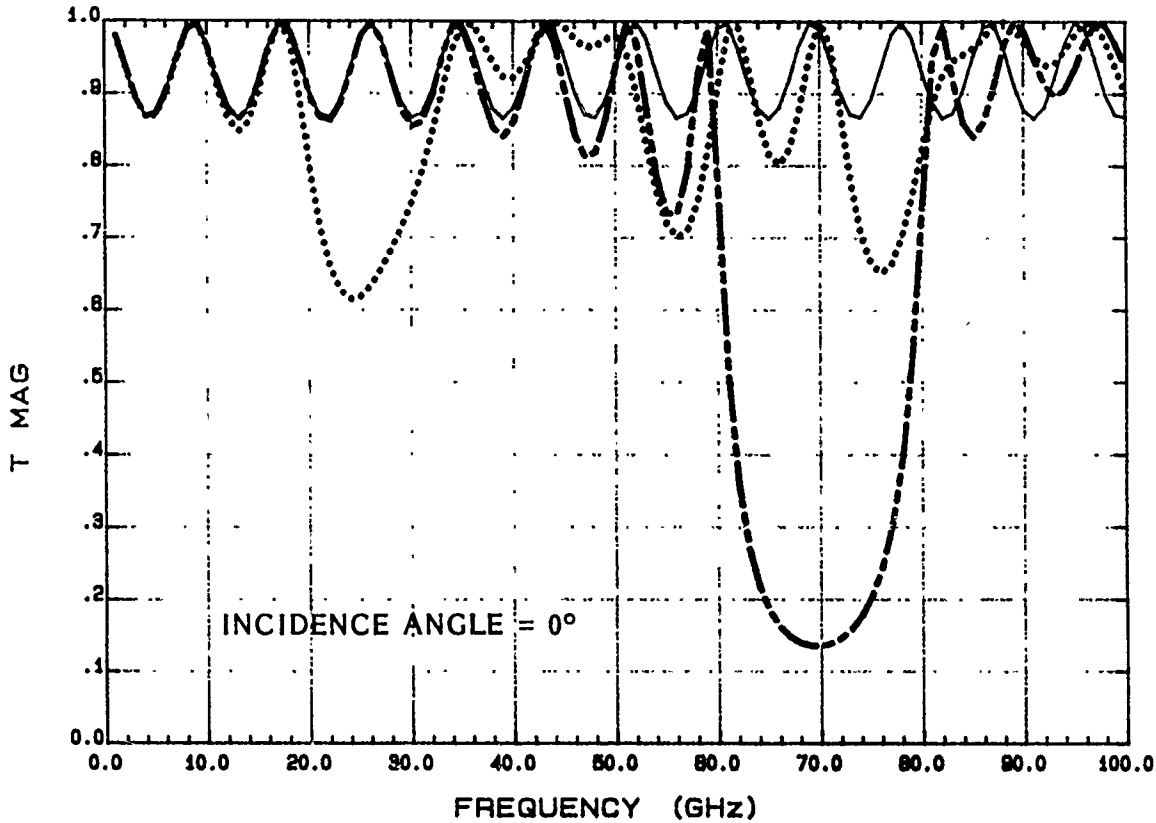


FIGURE 1. Two-component, repetitive laminate with equal layer thicknesses and overall thickness 1 cm;  $\epsilon_1=2$ ,  $\epsilon_2=4$ ,  $d_1:d_2=1:1$ , incidence angle =  $0^\circ$ . Heavy broken line = 16-layer laminate; heavy dotted line = analogous 6-layer laminate; light solid line = corresponding uniaxial single-layer "artificial-dielectric" model ( $\epsilon_x=3.000$ ,  $\epsilon_z=2.667$ ).

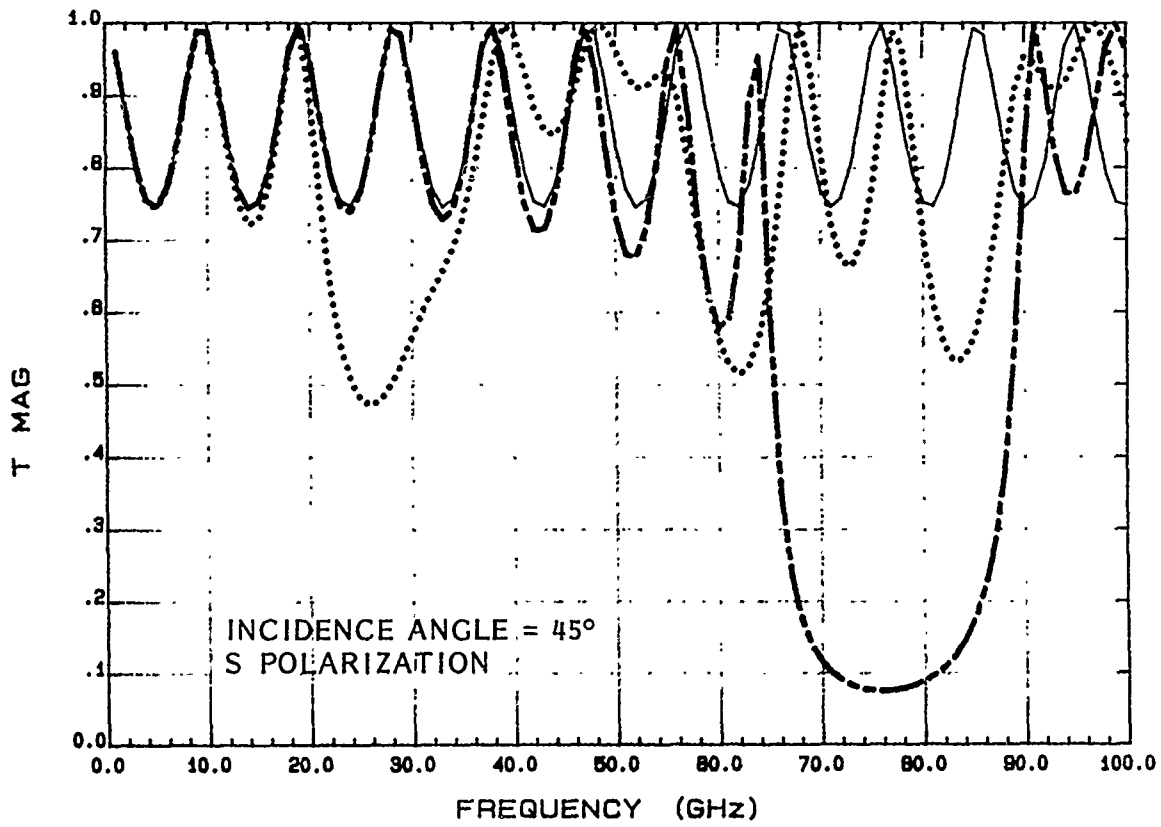


FIGURE 2. Same as Figure 1 except incidence angle = 45°, s polarization.

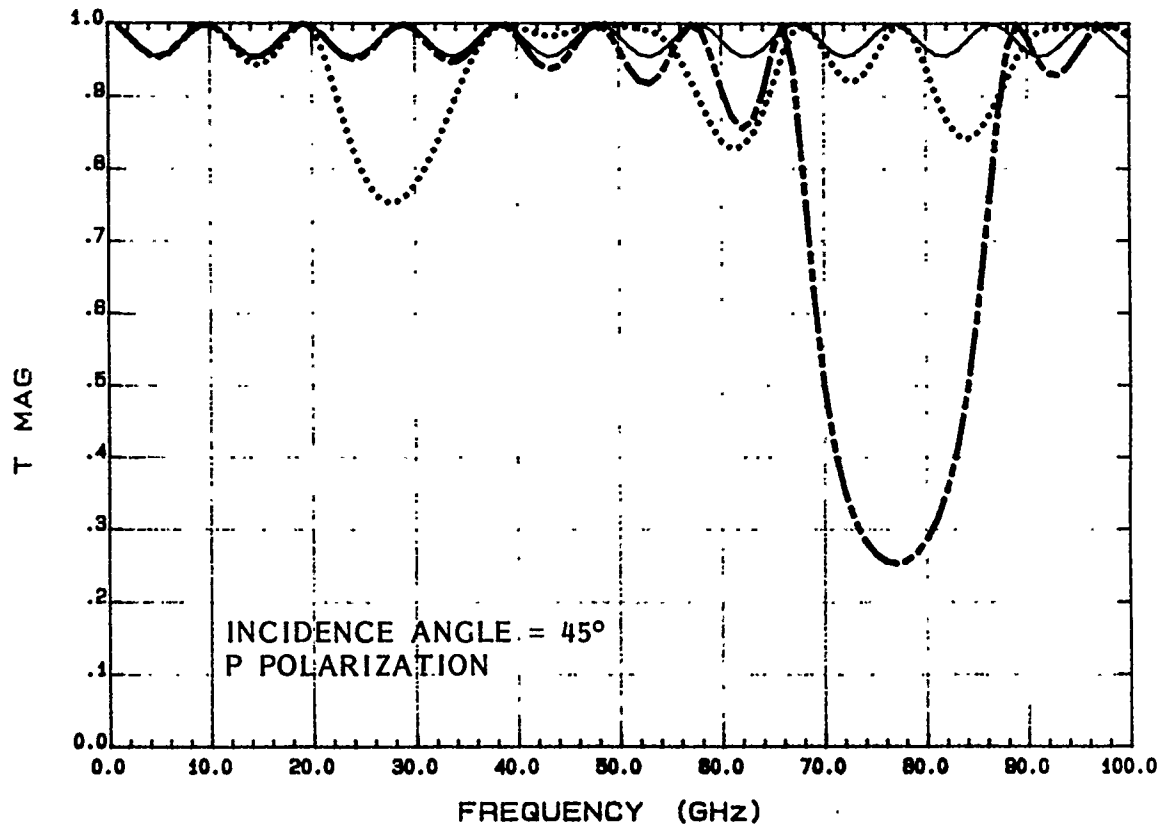


FIGURE 3. Same as Figure 1 except incidence angle = 45°, p polarization.

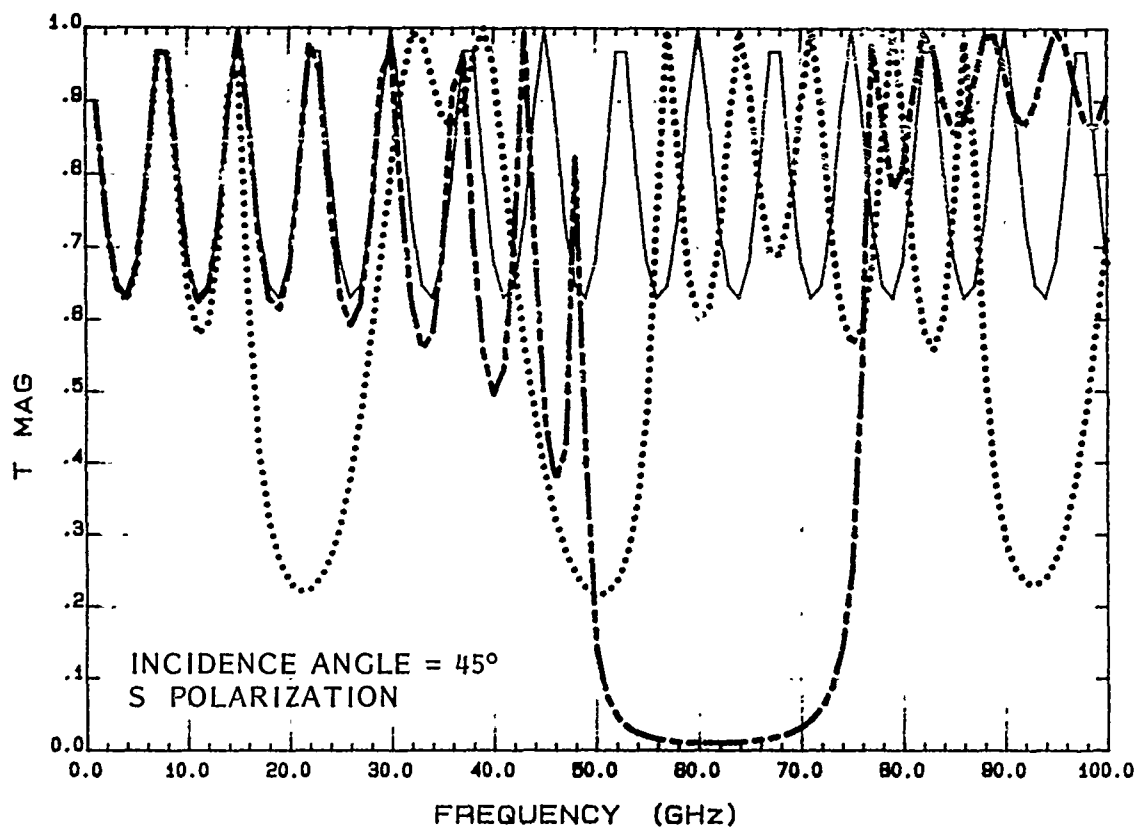


FIGURE 4. Same as Figure 1 except  $\epsilon_2 = 7$ , incidence angle = 45°, s polarization. Uniaxial single-layer model has dielectric constants  $\epsilon_x = 4.500$ ,  $\epsilon_z = 3.111$ . Illustrates effect of using a higher dielectric constant for one of the two component materials of the laminate.

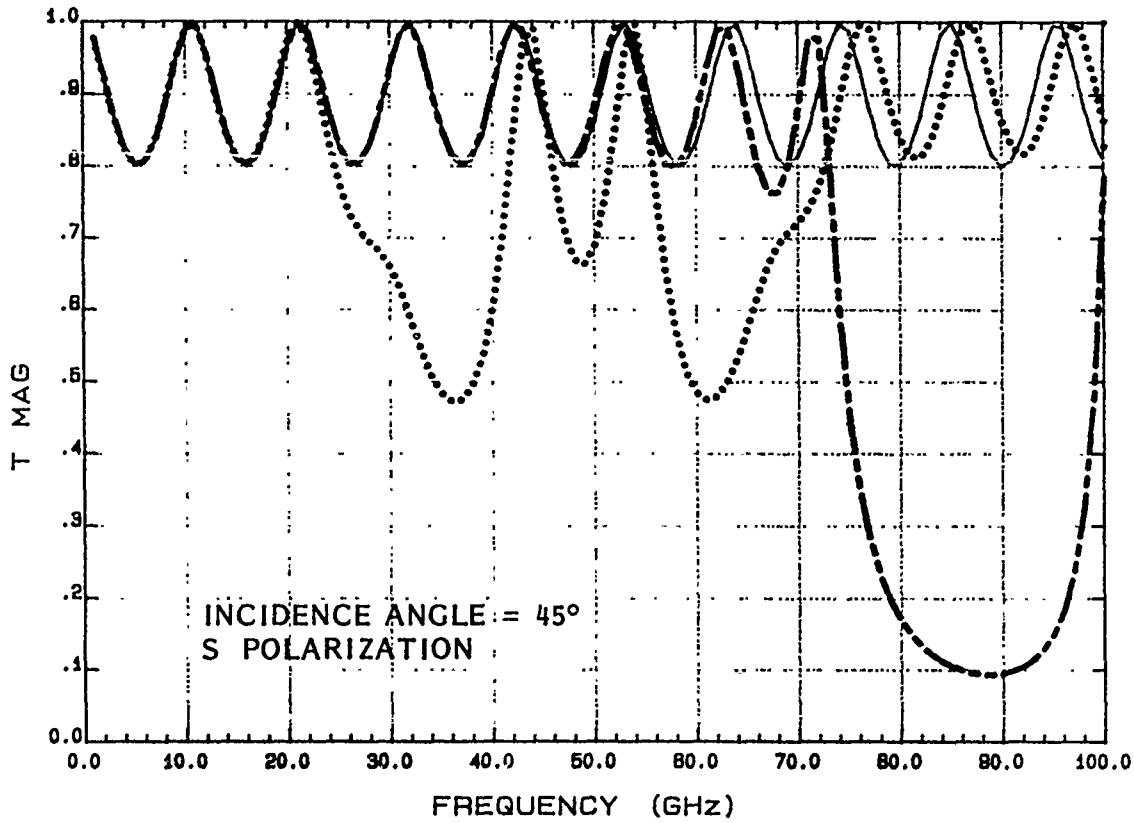


FIGURE 5. Same as Figure 1 except  $d_1:d_2 = 3:1$ , incidence angle =  $45^\circ$ , s polarization. Uniaxial single-layer model has dielectric constants  $\epsilon_x = 2.500$ ,  $\epsilon_z = 2.286$ . Illustrates the effect of unequal thicknesses for the two component materials of the laminate.



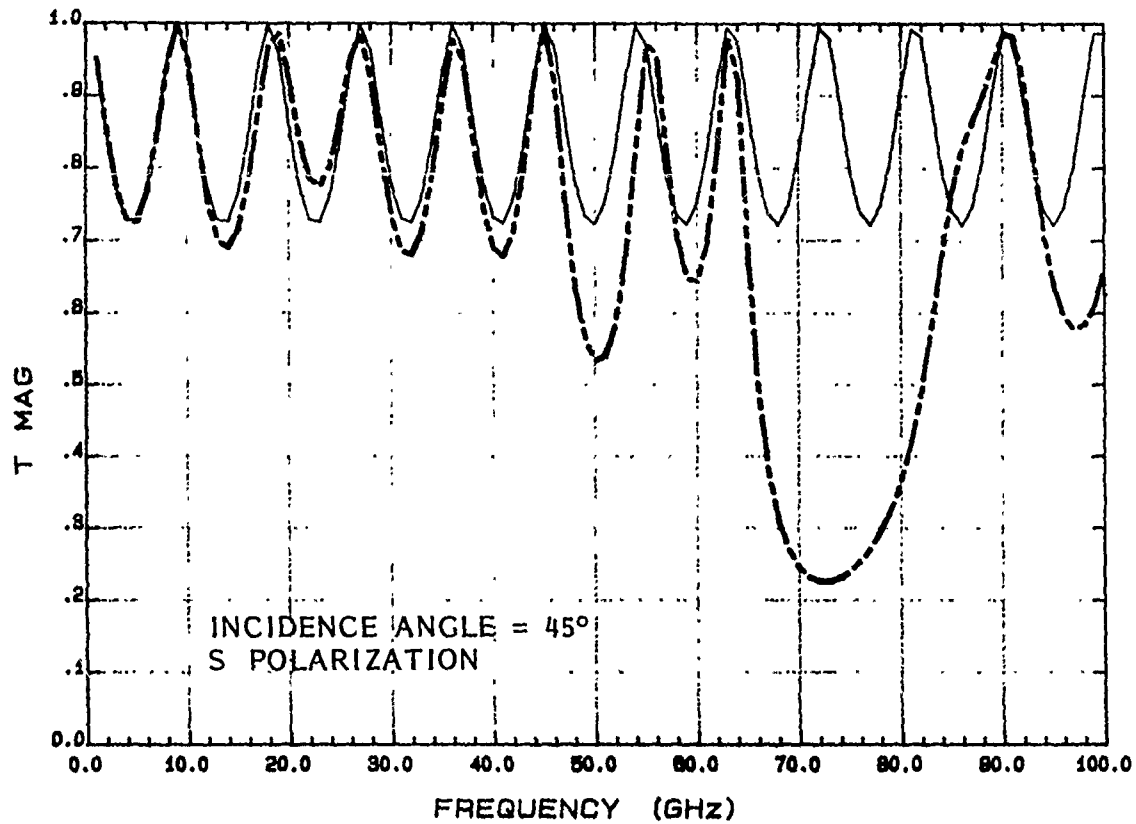


FIGURE 6. Two-component laminate with overall thickness 1 cm and non-repetitive layer thicknesses;  $\epsilon_1=2$ ,  $\epsilon_2=4$  (alternating). Heavy broken line is 16-layer laminate with layer thicknesses  $d_i$  in units of 1/64 cm: 4, 5, 3, 6, 2, 7, 1, 4, 5, 3, 4, 6, 2, 4, 3, 5. Light solid line is corresponding uniaxial single-layer model ( $\epsilon_x = 3.250$ ,  $\epsilon_z = 2.909$ ).

AD-P004 359

B. Pupko, D. Gordon, S. Starobinets.  
 Israel Aircraft Industries  
 Materials & Process Engineering  
 Ben-Gurion International Airport  
 Israel 70100.

ABSTRACT

Image lobe intensities resulting from radomes enclosing large antennas ( $D \gg 15\lambda$ ) were evaluated using ray tracing and aperture integration of the reflected field. It is shown, that random phase approximation can be used when the greatest radius of curvature is less than  $D^2/8\lambda$ .

*A. Pupko, D. Gordon, S. Starobinets*

Image lobe (IL) intensity is probably the most critical design parameter in large, narrow band radomes. This parameter is closely related to the radome shape.

To get insight to the effect of the wall curvature to the IL intensities consider the reflection from the radome wall as an interaction between a curved (parabolic) and a planar antenna (See Fig. 1). Assume that both the antenna diameter,  $D$ , and the radius of curvature,  $R$ , of the parabolic antenna are much greater, than the wavelength ( $R \gg \lambda$ ,  $D \gg \lambda$ ). As a measure of the intensity reduction due to the antenna curvature we choose the ratio of signals in the receiver induced by a curved and that of second reference planar antenna :

$$\alpha = \frac{|S|^2}{|S_0|^2}$$

In the projected aperture field approximation [1]

$$\alpha = \frac{2\lambda R}{D^2} \left| F\left(\frac{D}{\sqrt{2\lambda R}}\right) \right|^2 \quad (1)$$

where  $F$  is the complex Fresnel function.

If the argument of the Fresnel function

$$\frac{D}{\sqrt{2\lambda R}} \geq 2$$

or

$$R \leq D^2/8\lambda \quad (2)$$

Then (1) reduces to

$$\alpha = \lambda R/D^2$$

The latter formulae may be obtained from geometrical optics approximation taking into account that  $\alpha$  is the ratio of an "angle of view" ( $\varphi_R \approx \lambda/D$ ) of the receiver antenna to the divergence angle ( $\varphi_T \approx D/R$ ) of the transmitter beam. Inequality (2) is a condition for application of the incoherent (or random phase) approximation to the IL calculations.

For three dimensional radome design, the incoherent approximation can be used when both radii of curvature are smaller than  $D^2/8\lambda$ .

We estimated the IL intensities for two, half-wave wall radomes, the contours of which are shown in Fig. 2. The basic assumptions applied were:

1. The dominant contribution to the far side lobes are the image lobes.
2. The appearance of the image lobes are resulted from specular reflections.
3. The radome can be considered as a collection of locally planar elements.

Two calculation models were used, both relying on ray tracing in receiving mode. In the coherent model [2] for uniform aperture distribution, the image lobe intensity in a direction  $\Omega$  from the antenna axis:

$$I(\Omega) = \left| \iint_A TR_y \exp(-ikL) dA \right|^2$$

where T is the wall transmission coefficient,  $R_y$  is the component of the complex reflected field in the direction of the antenna polarization and L is the ray path length between an external reference plane and the antenna. In a second model [3] the IL intensities were estimated by random phase approximation:

$$I(\Omega) = \iint_A |TR_y|^2 dA$$

The IL intensities were minimized by an iterative process for optimum wall thickness distribution. The results are summarized in Tables 1 & 2. Table 1 contains the IL peak intensities in an azimuth plane, directed to the tip of the radome. In Table 2 are listed the calculated peak and RMS IL intensities in the elevation plane.

It is apparent, that generally the incoherent model results in an overestimation of the IL levels - except for small angle gimbal positions. It is also noticed that relatively small changes in the radome geometry has an appreciable effect on image lobe intensities.

TABLE 1

Comparison of Coherent and Incoherent Models in Image Lobe  
Estimation

ANTENNA GIMBAL ANGLES		IMAGE LOBE PEAK LEVELS (DB)			
		RADOME "A"		RADOME "B"	
EL	AZIM	COHERENT	INCOHERENT	COHERENT	INCOHERENT
-4.5°	5°	-38.2	-37.9	-43.2	-42.7
-4.5°	10°	-39.2	-38.3	-42.4	-41.0
-4.5°	30°	-40.0	-32.1	-40.3	-34.1
-4.5°	60°	-41.6	-31.6	-40.9	-33.1

Table 2

The Effect of the radome shape on Image Lobe Level (Coherent Model)

ANTENNA GIMBAL ANGLES		RADOME "A"		RADOME "B"	
ELEV	AZIM	PEAK	RMS	PEAK	RMS
60	0	-37.6	-39.0	-34.8	-36.0
50	0	-37.9	-38.9	-35.0	-36.6
30	0	-38.2	-41.0	-36.5	-38.7
-50	0	-37.4	-39.3	-36.2	-38.0
-60	0	-38.2	-39.7	-35.1	-36.4

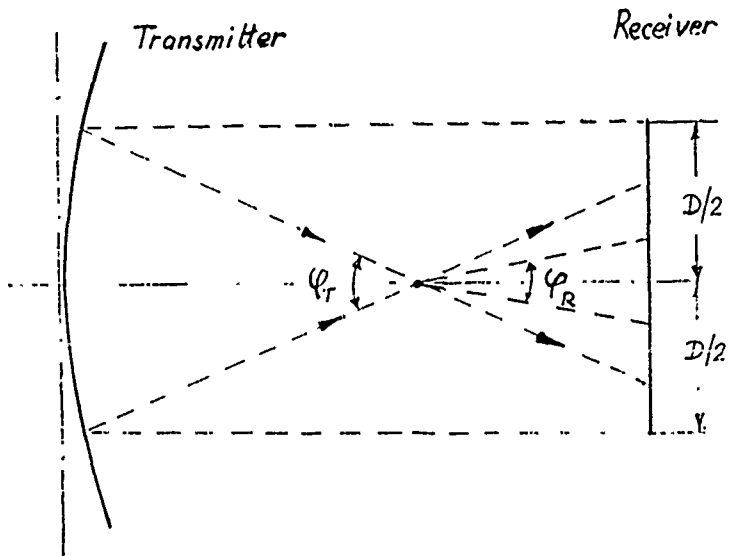


Fig. 1 Positioning Planar and Parabolic Antennas

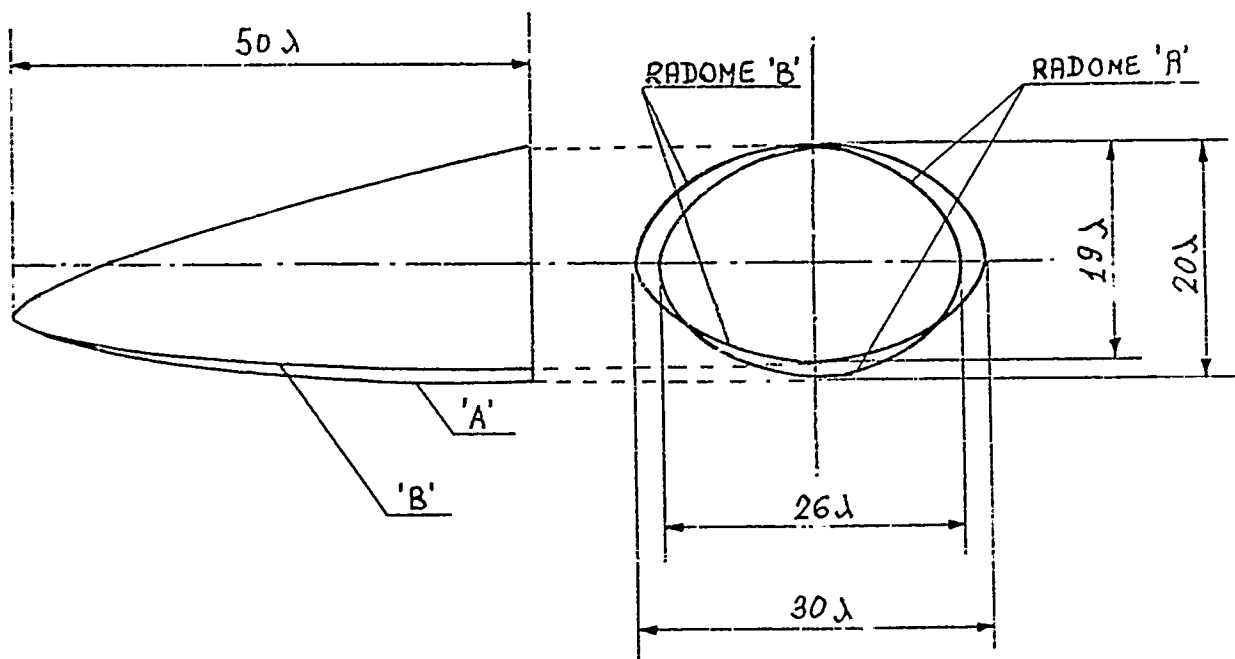
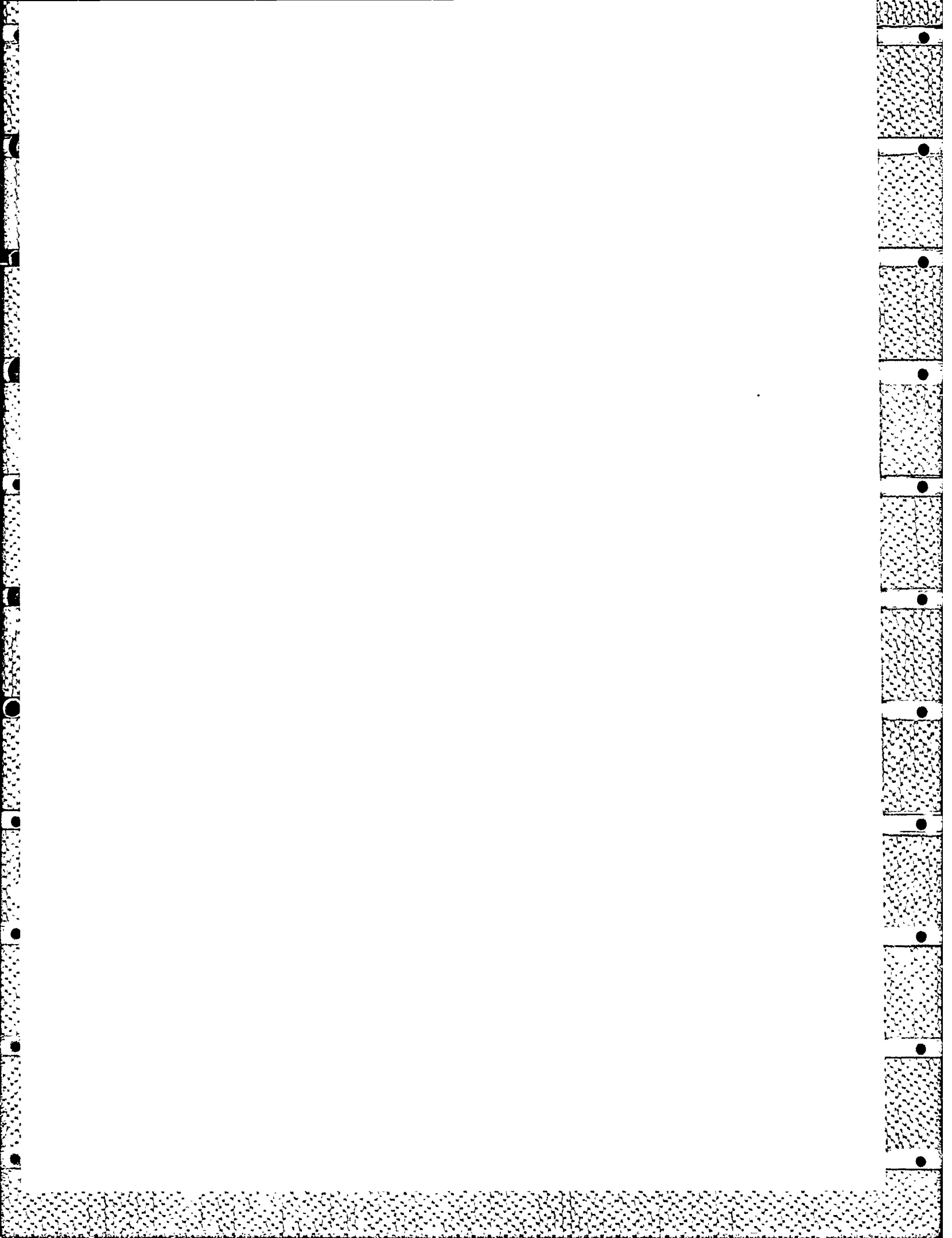


Fig. 2 Geometry of the Radomes ("A" & "B")  
 Antenna Limit Ellipse:  $16\lambda \times 22\lambda$

REFERENCES

1. R.H. Clarke and J. Brown, "Diffraction Theory of Antennas",  
Ellis Horwood Publ. 1980, Chap. 6, 7.
2. M. Chabah, "Computation of Antenna Pattern Distortion Due to  
Radome Insertion."  
Proc. Tenth Symposium on Electromagnetic Windows, Georgia Inst. Tech.  
Atlanta, Georgia 1970, PP 51.
3. M. Scorer, "The Calculation of Radome Induced Sidelobes",  
Radar 77 IEE Conference Publ. 155, London 1977, PP 414.





# HYPERSONIC RADOME STUDY

R. J. Joachim

Raytheon Company, Missile Systems Division  
Bedford, Massachusetts 01730

## ABSTRACT

During concept studies of a ground launched hypersonic interceptor missile, a thermal/structural investigation was made of various radome shapes constructed of hot pressed silicon nitride. Radome shapes studied included a tangent ogive, a 9.5 degree half-angle cone (with and without a protective cover for the initial portion of flight), and a combined 14 degree half-angle cone tip/tangent ogive body. A 1-D computer program was used to calculate thermal stresses and temperature profiles through the radome wall at two axial stations near the tip and one at the radome base. Ceramic wall thicknesses of  $X_0$ ,  $1.5 X_0$ , and  $2.0 X_0$  were investigated for most configurations.

Results indicated that a combined cone/tangent ogive shape was optimum, in that it alleviated the high thermal stresses at the tip associated with a tangent ogive and the high thermal stresses at the base experienced with a cone. The use of a protective tip cover that is ejected after launch can decrease inner wall temperature levels, thereby reducing the heating environment for internal components.

PREVIOUS PAGE  
IS BLANK



# SUPERSONIC TACTICAL MISSILE (STM) RADOME DEVELOPMENT

Arthur J. Thompson  
Brunswick Corporation  
Defense Division  
Marion, Virginia 24354

## AD-P004 360

### Introduction

The Supersonic Tactical Missile program included a radome development based on the geometry depicted, in Figure 1. The nose radome was a Von Karman body of revolution, 38 inches long with a 15 inch base diameter. The enclosed radiometer system utilized a 12 inch vertically polarized aperture providing four main lobes (an azimuth pair and an elevation pair) and operating over a narrow bandwidth (4.3%) centered at 35 GHz. This contrast seeker was gimballed on the radome longitudinal axis and limited to a primary tracking field of  $\pm 15$  degrees about this axis. Radome structural/environmental requirements were based on captive carry followed by free-flight air-to-ground modes with maximum durations approaching 160 seconds and temperature peaks above 900°F. Electrical requirements included the traditional transmissivity, boresight error magnitude/slope, and pattern distortion characteristics. Key specifications required transmission losses of less than 1.0 db (lobe gain imbalance of less than 0.5 db) while the boresight error maximum magnitude was fixed at 0.25 degrees and the error slope allowable at 0.05 degree/degree. The effects of radome emissivity under non-uniform heating conditions were also of concern due to the extreme sensitivity of the radiometer.

### Design Approach

A first order ("half-wave") solid laminate of Brunswick BPI-373 condensation polyimide with quartz fabric was selected for use. This configuration insured structural/mechanical integrity over the required time/temperature profiles. Environmental resistance was enhanced via the use of a metallic nose plug in conjunction with a thermal (wafer) barrier and a boundary layer trip. From an electrical standpoint, the first order low dielectric structure was well suited to the narrow frequency band and high incidence angles (up to 85 degrees), which were somewhat range limited by the scan sector.

PREVIOUS PAGE  
IS BLANK



As shown in Figure 2, sample laminate measurements, conducted by Microwave Consultants, indicated relative stability in dielectric constant at 35 GHz over the applicable temperature range; loss tangent values were higher than anticipated, however the associated ohmic or heat losses did not appear particularly severe in subsequent panel or radome measurements.

A white fluoroelastomer coating was initially planned for outer surface protection during "captive carry" with "clean departure" expected during the higher free-flight temperature conditions. This was consistent with existing test data and the dielectric data which indicated "no measurement" at 900°F due to material "melt". Based on electrical thickness sensitivity, the fluoroelastomer material was to be applied in a reduced thickness, however concern for emissivity variance or gradients during this "change-of-state" ultimately resulted in a coating change to a pigmented silicone based material. This provided good sealant and temperature resistance properties, but essentially no erosion or abrasion protection.

The electrical design was directed at achieving minimal reflection levels and low "direct path" phase variance. Analytical modeling was refined early in the design stage using flat panel fabrication/test, which also verified the extreme sensitivity to thickness variance. The resultant design used a nominal laminate thickness of .106 inches with no significant taper. The structural analysis confirmed the adequacy of the basic structure and finalized the attachment interface configuration.

#### Radome Fabrication

The radomes were fabricated on a male mandrel in a series of steps which included an extended post cure sequence in an inert gas atmosphere to insure a low void laminate of high temperature resistance. Since the electrical parameters displayed extreme sensitivity to small wall thickness changes and grind equipment capabilities were placed at  $\pm .002$  to  $\pm .003$  inches, an iterative process was used in the machining operation with a brief electrical test evaluation being conducted following each incremental grind of the shell wall. This evaluation utilized frequency variance and dielectric tape application to discern electrical trends and prescribe the succeeding grind. Following this effort, the radome assembly was completed

(i.e. nose tip and attachment hardware, exterior coating, etc.) and then subjected to the prescribed tests.

### Test Measurements

Electrical measurements included transmission loss, which was typically in the range of 0.7 to 0.8 db (85 to 83%) maximum with improvements to about 0.5 db (90%) or better as the 15° scan limits were approached. These trends are shown in Figure 3 for the two principal, orthogonal scan planes through the radome centerline at 35 GHz.

Boresight error displayed peak magnitudes of two to three milliradians (0.11 to 0.17 degrees). As shown by the typical mid-frequency scans in Figure 4, inplane error polarity or sense was generally divergent with maximums at 6 to 8 degree angular offsets in both principal scan planes. Deflection levels were extremely sensitive to nose region wall thickness changes with classically predictive behavior. Error slope, derived directly from the magnitude data, showed typical peak values through the nose region of 0.4 mr/degree (.023 degree/degree) however a maximum of 0.6 mr/degree or .034 degree/degree (5 degree average) was encountered on one unit.

Radiation pattern measurements were evaluated with respect to the common parameters of sidelobe increase, beamwidth change, and lobe imbalance. In general, no severe distortion was evident, although some isolated, individual sidelobes did show increases above specification objectives.

Electrical tests were also conducted using the radiometer outputs, which provided voltages proportional to the amplitude differences in the beam "pairs" (azimuth and elevation). In the test arrangement, a "hot" source swept the band (10 millisecond sweep time) while the radiometer "pattern" was generated over a  $\pm 10$  degree scan sector centered on the boresight axis. Direct analog recordings were obtained as well as digital data via desktop computer control, the latter being used in rather extensive evaluation procedures. A typical azimuth channel output for an azimuth scan through the elevation beam pair "null" or "cross-over" is shown in Figure 5 for both free-space and "with radome conditions (+3° azimuth/0° elevation offset). In general, the radome introduces no unusual or significant

distortion in the differential voltage response other than the attenuation associated with the radome insertion loss.

Environmental tests included thermal, vibration, altitude and humidity. The humidity test sequence, which was of most interest, resulted in a 0.6% weight increase of the radome shell (excluding hardware). This in turn caused a temporary transmission loss increase of up to 0.5 db. Return to the "pre-humidity" levels occurred following exposure to ambient conditions.

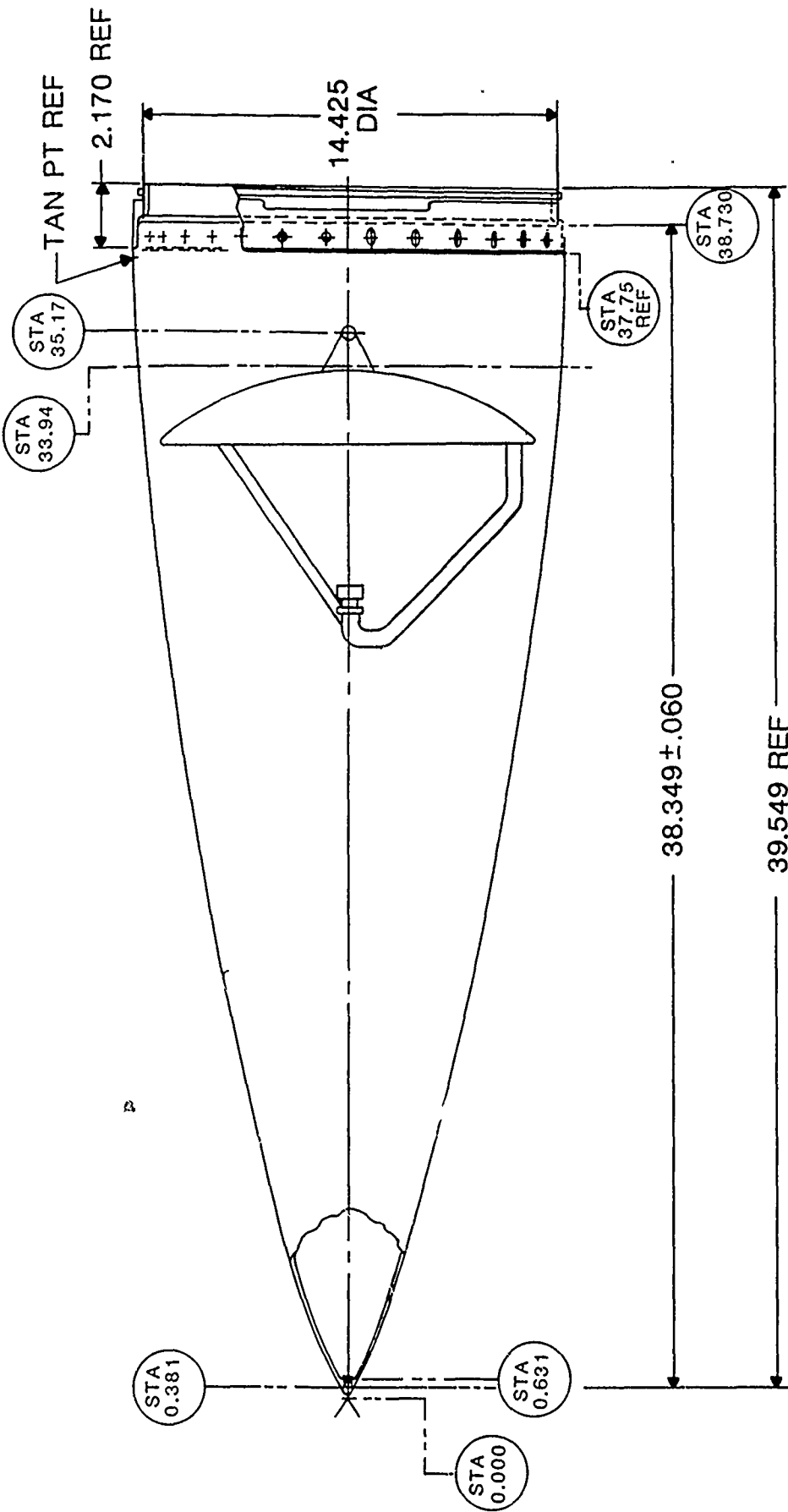
Structural tests were conducted with temperature compensated loads (combined shear/moment and axial) being applied in increments up to 125% of limit (ultimate) and later to 140% of limit load without failure. Some residual deflection was observed and attributed primarily to deformation of the "O" ring in the Marmon clamping mechanism.

#### Summary

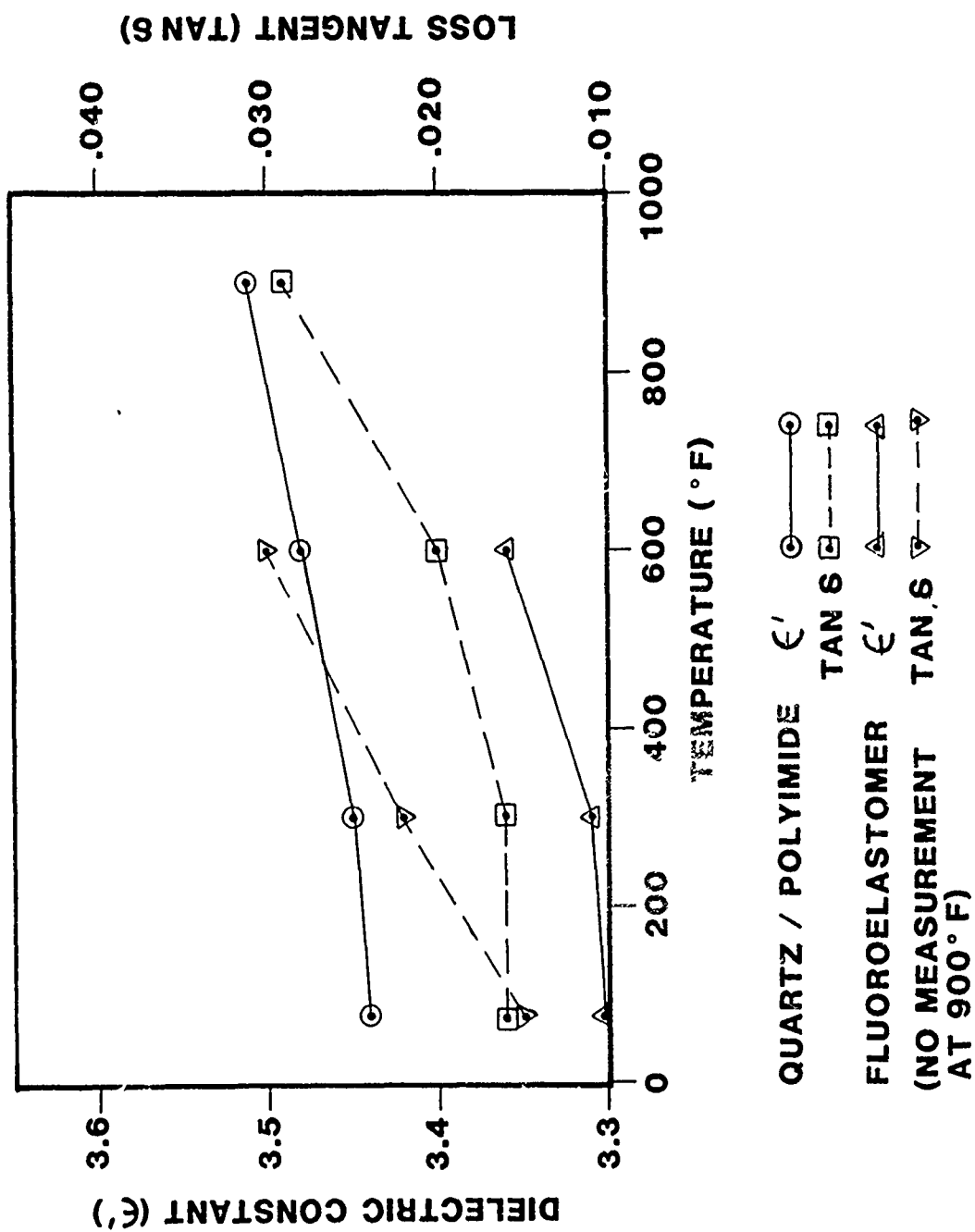
The development program was successful in producing a nose radome assembly which met the basic requirements of the Supersonic Tactical Missile application with no difficulties being encountered in the limited flight test program. Figure 6 shows a "captive-carry" mounting of the STM during this segment of the program. Potential problem areas identified included the common ones of exterior surface protection and moisture absorption. Radome electrical performance was considered good and indeed somewhat better than expected. The work performed in optimizing these performance levels provided a renewed appreciation of the tolerances associated with Ka-band frequencies and the desirability of electrically large apertures.

#### Acknowledgement

This work was performed under contract to Vought Corporation (Government Contract No N00123-78-C-0074). The author acknowledges the helpful discussions and insight provided by Mr. Tom Leeth of Vought Engineering.

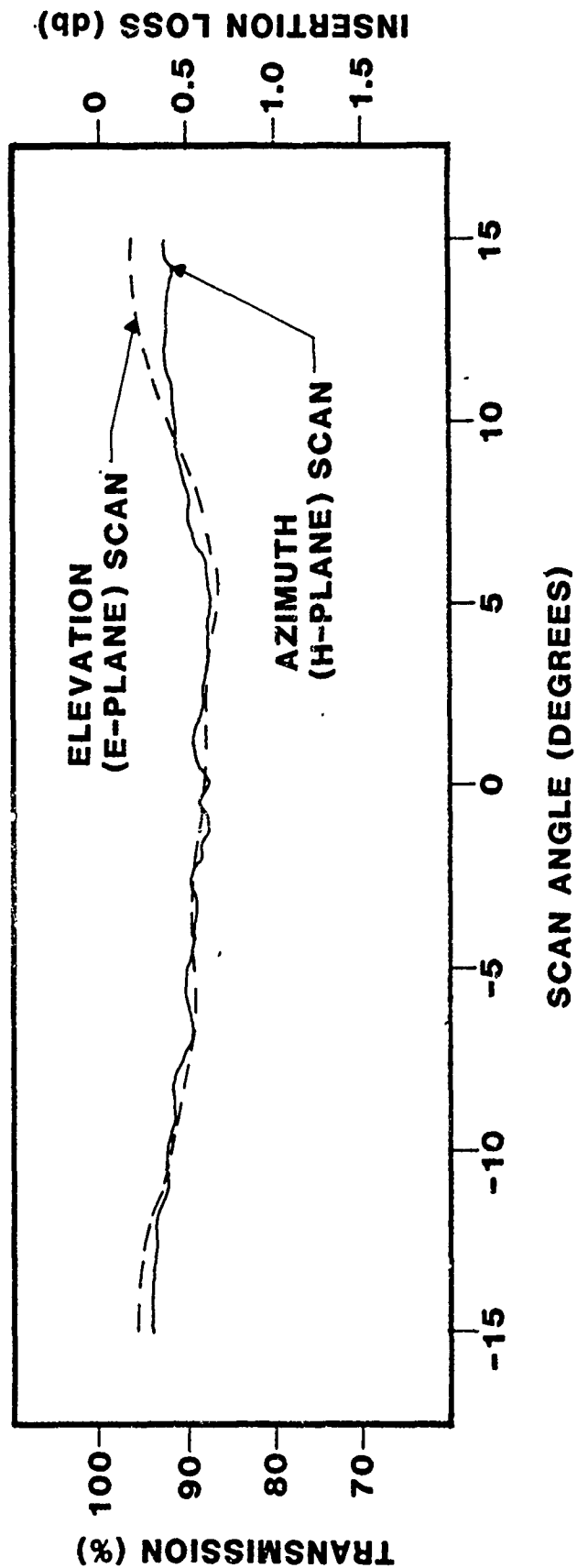


**FIGURE 1: STM ANTENNA/RADOME GEOMETRY**

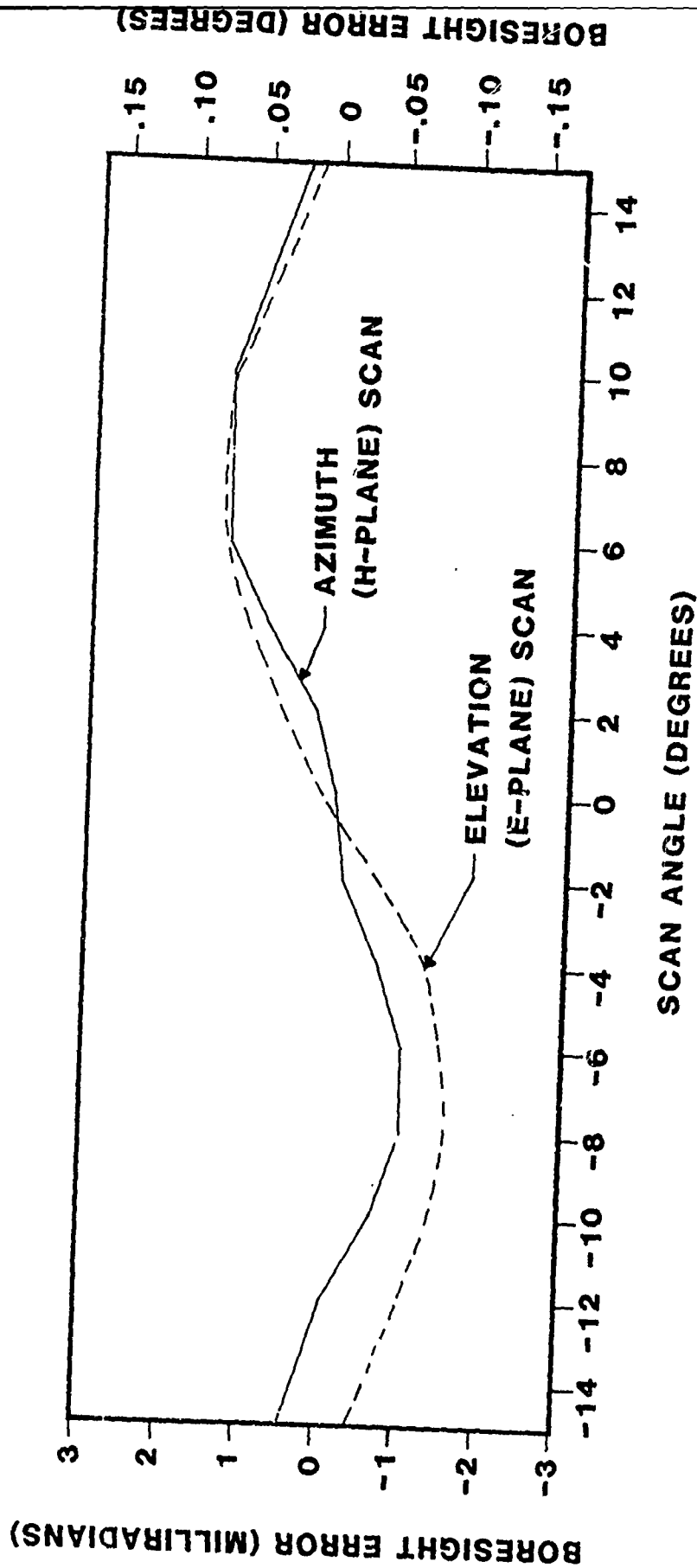


**FIGURE 2: MATERIAL DIELECTRIC PROPERTIES AT 35GHZ**

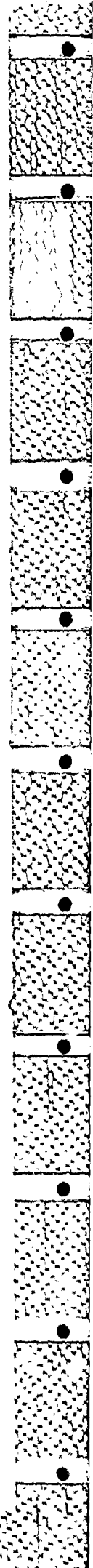


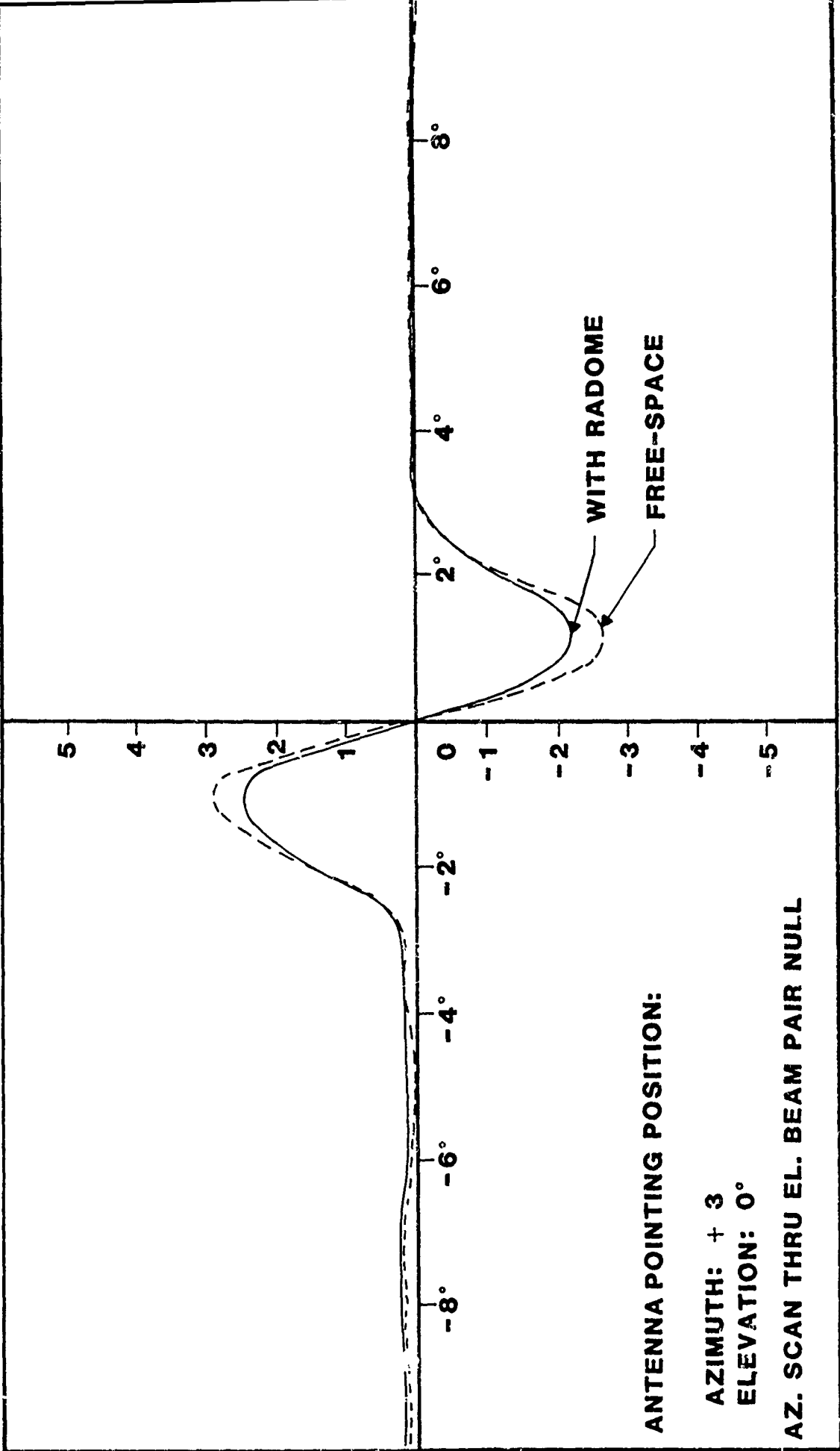


**FIGURE 3: TYPICAL TRANSMISSION RESPONSE AT 35GHZ  
(LEFT AZIMUTH BEAM)**



**FIGURE 4: TYPICAL IN-PLANE BORESIGHT ERROR RESPONSE AT 35GHZ**





SCAN ANGLE (DEGREES)

FIGURE 5: RADIOMETER RECEIVER AZIMUTH OUTPUT

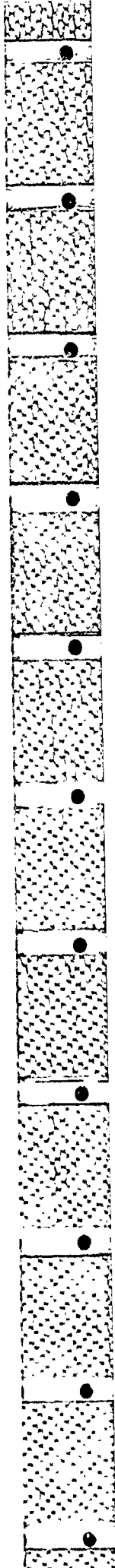




**FIGURE 6: STM FLIGHT TEST PREPARATION**

ABSTRACT

SILICON NITRIDE RADOME DEVELOPMENT  
FOR BROADBAND HIGH TEMPERATURE APPLICATIONS

James F. Schorsch and Gary E. Miller

Engineering Technology  
BOEING AEROSPACE COMPANY

This paper describes the design, development, fabrication and test of a large broadband silicon nitride radome for hypersonic missile applications. Both partial size (typically the forward third of a full size radome) and full size radomes were fabricated and subjected to extensive testing at room and elevated temperatures. Results of electrical testing conducted on two radomes at room and elevated temperatures are presented. Radome electrical performance tests included radiation pattern measurements of a large aperture scanning antenna and a small aperture wideband antenna over a multioctave frequency range.

This program was sponsored by the Avionics Laboratory, AFWAL under Contract F33615-79-C-1836. Project Engineer was Alan Blume.

A MILLIMETER WAVE APPARATUS FOR FREE-SPACE MEASUREMENT  
OF DIELECTRIC CONSTANTS AT HIGH TEMPERATURE

D. R. Gagnon and D. J. White  
Michelson Laboratory  
Naval Weapons Center, China Lake, California 93555

**AD-P004 361**

INTRODUCTION

Radome materials are being required to withstand increasingly higher temperatures. There is, therefore, a continuing need to measure the dielectric properties of these materials at elevated temperatures, particularly at millimeter wavelengths where the data base is still relatively sparse. At the Naval Weapons Center (NWC) an apparatus has been constructed to measure the complex transmission coefficient of flat panel samples at 35 GHz. The complex permittivity of the sample is calculated from the transmission measurements which are made in a free-space bridge. An array of high-intensity infrared lamps is used to heat the sample and bulk temperatures up to 1000°C have been obtained thus far. This heating arrangement allows measurements to be made at large angles of incidence. As a result, measurements can be made at the Brewster angle which greatly simplifies data acquisition and analysis.

MEASUREMENT APPARATUS AND TECHNIQUE

A block diagram of the apparatus is given in Figure 1. The microwave beam is directed through the sample by a pair of lens focused horns. For the current setup, the horns focus to a 3-dB spot size of 1.5 wavelengths at a focal distance of 18 inches. The receive horn sits upon a carriage which can move the horn along the beam and across the beam using micrometer screws which read position to 0.0001 inch. The reference arm of the bridge

PREVIOUS PAGE  
IS BLANK



contains a phase shifter and a variable attenuator which are used to precisely "null" and balance the bridge prior to inserting the sample.

A lock-in amplifier is used to measure the detected signal from the bridge. The lock-in amplifier provides greatly increased sensitivity over the use of a direct current (DC) voltmeter permitting measurement of a very small power imbalance on the bridge. This, in turn, allows the measurement of transmission loss through very low-loss materials.

The radio frequency (RF) source consists of a 10-mW klystron at 35 GHz which is phase locked to a stable 5 MHz crystal oscillator. The 35 GHz signal is square-wave modulated at a frequency of 500 Hz for the use of the lock-in amplifier.

The sample heater consists of a set of 10 high-intensity incandescent lamps with collimating reflectors. The lamps are arrayed in circular arcs on either side of the sample to focus their output onto a narrow strip on the sample surface. At full power each lamp produces an output heat flux of approximately 1 kW on a 1.5- by 6-inch aperture with peak output at about 1 micron. The sample temperature is measured with a thermocouple placed below the sample surface. A temperature controller provides sample temperature setability.

Measurements are made by setting the phase shifter and attenuator so that the bridge is very precisely balanced, i.e., the output of the detector is zero, with the sample removed. With the sample in place, the bridge is renulled at each temperature by adjusting the separation of the focused

hoins. The phase shift through the sample is then read from a micrometer [1]. Transmission loss through the sample is determined by using the lock-in amplifier to measure the detected power imbalance of the bridge with the sample in place at the Brewster angle.

While measurements are certainly not limited to Brewster angle incidence or parallel polarized incidence in our apparatus, the permittivity measurement is greatly simplified by this arrangement. At arbitrary angles of incidence, the flat panel transmission coefficient must be inverted by numerical iteration to yield the sample permittivity. At the Brewster angle, the relative dielectric constant and loss tangent are given by [2].

$$\epsilon_r = 1 + \left(\frac{\Delta L}{d}\right) \cos \theta + \left(\frac{\Delta L}{d}\right)^2 \quad (1)$$

$$\tan \delta = \frac{-\lambda \ln(t) \sqrt{\epsilon_r - \sin^2 \theta}}{\epsilon_r \pi d} \quad (2)$$

where  $d$  is the sample thickness,  $\Delta L$  is phase shift through the sample in the same units as  $d$ , and  $t$  is the magnitude of the voltage transmission coefficient. The quantity  $t$  is given in terms of measured data by the following expression

$$t = \frac{1 - \sqrt{P}}{1 + \sqrt{P}} \quad (3)$$

where  $P$  is  $P_{\min}/P_{\max}$ , the ratio of minimum to maximum detected power as the relative phase on the bridge is rotated through 360 degrees with the sample in place.



## PRELIMINARY PERFORMANCE DATA

The performance of the measurement system was evaluated by making measurements of the relative dielectric constant of fused quartz versus temperature up to 900°F. Higher temperatures can be achieved by blackening the surface of the sample since quartz is nearly transparent at the peak output wavelength of the heat lamps. Total thickness of the quartz plate sample was 0.578 inch.

Figure 2 gives a plot of the measured results along with measurements made by W. Ho [3] of Rockwell Science Center. Ho claims a measurement accuracy of better than 1% and our results agree with his to within about 2%.

## CONCLUSIONS

We find that the NWC high temperature permittivity measurement apparatus provides sufficient precision to measure the relatively small changes in dielectric properties which occur as quartz is heated. This precision should be more than adequate to characterize the electrical properties of most radome materials at high temperatures.

The current arrangement for heating the sample does cause a problem which limits the sensitivity of the apparatus due to proximity heating of the dielectric lenses on the focused horns. It turns out that a rise in lens temperature of a few degrees produces fairly large measurable changes on the output of the bridge. For this reason, the sensitivity of the apparatus is reduced so that we have not yet been able to measure the small temperature variation of loss tangent for quartz. By improving the thermal isolation of the sample, the sensitivity of our apparatus could be increased considerably.

## REFERENCES

1. G. R. Blair, "An Ultra-Precise Microwave Interferometer," IRE National Convention Record, Part 1. 24-27 March 1958, New York, NY.
2. R. M. Redheffer, "The Measurement of Dielectric Constant" in *Technique of Microwave Measurements*, C. G. Montgomery, Ed., McGraw-Hill, 1947, New York.
3. W. W. Ho, "High Temperature Millimeter Wave Characterization of the Dielectric Properties of Advanced Window Materials," AMMRC TR 82-28, Final Report to Army Materials and Mechanics Research Center, 1982.

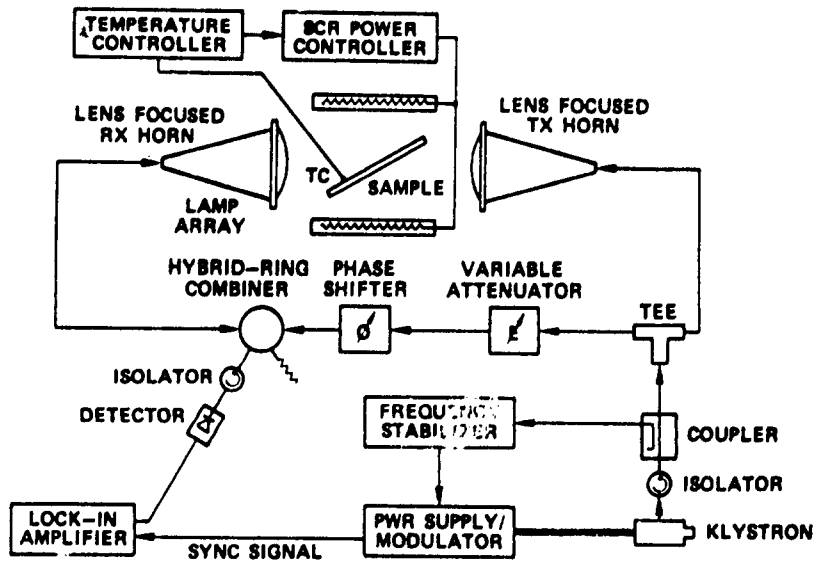


Figure 1. Block diagram of the measurement apparatus

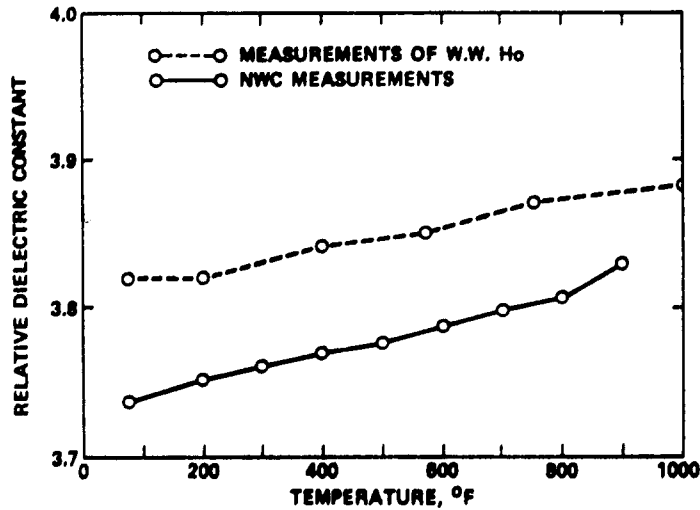


Figure 2. Relative permittivity measurements for fused quartz

## AUTOMATED RADOME TESTING

by

CHARLES E. MOORE

JOHN B. STYRON

BRUNSWICK CORPORATION

DEFENSE DIVISION

MARION, VA 24354

# AD-P004 362

### Introduction

An automated test system has been developed for correction and electrical testing of F-16 Nose Radomes, and is currently in use. A computer control/data acquisition system is utilized in the measurement of transmission efficiency, boresight error, and radiation pattern parameters for each radome. Major components of the facility and equipment include an anechoic chamber and compact range, a five (5) axis positioner with encoders on all axes, and a control/data acquisition console.

The F-16 Nose Radome is a half-wave wall utilizing filament wound construction and precision grinding to provide optimized X-band performance. The F-16 aircraft antenna is a flat plate array utilizing a sequential lobing technique for boresighting, where the boresight axis is determined by equal amplitude crossovers between beam positions. Beam steering over the required squint angle is accomplished by the switching of four (4) uniphasors in the array manifold to produce an up-down-right-left sequence of the main beam.

### Facilities

The facility configuration and major equipment items are shown in Figure 1. Equipment located in the anechoic chamber consists of the RF reflector and feed assemblies, the radome test positioner, remote control station and display, and the personnel hydraulic lift platform. Pyramidal RF absorber material (8 and 12 inch) covers the walls, ceiling and floor of the chamber and is backed with a metalized surface. The size of the chamber is 36'L x 20'W x 17'H. Height of the positioner boresight axis from room floor level is 9'6". A radome dolly with hydraulic lift is used to mount and dismount the radome. After the radome is mounted on the positioner, it can be opened and closed by means of a hydraulic hinge and latch system which permits the adjustment of RF power free space reference levels and also allows the installation of correction tape without removing the radome from the positioner itself. The remote control unit and associated 19" CRT display permits the technician to perform baseline data and correction scans from the anechoic chamber location. The computer control and data acquisition system is housed in eight console racks, with all operating subsystems mounted above the writing surface. The area below this surface contains the air plenums and blowers.

## RF Systems and Controls

A block diagram of the R-F system and controls is shown in Figure 2. The transmission system consists of a sweep generator frequency source, 10 watt TWT amplifier, frequency counter, power control unit and a transmit power monitor. Operation of this equipment is by computer control and provides a power stability of  $\pm 2\%$  as monitored at the RF feed assembly. The transmitted power is compared to the preset free space level at the start of each scan and adjusted by the computer. The receiving system is divided into three categories, transmission ( $T^2$ ) measurement, pattern measurement and boresight error measurement. For transmission measurement, the RF power from the system antenna is detected at the RF output port, amplified and then modulated by the transmission synthesizer and coupled to an SWR meter, the analog output of which is converted by the computer to transmission efficiency in percent. For pattern measurement, the antenna RF output is coupled to an IF frequency converter and then to the pattern receiver where the analog output is converted by the computer to pattern level change in DB. For boresight error measurement, the antenna RF power is detected at the antenna output and coupled through the boresight error comparator which supplies the relative voltage levels of the right-left and up-down lobe sequence positions of the antenna RF pattern. This information is coupled to the antenna azimuth and elevation microcomputer digital control systems which continuously position the antenna to its RF boresight axis during the scan.

The range reflector feed is also computer controlled to provide either horizontal or vertical linear polarization dependent upon requirements. The radome is tested in an on-side position with horizontal polarization for all transmission and boresight error measurements.

## Test Positioner and Controls

The radome positioner and control console are shown in Figures 3 and 4. The positioner has five axes of movement; azimuth, elevation and roll associated with the positioner itself and azimuth and elevation movement of the antenna gimbal axes. All axes are controlled by stepper motor drives operated by their associated computers. The positioner radome roll assembly is equipped with a hydraulically operated hinge mechanism allowing the radome to be opened and closed without removing the radome from the positioner. The angular positions of each of the five axes are monitored by 18 bit absolute reading optical encoders.

The positioner and controls are designed to provide a counter-rotation of the antenna as the basic azimuth and elevation movements of the radome positioner are rotated. This arrangement permits the continuous controlled movement of the antenna to any position within the aircraft controlled window zone and eliminates the quadrant scanning method required when using a fixed support for the system antenna. This continuous scan test method coupled with the automated control provided by the test range computers result in a substantial reduction in radome test time compared to that of the more conventional fixed antenna support system. Computer Control, Data Acquisition, and Display Computers (five total) are used to operate the system during correction or acceptance testing. Three of the units are microcomputers dedicated to specific preset functions; antenna azimuth and elevation gimbal axis control and antenna lobing sequencer drive. The two

primary mainframe computers are equipped with operator terminal interfaces and are used to control the positioner axis movement, provide data acquisition during each scan, control the R-F system and provide various housekeeping functions. A graphical display of the radome performance data in analog format is displayed on a scan by scan basis on the 19" CRT. Included are horizontal and vertical boresight error components,  $T^2$  and pattern performance, and radome test performance specification limits. Data acquisition is accomplished by reading analog outputs of the RF receiving system and binary outputs of the shaft angle encoders.

### Baseline Data and Correction

Operator interface to the system for baseline data and correction is thru the remote control station located in the anechoic chamber. This station consists of a switch operated logic interface to the primary range computer and permits the technician to perform any scan defined in the test procedure in any random sequence. Out-of-spec scan segments can be examined (CRT display) and the appropriate correction techniques employed to change the radome performance values to comply with specification limits. For boresight error tests, the limit magnitudes are also displayed for each scan.

### Radome Testing

Upon initiation of the test sequence, the antenna is automatically positioned such that the main beam is on the range boresight axis. With the radome in an "open" position, the operator adjusts the transmission pattern power level to 100% or 0 DB free space reference level. The radome is then closed over the antenna and the test sequence begun.

Operating in the boresight error/ $T^2$  mode, the system antenna is continuously counter-rotated to the RF amplitude null in both the horizontal and vertical planes as the radome is rotated about the range boresight axis. Bore-sight error performance is recorded in both planes as a function of the antenna axis movement required to maintain the null and compared to the same scan performed for free space conditions. The algebraic comparison of radome versus free space data essentially normalizes repeatable scan anomalies to zero with the remaining data representing the two planes of radome boresight error performance. Power transmission is simultaneously recorded in percent change as a function of scan angle. Measurements are made continuously over a 120° scan angle (aircraft azimuth) for various elevation offsets. Operating in the Pattern Mode, the antenna is offset to the angle required relative to the radome, and the radome and antenna are then rotated through the required scan coverage with the pattern performance being recorded in DB attenuation each 1/3° of scan angle.

### Data Acquisition and Reduction

RF power data (Transmission and/or Pattern) is acquired by means of A/D converters coupled to the analog outputs of the RF measurement equipment. Bore-sight error data is acquired in binary format of encoder shaft angle position on a free space versus radome algebraic comparison basis. For boresight error testing, approximately 3,000 data points are taken per 120° of scan. This high number is required because of the null crossover nature

of the counter-rotating servo control loop. This crossover occurs at an approximate 50 Hz rate during the scan and has an oscillatory peak to peak value of approximately  $\pm 300$  microradians. The raw data waveform can be considered analageous to an amplitude modulated carrier frequency with the modulation representing the radome boresight error. Since the oscillation is basically a function of the positioner scanning speed and the computer servo loop control speed (which are essentially preset values), it is periodic or repetitive in nature. This characteristic permits mathematical normalization of the oscillation peak to peak level to within an average value of approximately  $\pm 150$  microradians of the true radome boresight error measurement values.

Each radome test data scan is stored using one of the data acquisition computer flexible disk drive units and is retained as a permanent record of the radome performance. X-Y plotter hard copy of each scan can be provided when required. A summary of the radome performance and verification of specification compliance is provided by the computer printer for each unit tested.

### Results

In evaluating a test system of this nature, the predominant question that is always asked is "what are the day to day repeability performance values?" Figures 5 and 6 are actual F-16 transmission, boresight error and pattern azimuth scans performed on a repeat (3) basis. The difference between the smoothness of the vertical and horizontal boresight error components is due to the remaining carrier oscillation present on the horizontal component after data processing. Since the only movement of the elevation gimbal axis of the antenna during the scan is that due to the radome itself, the vertical boresight error carrier oscillation level remaining after data processing will obviously be much lower than that associated with the horizontal component.

With the automated test system and the indoor compact range facility, the time required to correct and test radomes was reduced by 50% when compared to a conventional outdoor test range. Day to day repeatability was also drastically improved such that "free-space" scans need only to be performed once per month for calibration.

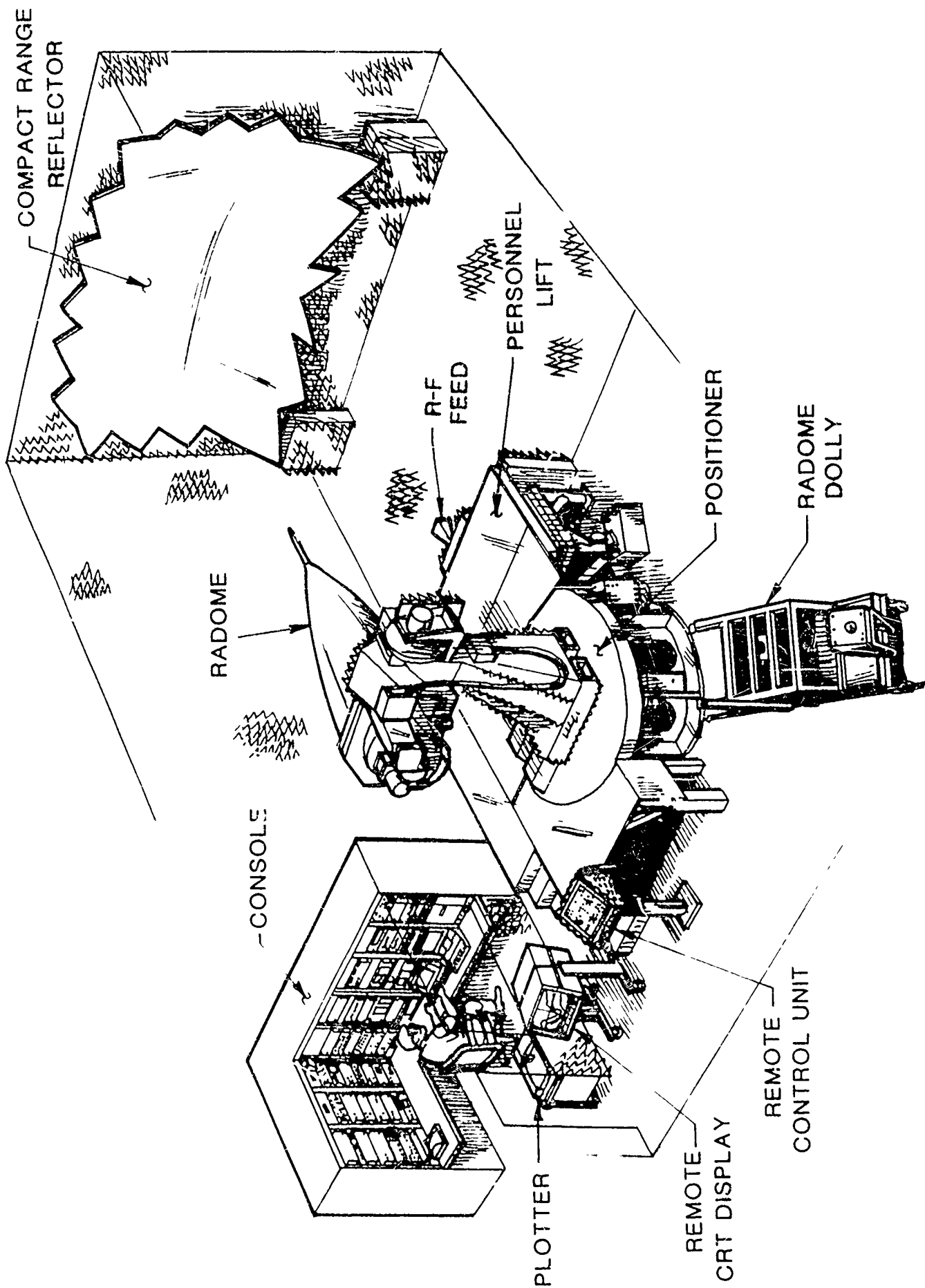


**FIGURE 1: FACILITIES AND EQUIPMENT**



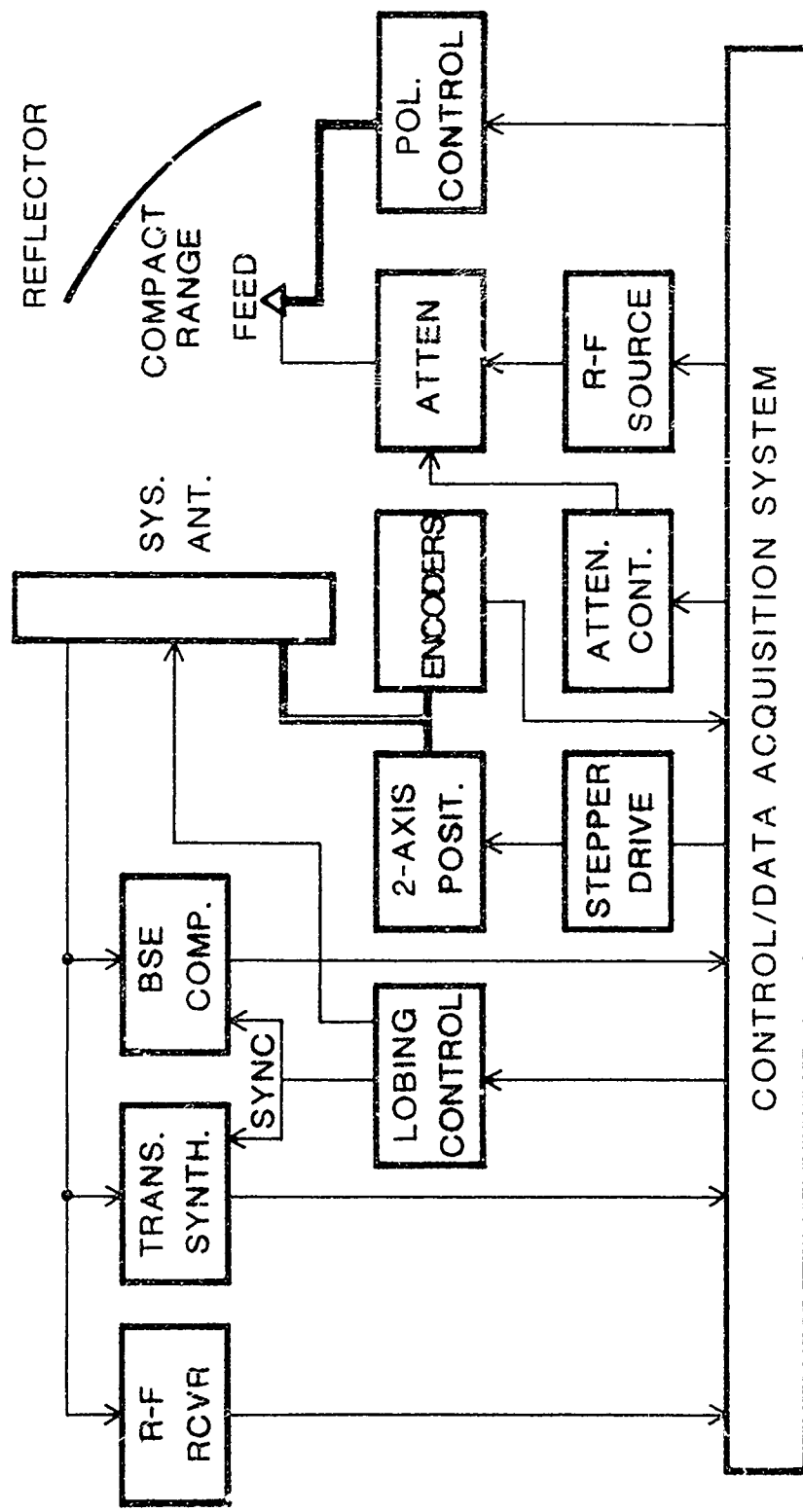


**FIGURE 2: R-F SYSTEM/ANTENNA CONTROL**

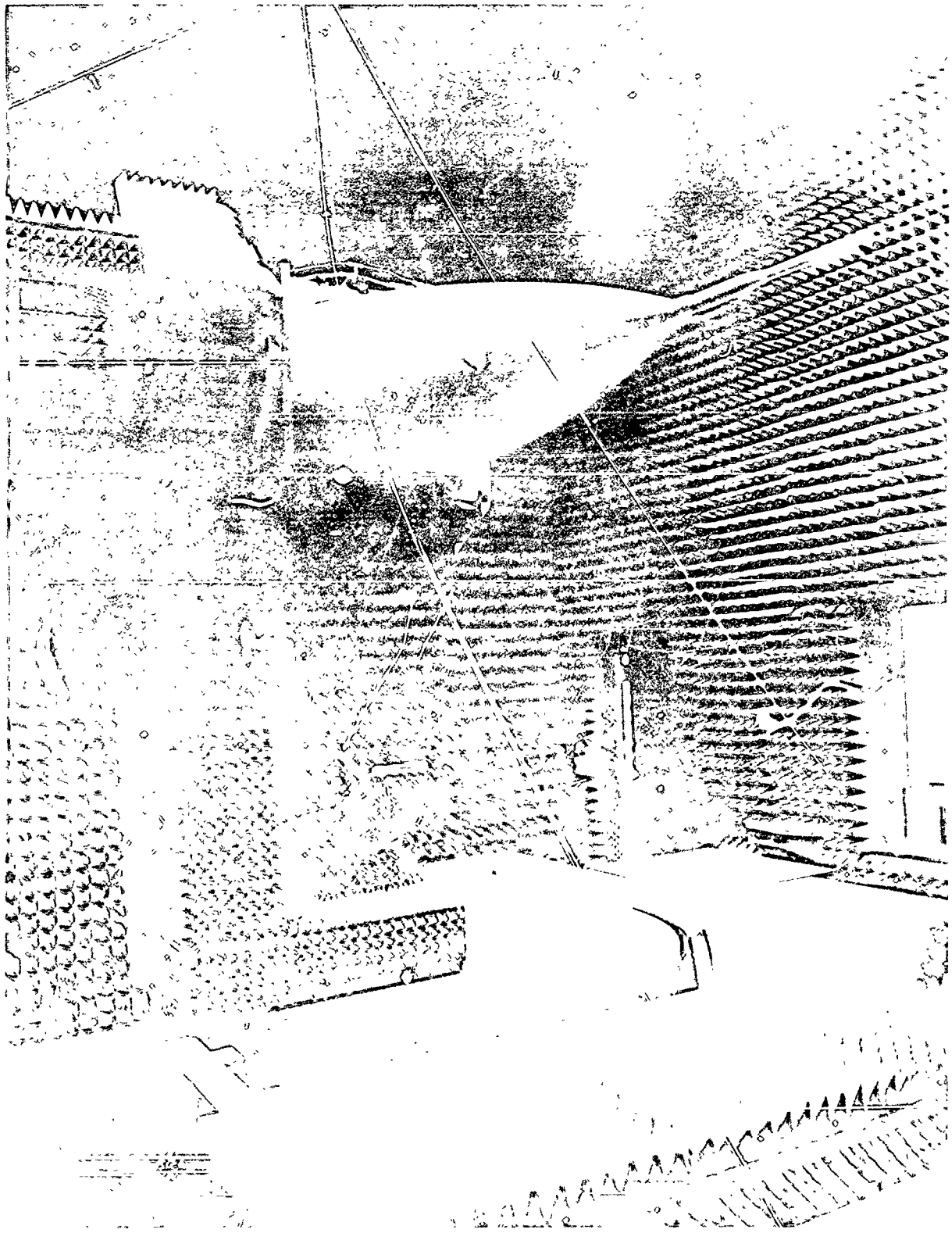
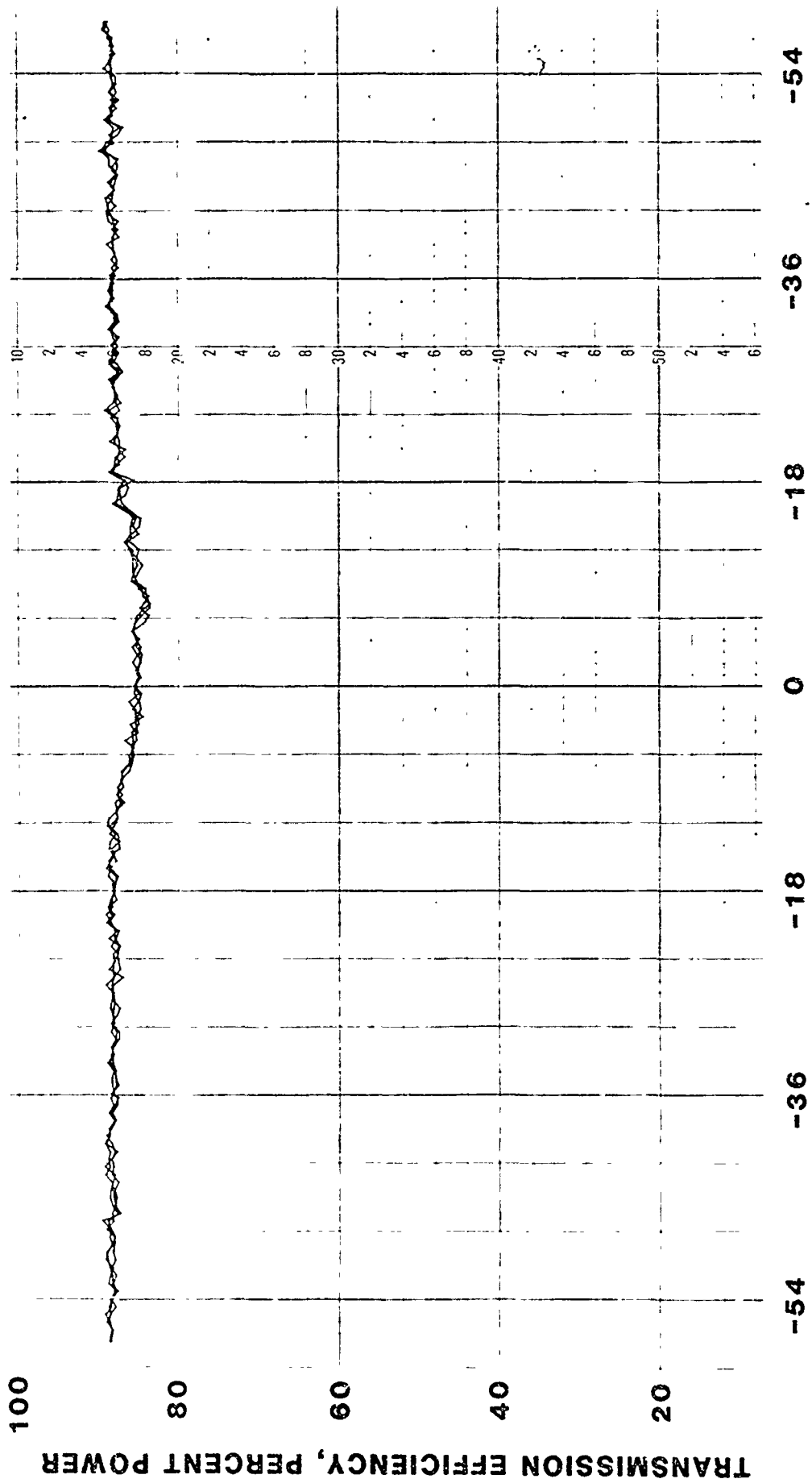


**FIGURE 3: F-16 RADOME ON POSITIONER**

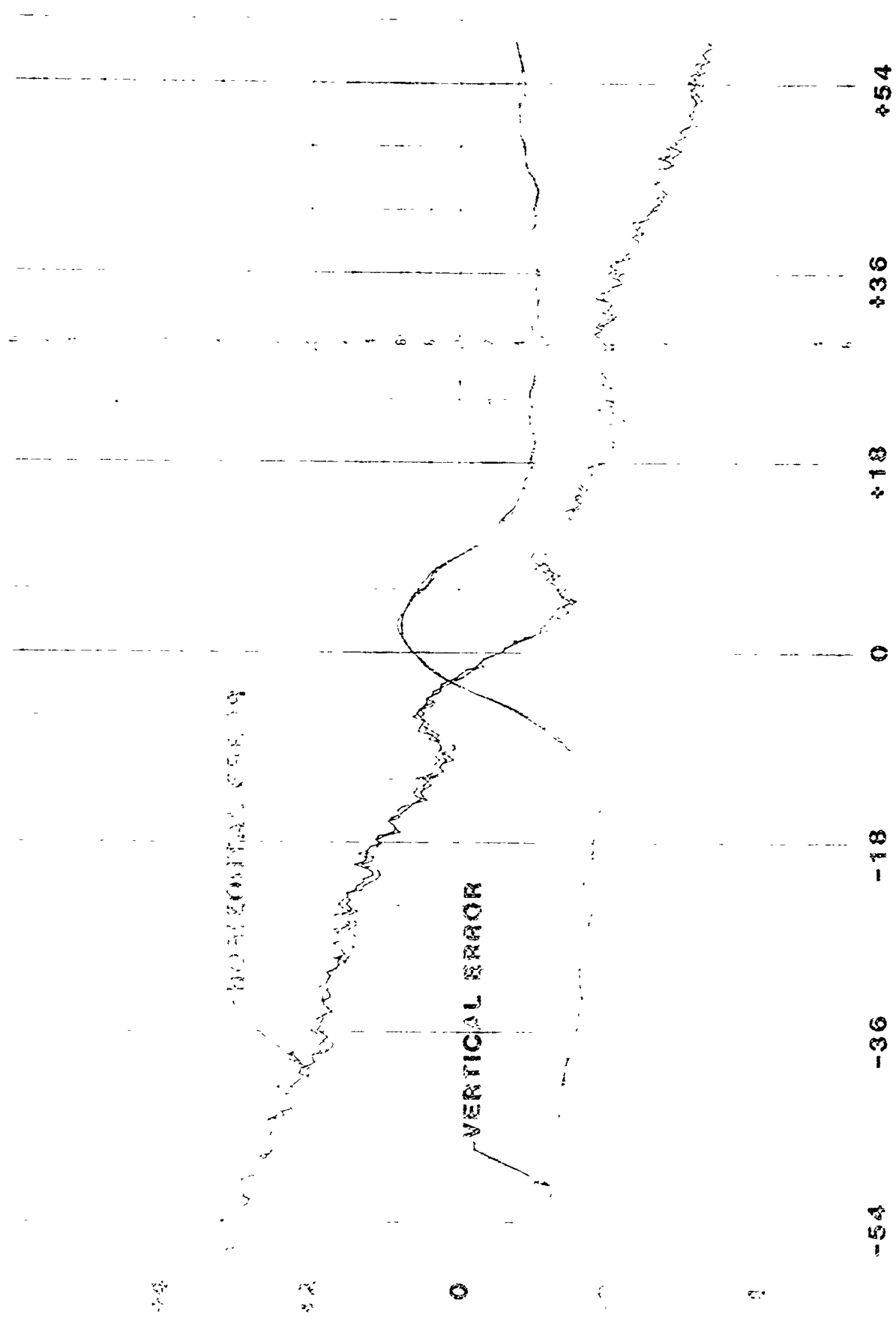
**FIGURE 4: CONTROL CONSOLE**



ANTENNA AZIMUTH SCAN ANGLE, DEGREES

FIGURE 5: TYPICAL RADOME TRANSMISSION EFFICIENCY

BORESIGHT ERROR (FT)



ANTENNA AZIMUTH SCAN ANGLE, DEGREES

FIGURE 6: TYPICAL RADOME BORESIGHT ERROR

## DESIGN AND CALIBRATION OF A 35GHZ DIELECTROMETER

J. HANSON and J. BRAZEL

MATERIALS DEVELOPMENT & CHARACTERIZATION LABORATORY  
GENERAL ELECTRIC COMPANY, RE-ENTRY SYSTEMS  
PHILADELPHIA, PA 19101

**AD-P004 363**

### INTRODUCTION

A 35 GHz (fixed frequency) dielectric measurement facility has been designed and calibrated for use in our laboratory, principally for support to development of  $K_A$  band and millimeter wave radome materials. This paper describes the basic design, gives some details of the construction and electronic instrumentation and presents the results of inter-laboratory calibration on Dynasil 4000 fused quartz.

### DESCRIPTION OF DIELECTROMETER

The complete assembled dielectrometer apparatus is shown in Figure 1. The waveguide hardware, solid state electronics and the corresponding dimensions of the measuring section itself make for a compact tabletop installation.

The dielectrometer uses the shorted waveguide technique and is adapted from the 24 GHz apparatus previously developed by W. Westphal at MIT (Ref. 1). A block diagram of the facility is shown as figure 2. The slotted waveguide and heated sample holder section use a 1/4" diameter circular waveguide excited in the  $TE_{11}$  mode. The energy source is a phase locked Gunn diode (Hughes model 47741H-2210). The output is modulated with a ferrite device and coupled to a short piece of coax with a tuned waveguide adapter. The energy is then coupled to the slotted line with a loop at the center of a shorting plunger.

A closeup view of the slotted line assembly is shown in figure 3. In this photograph, which shows the high temperature configuration, the waveguide section is behind the rectangular (probe carriage) enclosure. The sample holder/furnace assembly is at bottom and the precision micrometer probe positioning assembly is at the top.

The slotted line has an 8 mil wide axial slot, long enough to allow approximately one half wavelength of probe travel. The probe is a .0015" diameter gold plated tungsten filament. Energy picked up by the probe is detected by a diode in the probe carriage. The probe depth is adjustable. Also, tuning is provided in the carriage to optimize sensitivity at different probe depths. This tuning is provided by a coax shorting plunger built into the probe carriage. The position of the carriage is adjusted and measured with a large barrel micrometer. The end of the slotted line is threaded to attach to the sample holder.

The room temperature sample holder is simply a copper tube with a flat bottom short provided with a small central hole to press samples out. The high temperature sample holder is a longer platinum tube with similar flat bottom short and knock out hole. A water cooled plate is soldered to the top of the sample holder to keep the slotted line from being heated. The sample holder is heated with a platinum-iridium alloy coil which is wrapped around an alumina tube and muffled with the lower thermal conductivity porous fire brick cylindrical enclosure visible in the photo. The wall thickness of the section of platinum tube between the heater and the cooled section was thinned in order to reduce heat loss out of the high temperature holder and furnace into the waveguide section.

The principal instrumental difficulties encountered in the 35 GHz scale version of the Westphal's earlier 24 GHz design were in the closer machining and part positioning tolerances required. Dimensional errors of mispositioning of the 0.2497 inch diameter sample or the blind end sample holder/waveguide section and extremely slight misalignments of the travelling voltage probe were found early in the calibration effort to give larger error sensitivity than previously experienced.

In the electronics, the purchased components have worked to specifications, but our earliest work was delayed by phase locked oscillator instabilities until the need for an isolator between the Gunn diode source and ferrite modulator was identified.

#### MEASUREMENT PROCEDURE:

When using the dielectrometer for room temperature measurements, the position and 3D width of a null are first measured with the slotted line with no sample in the holder. These measurements are then repeated with the sample in the holder. Measurements are usually repeated with the holder rotated 90° and with the sample flipped end from end to check on sample uniformity.

Elevated temperature data is taken in the same way. Null width and position are measured as the sample holder is heated in approximately 100°C steps. Data is then reduced using computer coded algorithms. These codes allow and correct for such effects as differential thermal expansion and growth of the specimen, including sample to waveguide fit effects.

#### MEASUREMENT RESULTS:

The results of measurements on a sample of Dynasil 4000 fused quartz (clear glass vitreous fused silica) are presented in Table 1. As described above, the room temperature copper holder measurements were made in a combination of two rotational positions and with the cylinder faces reversed. This is the practice regularly observed in W. Westphal's data and serves as a measure of homogeneity and isotropy.

High temperature measurements using the platinum waveguide/sample holder have been performed up to 1175°C at the time of preparation of this paper. The furnace design and platinum holder are however expected to be capable of 1400-1500°C. We have been reluctant to jeopardize conduct of several programs requiring dielectric measurements in this lower temperature range with this apparatus but expect to push the platinum holder to above 1200°C in the near future.



These data are plotted in Figures 4 and 5, compared to the corresponding previous measurements by Westphal (Ref. 2) and Ho (Ref. 3). Two sets of measurement runs have been made on one specimen, the first to 748°C and a second in the high temperature holder only, to 1176°C. The dielectric constant data are remarkably close to these references, well within 1.0%. Our loss tangent data are however higher; e.g. an average value of 0.00072 at 25°C using the copper holder versus 0.00035 by Westphal and 0.00040 by Ho.

Transferral to the high temperature holder gives measured values of 0.00086 - 0.00090 for loss tangent at 25°C. At our first maximum measured temperature of 748°C the value is 0.00058, compared to 0.00020 for Westphal (807°C) and 0.00030 for Ho (800°C). For the second set of measurements to 1176°C, the difference is smaller: 0.0005 versus 0.00035 and 0.00030.

Regarding instrumental design differences, these are obviously extremely low loss tangents to measure by the shorted waveguide method and in our dielectric materials development work such low loss tangents would be considered excellent properties. The shorted waveguide method has the advantage of enabling measurements of materials with loss tangents rising up through the range 0.001 - 0.01 and higher where tuned cavity methods lose sensitivity. Westphal used the platinum foil enclosed cavity method, driving the tuned dimensions specimen with a  $K_A$  band klystron oscillator. This method would be expected to have superior sensitivity in low ranges of loss tangent. Ho used a cavity perturbation technique.

Another obvious consideration in these comparisons is that we have to date measured one specimen.

Future instrument development work will include higher temperature measurements on Dynasii 4000 and a reference higher dielectric constant material.

## REFERENCES

1. Westphal, W.B., "Dielectric Constant and Loss Measurements on High Temperature Materials", Technical Report 182, Massachusetts Institute of Technology, Laboratory for Insulation Research, October 1963
2. Westphal, W., "Dielectric Constant and Loss Data", Technical Report AFML-74-250, Part III, May 1977.
3. Ho, W.W., "High Temperature Millimeter Wave Characterization of the Dielectric Properties of Advanced Window Materials", AMMRC TR-82-28, Rockwell International Science Center, May 1982.

TABLE 1: DIELECTRIC CONSTANT AND LOSS TANGENT MEASUREMENTS  
ON DYNASIL 4000 FUSED QUARTZ AT 35 GHz

ROOM TEMPERATURE MEASUREMENTS IN COPPER HOLDER

<u>FACE</u>	<u>ROTATION (DEGREES)</u>	<u>DIELECTRIC CONSTANT</u>	<u>LOSS TANGENT</u>
1	0	3.833	.00071
1	90	3.828	.00076
2	0	3.829	.00073
2	90	3.828	.00069
AVERAGE		3.8295	.00072

HIGH TEMPERATURE MEASUREMENTS IN PLATINUM HOLDER

TEMPERATURE, °C

25	3.818	.00086
25	3.814	.00090
125	3.823	.00074
204	3.832	.00071
314	3.844	.00061
431	3.860	.00064
531	3.881	.00062
651	3.890	.00062
748	3.905	.00058
25	3.814	.00090

(Repeat on  
Cool Down)

REPEAT MEASUREMENTS, IN HIGH TEMPERATURE HOLDER

25	3.844	0.00093
54	3.849	0.00083
191	3.859	0.00077
305	3.872	0.00064
408	3.885	0.00067
535	3.901	0.00063
635	3.915	0.00057
763	3.933	0.00059
862	3.948	0.00057
955	3.962	0.00059
1055	3.976	0.00050
1176	3.993	0.00052

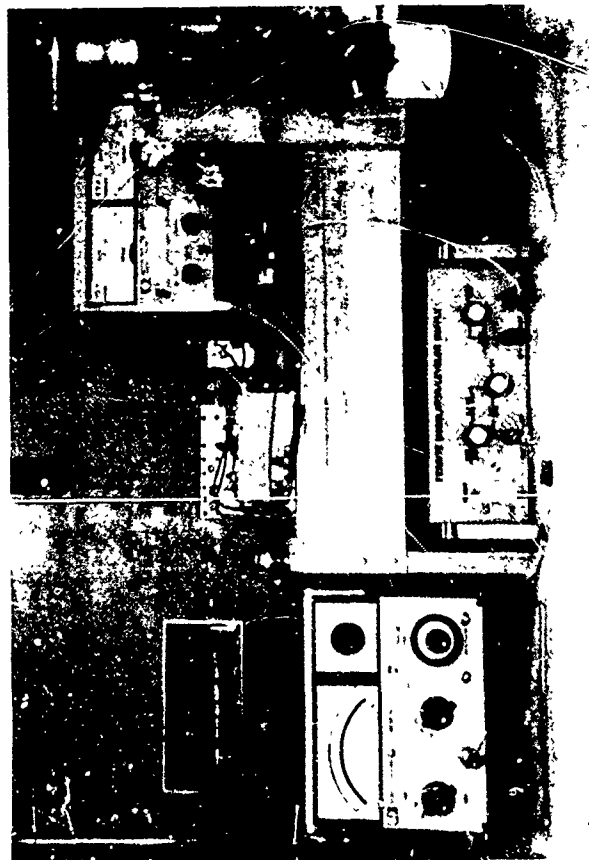


Figure 1: Photograph of the 35 GHz Slotted Line Dielectrometer

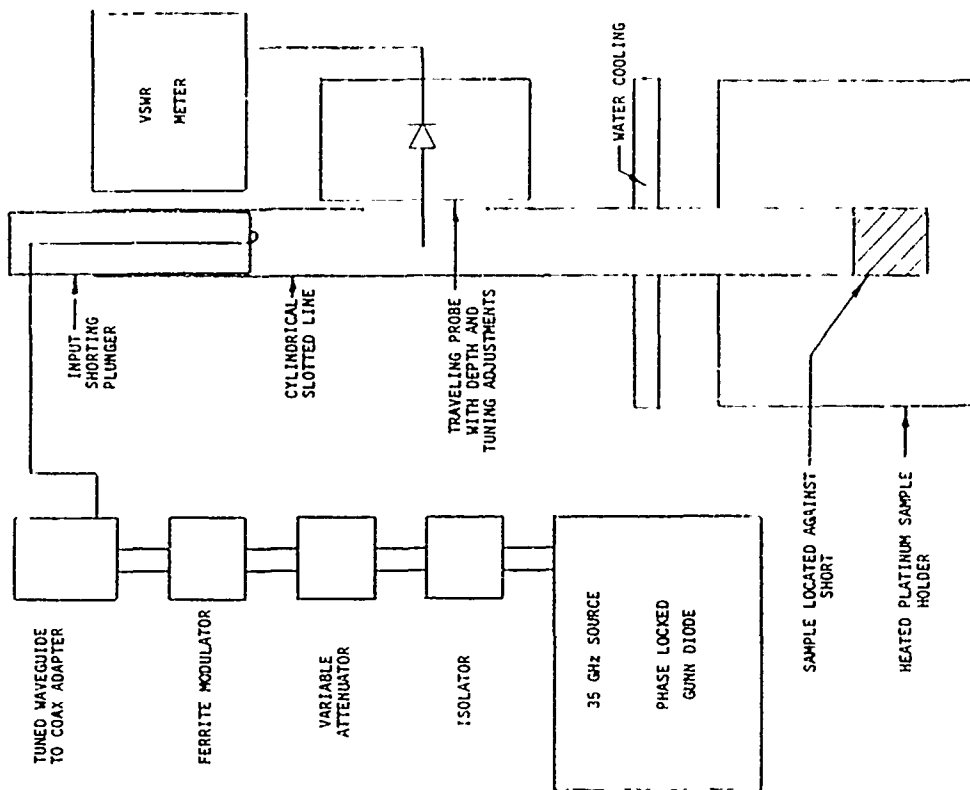


Figure 2: Schematic of the 35 GHz Slotted Line Dielectrometer

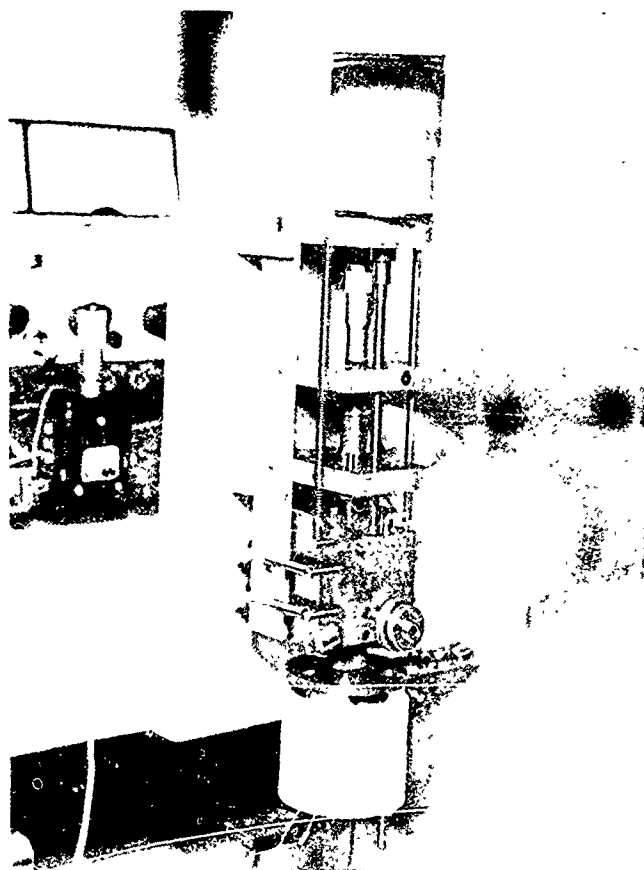


FIGURE 3: CLOSEUP VIEW OF SLOTTED LINE ASSEMBLY

FIGURE 4

COMPARISON OF DIELECTRIC CONSTANT DATA  
DYNASIL 4000 FUSED QUARTZ AT 35 GHz

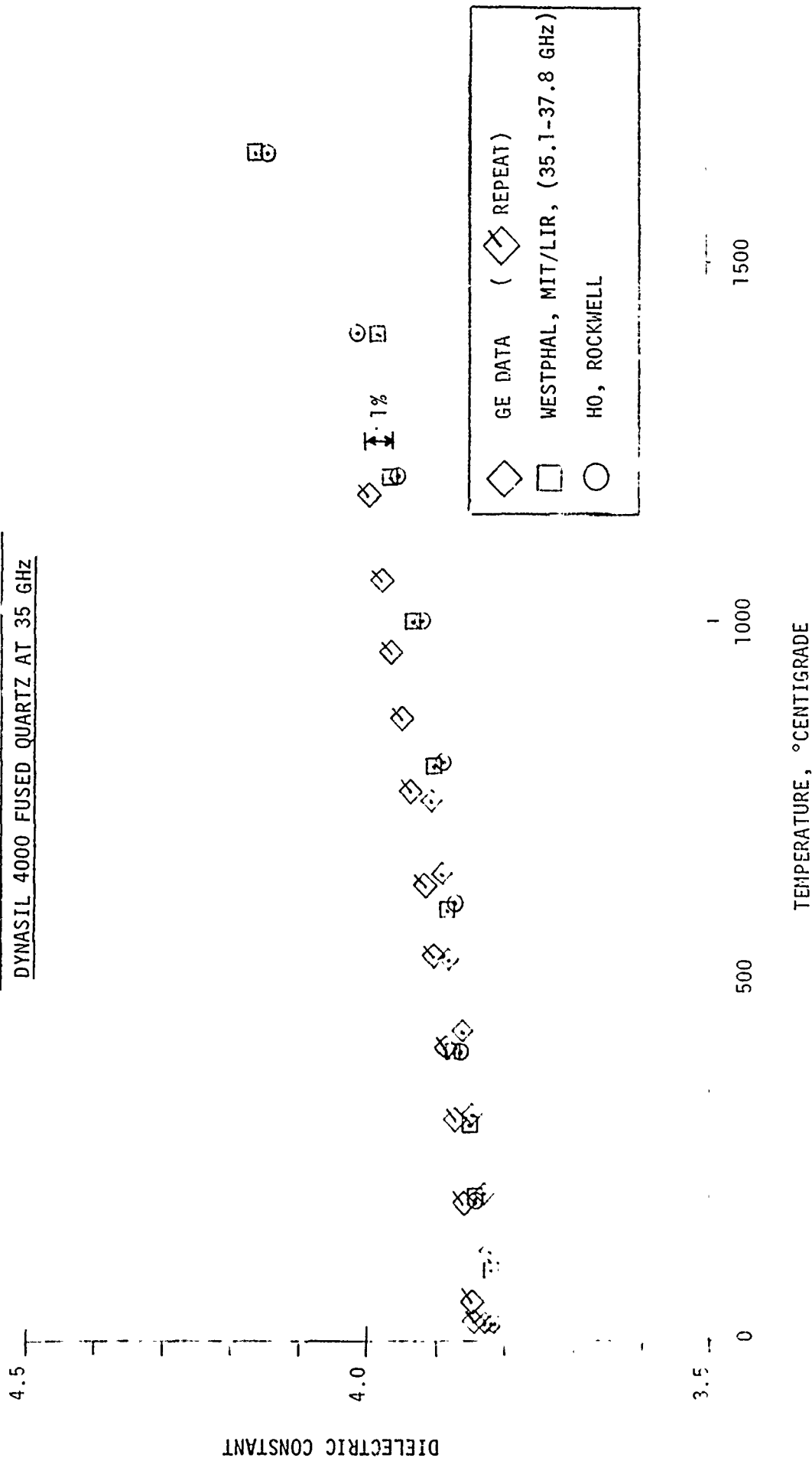
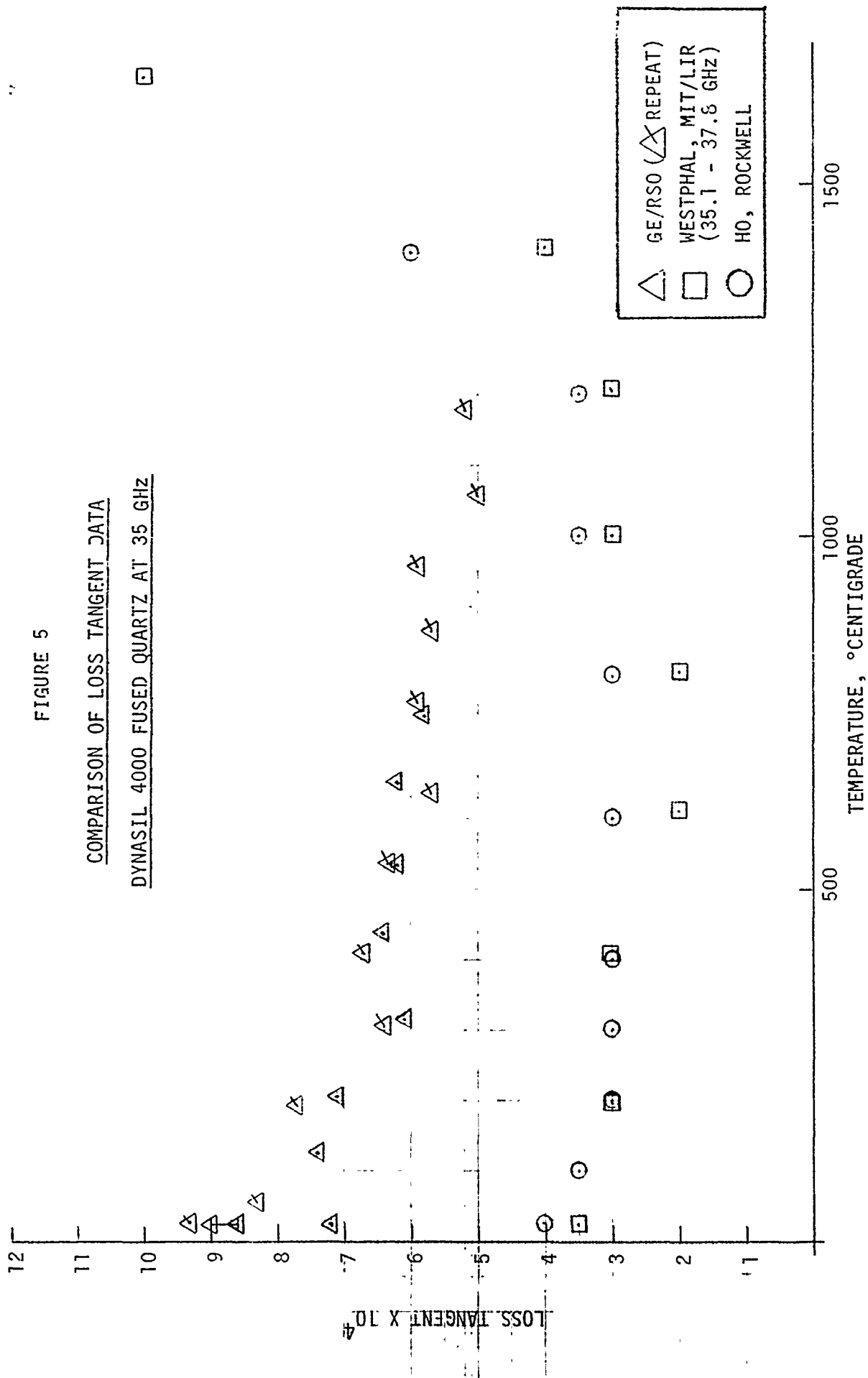


FIGURE 5

COMPARISON OF LOSS TANGENT DATA

DYNASIL 4000 FUSED QUARTZ AT 35 GHz



# HOT RADOME BORESIGHT ERROR MEASUREMENTS

C.S. Ward, M. Cerullo, and G. Plimpton  
Raytheon Company, Missile Systems Division  
Bedford, Massachusetts 01730

## AD-P004 364

### SUMMARY

A test facility has been developed which permits the convenient measurement of boresight errors on missile radomes heated to flight temperature profiles with peak temperatures approaching 1400°F. Its key ingredients are an electric oven and radome conformal heat socks having independent thermostatically controlled zones to produce desired longitudinal radome temperature tapers, and infrared video equipment to remotely monitor and record radome surface temperatures.

Hot radome error measurements from this facility<sup>1</sup> have been used to establish that: 1) radome heating causes significant changes in boresight error due to shifts in radome tuning frequency; and 2) radome wall thickness equivalents can be determined for aero-heating induced BSE changes<sup>2</sup>.

### INTRODUCTION

Typical materials used for missile radomes have a dielectric constant that increases with temperature as shown in Figure 1. This causes the radome walls to electrically look thicker, corresponding to a decrease in radome tuning frequency. The resulting effects on radome boresight error cannot be neglected in many applications.

An example is Pyroceram 9606, which has a dielectric constant that increases approximately 1% for every 200°F increase in temperature. Simple wall theory predicts that an average temperature increase of this size should correspond to 0.6% shift in tuning frequency for a radome with a half-wave wall at X-band. Such frequency shifts can cause significant changes in the boresight errors of missile radomes.

In view of the fact that average radome temperature increases above 200°F are frequently encountered, it is clearly desirable to make radome measurements at elevated temperatures to evaluate temperature effects on radome electrical performance. The hot radome boresight error test facility is intended to enable convenient, relatively low cost measurement of thermal effects on radome performance.



## FACILITY DESCRIPTION

The equipment used for radome heating, temperature measurement, and recording is shown in the photograph of Figure 2. In the center of this picture is a 10Kw electric oven that can be raised and lowered by a motor driven hoist. It is shown in the raised position above a heated radome resting on fire brick. This oven consists of open heating coils configured to match the radome shape and connected so as to form six independent zones, each of which is thermostatically controlled. The temperature of any zone can be preset at any desired level over a wide range, making it possible to reproduce a large variety of longitudinal temperature profiles upon radomes under test.

Mounted on a tripod at the left side of the figure is a commercial infrared video camera that senses heat radiation from the radome in the 8-12 micron wavelength range with a liquid air-cooled detector cell of mercury cadmium telluride. The camera has a line scan mode that permits television display of the thermal profile along any horizontal line in its field of view. Seen on the TV screen next to the camera is one such scan along the longitudinal axis of the radome under the oven. Temperature at each point is proportional to the vertical amplitude of the scan line trace. There is sufficient amplitude adjustment to permit a wide range of temperature display ranging from 10° to 1500°C full scale deflection on the TV screen. Calibration (before rf testing) is provided by a series of thermocouples mounted along the longitudinal axis of the radome which are connected, as shown in the figure, to a 16-channel data logger that records thermocouple readings directly in degrees. Also, comparison of IR signal levels for the radome with that of a black body at the same temperature permits direct measurement of the radome emissivity.

Figure 3 shows the results obtained in reproducing a typical radome temperature profile. Both the data logger and a TV tape recorder were started the moment the oven was lifted from the radome. One minute later, the data logger thermocouple readings were directly compared with the temperature readings from the video trace on the TV screen. Note that the two sets of temperature readings track one another within 5% and that the radome temperature is initially set everywhere above the analytically predicted or measured profile one desires to produce. Temperature of the radome is then continuously monitored by the IR camera during the time it is mounted on the boresight error test stand. Boresight error data is taken when the temperatures have decayed to the desired flight profile. Decay times must be minimized to protect antenna components from overheating.

The mounting of a heated radome on a test stand is shown in Figure 4, where temperature decay has been delayed by heating the radome with a three-zone portable thermal sock that can be carried with the radome into the test chamber. Removal of the heat source is then the last stage of the mounting process before starting to take RF data.

## EXPERIMENTAL RESULTS

Figure 5 shows a typical result of the effects of elevated temperature on the pitch plane boresight error of a Pyroceram radome measured at X-band. The dashed line is the boresight error measured at ambient temperature. The solid line is the boresight error obtained after uniformly heating the radome to a temperature increase of 215°F. This rise in temperature produces about a 75% change in the peak BSE.

It can be shown for uniform radome heating, that this result is primarily due to a shift in radome tuning frequency. This is illustrated in Figure 6 where the heated radome data of Figure 5 is overlaid by ambient temperature data on the same radome taken at a higher frequency,  $1.006 F_0$ .

In general, the observed temperature effects on radome boresight error are not only a frequency shift but also distortions caused by wall thickness tapers and radome tip-to-base temperature gradients<sup>(2)</sup>.

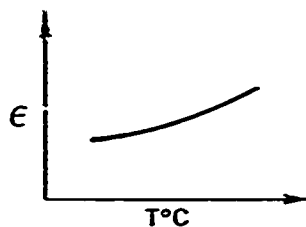
## CONCLUSIONS

Radome BSE and transmission tests and data displays are now available for simulated flight temperature profiles with Raytheon's Automated Radome Test Facility. The benefits are: 1) a significant improvement in hypersonic missile radome design capability; and 2) cost reduction in flight simulated radome electrical measurements.

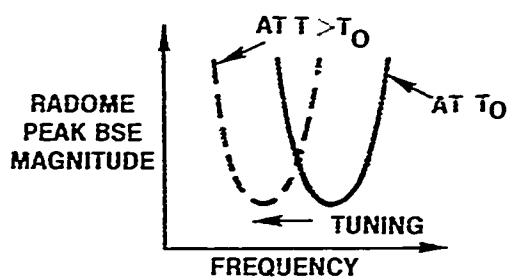
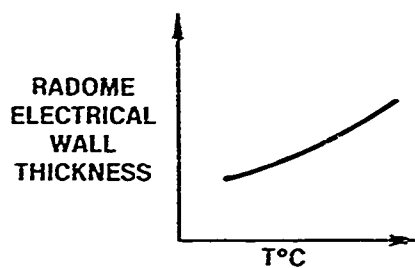
## REFERENCES

1. T. Dowling, M. Cerullo, C.S. Ward, and A.R. Chinchillo, "Automated Radome Test Facility", 14th Symposium on Electromagnetic Windows, Atlanta, Georgia, 21-23 June 1978.
2. G. Plimpton, "Radome Wall Equivalents to Aero Heating Induced BSE Change," MICOM Workshop on EM Windows/Domes, Redstone Arsenal, Alabama, 19-21 July 1985.

•  $\epsilon$  OF RADOME INCREASES WITH TEMPERATURE



- CAUSES RADOME WALLS TO LOOK ELECTRICALLY THICKER
- CAUSES DECREASE IN RADOME TUNING FREQUENCY



• RESULTS IN SIGNIFICANT CHANGES IN BSE WHICH MUST BE MEASURED AND COMPENSATED TO REDUCE ERROR SLOPES TO ACCEPTABLE LEVELS

Figure 1. The Effects of Radome Heating on Electrical Performance

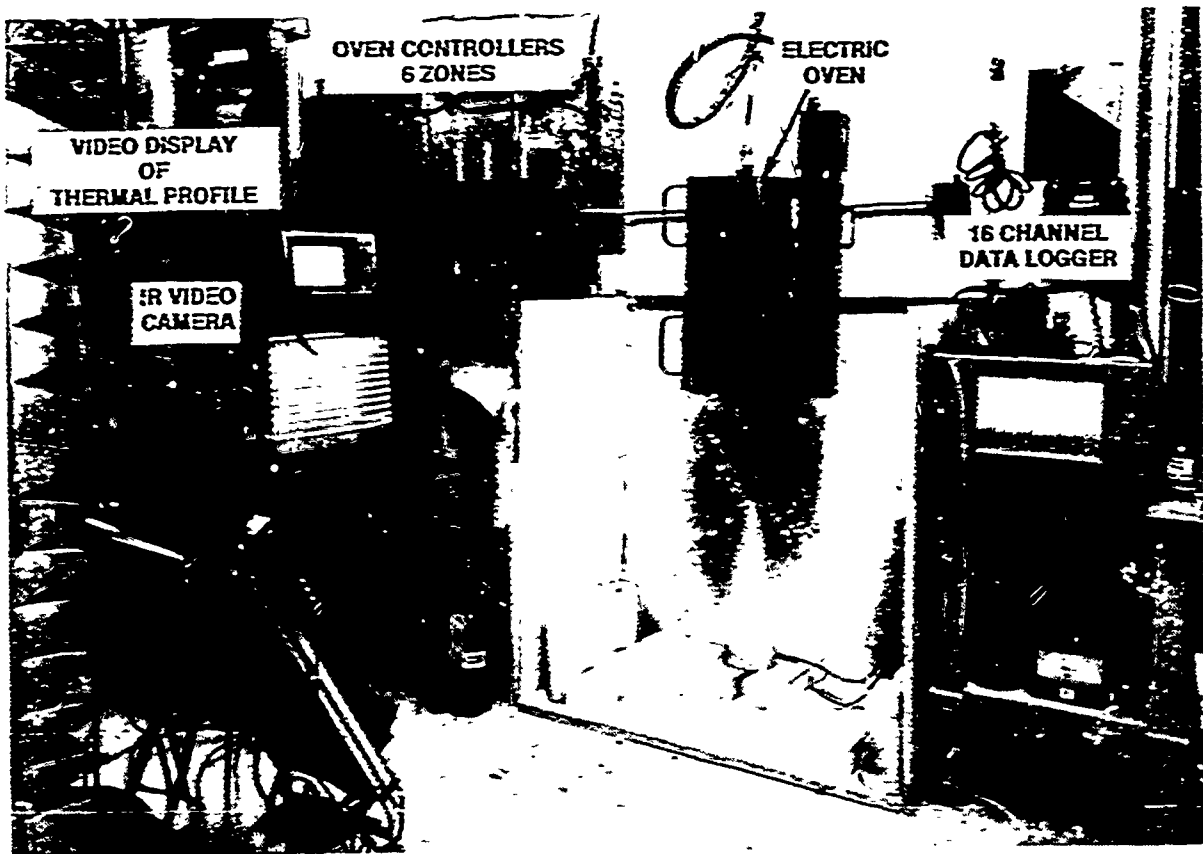


Figure 2. Equipment for Radome Heating and Temperature Recording

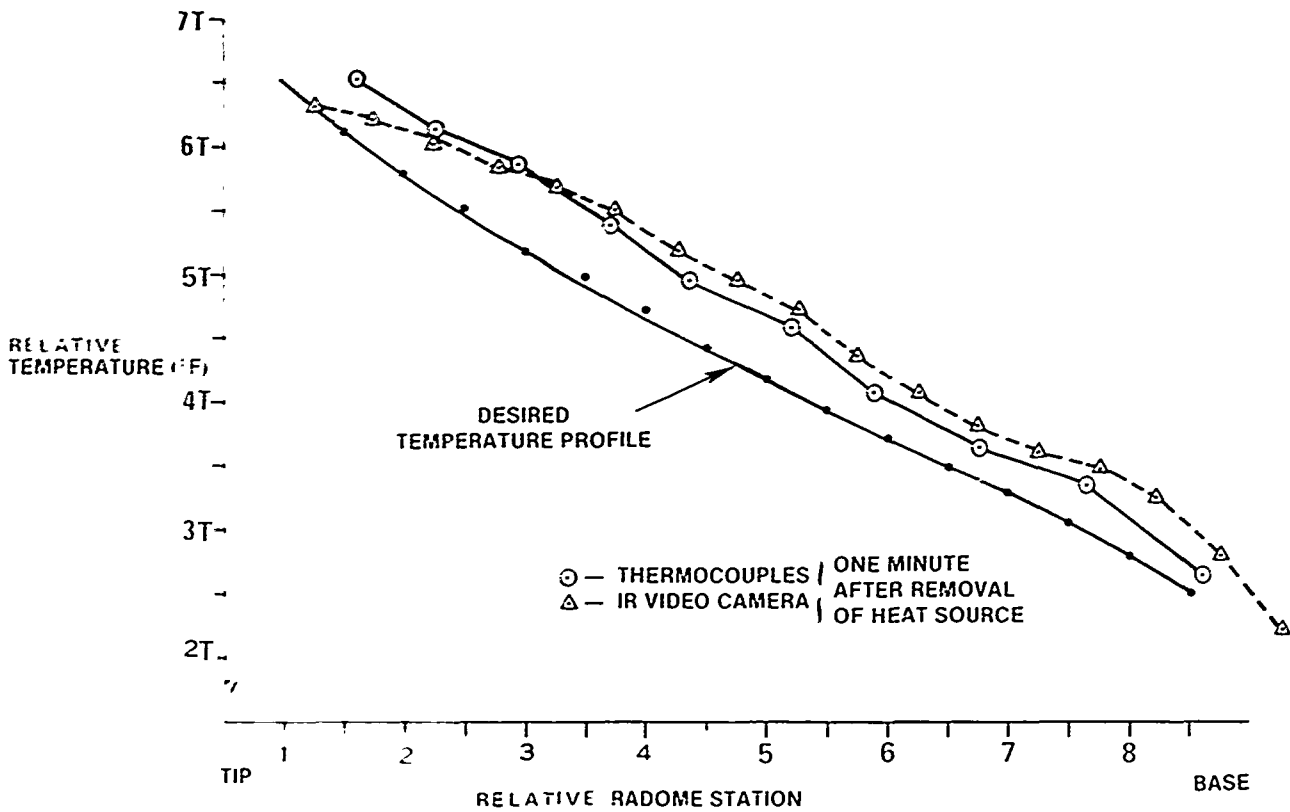


Figure 3. Laboratory Simulation of a Radome Temperature Profile

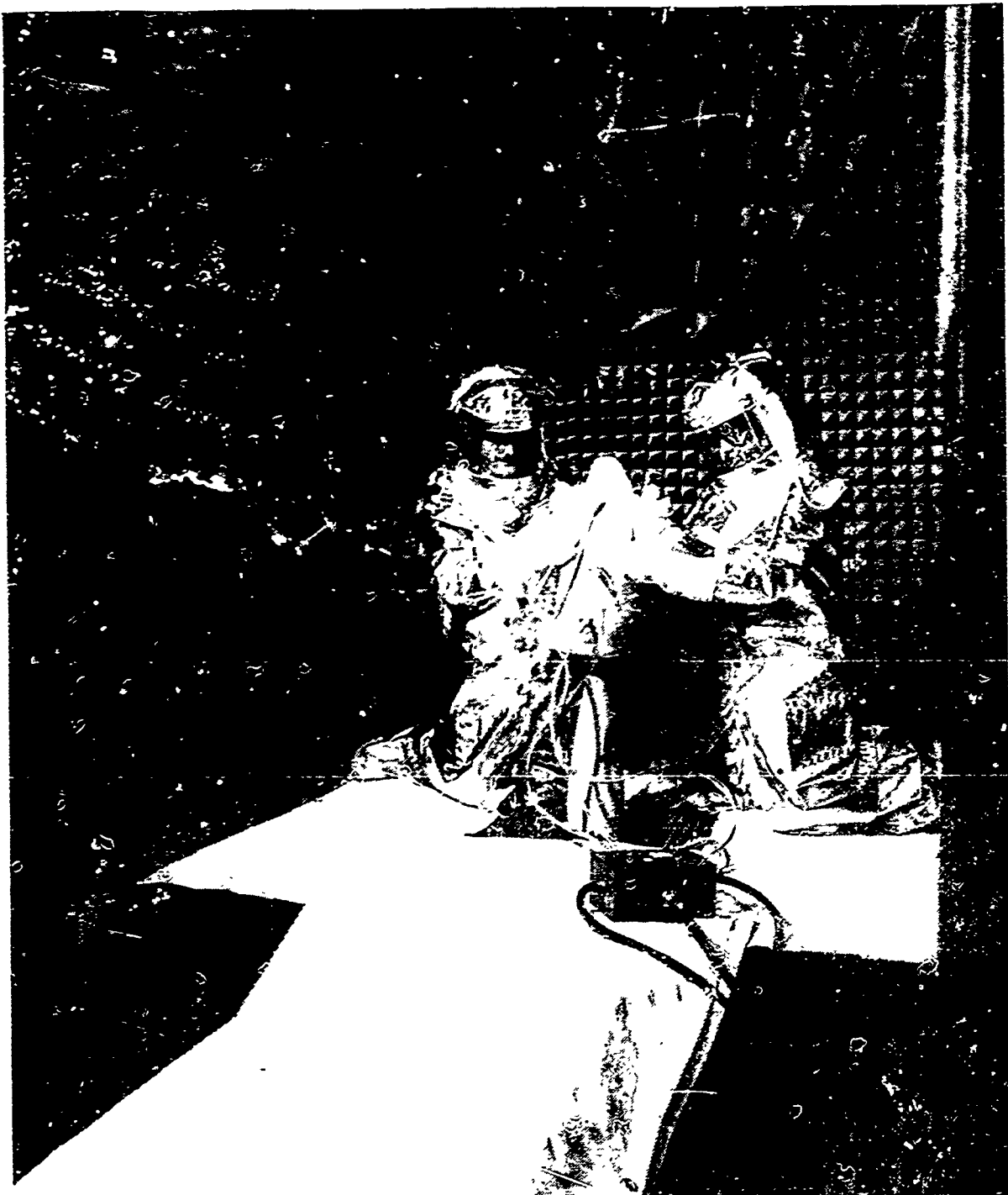


Figure 4. Hot Radome Installation on a Boresight Error Test Stand

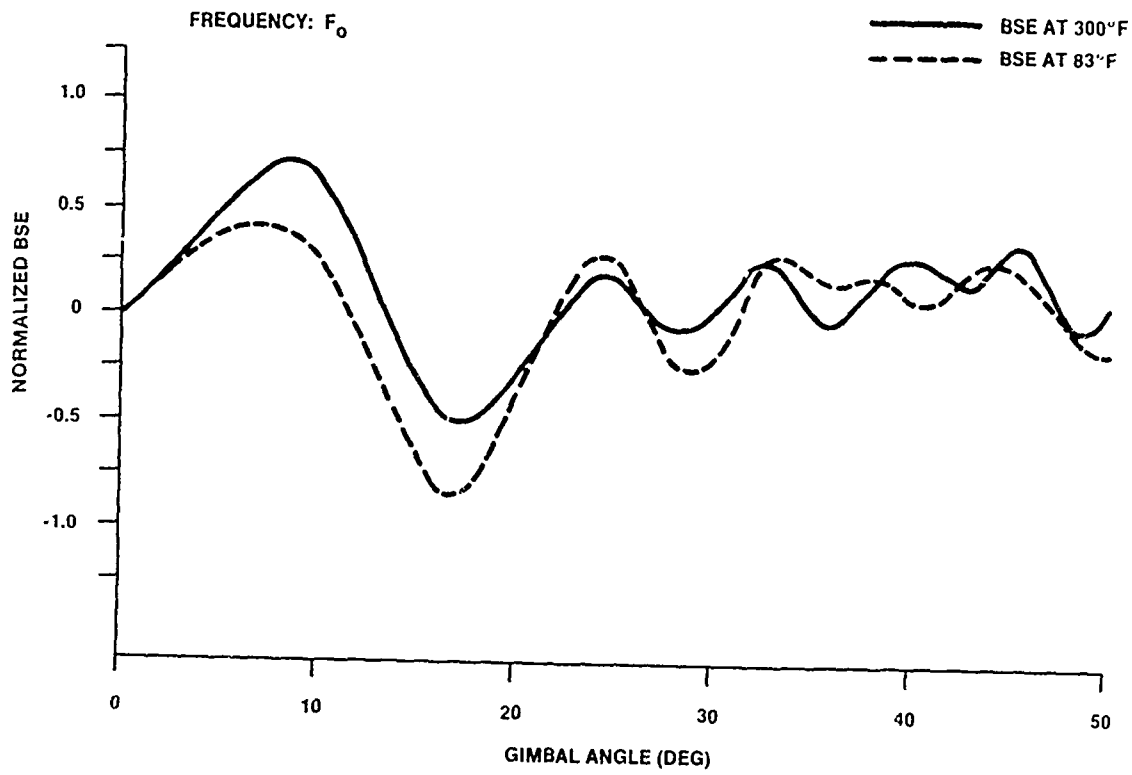


Figure 5. Temperature Effects on Pitch Plane BSE

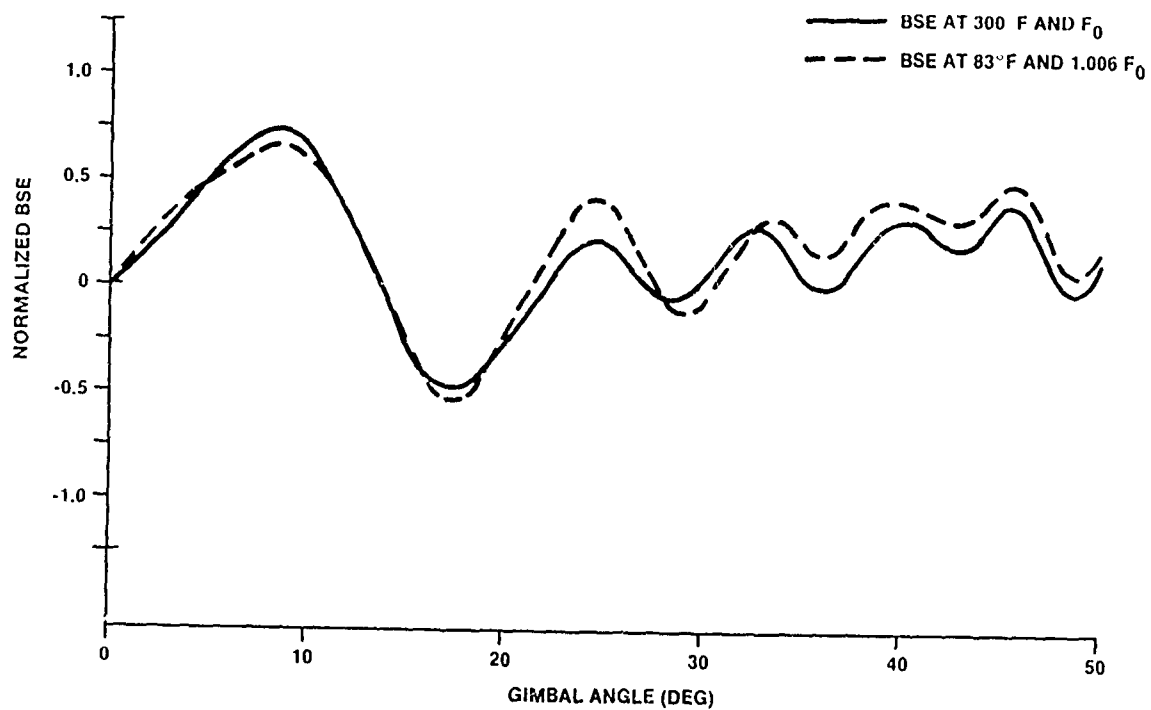


Figure 6. Temperature Effects on Pitch Plane BSE Simulated by Shifting Measurement Frequency

NEAR-FIELD TESTING TO  
INVESTIGATE RADOME  
ABERRATION PHENOMENA

David G. Burks  
Texas Instruments Incorporated  
P.O. Box 660246, MS 333  
Dallas, Texas 75266

Abstract

Near-field testing has been used extensively in the past as a method to determine far-field antenna patterns. Near-field testing has also been used in antenna diagnostic and alignment procedures by reconstruction of the aperture fields. Similar techniques can be employed to investigate radome induced aberrations such as variation of the wall transmission coefficient, tip scatter and bulkhead reflections. The advantage of near-field testing is that the various aberrations are localized whereas the far-field pattern is the superposition of all effects. The approach used here is based on the plane wave spectrum and back-projection algorithm. This theoretical foundation is presented along with a discussion of the limitations on resolution. The requirements of a measurement facility and experimental set up are discussed. Several examples are given to illustrate the power of the technique. These include measured results on a radome with thickness variation and scatter from a metallic tip.

PREVIOUS PAGE  
IS BLANK



## A BROADBAND KEVLAR RADOME FOR SHIPBOARD

by

JOHN B. STYRON  
ROBERT S. FRANCISCO  
BRUNSWICK CORPORATION  
DEFENSE DIVISION  
MARION, VA 24354

# AD-P004 365

### Introduction

A broadband radome for use on the Grumman M161 Hydrofoil craft was designed, fabricated, and tested. Dominant design considerations included electrical performance over a 2-18 GHz band in addition to a lightweight structure and compatibility with the shipboard environment. The requirement for a fire control radar to be mounted on top of the radome assembly also dictated a very rigid structure to minimize angular deflection errors.

This application is the largest known (10' diameter, 11' high) Kevlar<sup>®</sup> radome currently in shipboard use.

### Radome Design and Configuration

Major elements of the radome assembly are shown in Figure 1. They consist of three (3) aluminum vertical columns, two (2) internal equipment mounting platforms, the top platform for the fire control system, and six (6) curved window panels. The interface to the M161 Craft at Platform A is provided by bolted flanges on the vertical columns and turned-in solid laminate flanges on the window area panels. The vertical columns, being hollow, also function as air conditioning ducts for internal cooling and as tie points for electrical cables. The columns and appropriate areas of the internal equipment mounting platforms were covered with absorbers to minimize reflections.

Window area panel design was governed primarily by the 2 - 18 GHz performance, weight and rigidity requirements. The lower panels were also subject to pressure loads from "green-water" which resulted in a C-sandwich design in order to provide the necessary stiffness. An A-sandwich design was utilized for the upper panels. The panel skins utilized epoxy impregnated Kevlar skins with dielectric constant and loss tangent values of 3.4 and 0.02 respectively. Skin to core bonds were made with a thin film adhesive. Panel cross-sections for both upper and lower panel designs are shown in Figure 2.

PREVIOUS PAGE  
IS BLANK





### Fabrication

Window area panels were laminated and bonded in female molds. Each skin was laminated and pre-cured in the molds utilizing vacuum bag process with autoclave assisted pressure. This process resulted in a dense, low-void laminate for both inner and outer skins which was felt to be the key item in providing the necessary humidity resistance for the sandwich, especially in consideration of the known susceptibility of Kevlar to moisture absorption.

Following skin lamination, core bonds were then made, again using autoclave pressure. Each skin to core bond was processed with a separate cure to facilitate inspection for added reliability. The lower panel mold with an in-process panel is shown in Figure 3.

### Environmental Tests

Tests were conducted to establish the adequacy of the radome and/or components in the operational environment, with particular emphasis on electrical performance after humidity exposure.

Transmission efficiency was measured on the C-sandwich design both before and after panel exposure to temperature-humidity cycling as described by Method 507.1, Procedure IV, of MIL-STD-810C. This test is basically five (5) temperature cycles, 24 hours each, from 86 to 140°F while maintaining 95% relative humidity. Data was measured at Ku-band, using the more critical perpendicular polarization component. Panel edges were sealed prior to temperature-humidity exposure and the outer surface was coated with a linear polyurethane paint as used on the radome. The test data showed a typical transmission degradation after exposure of only 2 or 3% for incidence angles of 0 degree to 50 degrees, i.e., a level well within the design margin.

Radome vibration tests were conducted in accordance with Table I of MIL-STD-167-1 for Type I. For these tests, the CG of antennas were simulated by weights added to the test configuration. Resonance searches were conducted to determine resonant frequencies between 5 and 50 Hz in 3 axes. Endurance testing was then conducted for the worst-cases. The mast

assembly was particularly sensitive to vibration due to resonances occurring at low frequencies and required added strength at critical flexure points to achieve an acceptable configuration.

### Rigidity Test

A critical performance factor was radome rigidity under the worst case specified lateral loading conditions (3.5G). Minimal deflection was necessary to insure proper operation of the fire control antenna, mounted on top of the radome assembly. Acceleration loads were calculated using the total assembly weight and CG plus the weight and CG of all internally mounted equipment. The radome assembly was mounted to a fixture which simulated the attach area of the mating shipboard structure and lateral loads distributed and applied to the assembly using straps and hydraulic cylinders. Maximum overturning moment about the base plate in excess of 50,000 ft-lbs was applied. An angular deflection of the top platform of 0.9 milliradians was measured which was well within the design allowable.

### Electrical Tests

Measurements were also taken on the completed radome assembly to establish electrical performance level. An elevated outdoor test range was used with a throw distance of approximately 200 feet to satisfy  $20^2/\lambda$  criteria for the largest anticipated antenna to be used in the radome. The radome positioner and upper panel assembly is shown on the test range in Figure 4. Both transmission and radiation patterns were recorded for various antennas, polarizations, and frequencies. For these measurements, the supporting structure was covered by microwave absorber to minimize reflections. Data was recorded with the supporting structure and then with the window area panels added. Data evaluation was restricted to those sectors not influenced by the vertical support structure. Figure 5 shows the minimum power transmission for all antennas and polarizations. The design demonstrated low losses for all test conditions.

Radiation patterns were also evaluated for all antennas at discrete frequencies. Typical data derived from these measurements are shown below.

First Sidelobe Increase - 3 to 4 DB

3 DB Beamwidth Change - 3 to 4%

Pattern Ripple to 3 DB Level - 0.2 to 0.5 DB

#### Summary

This unique broadband application illustrates the feasibility of Kevlar reinforced sandwich radomes for shipboard use. With the process used, good performance was shown with minimal environmental effects. The finished radome assembly on the M161 Hydrofoil craft is shown in Figure 6.

#### Acknowledgements

The authors wish to express their appreciation and gratitude to Richard A. Sarraffe, Grumman Aerospace Corporation for his technical assistance and guidance during the program.

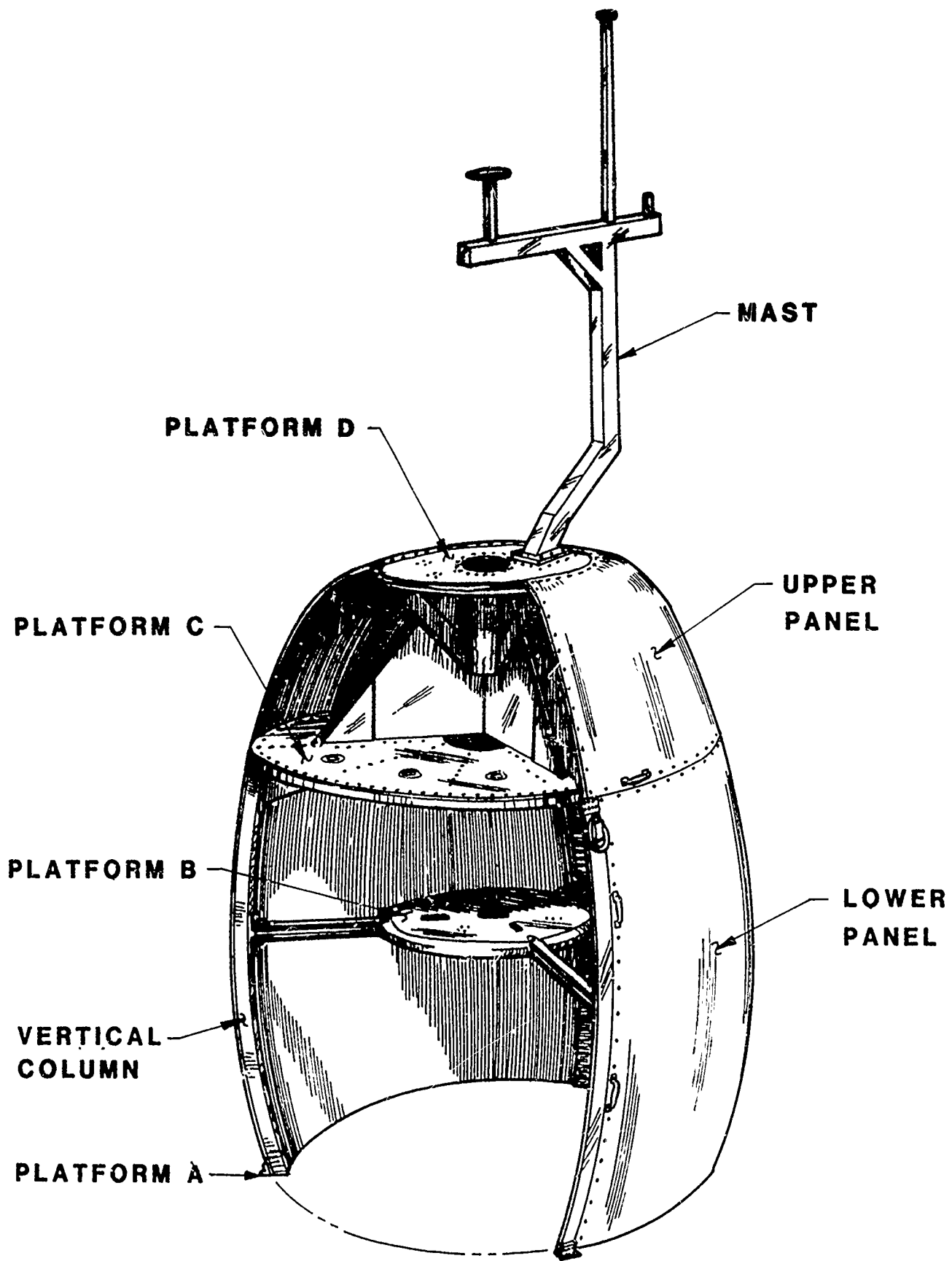
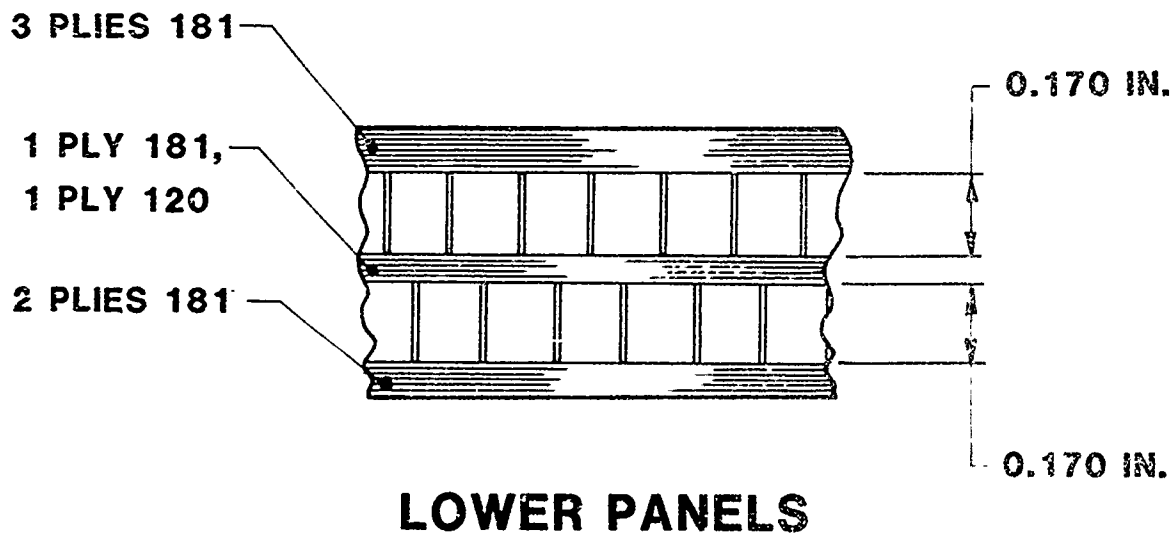
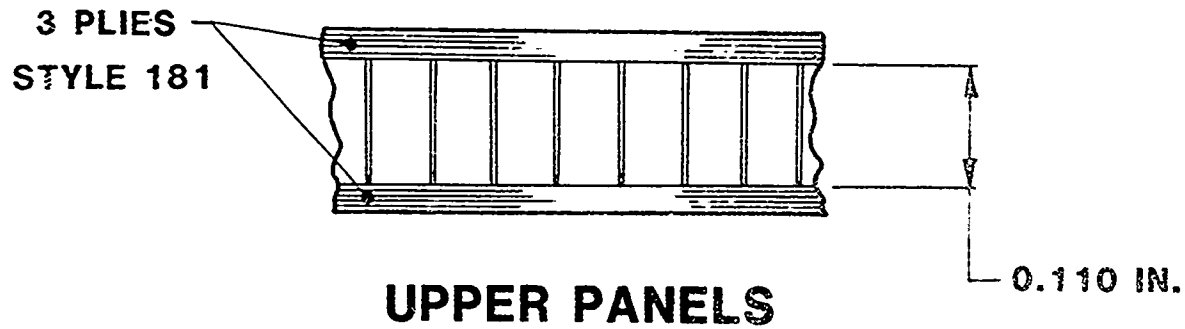


**FIGURE 1: M161 HYDROFOIL  
RADOME ASSEMBLY**



LAYERS	MATERIAL
EXTERIOR PAINT	ALIPHATIC POLYURETHANE
SKINS	EPOXY IMPREGNATED KEVLAR
HONEYCOMB	NYLON PHENOLIC, NP 3/16-4.5
ADHESIVE, EACH INTERFACE	FM 96, 0.75 LBS./FT <sup>2</sup>

**FIGURE 2: WINDOW AREA CONSTRUCTION**

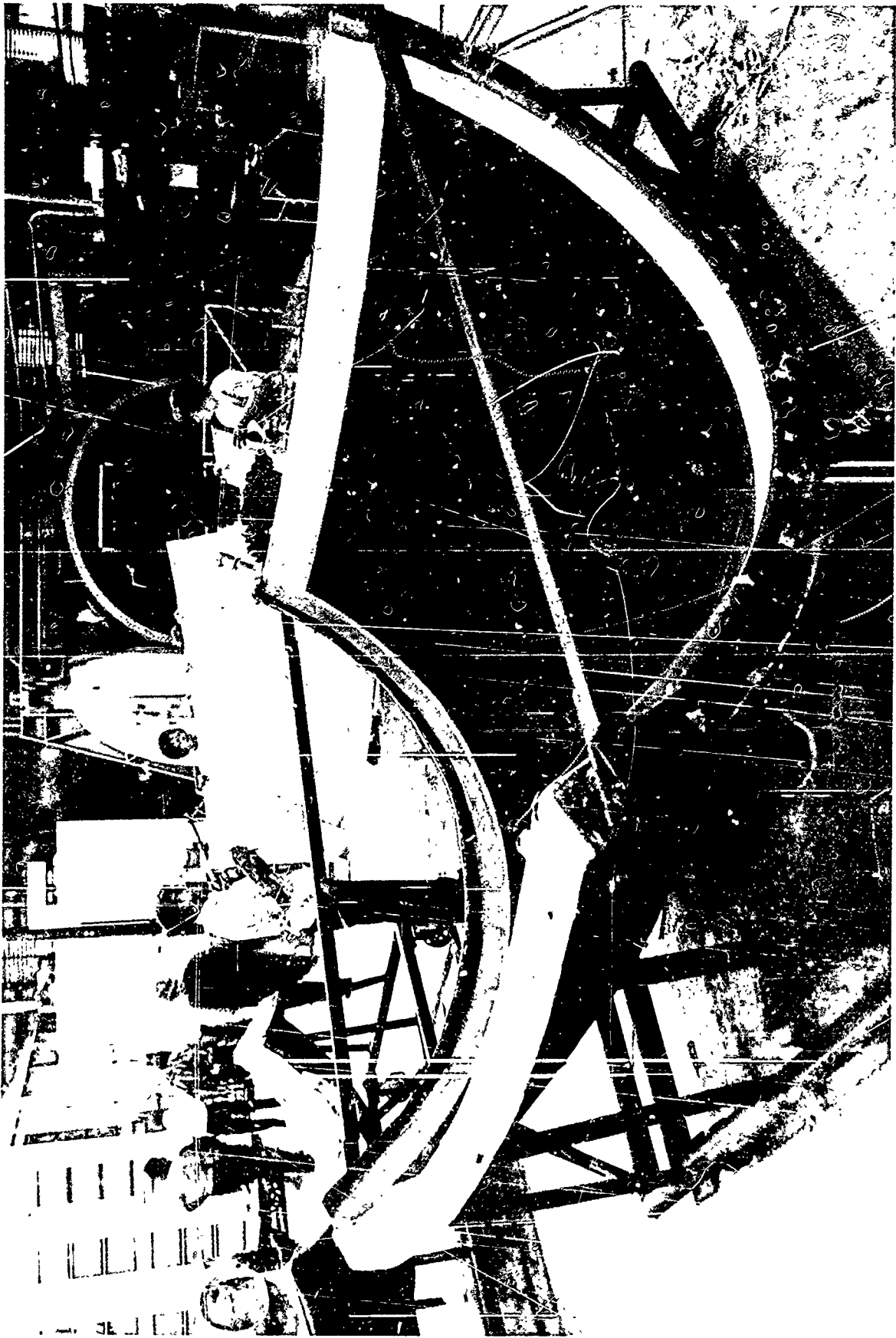


**FIGURE 3: FABRICATION OF LOWER PANEL**

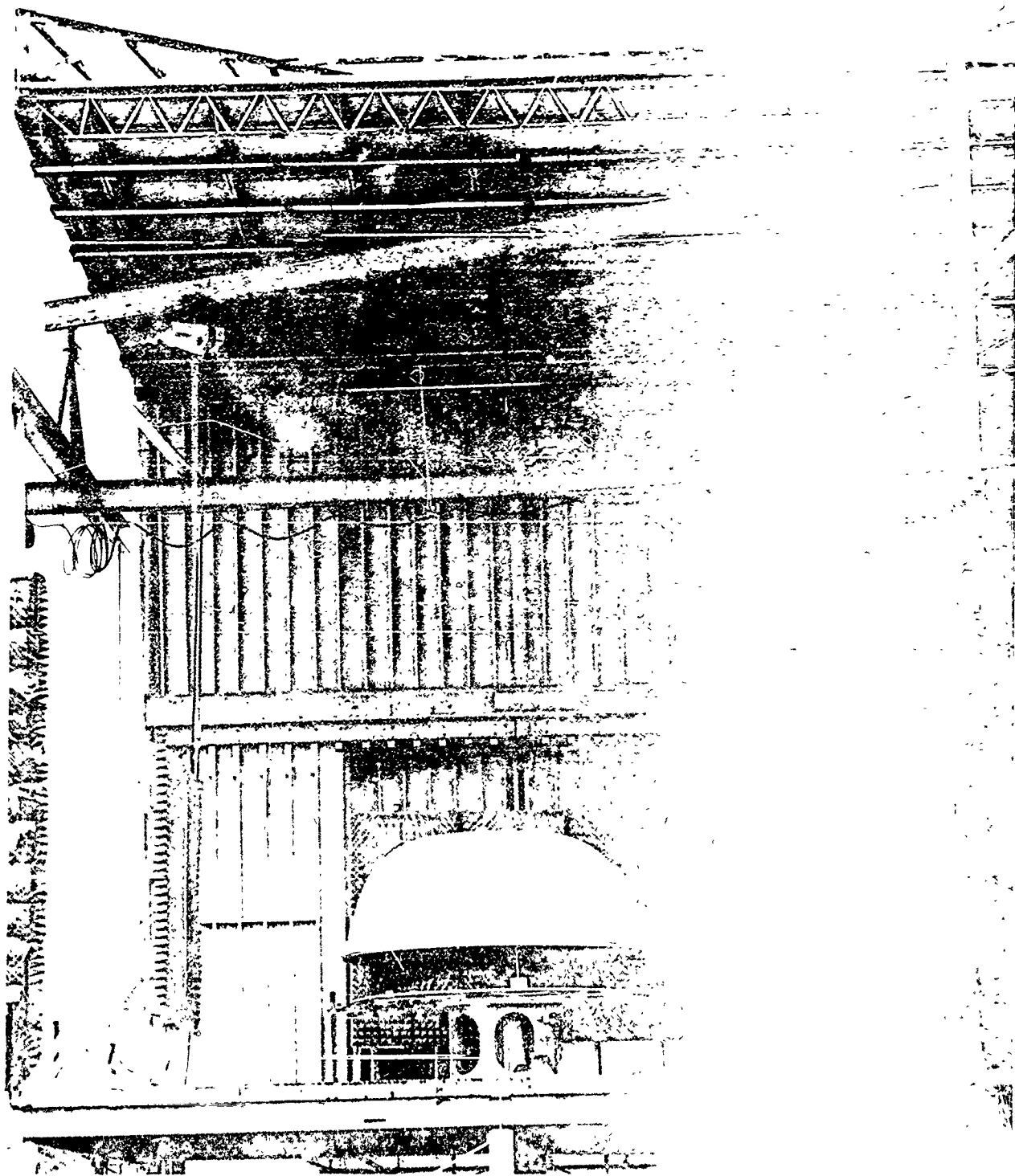


**FIGURE 4: UPPER PANEL ASSEMBLY FOR  
ELECTRICAL TEST ROOM**

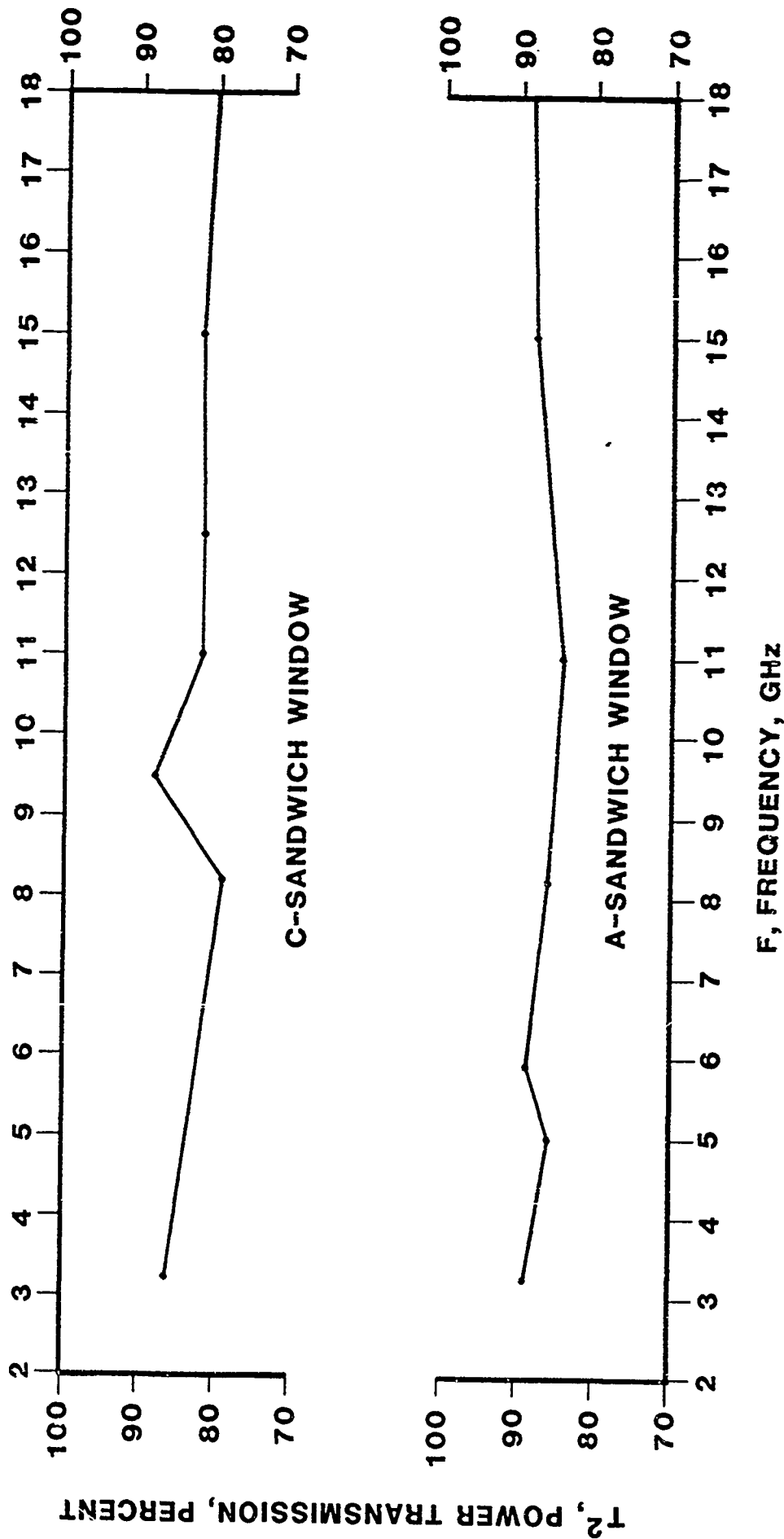


**FIGURE 5: MINIMUM POWER TRANSMISSION FOR ALL POLARIZATIONS AND ANTENNAS**



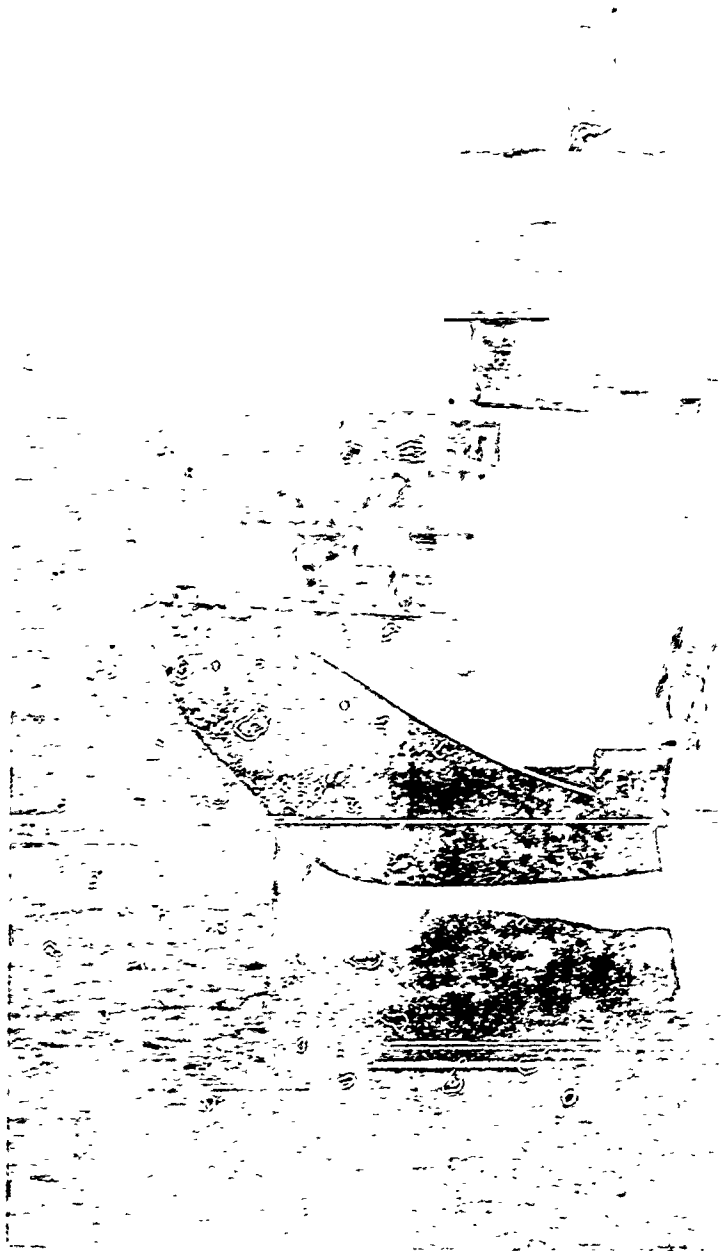


FIGURE 6: RADOME ON M16

by

F.P. Meyer\*, G.D. Quinn and J.C. Walck

Ceramics Research Division  
U.S. Army Materials and Mechanics Research Center  
Watertown, Massachusetts 02172

AD-P004 366

1. INTRODUCTION

During the past few years interest in composite materials having a use temperature above 300°C has increased greatly. Because ceramics offer substantial increases in use temperature, much of the research has been concerned with ceramic-matrix composites. Normally, the strength of a ceramic body is limited by the presence of critical flaws in the material that will initiate cracks and cause failure well below predicted strength levels. Recently, processing techniques have been developed which produce high purity ceramic fibers with almost pristine surfaces. The fibers are completely dense and exhibit strength levels and modulus of elasticity values that approach the theoretical binding forces. More specifically, it has recently been shown that the reinforcement of a low modulus glass matrix with high strength and stiffness fibers such as alumina, graphite and SiC was extremely successful in yielding a high modulus composite material.

The research reported here has been undertaken as a first step in an attempt to develop a fiber reinforced fused silica composite for hypersonic radome applications. In order to maintain isotropy in the composite material and to preserve the low and very temperature-stable dielectric properties of the matrix fused silica material, it was decided to use high purity silica fibers as the reinforcement. Fused silica is an inherently low strength and low modulus material. Having an elastic modulus of about  $4.5 \times 10^6$  psi —

---

<sup>†</sup> NOTE: "This paper has been prepared in accordance with the DOD Guidelines for Export Control of Composite Materials and Technology as set forth by Office of the Under Secretary of Defence for International Programs and Technology. These guidelines control the export and dissemination of certain technologies, particularly ceramic matrix composites. Specifically controlled is the transfer of technology for new techniques and parameters for consolidating, fabricating and forming ceramic matrix composites and performance test data related to specific military applications. In addition, technical reports, whether presented orally, visually or written, shall not contain references to previous work containing information on the above-mentioned areas of ceramic matrix composites. This information has been intentionally omitted."

---

\* Currently serving as exchange scientist to Physics Division, Materials Research Laboratories, P.O. Box 50, Ascot Vale, 3032, Victoria, Australia.

almost any fiber used could increase this value considerably. Two sources of high purity fused silica fibers were found, each reporting a value of approximately  $10 \times 10^6$  psi for the elastic modulus of their fiber. Additionally, it was decided to use simple, well-established processing techniques to fabricate the composite materials. Therefore, short, chopped high purity fused silica fibers were incorporated into the fused silica matrix so that the fibers were evenly distributed and randomly oriented throughout the composite. The fibers were nominally 10  $\mu$ m in diameter and have aspect ratios from 5 to 50.

## 2. EXPERIMENTAL PROCEDURE

High purity fused silica fibers were used to reinforce a high purity fused silica matrix. Samples containing 0, 2.5, 5.0, 7.5 and 10.0 volume percent fibers were fabricated as flat tiles 10 cm by 10 cm by 1.5 cm thick. Each tile was carefully dried and sintered. All tiles had their two flat faces ground flat and parallel to  $\pm 0.05$  mm. Density measurements were performed based on Archimedes principle. The modulus of elasticity of each sample was determined using sonic techniques. Tiles were then submitted for machining and standard flexure test specimens were prepared. Each specimen was 6.4 mm x 6.4 mm by at least 50 mm in length. All surface grinding was done parallel to the long axis of the specimen. The density of each specimen was determined from its weight and volume.

Single Edge Notched Beam (SENB) specimens were prepared by notching the bend bars with a diamond wheel 0.4 mm thick. These bars were tested in four point loading using an outer span of 4.06 cm and an inner span of 2.03 cm. The depth of the notch was measured and recorded for each specimen and varied from 3.0 to 3.3 mm. The experimental procedure is depicted in Figure 1a. A loading rate of 0.5 mm/min was used for each test to ensure that only fast fracture occurred. Results of these experiments are tabulated in Table I. A comparison is made for the fracture toughness of unreinforced fused silica to samples of fused silica obtained from two commercial sources in Table II (1).

The Work of Fracture (WOF) specimens were also notched with a 0.4 mm thick diamond wheel. The chevron notch for all specimens had a d/b of 0.7, where d and b are the vertical and horizontal notch dimensions, respectively. This led to stable crack growth during the experiments.

The experimental set-up is shown in Figure 1b and involved loading the specimen very slowly to allow the crack to grow. Continued loading of the sample propagates the crack slowly through the triangular cross-section of the sample. The work required to propagate the crack through the specimen is calculated from the load-displacement curve from the test instrument. Results of these experiments are shown in Table III.

Additionally, small cone frusta were fabricated for rocket sled rain erosion testing. These samples each had an included cone half-angle of

22.5°. Samples were fabricated approximately 3 mm oversize and diamond ground to final dimensions. The bulk density of each sample was determined by Archimedes principle after machining. A surface profilometer was used to obtain a trace of the surface finish on each sample. Samples were then mounted on the U.S. Army MICOM rocket sled test fixture for rain erosion testing. The rocket sled is propelled through the rainfield at MACH 5. The rainfield itself is 610 metres in length, the rainfall rate being 67.4 mm/hr. The average rain drop diameter is 1.4 mm.

After erosion testing, each sample was carefully weighed and then surface profilometer traces were taken.

3. EXPERIMENTAL RESULTS AND DISCUSSION

Typical microstructures are shown in the photomicrographs in Figures 2 and 3. These are fracture surfaces subsequent to the chevron notch test. Several inconsistencies are evidenced in the micrographs. Most important is the fact that the fibers are not evenly distributed throughout the matrix. There are areas of high fiber concentration and also large areas with few if any fibers at all. In general, the fibers are randomly oriented in the matrix with no preferred orientation visible. It is also evident that a fiber B varies in diameter from 5 to 20  $\mu$ m.

The photomicrographs also show that not all fibers are bonded well to the matrix and therefore not all fibers are participating in strengthening the composite. Even in the sample with the highest work of fracture (7.5 v/o Fiber A) there is evidence that a fiber was not well bonded and pulled out of the matrix. The poor bonding is due to incomplete sintering. Minimum sintering temperatures and times are used to preclude cristobalite formation in the silica and these have not been sufficient to bond the fibers and matrix. This fact is also evidenced by the low densities achieved in some of these composites as compared to 1.96 g/cc for fully fired fused silica.

The data in Table I does indicate however, that higher maximum loads were required to break several of the reinforced samples than that required to cause failure in the unreinforced silica. Some of the fibers have sintered well into the matrix and are strengthening the composite.

(a) SENB Tests

The SENB test is designed to measure the fast fracture toughness,  $K_{IC}$ , in a ceramic specimen (2). It basically determines the energy necessary to initiate the crack. As seen in Figure 4 there is no effect on fracture toughness caused by the addition of fibers to the fused silica matrix. It would not be expected that fiber reinforcement would help prevent the initiation of cracks of this phenomenon is dependent upon the occurrence of surface flaws in the ceramic and the fibers have no effect on the sample surface. The number, size and distribution of surface flaws in these composites would not be a function of fiber content.

(b) WOF Tests

Work of fracture tests will measure the resistance of a ceramic to crack propagation. The amount of energy required to propagate a crack through the sample is measured by the load-displacement record on the test instrument. As shown in Figure 5 there is a significant effect of fiber content on the work of fracture for these composites. The addition of 7.5 v/o of Fiber A and 2.5 v/o Fiber B has increased the work of fracture dramatically.

Four mechanisms might be responsible for the fracture energy behaviour shown in Figure 5:

- (1) Energy might be absorbed by the stiffer, higher strength second-phase dispersion, the fibers.
- (2) The generation of new fracture surface areas will increase the calculated fracture energy.
- (3) Friction forces between parting surfaces can absorb energy during fracture.
- (4) Interaction of the crack with the dispersed fibers can change the direction of crack propagation and the path length, both absorbing energy.

Composite systems are usually designed to incorporate a high modulus fiber into a low modulus matrix so that the stresses are transferred to the fiber and many of the bulk properties of the matrix are retained. The SEM examination of samples failed to indicate any significant contribution by the fibers in absorbing energy by stopping cracks. Quite the opposite was observed. The fibers seem to act as a weak second phase that channelled the cracks down their length thus pulling out of the matrix virtually intact. Vacant channels can be seen in many photomicrographs where substantial lengths of fiber have come out of the matrix. This mechanism will require additional energy because the crack direction will be re-directed along the fiber and the path length will be greatly increased. Also, as the fiber pulls from the matrix, frictional forces will also absorb energy, thus increasing the fracture energy.

The fracture surfaces of the fiber reinforced materials had greater surface roughness than did the surface of unreinforced fused silica. Although the increase in surface roughness was small, it does indicate that additional surfaces have formed in the reinforced material, thus increasing fracture energy.

(c) Comparison of Work of Fracture to Single Edge Notch Beam

In order to compare the energy required to initiate a crack, as measured by SENB, to the amount of energy to propagate a crack, chevron notch test, a fracture energy for the SENB test was calculated from

$$\text{Work of Fracture} = \frac{K_{IC}^2}{2E}$$

where  $K_{IC}$  is the SENB fracture toughness and E is Young's Modulus. These computations are shown in Table I and plotted in Figures 6 and 7. The two fracture energies agree quite well for each type of composite. Usually for a ceramic the energy to initiate a crack is considerably larger than the energy to propagate a crack. In these composites, the energy to propagate the crack has been increased by the addition of fibers and is about equal to the energy to initiate cracks. This is due to the fibers dispersed in the matrix acting as crack blunters or crack arrestors.

(d) Rain Erosion Testing

Surface profilometer traces of the fiber reinforced silica samples after rain erosion testing showed about the same mean depth of penetration as for nominal fused silica. The erosion of the composite samples was a bit more even around the sample surface than that for unreinforced fused silica. In previous tests, using 22.5° samples, unreinforced fused silica has cracked catastrophically and large pieces of the sample have been lost. The fiber reinforced samples did not crack and were intact when the sled came to rest.

The mass loss ratio, the mass of sample lost due to erosion divided by the mass of rain encountered by the sample, was improved by about 10% by the addition of fibers to fused silica. The fibers acted as crack stoppers and confined the damage due to a raindrop impact to a very localized area. Although considerable material was removed from each sample, the damage was more evenly distributed over the sample surface than for unreinforced silica.

4. CONCLUSIONS

1. The fabrication of high purity fused silica reinforced with from 2.5 to 10 v/o of short, high-purity silica fibers which were randomly oriented in the matrix was demonstrated.

2. The addition of the fibers had virtually no effect on the fracture toughness or flexural strength of the composites. This was due to poor fiber-matrix bonding, with the result that few fibers participated in the transmission of stress.

3. The fibers were not evenly distributed throughout the matrix and this resulted in density and elastic modulus variations in the same sample.

4. The work of fracture, as measured by the chevron notch beam test, was increased dramatically in the composite material, particularly for additions of 7.5 v/o Fiber A and 2.5 v/o Fiber B. This was due in part to the absorption of energy to produce new crack surfaces (surface roughness) in the composites and partly due to the energy absorbed through frictional forces as fibers pulled out of the matrix. It was mainly due to the fibers acting as a weak second phase and channelling the cracks along the length of the fiber, increasing the crack length and changing the direction of crack propagation.

5. The rain erosion resistance of the composites tested was enhanced due to the increased energy required to propagate cracks in the material and the channelling of the cracks along the fiber. Impacting rain drops initiated cracks but the cracks were quickly propagated along the fibers and only localized failure was incurred. Catastrophic cracking did not occur during rain erosion testing of the composites as it did for unreinforced fused silica under identical test conditions.

6. The addition of short, chopped silica fibers to a high purity fused silica matrix results in a composite that contains a dispersed weak second-phase. The weak second-phase gives the crack a path of lower resistance to follow but re-directs the crack and increased the crack path length and in doing so, absorbs more of the cracks energy than would unreinforced silica.

#### REFERENCES

1. G.D. Quinn, unpublished work.
2. W.R. Brown and J.E. Srawley, Amer. Soc. Testing Materials, Special Tech. Publ. no. 10, (1966).
3. K.N. Letson, U.S. Army MiCOM, personal communications.

TABLE I. Result of Single Edge Notch Beam Measurements

Specimen (#) [Number Tested]	Fiber Content (v/o)	Density (g/cc)	Young's Modulus (MN/m <sup>2</sup> )	Notch Depth (mm)	Maximum Load (kg)	K <sub>Ic</sub> (MN/m <sup>3/2</sup> )	Work of Fracture (J/m <sup>2</sup> )
161-B [7]	0	1.93	0.044	3.18	5.34	0.93 ± 0.07	9.90
177-A [9]	2.5 Fiber A	1.96	0.044	3.18	5.15	0.89 ± 0.08	9.04
163-A [10]	5.0 Fiber A	1.97	0.043	3.15	5.47	0.95 ± 0.07	10.49
171-A [7]	7.5 Fiber A	1.89	0.030	3.14	5.79	1.00 ± 0.10	16.81
174-A [9]	10.0 Fiber A	1.88	0.033	3.13	4.78	0.82 ± 0.05	10.81
173-A [10]	2.5 Fiber B	1.91	0.035	3.15	5.55	0.95 ± 0.08	12.92
169-A [10]	5.0 Fiber B	1.90	0.036	3.16	5.16	0.88 ± 0.07	10.79
172-A [8]	7.5 Fiber B	1.90	0.038	3.16	5.17	0.89 ± 0.04	10.54

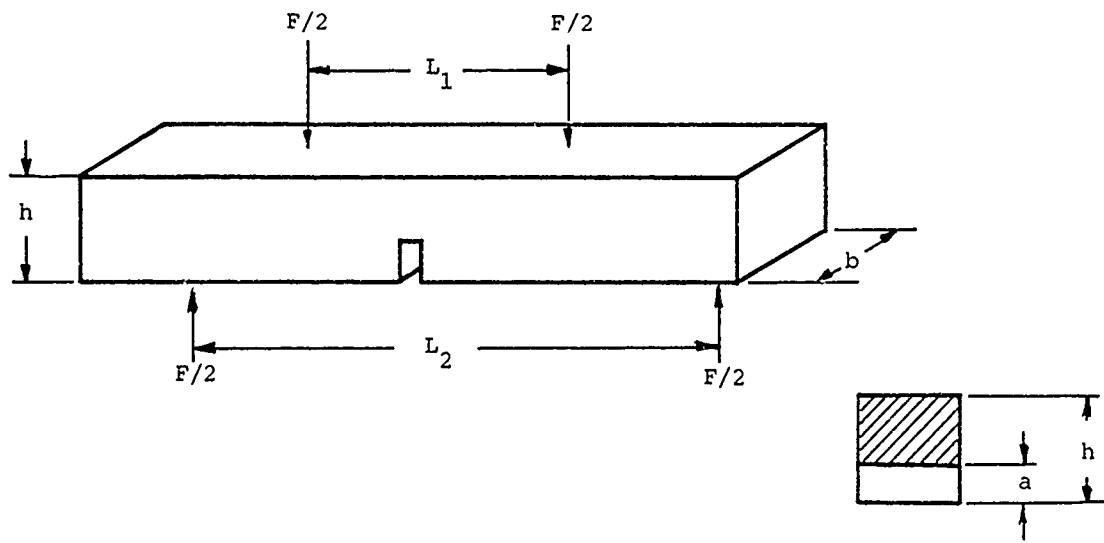


TABLE II. Comparison of Fracture Toughness Values for Three Different Fused Silica Materials

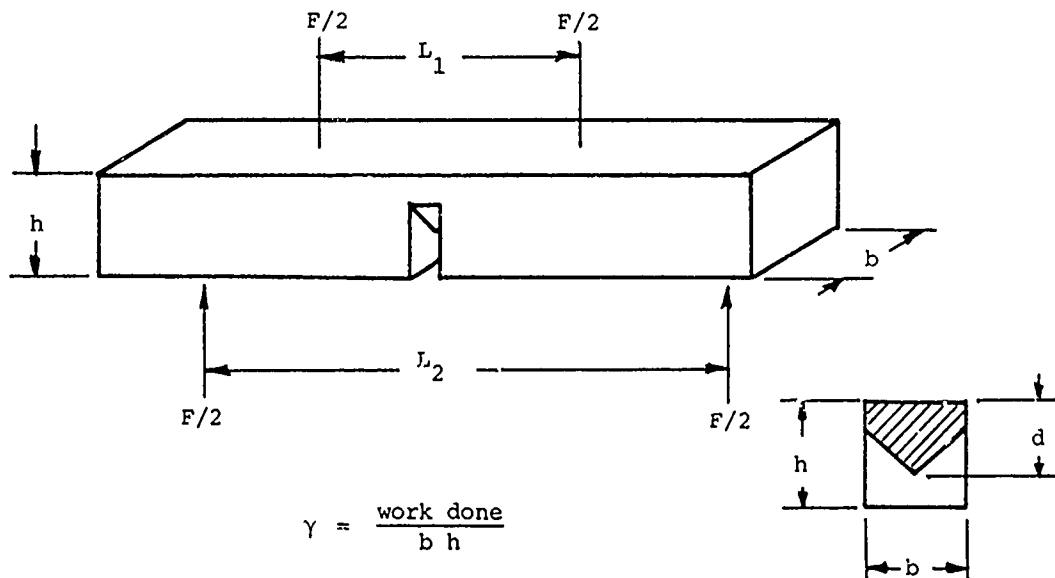
Sample Source	$K_{Ic}$ ( $MN/m^{3/2}$ )	Technique
161-B	$0.93 \pm 0.07$	Single Edge Notch Beam
Vendor 1	$0.92 \pm 0.04$	Double Torsion
Vendor 2	$0.92 \pm 0.04$	Double Torsion

TABLE III. Results of Work of Fracture Measurements

Sample (#) [Number tested]	Fiber Content (v/o)	Density (g/cc)	Vertical Notch Depth (mm)	Work of Fracture ( $J/m^2$ )
161-B [8]	0	1.93	4.45	8.58
177-A [8]	2.5 Fiber A	1.96	4.61	9.49
163-A [8]	5.0 Fiber A	1.97	4.52	9.39
171-A [8]	7.5 Fiber A	1.89	4.45	18.72
174-A [8]	10.0 Fiber A	1.88	4.45	13.27
173-A [8]	2.5 Fiber B	1.91	4.50	16.46
169-A [7]	5.0 Fiber A	1.90	4.59	12.64
172-A [9]	7.5 Fiber B	1.90	4.50	10.80



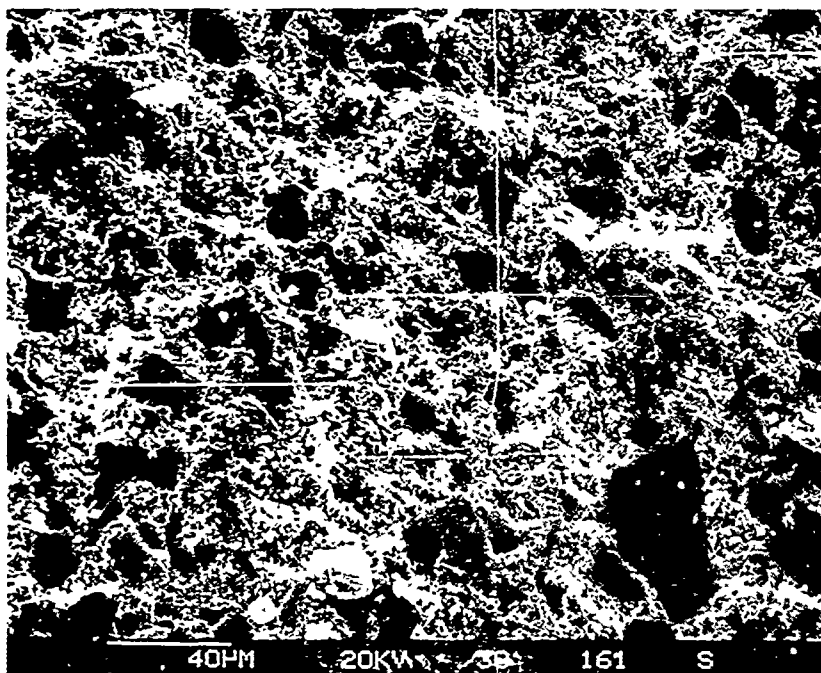
a. Single Edge Notch Beam.



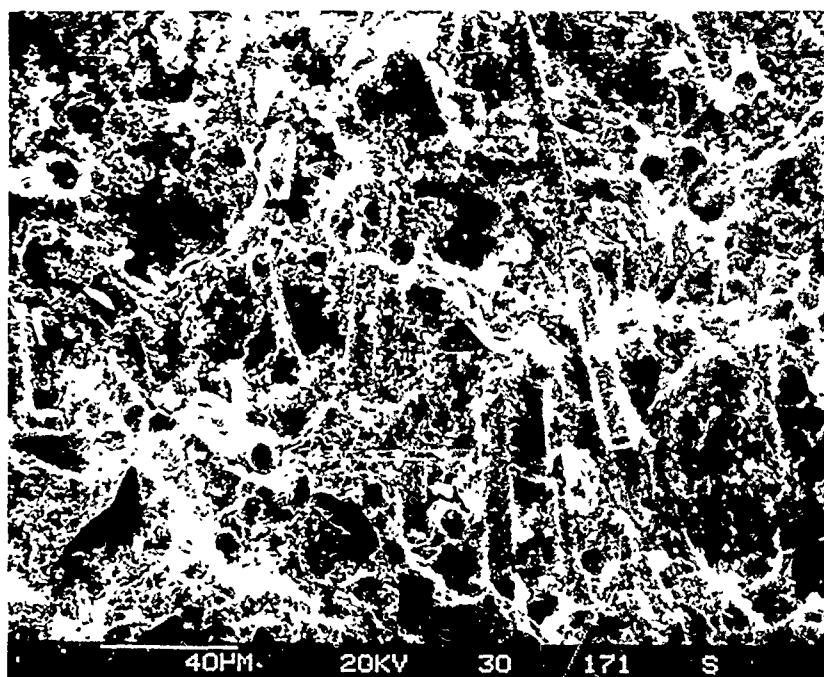
$$\gamma = \frac{\text{work done}}{b h}$$

b. Work of Fracture - Chevron Notch Beam.

Fig. 1 Specimen Configuration and Experimental Procedure for Fracture Energy Determinations.

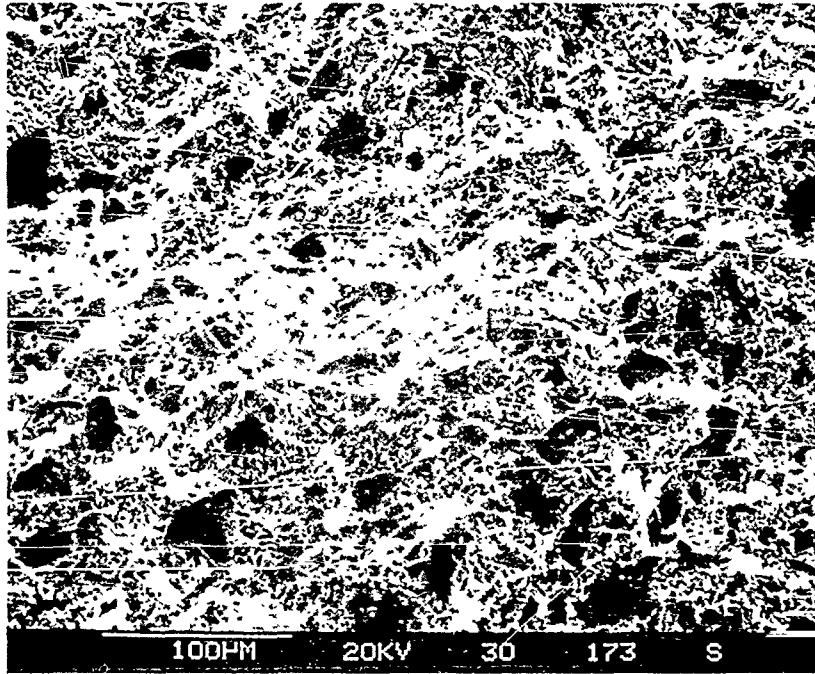


a. 0 v/o Fiber

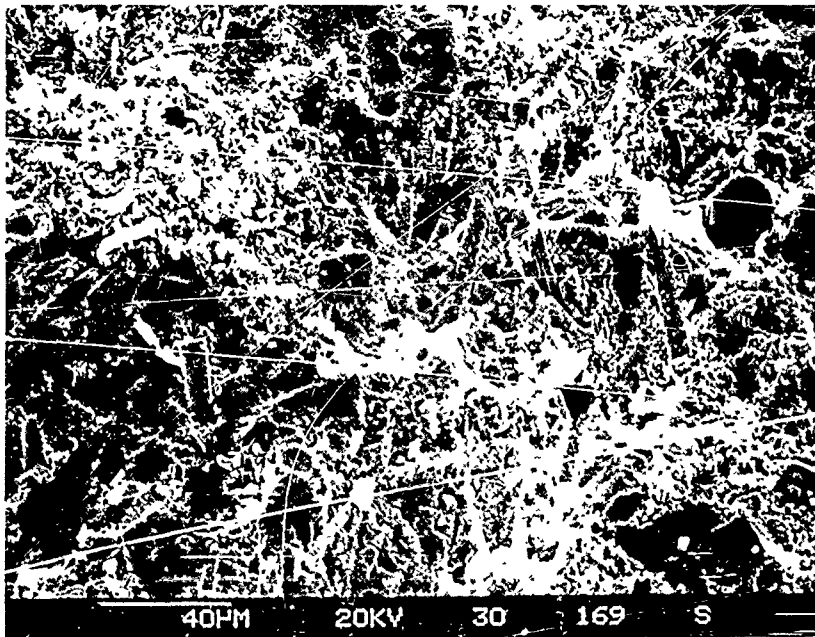


b. 7.5 v/o Fiber A

Fig. 2. Fracture Surfaces of Fiber Reinforced Fused Silica.



a. 2.5 v/o Fiber B



b. 5.0 v/o Fiber B

Fig. 3. Fracture Surfaces of Fiber Reinforced Fused Silica.

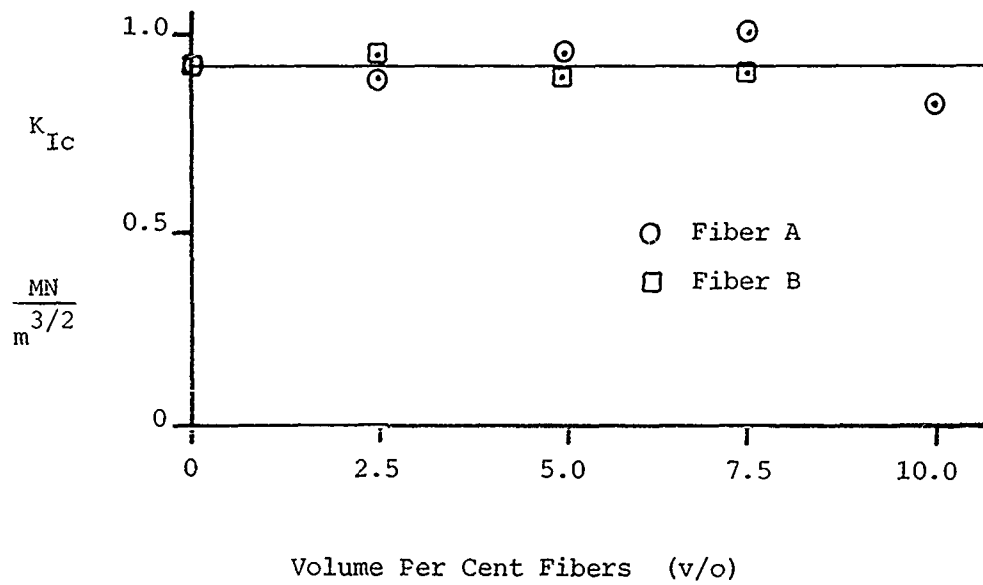


Fig. 4. Fracture Toughness of Fiber Reinforced Fused Silica as a Function of Fiber Content.

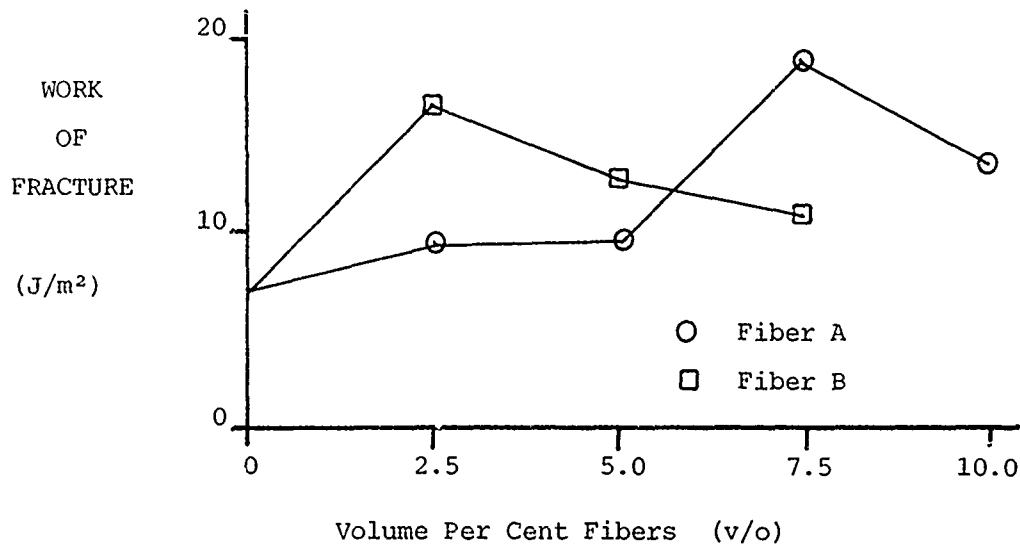


Fig. 5. Work of Fracture of Fiber Reinforced Fused Silica as a Function of Fiber Content.

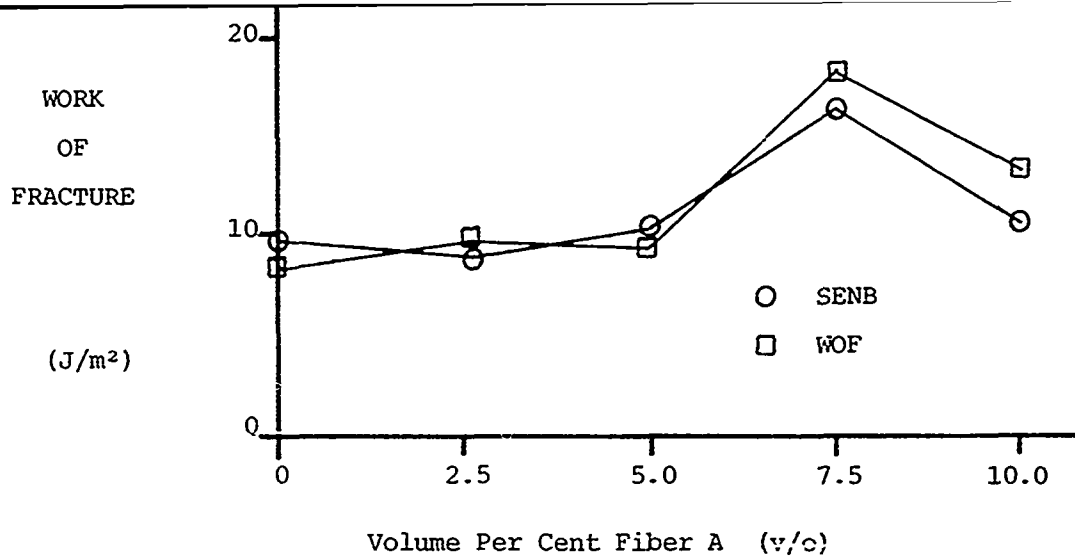


Fig. 6. Comparison of Work of Fracture Determined by SENB and Chevron Notch Tests for Fused Silica Reinforced with Fiber A.

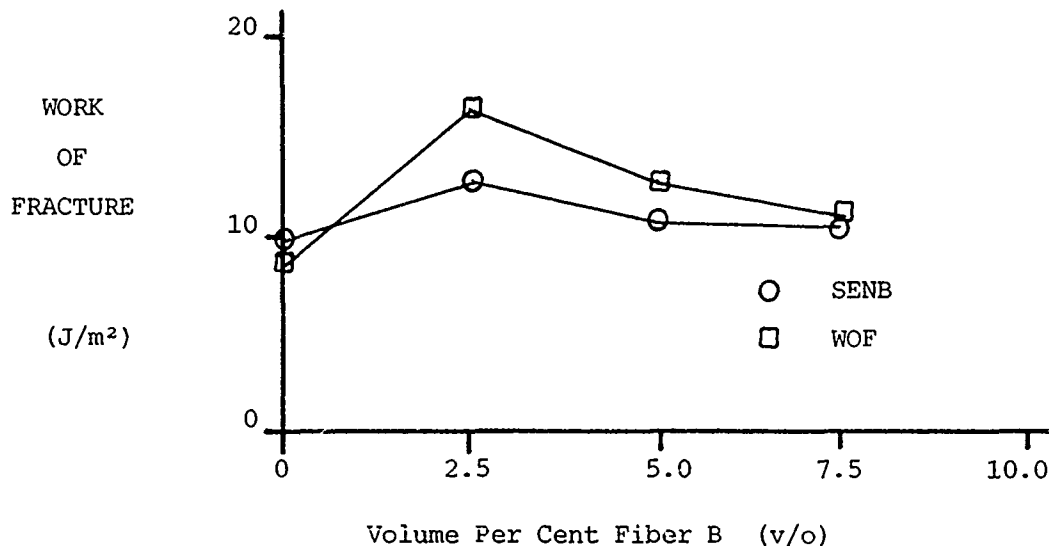


Fig. 7. Comparison of Work of Fracture Determined by SENB and Chevron Notch Tests for Fused Silica Reinforced with Fiber B.

PRESSURELESS SINTERED SILICON NITRIDE  
AS A PROMISING CANDIDATE FOR RADOME MATERIALS

By M.Y. Hsieh, H. Mizuhara and P.W. Smith  
GTE - WESGO Division, Belmont, California 94002

**AD-P004 367**

Introduction

Pressureless sintered silicon nitride has several favorable features and properties which make it a promising candidate for radome materials (Fig. 1). First of all, pressureless sintering provides relatively unlimited shape forming capabilities. Process can be controlled reproducibly. Parts can be made relatively inexpensive. Pressureless sintered silicon nitride provides some excellent physical and mechanical properties which approach hot pressed silicon nitride. It has excellent oxidation resistance to 1350°C. It provides high strength from room temperature to above 1250°C. Excellent thermal shock resistance due to low thermal expansion and high strength provides opportunities of wide applications. This paper describes some properties of pressureless sintered silicon nitride developed by GTE WESGO. SNW-1000 body is used to illustrate the state of the art of pressureless sintered silicon nitride development. Brief discussion of various silicon nitride bodies is given. Some recent results of dielectric properties are given. Size and shape forming capabilities are given.

Processing

Pressureless sintered silicon nitride can be shape-formed by several conventional ceramic processing techniques, such as dry-pressing, isostatic pressing, green machining, slip casting and tape casting. Two technically and economically feasible processes, based on slip casting and isostatic pressing are illustrated in the flow chart of Fig. 2. Near net shape silicon nitride parts are usually made by these two processes, in addition to other techniques, such as dry-press.

Pressureless sintered silicon nitride parts of various sizes and shapes are being fabricated and marketed by GTE WESGO. Typical pressureless sintered silicon nitride bodies are designated SNW-1000 and SNW-2000.



## Properties

Some typical properties of SNW-1000 are listed in Table 1. Typical strength along with fracture toughness and thermal properties of pressureless sintered silicon nitride SNW-1000, along with other silicon nitrides and AL-99 alumina are shown in Fig. 3.

Fig. 3 (a) show the strength of pressureless sintered silicon nitride SNW-1000 along with other silicon nitrides and 99.5 Al<sub>2</sub>O<sub>3</sub> as a function of temperature.

Typical strength is about  $95 \times 10^3$  psi at room temperature, about  $85 \times 10^3$  psi at 1000°C and about  $75 \times 10^3$  psi at 1200°C.

Pressureless sintered silicon nitride, such as SNW-1000 has elongated grain structure about half micron to 1 micron width and 2 to 4 micron length. Microstructure of fractured SNW-1000 is shown in Fig. 4 as SEM picture at 10,000X magnification.

## Dielectric Properties

Dielectric properties of SNW-1000 based materials measured at room temperature at 9.3 GHz are listed in Table 2. Dielectric loss  $\tan \delta$  varies according to variation of process and/or composition. Dielectric loss  $\tan \delta$  as low as  $1.08 \times 10^{-3}$  is obtained. Samples listed in this Table are isopressed, green machined and pressureless sintered rods. Data are measured by Coors/Spectro-Chemical lab. The dielectric constant, although higher than desired value, is still equivalent to hot pressed silicon nitrides, and is within useful range. The dielectric loss tangent is reasonably low, which is equivalent or better than hot pressed silicon nitride. Table 3 lists also dielectric data of SNW-1000 based silicon nitride, measured by Rockwell International at room temperature and 35 GHz. Samples are processed based on slip casting. Dielectric constants and loss tangent values are slightly higher than those listed in previous table. This may be due to higher frequency of 35 GHz. Nevertheless, results are quite satisfactory.



## Dielectric Properties (Cont)

Data of samples, based on isostatic pressing and pressureless sintering are further listed in Table 4. Values of recent development and earlier results are included for the purpose of comparison. In addition, the effective matrix dielectric constants, which represent the bulk as well as grain boundary properties of sintered silicon nitride, are calculated and listed in this table. The Maxwell dielectric mix rule and two phase model of closed pores dispersed in matrix of silicon nitride are used for calculation. The calculated value represents the effective dielectric constant of bulk as well as grain boundary phases of pressureless sintered silicon nitride. It is clear that the matrix dielectric constants and loss tangents of SNW-1000 based silicon nitride are reduced and improved compared with earlier work. In order to obtain a better picture of the state of the art of development of pressureless sintered silicon nitride as radome application, the dielectric properties as a function of temperatures are reviewed.

The dielectric properties of GTE-WESGO pressureless sintered SNW-1000 based material, along with hot pressed silicon nitrides as a function of temperatures are shown in Fig. 5 and Fig. 6 for comparison. The data of samples hot-pressed by Ceradyne were measured by Dr. W.W. Ho from Rockwell International Science Center (Ref. 1).

It is clear the pressureless sintered SNW-1000 by minor additive & process modification has dielectric properties equivalent to or better than hot-pressed silicon nitride. One of the samples, designated as Sample E, has lowest dielectric loss and little variation as a function temperature, i.e., varying from 0.0011 to 0.0015 from 23°C to 920°C. Data of this sample is listed in Table 5.

Dielectric properties of pressureless sintered silicon nitride are expected to be further improved by modifications of composition and processes, based on demonstrated results of SNW-1000 based silicon nitride.

### Conclusions

1. Pressureless sintered silicon nitride SNW-1000 based materials has sintered density of 3.30-3.33 g/cc. The strength of this material at room

## Conclusions (Cont)

temperature, as well as high temperature appears to be suitable for high temperature radome application.

2. Pressureless sintered process provides relatively unlimited size and shape forming capability and is the most economical way of processing radome.

3. Dielectric properties of pressureless sintered silicon nitride based on GTE-WESGO SNW-1000 based materials are equivalent or superior to some of the best hot-pressed silicon nitride known.

4. Best processed SNW-1000 based silicon nitride sample has dielectric loss tangent of about 0.0011 at 35 GHz and relatively little variation as a function of temperature of up to about 1000°C, i.e., loss tangent changed from 0.0011 to 0.0013 from room temperature to 920°C.

## Reference

1. W.W. Ho, "High Temperature Millimeter Wave Characterization of the Dielectric Properties of Advanced Window Materials", Technical Report, AMMRC TR 82-28, Contract No. DAAG46-79-C-0077, SC5235. 18FR, May 1982.

## Acknowledgement

Authors would like to thank Dr. W.W. Ho for dielectric measurements and valuable discussions.

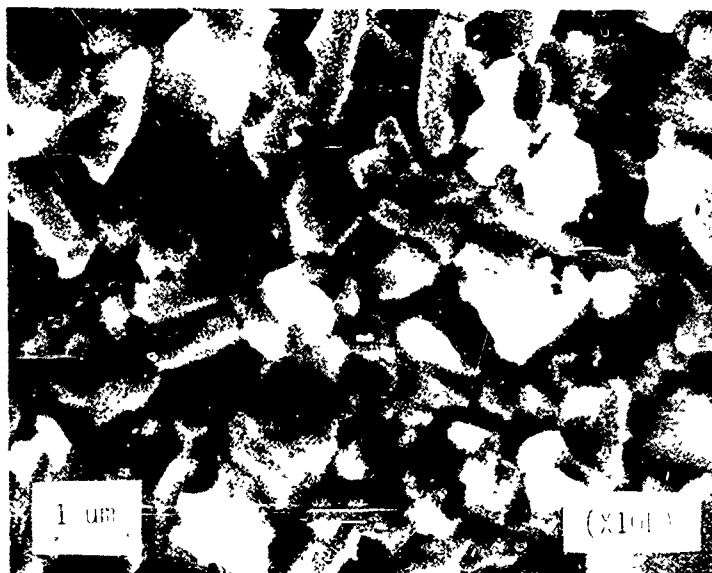


Fig. 3 Pressureless Sintered Silicon Nitride Radomes of SNW-1000 (left) and SNW-2000 (right).

Fig. 4 Microstructure of Pressureless Sintered Silicon Nitride, SNW-1000

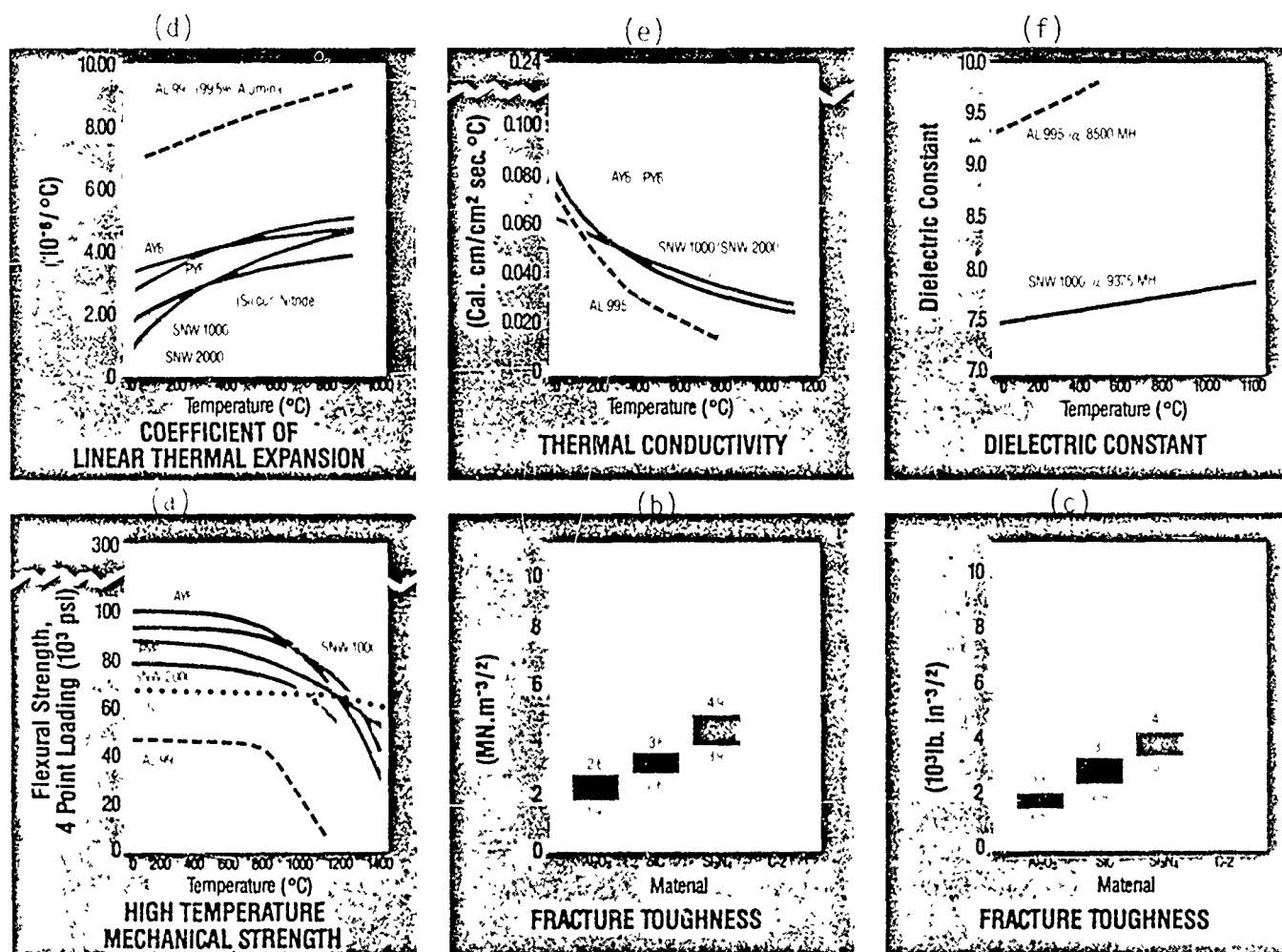
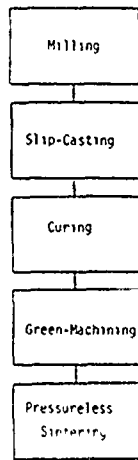


Fig. 5 Properties of Silicon Nitride

(a) Slip Casting Process



(b) Isostatic Pressing Process

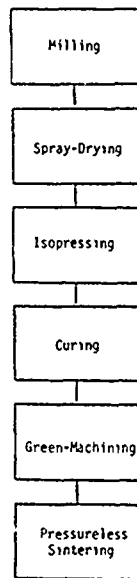


Fig. 2 Flow Chart of Manufacturing Processes

TABLE 1

## PROPERTIES OF PRESSURELESS SINTERED SILICON NITRIDE, SNW-1000

COLOR	Gray	
WATER ABSORPTION	0%	
POROSITY	Vacuum Tight	
CRYSTAL STRUCTURE	Hexagonal	
SINTERED DENSITY (g/c.c.)	3.30 - 3.34	
YOUNG'S MODULUS (10 <sup>6</sup> psi)	40	
SHEAR MODULUS (10 <sup>6</sup> psi)	16.3	
BULK MODULUS (10 <sup>6</sup> psi)	36	
POISSON'S RATIO	0.23	
THERMAL DIFFUSIVITY (ft <sup>2</sup> /hr)	25°C	0.55
	1100°C	0.13
SPECIFIC HEAT	°C	J/m <sup>2</sup> °K
	25	810
	220	990
	440	1060
	660	1120
	880	1140
	1100	1170
HARDNESS	Rockwell 45N	83-85

Table 2

Dielectric properties at 23°C of SNW-1000 based, pressureless sintered silicon nitride ceramics (samples are based on isopressed rod of 0.250" diameter x 1.6" long)

(1984) (±) SNW-1000 Based Specimens (*)	Dielectric Constant ε at 9.3 GHz	Dielectric Loss tan δ at 9.3 GHz
Sample A(1)	7.72	1.70 x 10 <sup>-3</sup>
Sample B(1)	7.50	1.40 x 10 <sup>-3</sup>
Sample D(1)	7.65	1.08 x 10 <sup>-3</sup>

(±) 1 - Indicates pressed and pressureless sintered isostatic sample, with sintered density = 3.30 g/cc.

(\*) - Dielectric data were measured by Coors/Spectro-Chemical lab.

Table 3

Dielectric properties at 23°C of SNW-1000 based, pressureless sintered silicon nitride ceramics (samples are based on slip cast discs of about 1.750" diameter x 0.175" thickness).

(1984) (±) SNW-1000 Based Specimens (*)	Dielectric Constant ε at 35 GHz	Dielectric Loss tan δ at 35 GHz
Sample A (S)	8.16	2.7 x 10 <sup>-3</sup>
Sample B (S)	8.13	2.5 x 10 <sup>-3</sup>
Sample C (S)	8.13	1.8 x 10 <sup>-3</sup>
Sample D (S)	7.99	1.7 x 10 <sup>-3</sup>
Sample E (S)	7.93	1.1 x 10 <sup>-3</sup>

(±) S - Indicates slip cast samples with sintered density = 3.30 g/cc.

(\*) - Dielectric data were measured by W.W. Ho, Rockwell International = 8.0 to 8.2.

Table 4

Dielectric properties at 23°C of SNW-1000 based, pressureless sintered silicon nitride (comparison of earlier work and recent work)

(±) SNW-1000 Based Specimens	Sintered (*) Density (g/cc) (%Theoretical)	Dielectric Constant ε	Dielectric Loss Tan δ	Calculated Effective Matrix Dielectric Constant (±)
1976 (1)	3.06 (91%)	7.33 (8.5 GHz)	2.30 x 10 <sup>-3</sup> (8.5 GHz)	8.2 (at 8.5 GHz)
1977 (1)	3.23 (96%)	7.95 (8.5 GHz)	8.7 x 10 <sup>-3</sup> (8.5 GHz)	8.36 (at 8.5 GHz)
1984 (1) Sample D	3.30 (98.5%)	7.65 (9.3 GHz)	1.08 x 10 <sup>-3</sup> (9.3 GHz)	7.8 (at 9.3 GHz)

(\*) Based on Theoretical density = 3.35 g/cc.

(±) Based on Maxwell dielectric mix rule.

(±) 1 - Indicates isostatic pressed and pressureless sintered samples

Table 5

Dielectric properties of SNW-1000 based, pressureless sintered silicon nitride as a function of temperatures, Sample E. (S).

SNW-1000 Based Specimens Temperature (°C) / Sample E(S) (±)	Dielectric Constant at 35 GHz	Dielectric Loss Tan δ at 35 GHz
23	7.93	0.0011
375	8.11	0.0011
570	8.23	0.0012
680	8.39	0.0014
920	8.51	0.0015

(±) Slip Cast Sample

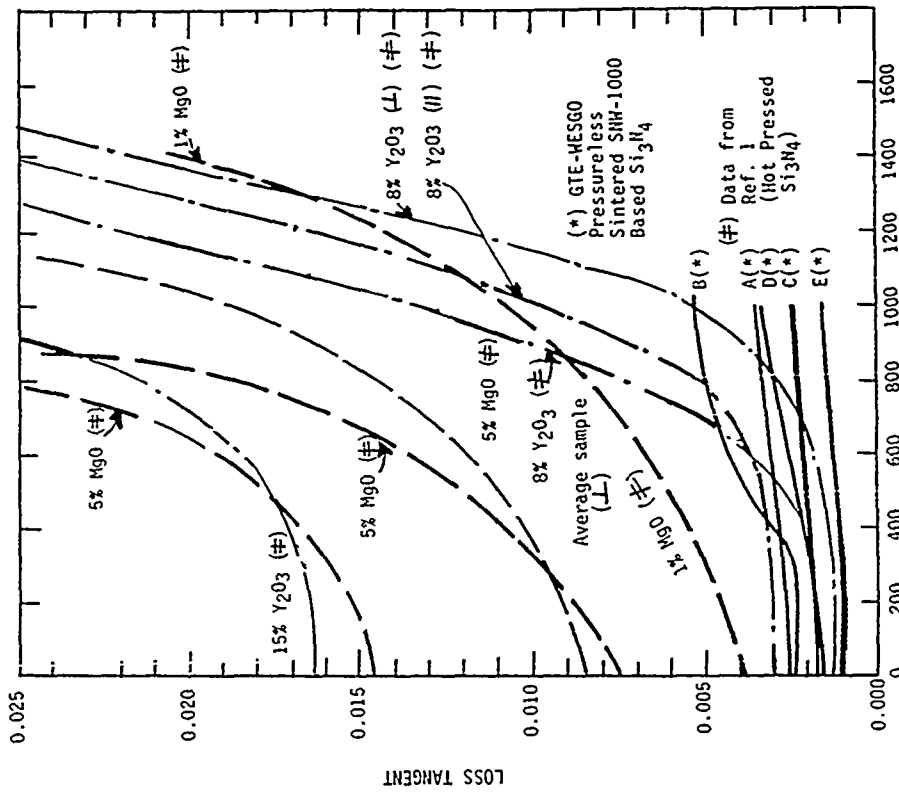


Fig. 6 Measured Dielectric Loss Tangent of Pressureless Sintered SNW-1000 Based Silicon Nitride (\*) and Hot Pressed Silicon Nitride (#) at 35 GHz.

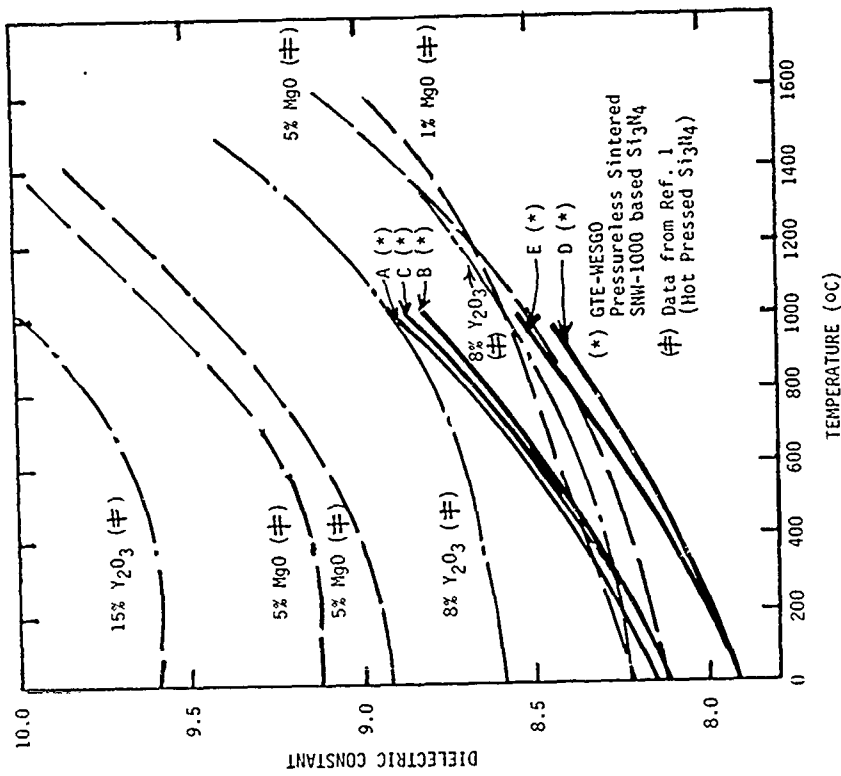


Fig. 5 Measured Dielectric Constant of Pressureless Sintered SNW-1000 Based Silicon Nitride (\*) and Hot Pressed Silicon Nitride (#) at 35 GHz.

LL-100 - A NEW POLYBUTADIENE  
(Resin System for Radome Applications)

by  
G. WAYNE EASTRIDGE  
BRUNSWICK CORPORATION  
DEFENSE DIVISION  
MARION, VA 24354

AD-P004 368

Abstract

Low Dielectric and Loss Tangent properties make the LL-100 System extremely attractive for radome applications. The LL-100 Polybutadiene also costs typically the same as an Epoxy System and processes like an epoxy. Unlike epoxies, however, the LL-100 System may be utilized for extended periods at 450°F similar to BMI Polyimide Systems. The LL-100 Prepreg has excellent tack and drape and requires no refrigerated storage. This system has been utilized successfully for radome applications up to 94 GHz without substantial change in electrical properties.

Introduction

Polybutadiene Resin Systems are not new to the reinforced composite industry. They have, however, suffered some adverse advertising brought on by poor strength properties at elevated temperature. Extensive development efforts lead to the formulation of a new Polybutadiene System designated LL-100. This paper will provide data to support the LL-100 Polybutadiene as a viable candidate for radome applications.

PREVIOUS PAGE  
IS BLANK



## Discussion

The basic polybutadiene Resin Systems are available in several forms or microstructures:

- 1,2 Microstructure - A thermosetting polybutadiene resin system utilized in reinforced composite applications.
- 1,4 Microstructure - An elastomeric polybutadiene commonly utilized in tire manufacture.
- 1,2 to 1,4 Microstructures - Polybutadiene blend utilized to add toughness or elasticity to the finished thermosetting polymer.

In developing the polymer designated Brunswick Corporation's LL-100 Polybutadiene, several aspects common to resin formulation were evaluated. Available polybutadiene systems were selected and blended with various diluents, co-reactive monomers and catalysts. The resins formulated were preimpregnated (prepregged) into E-glass, Style 181 Fabric and processed into 12-ply laminates using vacuum bag/autoclave cure techniques. The screening of the resin formulation was based on mechanical, physical, and electrical performances.

Table I lists properties of a 12-ply laminate of LL-100 Polybutadiene reinforced with 7781 E-glass. Flexural strength testing is a common test characterizing best the adhesion of the polymer to the glass fabric.

In view of the data in Table I, some important characteristics of the LL-100 Polybutadiene system can be seen. First, the use temperature is 450-475°F, achievable previously only with polyimide type systems. The strengths are generally lower at elevated temperatures but remain quite adequate for most radome designs. Secondly, the dielectric constant and

loss tangent properties for the laminate are lower than for laminates made from other thermosetting systems. Of particular interest is the loss tangent value. In an E-glass reinforced composite, this value is in a class by itself.

To demonstrate the optimum radome design parameters of the LL-100 Polybutadiene system, the LL-100 was combined with 581 Style Quartz Fabric and processed into a 12-ply laminate and tested. Table II gives typical properties of the LL-100/581 Quartz System as compared to the other "household" polymers. This combination of LL-100 Polybutadiene Quartz reinforced is, from an electrical designer's viewpoint, an unbeatable combination. Again, note the thermal stability at 450°F.

Other aspects and characteristics of the LL-100 System also add to its usefulness for radome applications. The cost of the LL-100 prepreg system is compatible to typical MIL-R-9300 Epoxies purchased from a variety of suppliers. The LL-100 Prepreg also has an unlimited shelf life at ambient conditions. The prepreg will retain an aggressive high tack and drape condition in excess of one year at room temperature. This aspect reduces scrap due to exceeded out time and also allows for one-time purchasing of volumes of prepreg needed in lieu of drop shipments required for perishable prepreps.

Processing of the LL-100 Polybutadiene has a forgiving cure cycle quite similar to most epoxy systems. Processing is normally a bleed system using vacuum bag with oven or autoclave assisted cure at temperatures from



300-350°F. Postcure may be required if temperatures greater than the cure temperature is needed. The glass transition temperature of LL-100 exceeds 500°F.

The oxidative stability and moisture resistance of Polybutadiene polymers are shown in Figures 1 and 2. The polymer resistance to oxidation and moisture absorption is enhanced by incorporation of co-reactive monomers in lieu of 100% Polybutadiene monomers. The data shown again demonstrates attractive characteristics of Polybutadiene for radome applications.

### Experience

To date, Brunswick Corporation has utilized the LL-100 Polybutadiene system in several radome and composite applications. Table III lists programs which have successfully utilized this system.

### Conclusions

LL-100 Polybutadiene composites exhibit excellent properties for radome applications.

The low loss properties make the LL-100 system attractive for exacting electrical designs, particularly high frequency.

LL-100 high temperature properties (450°F) bridge the gap between the epoxy and addition polyimides allowing the radome designer more latitude in material selection.

**TABLE I**  
**LL-100 (RF-374) LAMINATE TEST DATA**

LAMINATE I.D.	LL-100	LL-100
W.O. NO.	81077-1A	
<b>FLEXURAL STRENGTH, KSI</b> R.T. 210° F 350° F 450° F	<b>PREPREG. QUAL. PANEL</b> 76 48 25 20 72 50 28 22	
<b>FLEXURAL MODULUS, KSI x 10<sup>3</sup></b> R.T. 200° F 350° F 450° F	2.8 2.6 2.1 2.0 2.9 2.7 2.2 2.0	
<b>BARCOL HARDNESS :</b> <b>AFTER POSTCURE</b> <b>THICKNESS (INCHES)</b> <b>RESIN CONTENT</b> <b>SPECIFIC GRAVITY</b> <b>% VOIDS</b> <b>DIELECTRIC CONSTANT (9.375GHZ)</b> <b>LOSS TANGENT (9.375GHZ)</b> <b>POSTCURE CONDITIONS</b>	68-70 .106 27.2 1.80 .39 4.18 .0072 12 HOURS @ 375° F 68-70 .106 27.2 1.80 .39 — — 12 HOURS @ 475° F	

TABLE II

TYPICAL PROPERTIES OF COMPOSITE MATERIALS REINFORCED WITH 581 QUARTZ

PROPERTY	MATERIALS				ADDITION POLYIMIDE
	LL-100 POLYBUTADIENE	CONDENSATION POLYIMIDE	EPJOXY	POLYESTER	
FLEX STR. (KSI)					
R.T.	65	70	80	70	70
250° F	50	—	50	40	—
350° F	25	50	—	—	50
450° F	20	—	—	—	40
600° F	—	40	—	—	—
FLEX. MOD. (KSI x 10 <sup>3</sup> )					
R.T.	2.8	2.8	2.8	3.0	2.5
250° F	2.6	—	2.2	2.5	—
350° F	2.2	2.5	—	—	2.4
450° F	2.0	—	—	—	2.0
600° F	—	1.8	—	—	—
RESIN CONTENT, W/O	~ 25	~ 30	~ 32	~ 32	~ 35
VOID CONTENT, V/O	< 2	< 5	< 2	< 2	< 5
DIELECTRIC CONSTANT (9.375 GHz)	3.0	3.4	3.2	3.3	3.4
LOSS TANGENT (9.375 GHz)	.003	.006	.020	.009	.006

# TABLE III

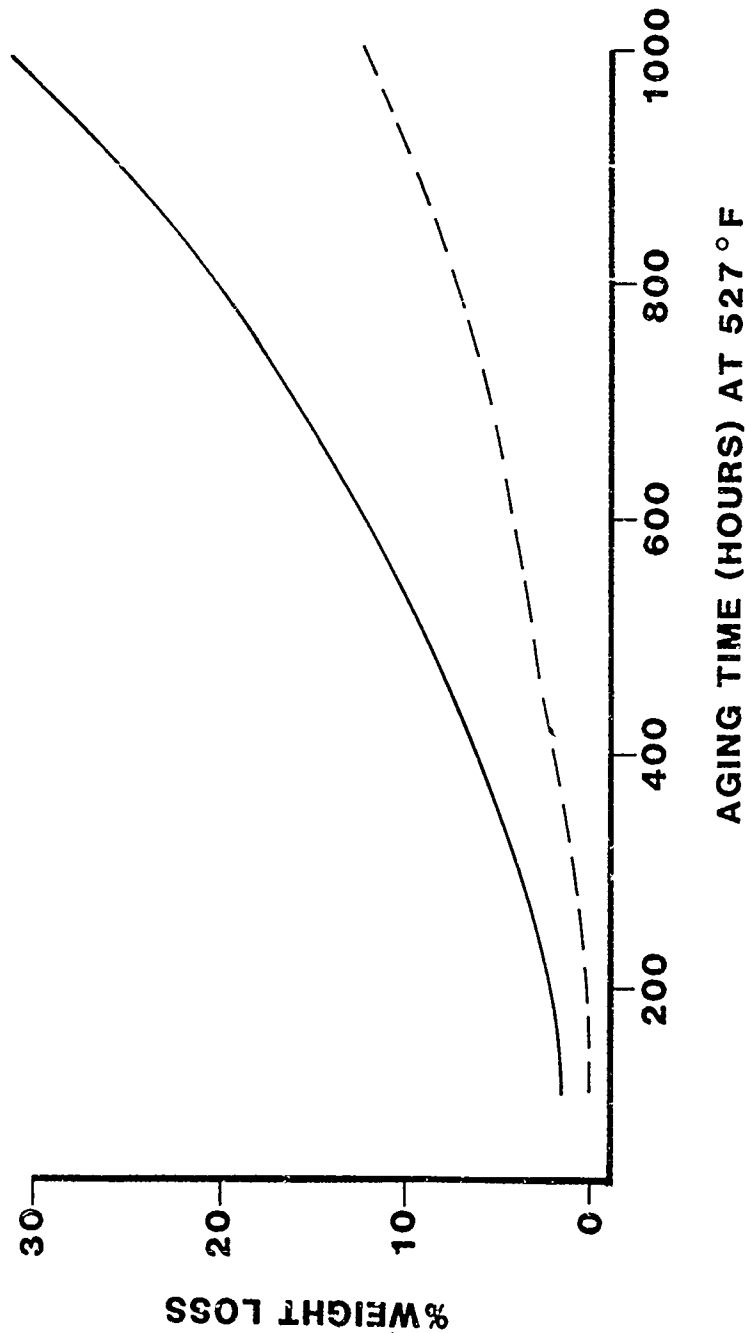
## LL-100 RADOME EXPERIENCE

### RADOME DESCRIPTION

- WX-50 KA-BAND RADOME  
(SOLID LAMINATE, .14" THICK)
  
- MICRAD ATIGS RADOME KA-BAND  
(SOLID LAMINATE, .13" THICK)
  
- 42.44" DIA POD RADOME, 95GHz  
(SOLID LAMINATE, .10" THICK)
  
- F-5 SHARK NOSE PROTOTYPE  
(SANDWICH RADOME)
  
- SANDWICH RADOME-GROUND SERVICE  
(THIN SKINS, .020" THICK,  
POLYURETHANE FOAM CORE)

— POLYBUTADIENE HOMOPOLYMER

- - - POLYBUTADIENE WITH  
COREACTIVE MONOMER

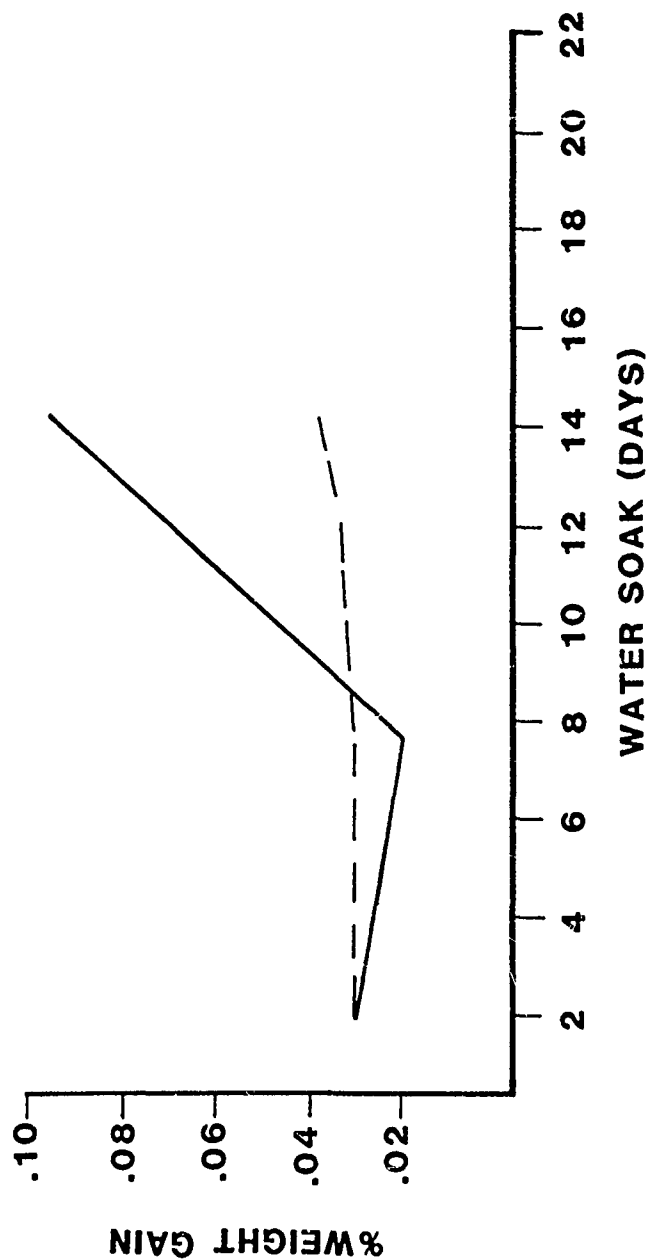


AGING TIME (HOURS) AT 527 °F

\* DATA FROM COLORADO CHEMICAL CORPORATION'S TECHNICAL BULLETIN

FIGURE 1  
EFFECT OF HEAT AGING ON POLYBUTADIENE CASTING

— POLYBUTADIENE HOMOPOLYMER  
- - - POLYBUTADIENE WITH  
COREACTIVE MONOMER



\* DATA FROM COLORADO CHEMICAL CORPORATION TECHNICAL BULLETIN

FIGURE 2  
EFFECT OF WATER SOAK ON POLYBUTADIENE CASTING

Kurt Hollenbeck and Matt Rehr  
Texas Instruments - Antenna Laboratory  
Dallas, Texas

Radomes requiring frequency coverage from S through K band present a difficult design challenge. Past experience with broadband antenna systems has shown that a low finess ratio "A" sandwich radome offers the best electrical performance. However, a blunt "A" sandwich which performs well electrically typically has skins which are too thin to provide adequate rain erosion and ground handling protection. Therefore, the designer has been forced to either sacrifice electrical performance or face increased rain erosion and ground handling damage. To achieve the necessary electrical and mechanical properties, new radome designs incorporating thermoplastic materials have been developed. These new thermoplastic radomes can meet both the mechanical and electrical requirements while remaining relatively low cost. //

The standard materials used for an "A" sandwich radome include fiberglass composite skins seperated by a nomex honeycomb core. To achieve adequate rain erosion protection from a fiberglass composite material the outer skin needs to be 0.040" thick or greater.<sup>1</sup> However, to perform well electrically, the outer skin thickness should be 0.020" or less. In an effort to circumvent this problem, Ed Greene from IBM developed a 100% polycarbonate radome. By changing from traditional composite materials to polycarbonate materials both electrical and rain erosion performance were improved. Texas Instruments has taken the work done by Ed Greene and expanded it, and is currently producing these polycarbonate radomes under contract to the military.

The 100% polycarbonate radome consists of two vacuum molded polycarbonate skins bonded to a polycarbonate honeycomb core.<sup>2</sup> An injection molded glass filled polycarbonate base ring is bonded into the structure for rigidity and attachment purposes. The entire radome is bonded together using an elastomeric polyurethane adhesive.<sup>3</sup> A cross-section of this structure is shown in Figure 1.

The electrical performance of polycarbonate radomes is superior to their fiberglass composite counterparts. Most of the reason for the improved performance is the relatively low dielectric constant of the polycarbonate (2.77) compared to fiberglass (4.3). A second order effect is the lower loss tangent of polycarbonate (0.007) compared to fiberglass (0.02). Because the dielectric constant of polycarbonate is less than fiberglass, the skin thickness can be physically increased while remaining electrically constant. Figures 2 and 3 show a three dimensional contour plot of two "A" sandwich wall designs. Figure 2 shows a polycarbonate wall with 0.025" skins and a 0.190" core. Comparing this to Figure 3, which shows the same physical design with fiberglass skins it is observed that the polycarbonate radome offers increased performance. It should be noted that the dielectric constant of the polycarbonate honeycomb is very nearly that of nomex (1.08). However, because of fabrication methods used in producing the polycarbonate honeycomb, it is isotropic with respect to orientation while the nomex honeycomb is not. The orientation effect found in nomex honeycomb is not great but is measureable as is shown in Figure 4.



The very high impact strength of polycarbonate translates into excellent rain erosion resistance and this is the primary reason for its choice for thermoplastic radomes. The high impact strength also makes the radome resistant to handling damage. A thin skinned polycarbonate sandwich radome can be dropped from a height of five feet without being damaged. In comparison, a fiberglass laminate would suffer extensive damage. Even a drop of one foot will produce fracture lines in the laminate. These lines serve as porous paths for water migration into the honeycomb.

The reason for the increased resiliency of the polycarbonate radome over the fiberglass radome is threefold. First, the brittle nature of the fiberglass skins does not allow significant deformation. Therefore when struck, the fiberglass material cannot absorb the impact energy and the skin cracks. On the other hand, the polycarbonate skin deforms elastically on impact. This allows the polycarbonate skin to absorb the impact energy and then spring back to its original shape. Second, the standard nomex honeycomb core becomes crushed with repeated impacts. After the core crushes, the skin becomes unsupported and skin failure occurs. The polycarbonate core does not crush as quickly with repeated impacts. Instead, it absorbs the impact energy through elastic deformation then springs back to its original shape. Thirdly, the bonding agent between the skins and core affects resiliency. For the standard "A" sandwich radome, the resin in the skin acts as the bonding agent. Usually this resin is a brittle type of epoxy or polyester. On impact, this bond cracks in the same way as the fiberglass skin. For the polycarbonate radome, the bonding agent is an elastomeric urethane. Upon impact, this adhesive deforms elastically to flex with the skins and the core. The structural integrity of the bond is not degraded even after many impacts. Figure 5 shows the rain damage mechanisms of the standard "A" sandwich wall compared to the polycarbonate "A" sandwich wall.

The excellent impact properties of polycarbonate are accompanied with low stiffness in comparison to a fiberglass laminate. The modulus of elasticity is about one tenth, and the strength is about one eighth of a fiberglass laminate. Because of the reduced strength of polycarbonate, special design of the base is required. For spheroidal radomes, the nose will usually have adequate strength when fabricated from polycarbonate due to the special stiffness properties of spherical surfaces. Toward the base, where the radome is usually more cylindrical or gently curved, extra mechanical stiffness will be needed. In regions outside of the window area, the injection molded base ring is integrated into the wall. Additionally, the glass filled base ring acts as a stabilizer to prevent cold flow of the polycarbonate skins around the attachment screws. Figure 1 illustrates the construction of the reinforced radome.

While polycarbonate radomes offer distinct electrical, rain erosion and ground handling advantages over traditional fiberglass radomes, there are some drawbacks. One of the major inadequacies of polycarbonate is its low operational temperature. Typically, polycarbonate radomes cannot be used where temperatures reach above 230 degrees F. Not only does the polycarbonate become weakened, but the urethane adhesive degrades. This precludes using a polycarbonate radome for sustained speeds of Mach 1 or above. Another disadvantage of polycarbonate is that it is not resistant to some chemicals. This lack of chemical resistance might cause problems where the radome is subjected to flightline environments. To eliminate these two drawbacks of polycarbonate radomes, while still retaining the desirable electrical and rain erosion properties, new materials need to be used.



Texas Instruments is investigating the use of new thermoplastic materials for radome applications. These new second generation materials were chosen for their high temperature capability and their relatively high impact resistance. Additionally, each of these materials offers a substantial increase in chemical resistance over polycarbonate. Candidate skin materials include polyarylsulfone, polyarylate, and polyether-ether-ketone. Each of these materials is capable of withstanding temperatures of 320 degrees F and above. Samples of these materials have been sent to Dayton, Ohio for rain erosion testing. After the samples have been tested and a single material is selected, the process of how to form the skins into the desired shape will need to be determined.

A good candidate for a high temperature core material is Ultem 1000.<sup>4</sup> This material is a polyetherimide thermoplastic which retains adequate strength up to 325 degrees F. The impact resistance of this core closely approximates that of a polycarbonate core which makes it a logical choice. To further insure that the core does not crush while impacting rain at supersonic speeds, a 1/16 inch cell size will be used. This cell size gives a core with density of about 9 pounds per cubic foot and should be of more than adequate stiffness to insure that failure does not occur. Testing using a 1/16 inch cell polycarbonate honeycomb has indicated that the rain erosion properties of this higher density core are more than adequate. Because this core has a high stiffness value, it will need to be preformed to the desired shape before the radome can be assembled together. Preliminary tests on the high density polycarbonate core, show that preforming the core will not be a serious problem.

With a good choice of skin and core materials the final area of investigation involves an adhesive. Several different high temperature elastomeric adhesives are now under investigation. Some of these adhesives include silicones, urethanes, fluorosilicones, fluorohydrocarbon (Viton),<sup>5</sup> and epoxies. Preliminary work indicates that silicones form too weak a bond to function adequately. Urethanes do not retain adequate strength at elevated temperatures to be of much use. Fluorosilicones hold promise but it has been difficult to locate vendors. Fluorohydrocarbon (Viton)<sup>5</sup> has been used as a rain erosion coating and appeared to be a likely candidate. However, the ratio of 20% adhesive to 80% solvent (Methyl-Ethyl-Ketone) attacked some of the thermoplastics. More work in this area is needed including trying another, less active, solvent base. Current work indicates that the high temperature epoxies hold the most promise of working. The only drawback to an epoxy is that it is very brittle and degrades quickly on impact. More work is being conducted in the epoxy area including adding a softening agent to allow the epoxy to remain elastomeric while retaining its high temperature properties.

The need to broadband high velocity radomes is driving the thermoplastic radome technology into higher temperature ranges. The current broadband polycarbonate radomes cannot fulfill the requirements at these elevated temperatures. Therefore, Texas Instruments is continuing to investigate the use of higher temperature thermoplastics, elastomeric adhesives, and the associated fabrication processes necessary to fabricate these second generation thermoplastic radomes.

FOOTNOTES

- 1 Schmitt, G.F., Jr., "The Subsonic Rain Erosion Response of Composite and Honeycomb Structures", SAMPE Journal, Sept/Oct 1979.
- 2 Plascore Inc., Zeeland, Michigan; Manufactures Polycarbonate Honeycomb.
- 3 Hartel Enterprises Inc., Pacoima, California; Produces HE 17017 Urethane Adhesive.
- 4 Ultem is a tradename of General Electric.
- 5 Viton is a tradename of DuPont.

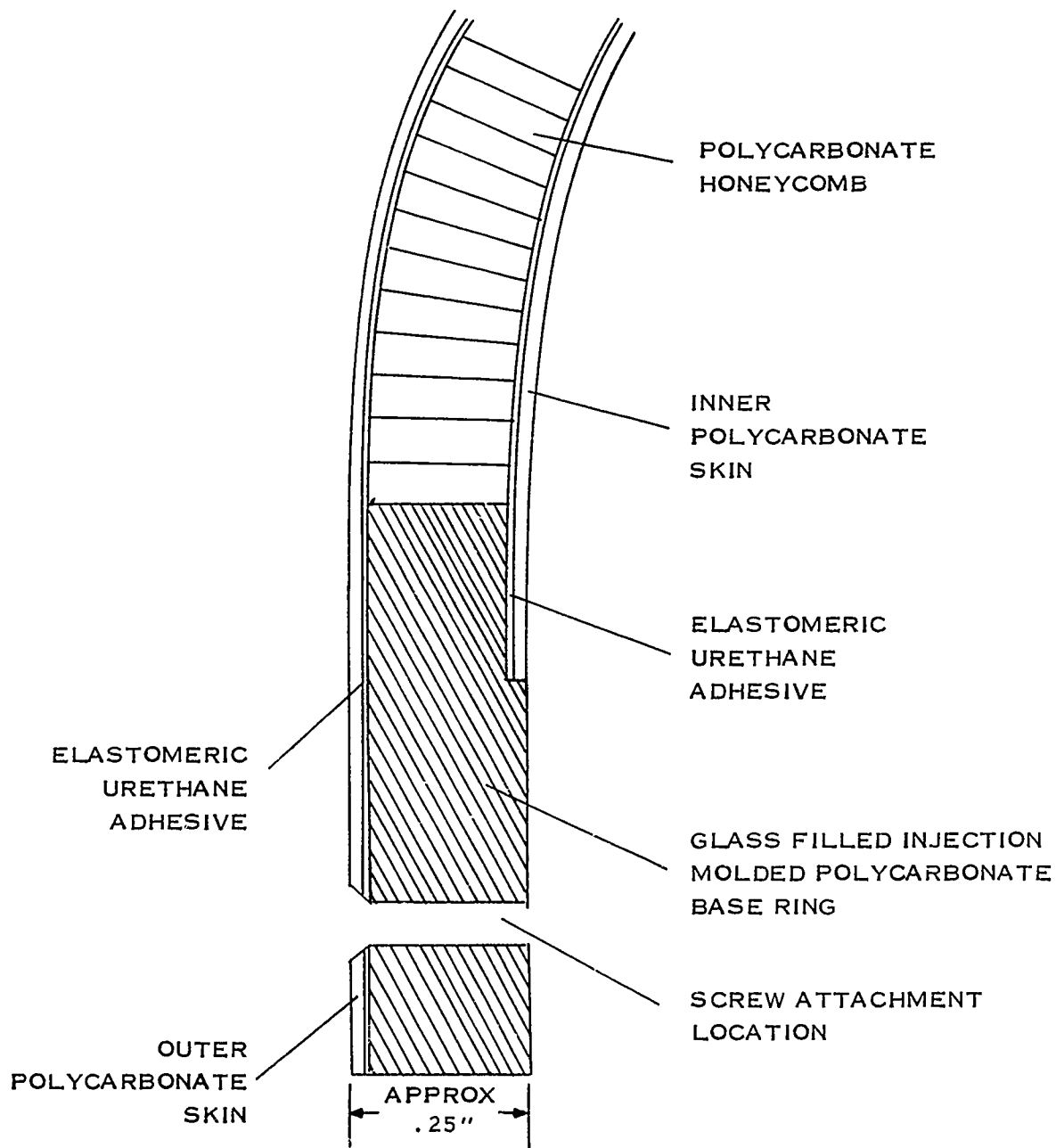


FIGURE 1. CROSSSECTION OF POLYCARBONATE RADOME WALL AND BASE RING

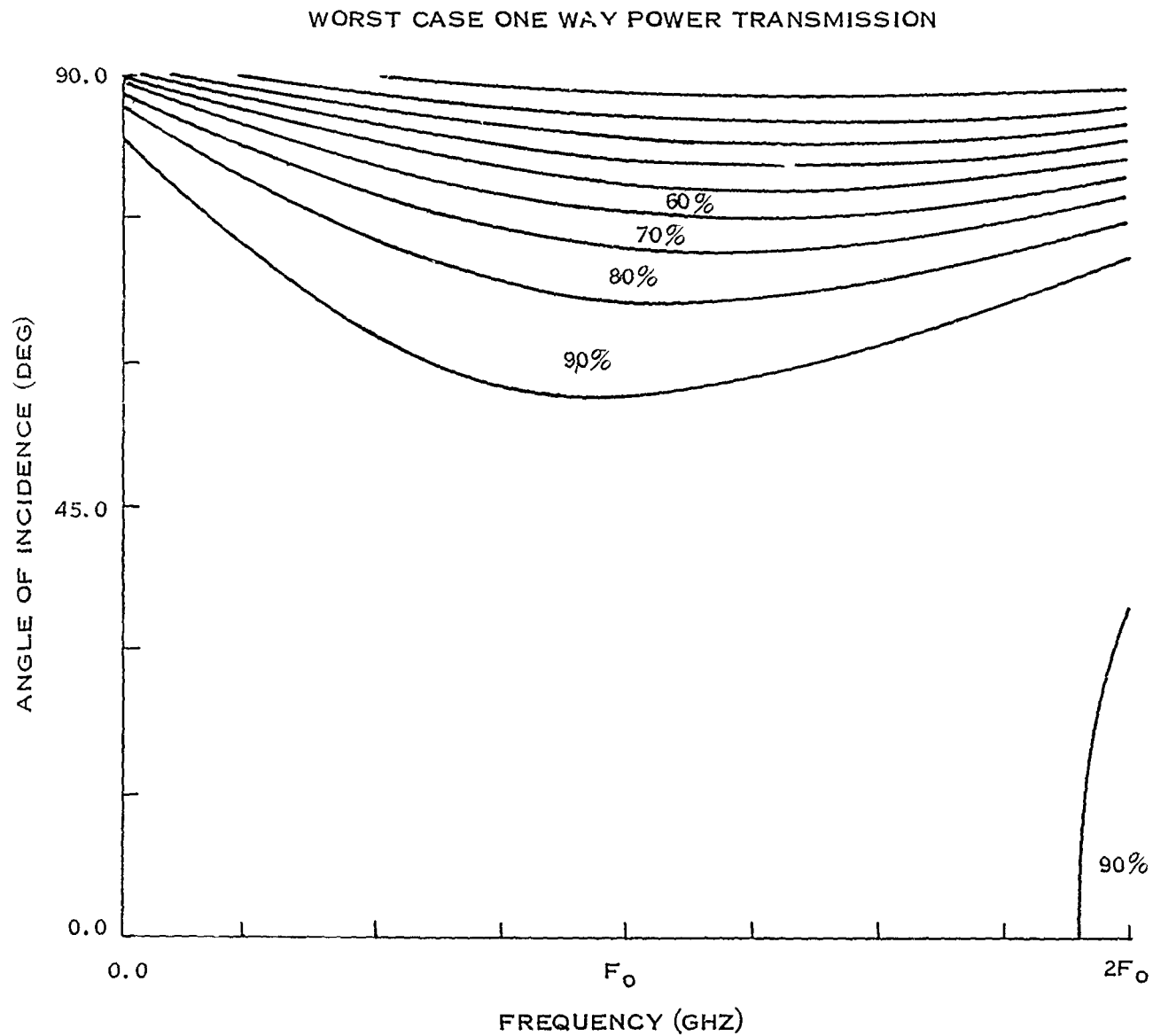


FIGURE 2. POLYCARBONATE RADOME WITH  
 0.025 INCH THICK SKINS,  
 0.190 INCH THICK CORE

WORST CASE ONE WAY POWER TRANSMISSION

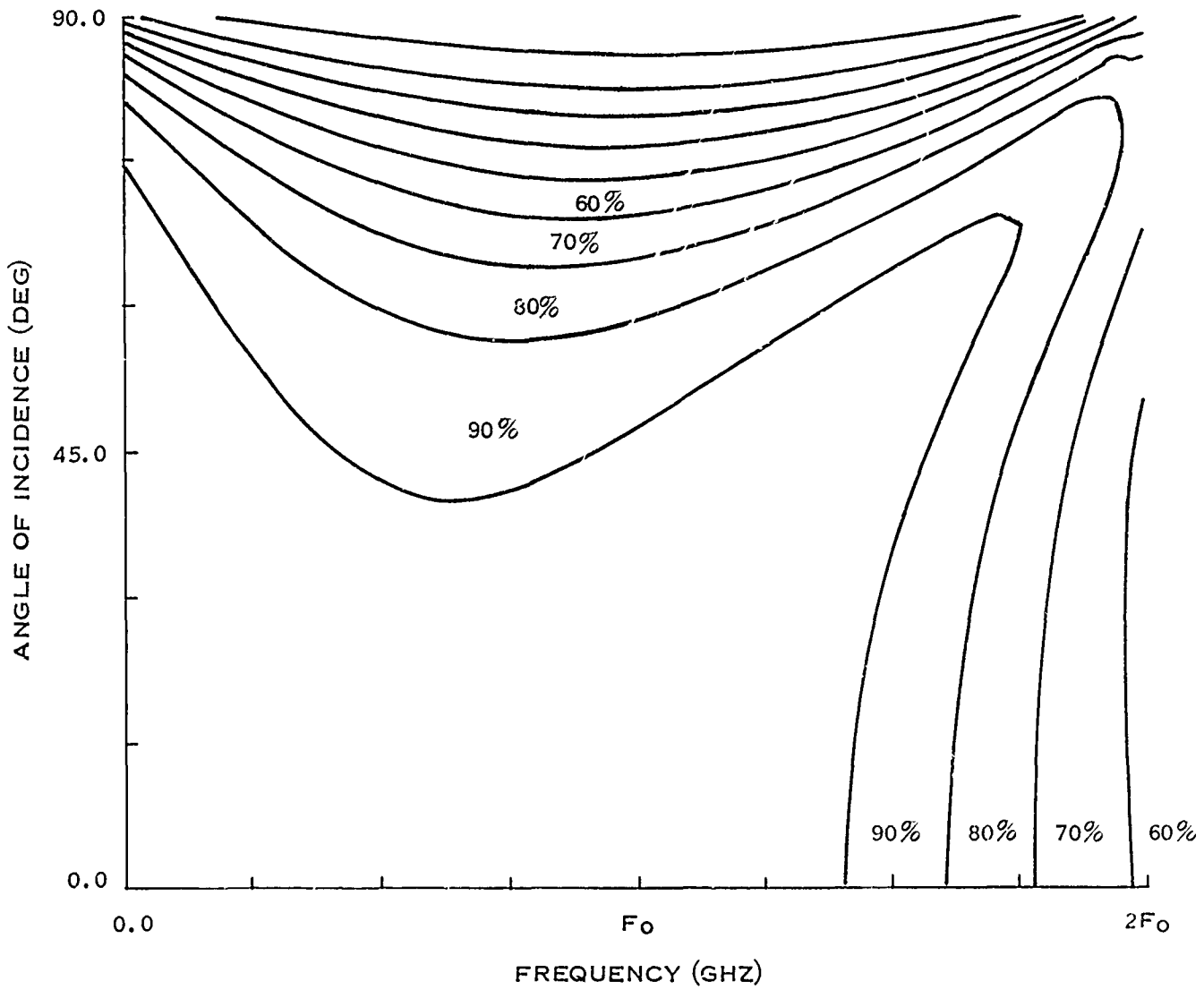


FIGURE 3. FIBERGLASS RADOME WITH  
0.025 INCH THICK SKINS,  
0.190 INCH THICK CORE

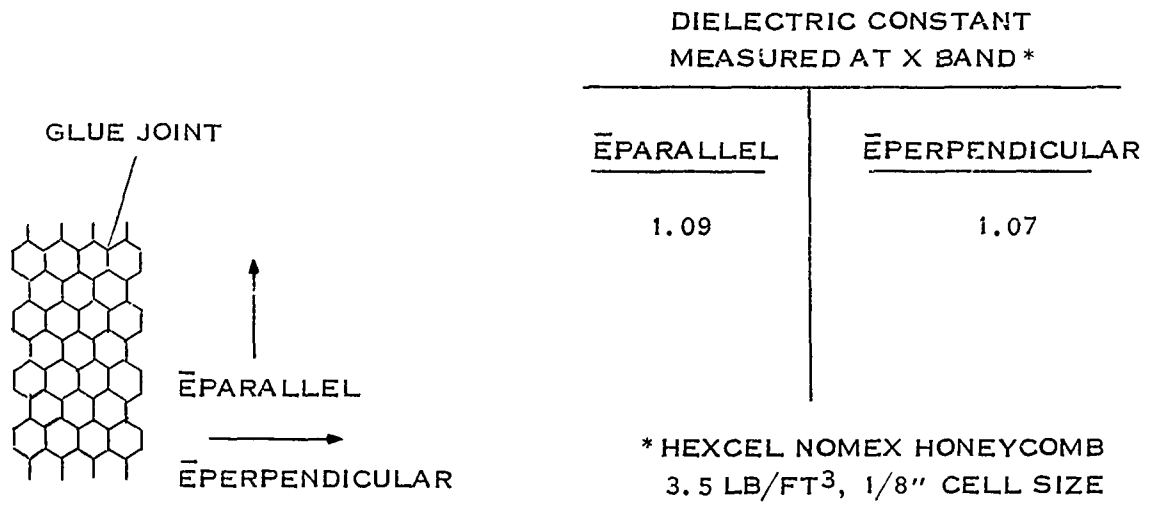
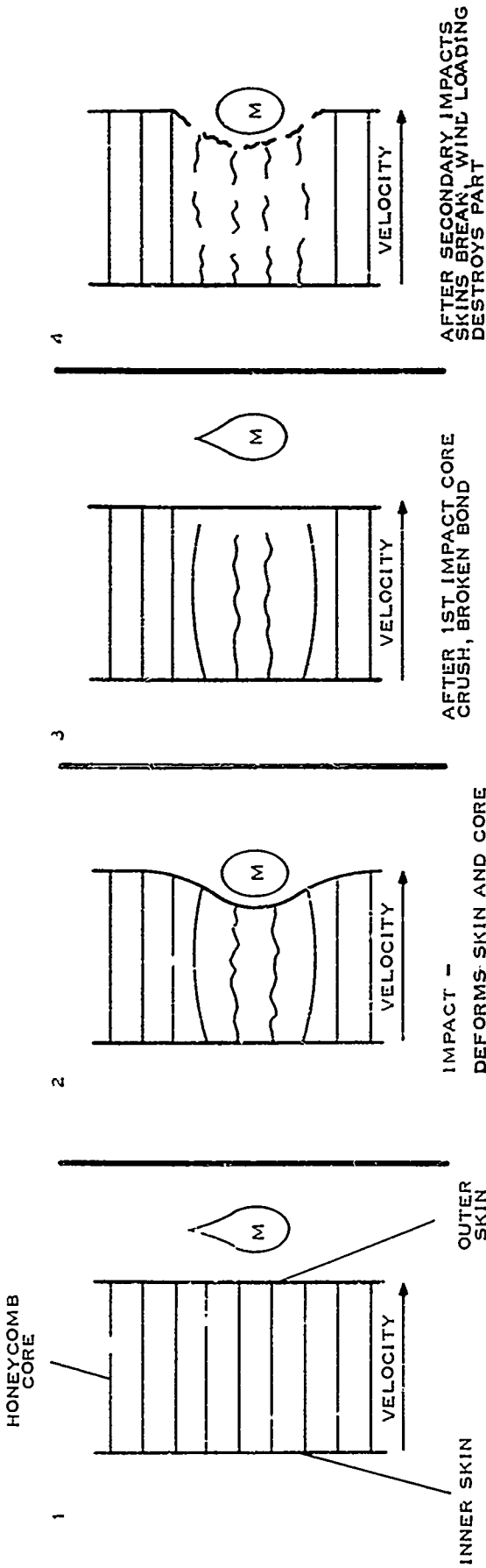


FIGURE 4. NON ISOTROPIC EFFECT  
OF NOMEX HONEYCOMB

FIBERGLASS SKINS, NOMEX CORE



ENERGY =  $1/2 MV^2$

POLYCARBONATE SKINS & CORE

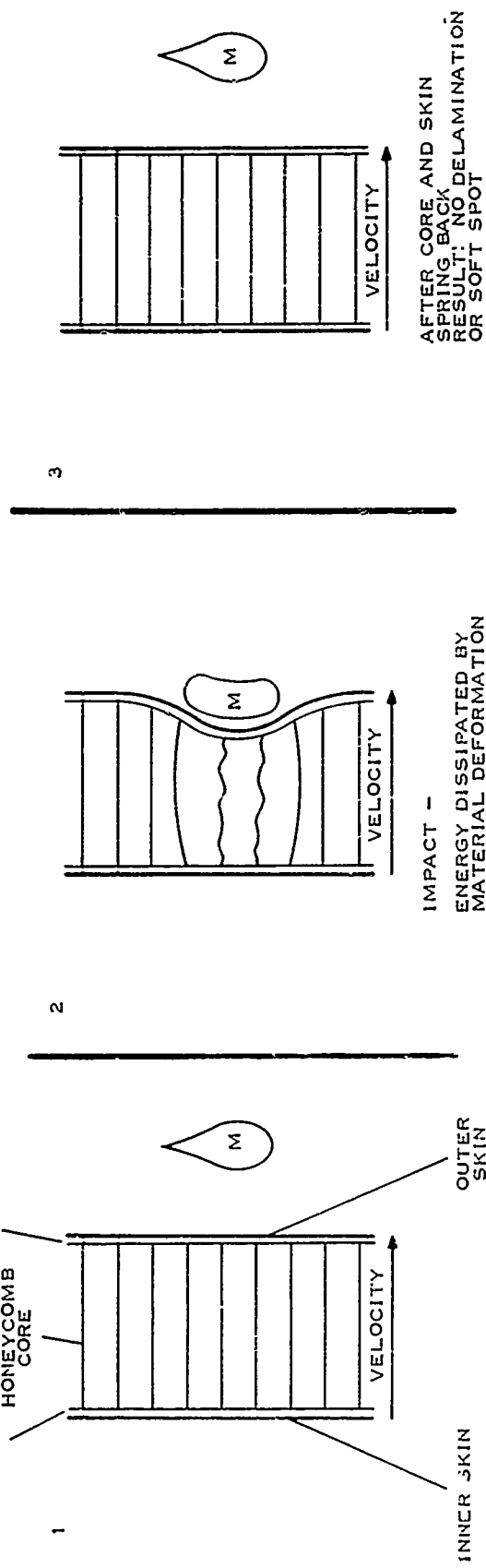


FIGURE 5. RAIN DAMAGE MECHANISM FOR THIN SKIN "A" SANDWICH

Progress on Transparent Yttria

By

W. H. Rhodes and E. A. Trickett

GTE Laboratories

Waltham, MA 02254

**AD-P004 370**

INTRODUCTION

$\text{La}_2\text{O}_3$  - doped  $\text{Y}_2\text{O}_3$  is of interest for infrared applications because it is one of the longest wavelength transmitting oxides. It is refractory with a melting point of  $2430^\circ\text{C}$  and has a moderate expansion coefficient. The thermal shock and erosion resistance is considered to be intermediate among the oxides, but outstanding compared to non-oxide infrared materials.

A major consideration is the low emissivity of  $\text{Y}_2\text{O}_3$ , which limits background radiation upon heating. This is illustrated in Figure 1 where the theoretical single crystal transmittance curves for  $\text{Al}_2\text{O}_3$  and  $\text{Y}_2\text{O}_3$  are shown together with the black body radiosity curve for  $1500^\circ\text{K}$ . The principle contribution to  $\text{Y}_2\text{O}_3$ 's emittance is the overlap of the radiosity curve and the absorption curve (crosshatched area) which is significantly less than that for  $\text{Al}_2\text{O}_3$  (slashed area under the curve). It is also known that the phonon edge gradually moves to shorter wavelengths as a material is heated. This could overlap the intended region of transmittance, say  $3\text{-}5\ \mu\text{m}$ , for  $\text{Al}_2\text{O}_3$ , whereas greater tolerance for heating is available with  $\text{Y}_2\text{O}_3$ .

$\text{La}_2\text{O}_3$  doped  $\text{Y}_2\text{O}_3$  is fabricated by standard ceramic powder processing methods. Near net shape sintering results in grinding and polishing savings as well as economical material usage. ONR sponsored research, over the last two years, has centered on improving the optical and mechanical properties with the goal of achieving a viable infrared candidate material.

PREVIOUS PAGE  
IS BLANK





## FABRICATION

The detailed sintering mechanism has been reported.<sup>1</sup> Briefly stated the process involves co-precipitating a  $\text{La}_2\text{O}_3 - \text{Y}_2\text{O}_3$  composition that has a high temperature two phase field, but a wide single phase solid solution field below approximately 2000°C. By sintering in the two phase field, grain growth is retarded due to the second phase because grain growth must occur by Ostwald ripening which is an extremely slow process. Pores remain on the grain boundaries until they are eliminated by the normal diffusional processes operating in sintering. The material is subsequently annealed in the single phase cubic field to achieve the equiaxed microstructure shown in Figure 2. This extremely low porosity structure represents an improvement over the material possible in the last report<sup>(2)</sup>. Discs 1 and 2 mm thick are shown in Figure 3. A major improvement in pore reduction has been achieved. Table I shows the correlation between pore density and transmittance. One sample (75H) did not correlate which could be related to absorption phenomena such as impurities or slight deviations from stoichiometry. The goal of the research was to achieve consistent results similar to 75NR or better. Table II shows total integrated scatter measured at two wavelengths by the Naval Weapons Center. It is interesting to note that the two samples have nearly equal values at 3.39  $\mu\text{m}$ , but a factor of four difference at the shorter wavelength. This indicates that pores are the major scattering source and that their diameter is close to 0.65  $\mu\text{m}$ .

TABLE I  
QUANTITATIVE PORE COUNT VERSUS TRANSMITTANCE

SAMPLE NUMBER	PORES/cm <sup>3</sup>	TRANSMITTANCE, 2.5 $\mu\text{m}$ (%)
YL 75H	$6.7 \times 10^3$	79.9
YL 75 NR	$8.1 \times 10^3$	83.0
YL 72 (2)-JM	$2.1 \times 10^4$	82.0
YL 74B	$2.9 \times 10^4$	81.0
YL 72	$2.4 \times 10^5$	78.4

TABLE II  
TOTAL INTEGRATED SCATTER

WAVELENGTH	SAMPLE NO. 103E	SAMPLE NO. 107C
0.6471	$1.12 \pm 0.29 \times 10^{-2}$	$4.36 \pm 3.00 \times 10^{-2}$
3.39	$5.99 \pm 2.83 \times 10^{-3}$	$6.38 \pm 2.17 \times 10^{-3}$

#### OPTICAL PROPERTIES

Figure 4 shows FTIR curves for 1 and 2 mm thick samples. The shape of the transmittance curve and phonon edge are well illustrated. A low level of absorption is present at 3200 wavenumbers. This is thought to be due to  $\text{OH}^-$  trapped in the structure, a condition often encountered in oxides. Various processing techniques have been employed to reduce absorption. The absorption generally decreases at longer wavelengths until encountering the phonon edge.

The transmittance of numerous samples was measured at the Naval Weapons Laboratory employing a well calibrated Perkin Elmer 221 spectrophotometer. Both the one and two sample methods have been employed where a refractive index of 1.90 was assumed in calculating absorption by the one sample technique. (A recent measurement on  $\text{La}_2\text{O}_3$  doped  $\text{Y}_2\text{O}_3$  found the refractive index to be 1.9699 at 546.1 nm). The two sample technique gives more accurate values and it is possible to measure levels below  $0.05 \text{ cm}^{-1}$ . Figure 5 shows the absorption curve for the current material along with data taken at the beginning of the ONR program and comparative data on  $\text{MgF}_2$ . It is interesting to note that the intrinsic absorption curves for  $\text{MgF}_2$  and  $\text{La}_2\text{O}_3$  - doped  $\text{Y}_2\text{O}_3$  are nearly equivalent, and that the extrinsic data for improved yttria is significantly lower than the state-of-the-art  $\text{MgF}_2$  infrared material.

#### MECHANICAL PROPERTIES

It was previously reported<sup>(2)</sup> that the 4-pt. bend strength could be as low as 117 MPa or as high as 202 MPa depending on microstructure. Within a given

microstructure, the strength variation was typically  $\pm 20\%$ . A nearly constant strength versus temperature (to 1600°C) relation was shown due to the refractoriness and single phase nature of the material. Young's modulus was found to be 164 GPa, and hardness 7.13 GN/m<sup>3/2</sup>.

In the last two years, mechanical property studies have centered on improving fracture toughness. This is expected to have benefits in rain and dust erosion resistance. Table III lists the range of fracture toughness values measured by the indentation technique. The principle variables are grain size and phase content. This shows it is possible to raise the single phase toughness by 47% over the single crystal value by controlling microstructure. It also shows that two phase structures are significantly tougher with a high of 165% improvement.

TABLE III  
FRACTURE TOUGHNESS OF REPRESENTATIVE SAMPLES

PHASES	GRAIN SIZE	$K_{IC}$
	$\mu\text{m}$	$\text{MN m}^{-3/2}$
1	single	0.88
1	135	1.02
1	68	1.23
1	23	1.29
2	8	1.45
2	6	2.34

The presence of 2nd phase lowers optical transmittance due to birefringent scattering. The loss in transmittance depends on second phase particle size and volume percent. Studies are underway to show the interrelationship between transmittance and toughness as shown in figure 6. Some toughening is achieved while retaining good optical properties. Beyond a certain threshold, the transmittance falls precipitously due to the retention of 2nd phase. This particular experiment addressed the concentration of 2nd phase, but not the grain size of that phase. Experiments are continuing in this area.

## CONCLUSIONS

La<sub>2</sub>O<sub>3</sub> - doped Y<sub>2</sub>O<sub>3</sub> shows promise as an infrared material due to its' intrinsic physical properties. Polycrystalline discs and domes have been fabricated by an economical sintering process. Improvements have been made in reducing absorption and scatter, and there is considerable promise for further progress. The fracture toughness has been improved for greater erosion resistance. Trade-off studies have shown that significant toughness improvement can be achieved before seriously degrading optical transmittance.

## ACKNOWLEDGEMENT

We acknowledge the support of the Office of Naval Research under Contract N0014-82-C-0452. We thank the many contributors from GTE, especially R. Thibodeau, M. Jiminian, and G. Baldoni. The optical characterization studies by the Naval Weapons Laboratory under H. Bennett and D. Burge were invaluable.

## REFERENCES

1. "Controlled Transient Solid Second-Phase Sintering of Yttria," W. H. Rhodes J. Am. Cer. Soc. 64,13 (1981).
2. "Transparent Polycrystalline Yttria for IR Applications," W. H. Rhodes, Proceedings of the Sixteenth Symposium on Electromagnetic Windows June 1982.

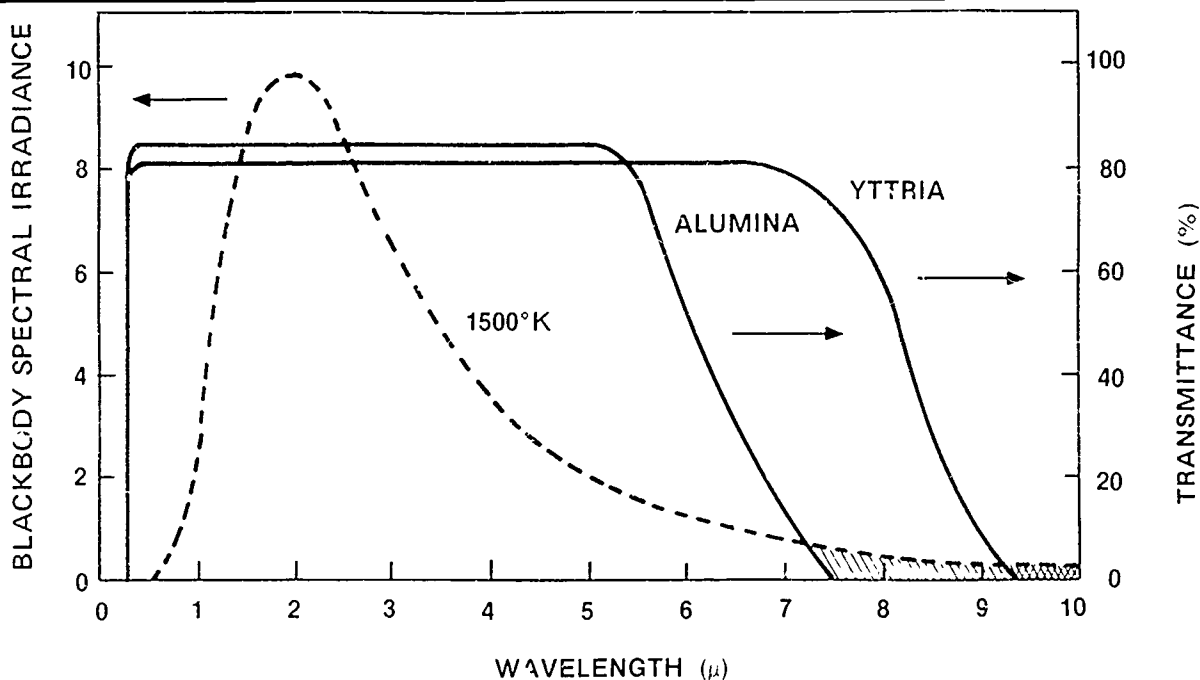


Figure 1. Theoretical Transmittance Curves for Alumina and Yttria Showing The Effect of Thermal Radiation on Emittance

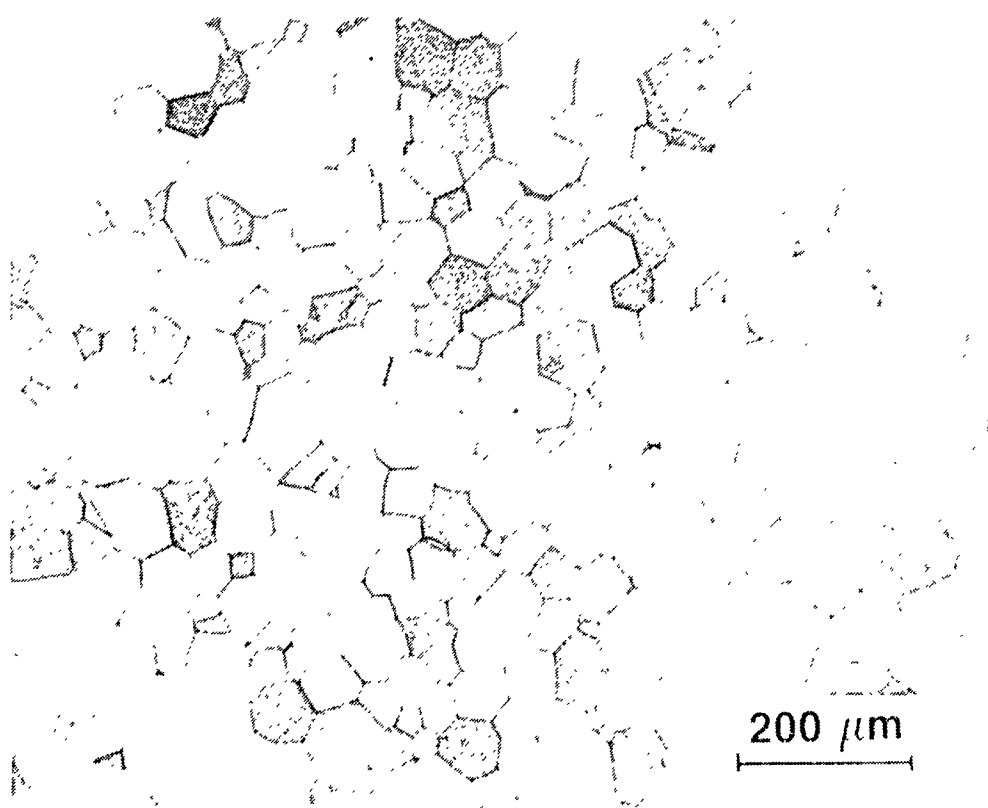


Figure 2. Microstructure of  $\text{La}_2\text{O}_3 - \text{Y}_2\text{O}_3$

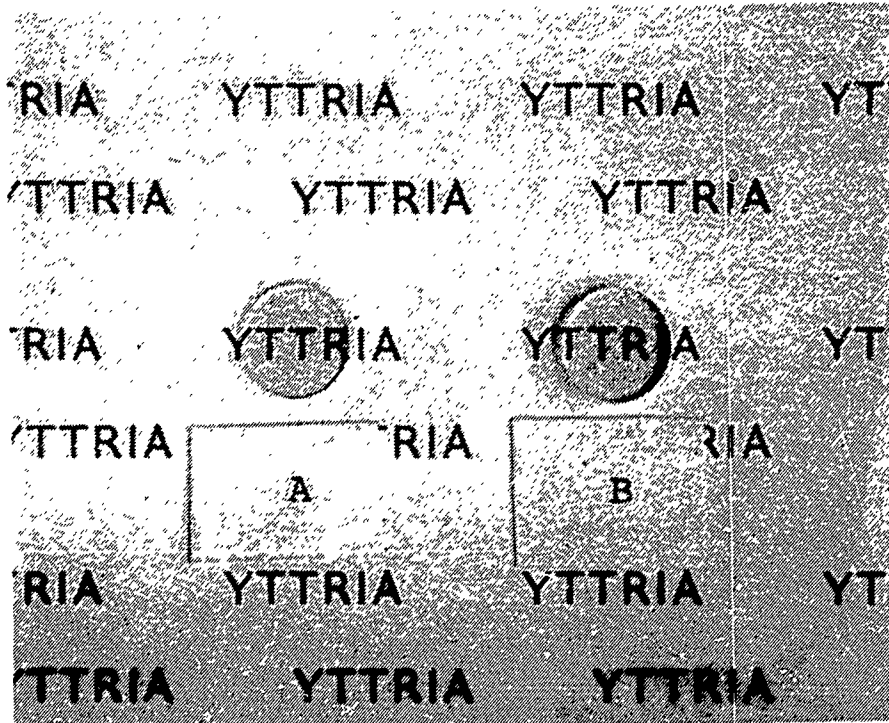


Figure 3. Appearance of (A) 1mm and (B) 2mm Thick Samples.

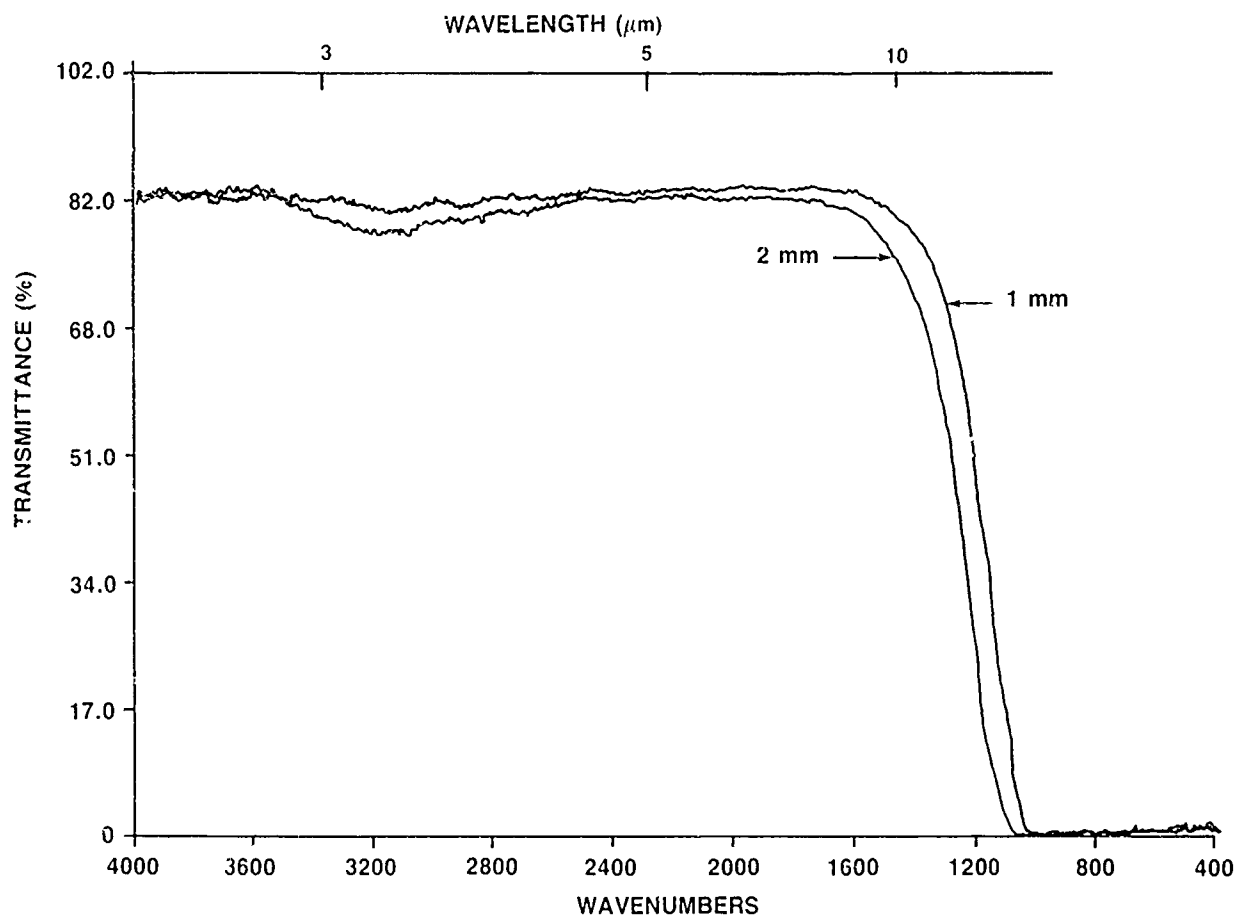


Figure 4. Transmittance of Sintered  $\text{La}_2\text{O}_3 - \text{Y}_2\text{O}_3$

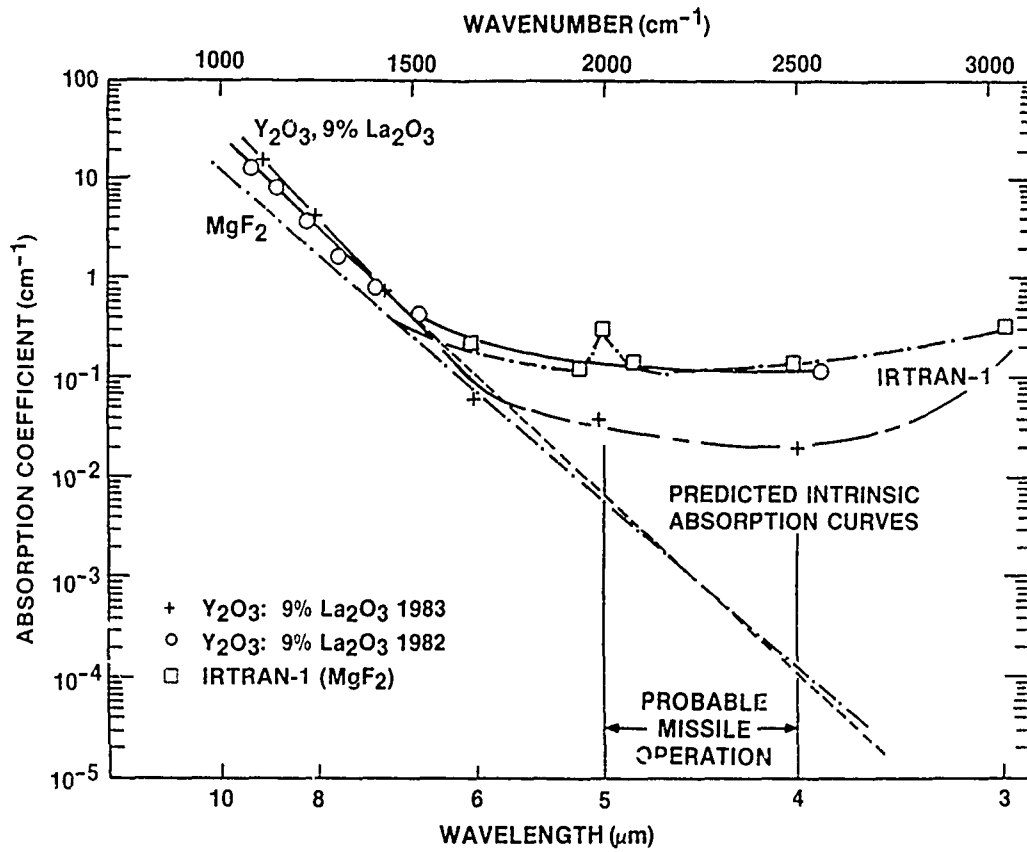


Figure 5. Absorption Coefficients of  $\text{La}_2\text{O}_3 - \text{Y}_2\text{O}_3$  and  $\text{MgF}_2$

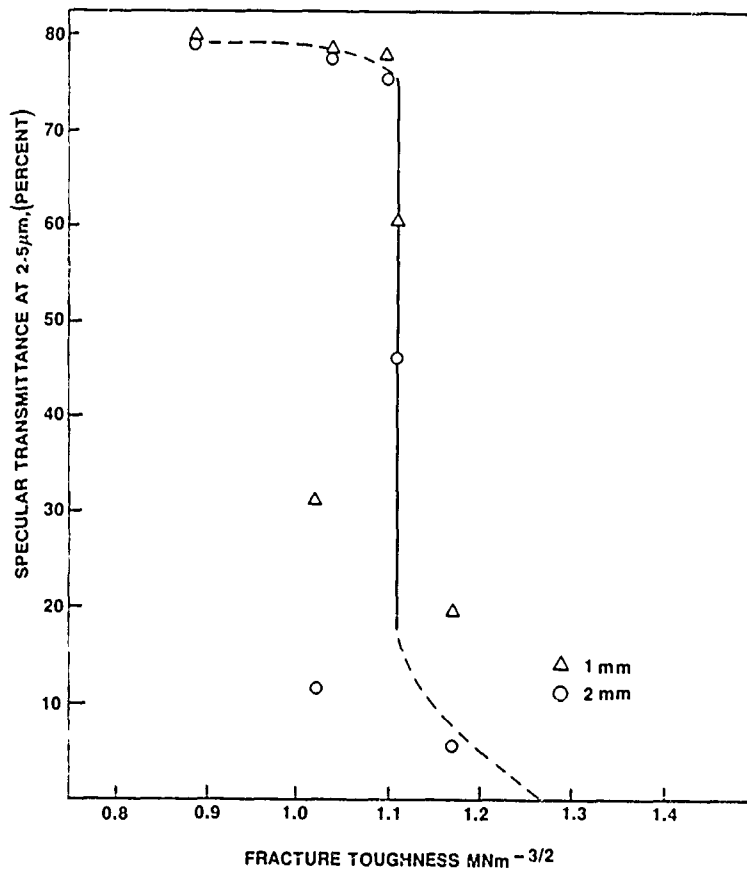


Figure 6. Interrelationship of Transmittance and Toughness

DEVELOPMENT OF A HIGH TEMPERATURE SINGLE  
IMPACT RAIN EROSION TEST CAPABILITY

by

KENNETH N. LETSON and STEVEN P. RISNER

US ARMY MISSILE LABORATORY

US ARMY MISSILE COMMAND

AD-P004 371

ABSTRACT

A single impact rain erosion test capability has been developed to obtain data on fiber loaded Teflon<sup>®</sup> (e.g. Duroid<sup>®</sup>) ablative radome materials at temperatures up to their ablating temperature (~1250 F). This effort was undertaken as a result of the prior inability to (1) obtain experimental data for single water droplet impacts on these materials at temperatures significantly above 400 F at velocities near Mach 5, and (2) identify a solid particle whose behavior is similar to or can be correlated to that of water droplets at all conditions of interest. This test capability allows one to dispense a stream of calibrated discrete water droplets in the path of aerodynamically heated samples on sleds at velocities up to 6000 ft/sec. Also, solid particles placed on nets in the path of other identical samples on the same sled provide craters at the same velocity and temperature for use in the search for a solid whose erosive behavior can be correlated to that of water droplets.

INTRODUCTION

To develop models for predicting the rain erosion behavior of the fiber loaded Teflon ablative radome materials, experimental erosion data are needed with respect to velocity, angle of incidence, temperature, and water droplet size as well as fiber orientation for each ablator. Previous efforts in FY82 to obtain these data were made in Tunnel G at Arnold Engineering Development Center (AEDC) with some success (1). Results from the AEDC tests indicate that mass loss ratio (mass of water impacted - mass of material removed) is independent of water droplet size for the Duroid materials. From these tests and from multiple impact tests on Holloman sleds (2) it was learned, also, that the rain erosion behavior of these ablators is strongly dependent upon material temperature, and that erosion appears to increase approximately one order of magnitude from ambient temperature to the ablating temperature. In the Tunnel G tests, the high acceleration loads of the powder gun launch caused samples that had been heated uniformly before launch to temperature above 400 F to be lost from the sample holder. Thus, to get data on materials heated to temperatures significantly above 400 F, other techniques were required.



Another method for generating erosion data on heated samples is one which involves firing solid particles at stationary samples heated by a radiant or other source. This method lacks validation because a solid particle that behaves like water droplets at all conditions of interest has not been identified. Thus the only currently available potential solutions involve obtaining data on aerodynamically heated samples or validating a solid particle that can be used in the laboratory to simulate water. To do the latter requires doing the former. The use of Holloman sleds to obtain these data was selected as the best means of accomplishing the objectives (3).

#### WATER DROPLET DISPENSER

Design, fabrication, and calibration of the water droplet dispenser were performed by Holloman Test Track personnel to provide the single water droplet environment specified to meet MICOM test objectives. These objectives required that three streams of 3 mm dia water droplets be dispensed at a rate that would provide the maximum number of impacts on the samples. After evaluating several water droplet dispenser designs, a design was selected that involves vibrating streams of water from one-eighth inch dia nozzles to break them into droplets of 3 mm dia at a rate of 100 drops per sec. A single nozzle prototype was first built and tested for feasibility. It was found that a simple one-eighth inch dia tube worked better than a converging nozzle. After the desired performance of the prototype was demonstrated, a three tube design was fabricated and calibrated. Calibration with the Knollenberg Probe indicated that water drop size can be controlled such that 95% or more of the liquid water content is contained in droplets from 2.8 to 3.2 mm dia with 90% confidence. The multiple tube arrangement dispenses water droplets at a controlled rate that can provide the sample nearest the dispenser with up to 12 droplet impacts. For the development test, the dispenser tubes were mounted vertically in a plane 45 deg to the sled rail and spaced so that the distance between centers of craters formed from each stream of droplets was three-eighths in. Figure 1 is a view of the dispenser in operation positioned over the track for the test.

#### TEST MODELS

Evaluation of the MICOM seven tip test vehicle with conical samples (4) revealed the need for a larger sample size to accommodate the five-eighths in. side-to-side motion of the sled. A flat sample shape was selected to simplify evaluation of the craters. A flat sample measuring 5/16" X 2 1/4" X 3 1/4" was designed to be mounted in two faces of a 60 deg wedge (Figure 2). The sample holder overlaps the four edges of the sample and provides exposed sample dimensions of 2" x 3". For the initial test, the test vehicle was oriented (Figure 3) such that the water droplet streams (positioned above the sled rail) would impact four flat samples (two wedges) and one split conical sample. Figure 4 shows samples in the top wedge impacting the streams of water droplets at a velocity of 4200 ft/sec. In addition, seven different types of solid particles were mounted on nets in the path of seven of the eight remaining flat samples. The eighth sample impacted nothing and served as a control.

## PARTICLE NETS

An array of six solid particles of each of the seven particle types was suspended in front of the corresponding sample to be impacted. The seven particle materials tested were nylon, teflon, butyrate, ceramic, acetate, polyethylene, and polypropylene with each particle being 3 mm in diameter. These particles were provided by General Research as part of their participation in the effort to identify a solid particle whose erosive behavior can be correlated to that of water droplets. The materials listed were selected from a screening effort at General Research. The particles were suspended on a net of #6-0 (92 $\mu$ ) surgical silk thread that was attached to a one in. thick circular styrofoam frame as shown in Figure 5. The particles were bonded to the net with a minimal amount of Eastman 910 adhesive. The combined mass of the thread and adhesive contributing to crater damage was less than one percent of the solid particle mass.

## TEST ARRANGEMENT AND CONDITIONS

The propulsion system used for the development test consisted of three NIKE motors as shown in Figure 6. This combination was used to propel the sled to a peak velocity of approximately 4200 ft/sec in ten seconds. The water droplet dispenser and particle nets were positioned over the track where maximum velocity was expected. Aerodynamic heating of the Duroid samples produced surface temperatures of about 1200 F. The calculated temperature gradient in the samples near time of impact with the water droplets and solid particles is shown in Figure 7 (5).

## DEVELOPMENT TEST RESULTS

The development test was highly successful with respect to obtaining good single impact data for both the water droplets and solid particles. Some of the representative craters caused by these impacts are shown in Figure 8. Data obtained from the craters as well as visual inspection revealed that the impact behavior of the solid particles was unlike that of the water droplets for this set of test conditions. This is reflected primarily in the mass loss ratio parameter and/or crater depth of Figure 8. The mean temperature of the material removed for all craters evaluated was approximately 1000 F.

## CONCLUSIONS

The test capability developed in this effort provides an excellent means of obtaining single impact rain erosion data at elevated temperatures and velocities near Mach 5. The water droplet dispenser performed very well and provided the desired environment for single water droplet impacts. As designed, the flat sample provided sufficient impact area for the water droplets and simplified crater evaluation. The sample holders received little or no damage and may be used again. Water droplet data from the development test confirm the AEDC and multiple impact sled results which indicate that rain erosion behavior is strongly dependent on material temperature, and that erosion (mass loss ratio)

appears to increase approximately one order of magnitude from room temperature to the ablating temperature. The particle nets provided a good way to suspend and align the solid particles in the path of the test vehicle. By impacting identical samples, the effects of the solid particles can be directly compared to that of water for each set of test conditions. However, more data are required to determine if there exists a solid particle whose behavior is similar to or can be correlated to that of water droplets for all conditions of interest.

#### REFERENCES

(1) Letson, K. N., "Behavior of Ablative Radome Materials in Single Impact Rain Erosion Tests," Proceedings of the 6th International Conference on Erosion by Liquid and Solid Impact, Cambridge, England, September 1983, pp. 25-1 to 25-6.

(2) Burleson, W. G., Letson, K. N., and Reynolds, R. A., Thermal Performance and Rain Erosion Behavior of Duroid Radome Materials for Conical Models on Mach 5 Sleds, US Army Missile Command, Redstone Arsenal, Alabama 35898, 15 September 1983, Technical Report RL-84-2.

(3) Letson, K. N., and Ormsby, P. A., Rain Erosion Sled Tests of Radome Materials at Mach 5, US Army Missile Command, Redstone Arsenal, Alabama 35898, 26 April 1976, Technical Report RL-76-19.

(4) Letson, K. N., and Ormsby, P. A., "Rain Erosion Testing of Slip Cast Fused Silica at Mach 5," ASME Publication 76-ENAs-6, April 1976.

(5) Norton, B. A., Calculated Thermal Effects on Reinforced Teflon Radome Samples for Wedges on a Sled at Mach 3.8, US Army Missile Command, Redstone Arsenal, AL 35898, November 1983, Special Report RL-84-1.

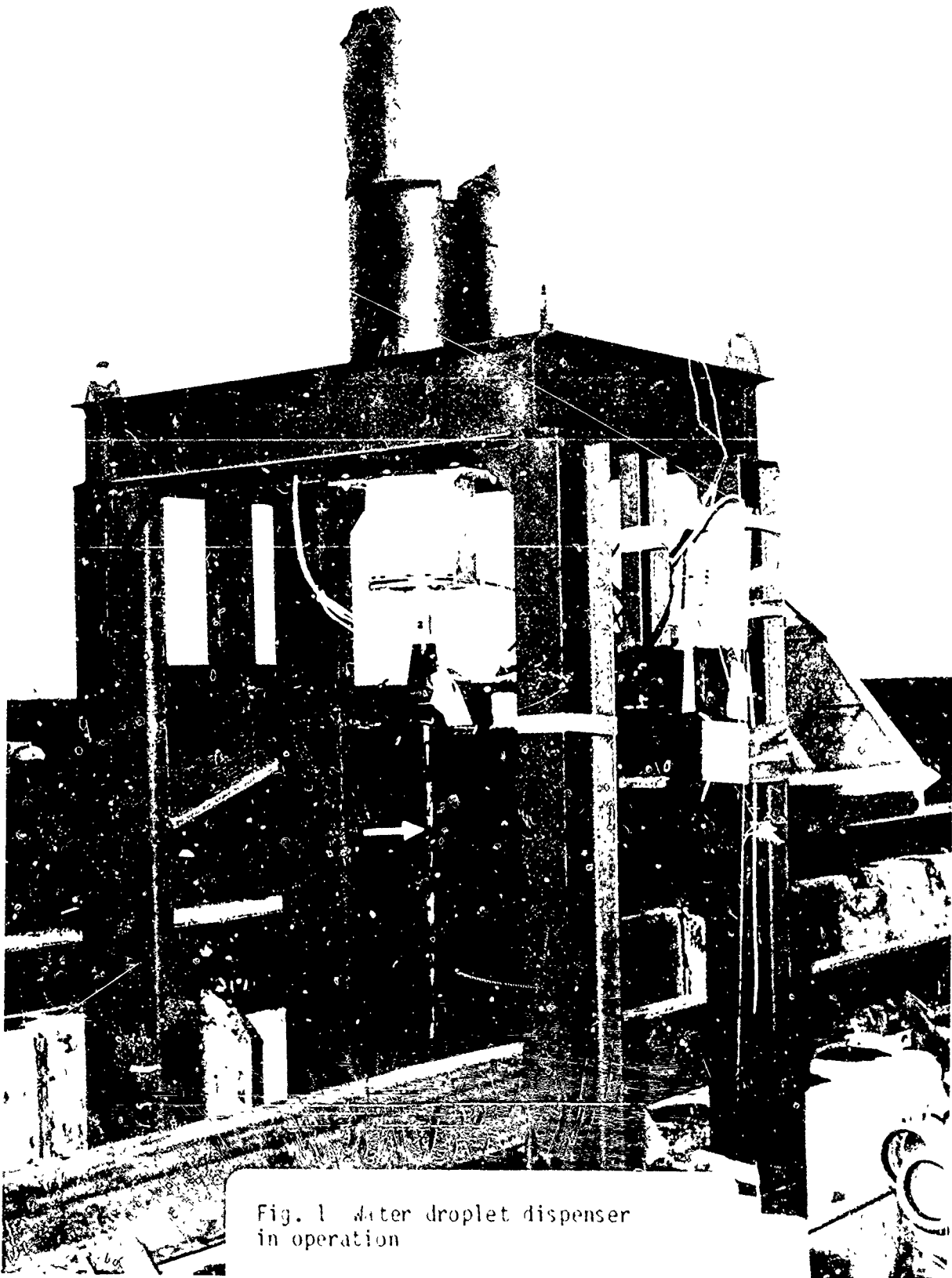


Fig. 1 water droplet dispenser  
in operation

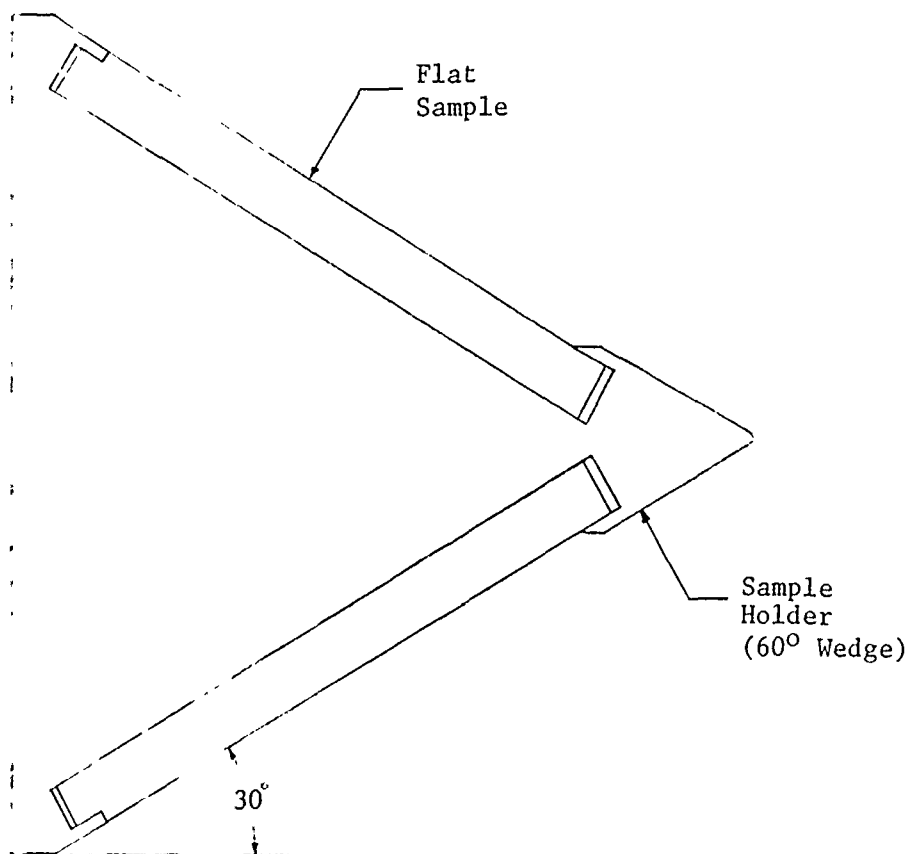


Fig. 2 Side view of sample in holder



Fig. 3 Close up view of sled  
and sample assemblies



Fig. 4 Water droplet impacts at a sled velocity of 4200 feet per second

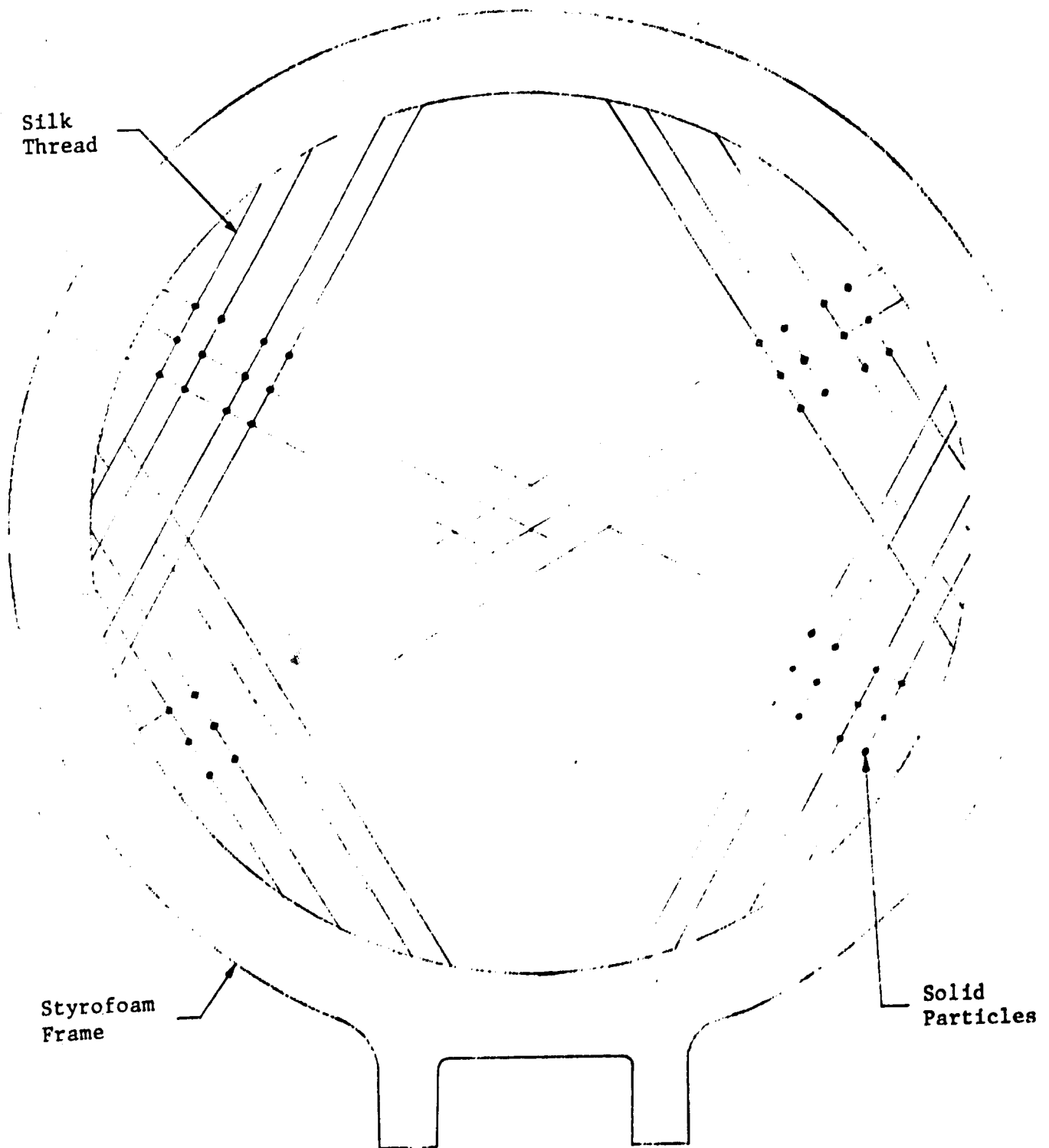


Fig. 5 Particle net assembly



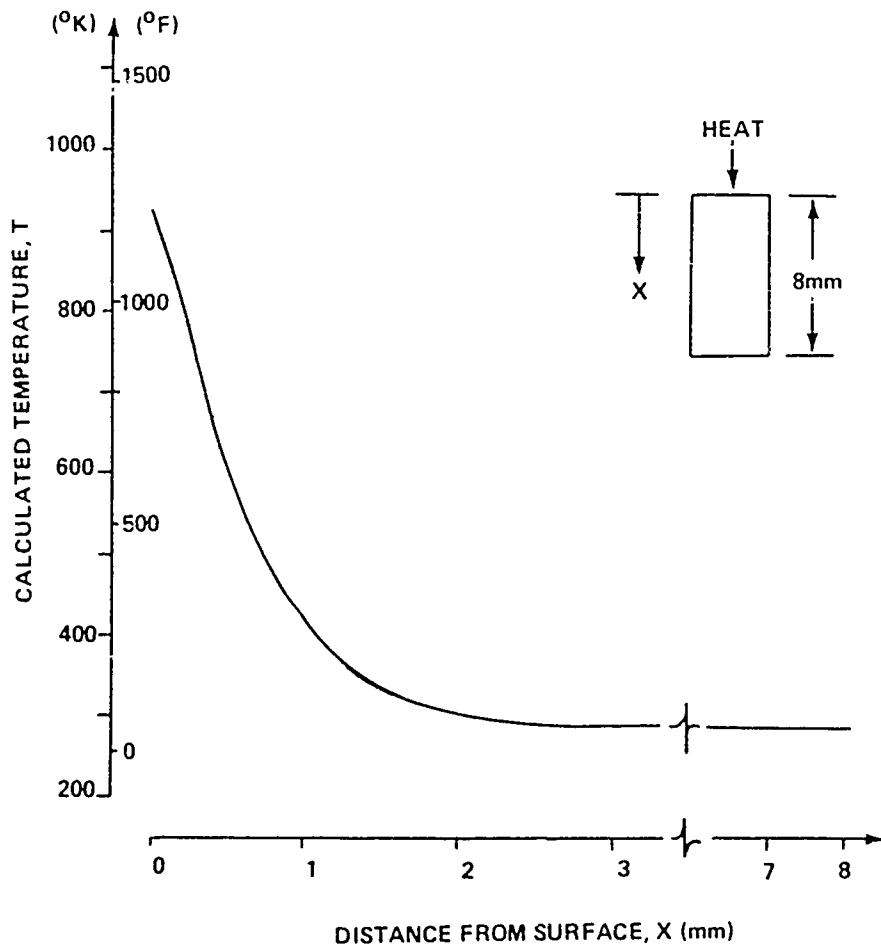


Fig. 6 Temperature gradient of Duroid samples at time of water droplet and solid particle impacts

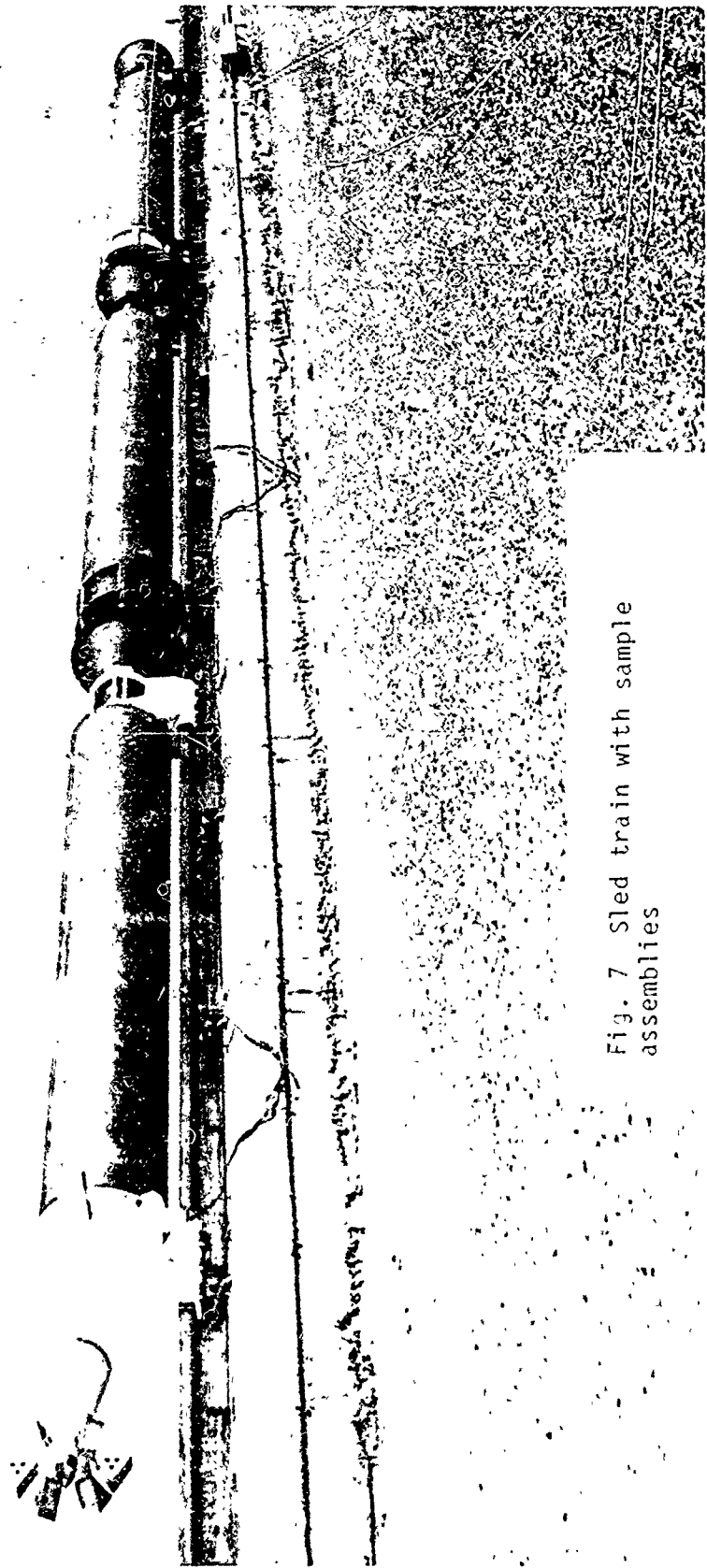


Fig. 7 Sled train with sample assemblies

Fig. 8 MICOM ABLATIVE RADOME MATERIAL SINGLE IMPACT RESULTS

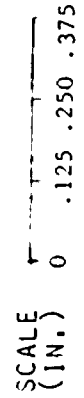
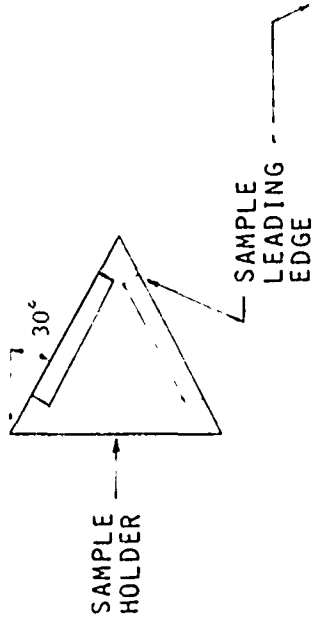
CRATERS CAUSED BY 3MM FREE FALLING WATER DROPLETS AND

SUSPENDED SOLID PARTICLES AT A SLED VELOCITY OF 4200 FEET PER SECOND.

PARTICLE IMPACTED:	POLYETHYLENE	WATER	NYLON
MAX. CRATER DEPTH (IN.):	.018	.020	.027
MASS LOSS RATIO (MASS REMOVED/MASS IMPACTED)	1.6	2.0	1.4

MATERIAL IMPACTED (ALL): RT/DUROID 5650M (PRESENT PII RADOME MATERIAL)	BUTYRATE	TEFLON	POLYPROPYLENE
	.022	.050	.023
	1.5	2.1	1.7



# INFRARED MATERIAL OPTICAL DAMAGE BY RAIN

Alain DEOM, George GAUFFRE, Daniel L. BALAGEAS  
Office National d'Etudes et de Recherches Aérospatiales (ONERA)  
Châtillon (France)

**AD-P004 372**

## SUMMARY

A comprehensive study of the optical damage and erosion of various infrared materials is conducted using a rotating arm. The optical damage is characterized by the evolution of the sample modulation transfer function (MTF). The velocity dependence for MTF deterioration is similar to that of the mass loss: occurrence time of damages is inversely proportional to a high-exponent power law of the velocity. For some materials like magnesium fluoride ( $MgF_2$ ), the optical damage occurs in synchronism with the erosion. Inversely, for others like zinc selenide ( $ZnSe$ ), optical damage occurs very early before the beginning of the erosion. Consequently, the screening of candidate materials for iridome must be based on transmission tests, or better on MFT tests, rather than on erosion tests.

## INTRODUCTION

The possible rain damage of infrared materials used for irdomes necessitates their evaluation by rain tests. Many characterizations of such materials may be found in the literature. They are performed by measuring the mass loss of the materials, without determination of their optical damages. As early as 1972, Hoff and Rieger [1] emphasized the interest of optical measurements. They performed transmission measurements, mainly in the visible and near infrared regions, up to  $5 \mu m$ . More recently, Corney and Pippett [2] presented transmission measurements at  $10 \mu m$  concerning germanium and zinc sulphide, materials usable in the 8-14  $\mu m$  range. For evaluating the optical damage of materials exposed to rain, ONERA chose to measure the modulation transfer function (MTF) rather than the transmittance. A setup was specially developed, which permits MTF measurements at various spectral ranges and spatial frequencies. This setup is used on the very place where rain exposure is performed.

Comprehensive study of the resistance of the main infrared materials is in progress. Here are presented some significant results obtained with magnesium fluoride ( $MgF_2$ ) and zinc selenide ( $ZnSe$ ) which demonstrate the interest of the optical evaluation technique used.

## RAIN SIMULATION TEST FACILITY

The rain exposure was achieved using the Saab-Scania rotating arm in Linköping (Sweden). A description of this facility may be found in references [3,4]. The sample holder technology used was developed previously for the erosion study of slip-cast fused silica [4]. The samples are cylinders 16 mm dia. and 6 to 10 mm thick. Impact angle may vary from  $90^\circ$  (normal impact) to  $30^\circ$ . Only normal impact data are presented here. The rain

conditions in the Saab facility are the following:

- drop diameter: 1.2, 1.6 and 2 mm;
- water concentration ranging from 0.08 to 1.2 g m<sup>-3</sup>, depending on the number of injectors (1 to 6) and on the drop diameter. These concentrations are relatively low. This is an advantage for the study of poor resistant materials like infrared materials. In effect, stronger concentrations may lead to very short exposure times conducting to a poor precision.

Like for slip-cast fused silica [5], it was verified that the damages are proportionnal to the water concentration. Consequently all the results are presented for a normalized time  $\bar{t}$  which corresponds to a reference water concentration  $C_0 = 1 \text{ g m}^{-3}$ . This normalized time is given by the relation:  
$$\bar{t} = t C / C_0.$$

After each rain exposure, the sample is separated from the holder, weighed and optically qualified with the optical setup.

#### OPTICAL MEASUREMENT SETUP

A schematic description of the optical measurement setup is given in Fig. 1. The infrared source is made of a SiC rod heated at 1000 K. A ZnSe lens  $L_1$  gives the magnified image of the source in the plane of the tested sample E. On the optical path, a rotating disk M holds eight series of slits of spatial periods ranging from 0.2 to 3 mm (spatial frequencies from 0.33 to 5 mm<sup>-1</sup>). The lens  $L_2$  gives the image ( $\Gamma = 1$ ) of the pattern onto the HgCdTe 50  $\mu\text{m}$  x 50  $\mu\text{m}$  square detector which is cooled by liquid nitrogen. A series of filters permits to vary the spectral range: 2-12  $\mu\text{m}$ , 2-3  $\mu\text{m}$ , 3.5-6  $\mu\text{m}$  and 8-12  $\mu\text{m}$ . The MTF is given by the evolution with the spatial frequency of the ratio of the signal amplitude delivered by the detector for a given spatial frequency to the amplitude which would be obtained at a zero spatial frequency. The optical damage of the sample is characterized by a variation of the sample MTF. The ratio of the MTF after exposure to the rain to the initial MTF measures the optical contrast loss. The measurement setup is controlled by a microcomputer allowing immediate analysis of the damages and consequently the definition of the next exposure time.

#### MATERIAL DAMAGES

The mass loss and MTF evolutions are observed all along the cumulative exposure.

##### Material erosion

The erosion study is classical. The mass loss is measured as a function of the rain exposure time (see Fig. 2a). The extrapolation for a zero mass loss of the linear part of the curves permits to define the incubation time  $\bar{t}_1$ , characterizing, with the erosion rate, the intrinsic erosion resistance of the material. The dependence of incubation time on the impact velocity for MgF<sub>2</sub> is given in Fig. 2. These results are in very good agreement with those

obtained by Hoof and Rieger [1]. A power law of the velocity, with a negative high exponent is found:  $\bar{t}_i \sim V^{-n}$ , with  $n = 12.8$ . This exponent is always high and much variable from one infrared material to another.

### Optical damages

For a sample of a given material, the experimental conditions being fixed, the evolution of the MTF may be studied with increasing exposure time (Fig. 3a). By comparing this MTF to the initial MTF, the optical contrast loss characterizing the optical damage may be deduced (Fig. 3b).

By adding the results obtained with various samples of a same material tested in the same conditions, but with different velocities, it is possible to study the dependence of optical damages on velocity (Fig. 4). Let us consider two critical levels of contrast loss: 10 % and 50 %. It is possible to relate them to normalized times  $\bar{t}_{0.1}$  and  $\bar{t}_{0.5}$ , and to study the variations of these times with the impact velocity (Fig. 4b). A power law of the velocity is also obtained:  $\bar{t}_{0.1} \sim \bar{t}_{0.5} \sim V^{-n}$ . The exponent  $n$  is dependent on the nature of the material. For  $\text{MgF}_2$   $n = 12.8$  and for  $\text{ZnSe}$   $n = 10$ . For other materials lower values are obtained.

The MTF is dependent on the spectral range. In particular, it may be noted that the damages in the 8-12  $\mu\text{m}$  are generally weaker than for shorter spectral lengths, a fact which was foreseeable. The influence of the spatial frequency is variable with the tested materials and the advancement of the damages. It can be observed in Fig. 4b that the optical contrast loss is more severe for the higher spatial frequencies when the exposure times become important. The influence of drop diameter is more complex and also dependent on the material. Generally this influence is rather limited. It causes variations by a factor  $\pm 2$  upon the characteristic times.

The differences from one material to another, quantitatively noted in the optical damages, are obvious when observing the impacted surfaces. For  $\text{MgF}_2$  (Fig. 5a) linear cracks appear concerning depths of several millimeters. These cracks are the cause of the mass loss and optical damages. For  $\text{ZnSe}$ , before the occurrence of the first mass loss, circular superficial microcracks are noted. Each individual impact may be located. An in-depth modification of the material, revealed by an opalescence, may be detected by a visual examination. This modification causes a decrease of the MTF.

### Simultaneous analysis of the two types of damages

These different behaviors are well observed when a simultaneous analysis of the mass loss and optical damages is performed. In the Fig. 6, the optical time  $\bar{t}_{0.1}$  is plotted versus the incubation time  $\bar{t}_i$ . It appears that, for  $\text{MgF}_2$  the two types of damages are synchronous, and that for  $\text{ZnSe}$  the optical damages precede the mass loss. In the first case the optical damages are due to the deterioration of the surface, in the second to an in-depth structural modification.

In other respects the Fig. 6 reveals an interesting phenomenon: for a

given material, the dependence of the two types of damages on velocity is the same:  $\bar{t}_i \sim \bar{t}_0, 1 \sim \bar{t}_0, 5 \sim V^{-n}$ . This is shown by the fact, verified by the other infrared tested materials, that the curves are parallel to the first bisectrix.

## CONCLUSION

The few results presented here concerning  $MgF_2$  and  $ZnSe$  are typical of the whole data obtained with all infrared tested materials. First, they show the necessity of measuring the evolution of the optical properties preferentially to a simple mass loss measurement. Secondly, they demonstrate the interest of a MTF measurement as compared to a transmittance measurement (influence of the spatial frequency).

Concerning the behavior of infrared materials, the following points have to be noted: i) for a given material, the ruin phenomena (erosion, optical damages) are highly dependent on velocity, obeying the same power law with the same high negative exponent; ii) the influence of drop diameter is complex and weak for the explored range (1.2 to 2 millimeter); iii) the shorter the spectral length and the higher the spatial frequency, the more severe the optical damages.

The physical nature of the phenomena responsible of the optical damages may vary from one material to another, due to either a superficial deterioration, or an in-depth modification. Consequently, there is synchronism or not between the two types of damages.

## Acknowledgment

The support of this research under DRET grant is gratefully acknowledged.

## References

- [1] G. HOFF and H. RIEGER, "Rain erosion of infrared transmitting materials", Proc. of 11th Symposium on Electromagnetic Windows, Atlanta (Georgia), 1972.
- [2] N.S. CORNEY and J.S. PIPPETT, "The rain erosion resistance of some radome and irdome materials", Proc. 6th In. Conf. on Erosion by Liquid and Solid Impact, Cambridge (UK), 1983.
- [3] S. ESKILSSON, "Design rules for neoprene coatings", Proc. 2nd Int. Conf. on Rain Erosion and Allied Phenomena, Meersburg (RFA), 1967, edit. RAÉ, Farnborough (UK).
- [4] D.L. BALAGEAS, "L'érosion à la pluie de la silice vitreuse frittée: résistance intrinsèque du matériau; revêtements de protection", Proc. 3rd Int. Conf. on Electromagnetic Windows, Paris, 1975.
- [5] D.L. BALAGEAS and A. HIVERT, "Rain erosion: a serious problem for slip-cast fused silica radomes", Proc. 13th Symposium on Electromagnetic Windows, Atlanta (Georgia), 1976.

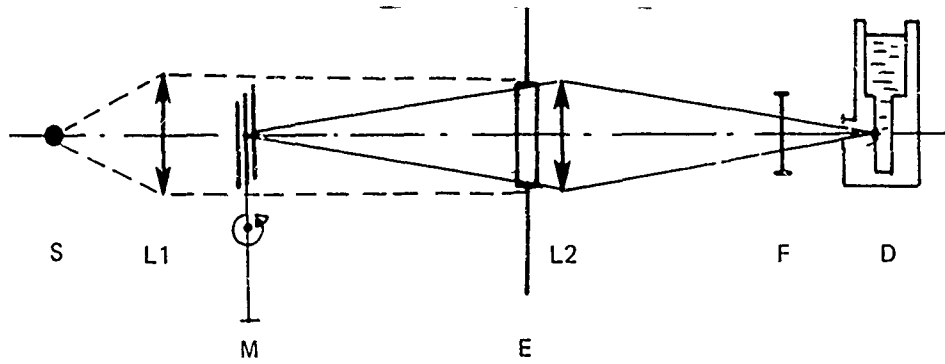
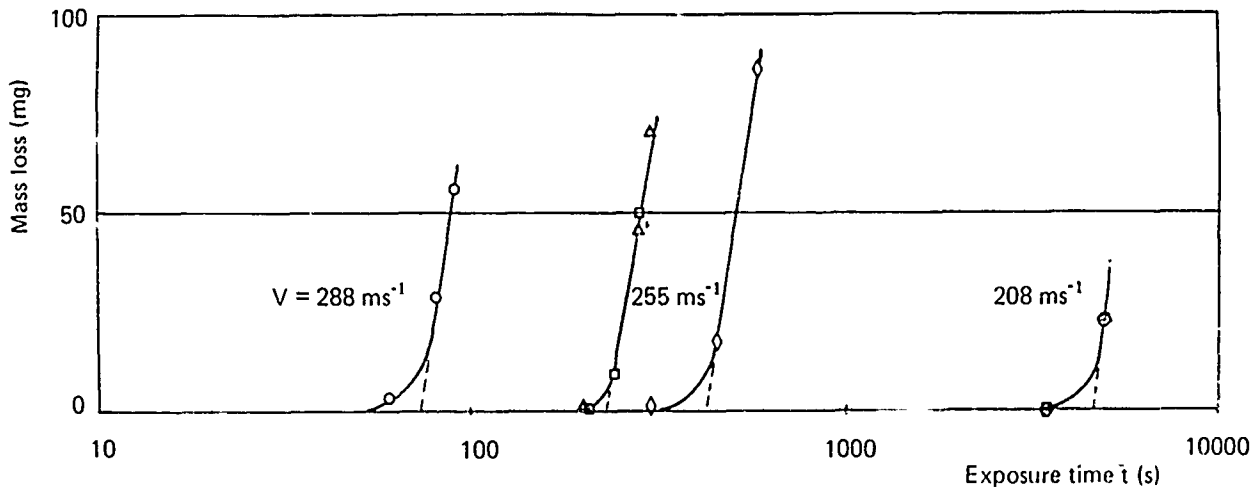


Fig. 1 – Schematic view of the measurement setup for modulation transfer function.



2a

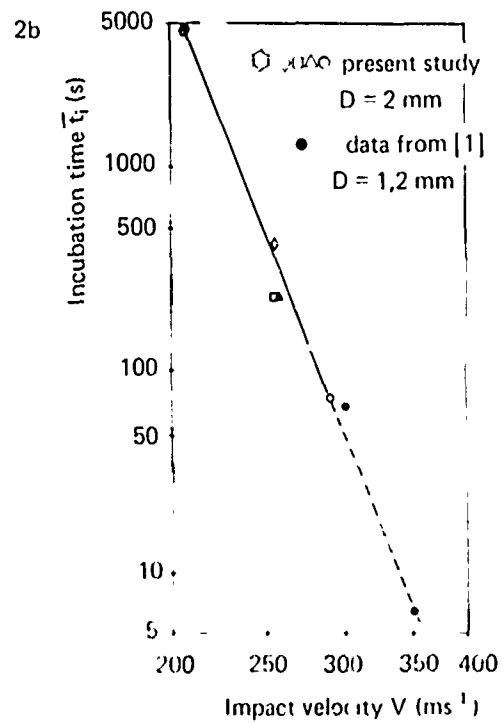
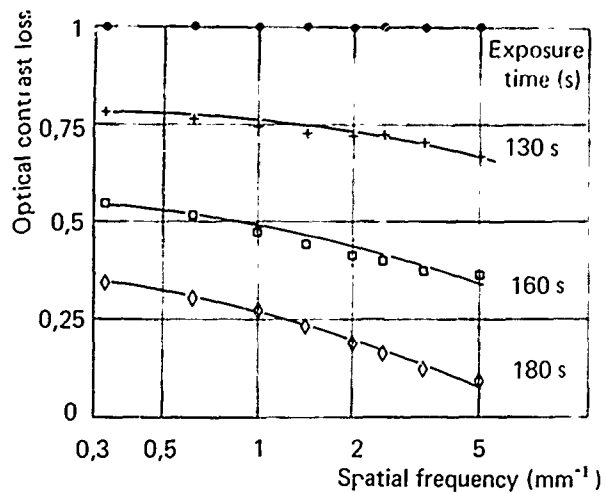
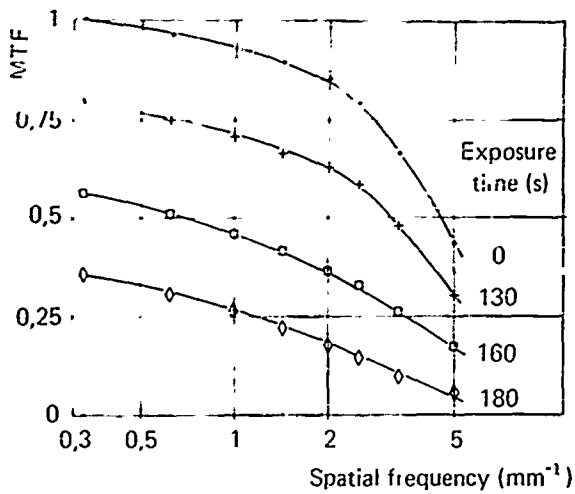


Fig. 2 – Erosion of  $MgF_2$  : impact velocity dependence.

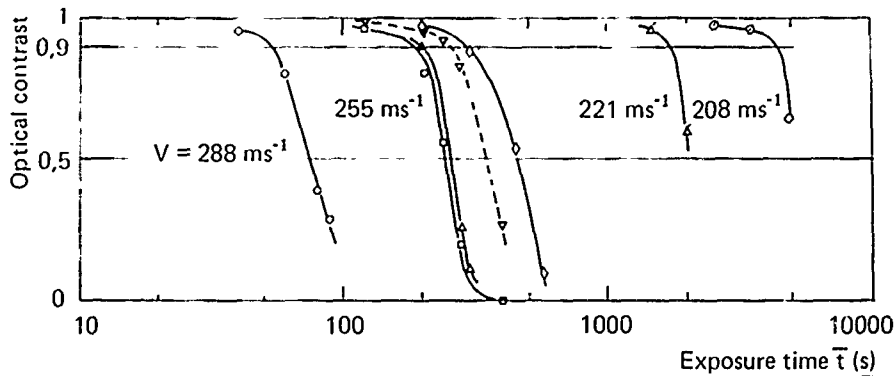
- a) Mass loss curves
- b) Incubation times.





3a Fig. 3 – Evolution with rain exposure time of the optical properties of a sample of  $MgF_2$  : a) Evolution of the MTF; b) Evolution of the optical contrast loss.

3b



4a

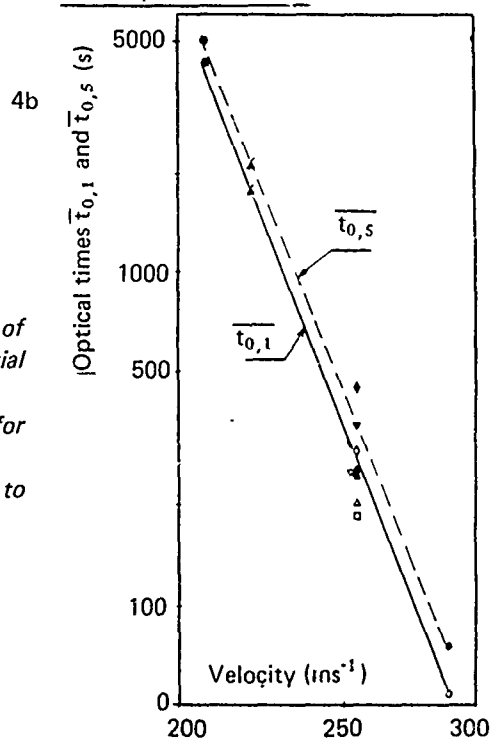


Fig. 4 – Influence of the impact velocity on the evolution of optical properties of  $MgF_2$  (spectral range : 2-6  $\mu m$  ; spatial frequency :  $0.33 mm^{-1}$  ; drop diameter : 2 mm) : a) Evolution of the optical contrast with the exposure time for various velocities. b) Evolution with impact velocity of exposure times related to optical contrast losses of 10 % and 50 %.

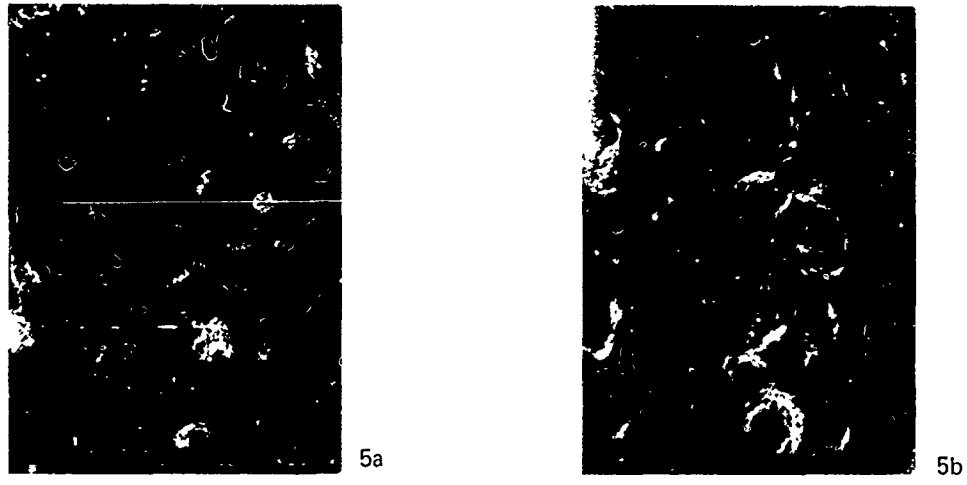


Fig. 5 – Compared physical aspect of rain exposed surfaces of  $MgF_2$  and  $ZnSe$  (drop diameter:  $2\text{ mm}$ , water concentration:  $0,2\text{ g m}^{-3}$ ; magnification:  $\Gamma = 4$ ):  
 a)  $MgF_2$  exposed 2340 s at a velocity of  $235\text{ m s}^{-1}$   
 b)  $ZnSe$  exposed 20 s at a velocity of  $207\text{ m s}^{-1}$ .

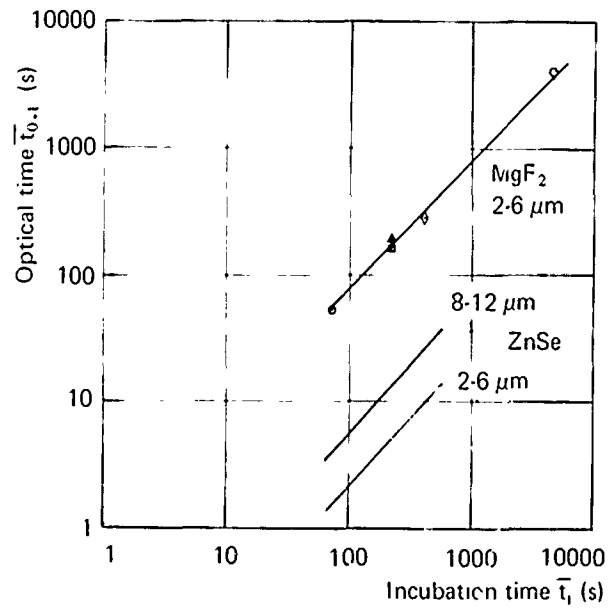


Fig. 6 – Comparison of the characteristic optical time  $\bar{t}_{0,1}$  and the incubation time  $\bar{t}_1$  for the materials  $MgF_2$  and  $ZnSe$ .

RAIN EROSION TESTS OF FULL-SIZE  
SLIP CAST FUSED SILICA RADOMES AT M3.5 AND M4.8

By

R. K. Frazer

Applied Physics Laboratory  
Johns Hopkins University  
Laurel, Maryland

-- ABSTRACT --

During the period 27 September to 12 October 1983 four rocket sled tests were conducted at the Holloman AFB Test Track. The purpose of the test series was to expose radome samples made of slip cast fused silica (SCFS) to a controlled artificial rain field at velocities between M3.5 and M5.0 and observe the resultant erosion patterns. Comparison of boresight errors made before and after the tests were to be correlated to predictive theories. The first test employed a steel test sample and served to verify the rocket motor and sled hardware structural performance. (A similar check-out run conducted in August 1983 resulted in a structural failure.) The September 27th test was completed successfully after achieving a peak velocity of about 3380 fps (M3.45). The artificial rain field was not used during this test. The three subsequent tests exposed separate SCFS samples to 1,000 feet, 4,000 feet and 6,000 feet of artificial rain at peak velocities of 3870, 3780, and 5350 ft/s, respectively. All samples showed measurable erosion but only the first two samples were successfully recovered. The last test item, after enduring the entire 6,000 feet of rain and an additional 12,000 feet of coast-out, failed catastrophically. A suitable explanation for the failure has not yet been made.

Erosion data from the test samples (including the last test sample after partial reconstruction) is discussed in the full body of this paper. The erosion data are compared with theories developed to predict wall thickness change vs. axial station along the radome. Boresight error measurements made before and after the tests that show the effects of the observed erosion will be presented. Correlation of the observed boresight errors with boresight errors calculated by a ray-trace model using an average observed material loss will be discussed.

PREVIOUS PAGE  
IS BLANK



SEVENTEENTH SYMPOSIUM ON ELECTROMAGNETIC WINDOWS

(ABSTRACT) -UNCLASSIFIED

"DUAL MODE COOLED METALLIC ANTENNA WINDOW DESIGN CONCEPT"

The design of a dual mode cooled metallic radar and infrared seeker radome/window for endoatmospheric interceptors represents a unique solution to the many technical problems which must be resolved for this high performance homing vehicle. The severe environmental conditions which must be accommodated include maneuvering hypersonic velocity flight in the mach 12 to 20 range, nuclear event exposure, dust and weather impacts and the plasma field generated over the radome/window body. In addition, the homing accuracies required for a non-nuclear kill vehicle for this range of interceptor may very well dictate the requirement for a dual mode, IR-discriminate early homing system combined with a terminal radar homing system. This paper reviews the critical design parameters for a synergistic cooled metallic radome/window and presents a conceptual design solution for an all-endo class of homing interceptor.

John W. Hidahl  
Thermal Management Projects  
Systems Engineering  
Aerojet TechSystems Company  
P.O. Box 13222  
Sacramento, California 95813  
(916) 355-6724

E. L. Kessler  
Program Manager  
Thermal Protection Systems  
Aerojet TechSystems Company  
Sacramento, California 95813  
(916) 355-2222

PREVIOUS PAGE  
IS BLANK



Un radome pour les systèmes de radars SSR pour le contrôle de la navigation aérienne

Rédigé par le personnel de l'Electronic Space Systems Corporation (ESSCO), Old Powder Mill Road, Concord, Massachusetts, États-Unis.

Une nouvelle génération de systèmes d'interrogation discrets à mono-impulsions a été développée pour des applications de contrôle de la navigation aérienne présentant des défis importants à la conception et aux performances globales du système. Le fonctionnement fiable du système d'antenne est essentiel étant donnée la congestion croissante de la navigation aérienne aujourd'hui. Un composant important du système global est un radome protégeant l'antenne de l'environnement et permettant des performances électro-magnétiques homogènes et fiables. Les différents types de radomes employés au fil des ans pour protéger les antennes sont discutés et évalués en fonction de l'application du radar au contrôle de la navigation aérienne. Le radome sandwich a été choisi comme la meilleure option, et une analyse détaillée de sa conception est présentée. Elle prend en considération les caractéristiques vitales de capacité de transmission, d'erreur de portée optique et de perturbations du lobe secondaire. Ces caractéristiques doivent être pratiquement négligeables pour permettre une performance précise et fiable de l'antenne de radar, comme illustré, par exemple, par les transmissions de radome égales ou supérieures à 97%. Les résultats de l'analyse et les données expérimentales montrent que des transmissions dépassant 97% sont possibles avec des effets minimums sur les niveaux des lobes secondaires des antennes et la précision de la poursuite.

"A Radome For Air Traffic Control SSR Radar Systems"

Written By: The Staffs of:

Electronic Space Systems Corporation  
(ESSCO)  
Old Powder Mill Road  
Concord, Massachusetts, USA 01742

ESSCO Collins Limited  
Kilkishen, Co. Clare, Ireland

A new generation of monopulse and discrete interrogation systems has evolved for air traffic control applications that presents significant challenges to total system design and performance. Reliable operation of the antenna system is essential in today's ever increasing air traffic congestion. An important component of the total system is a radome to protect the antenna from the environment and to enable consistent, reliable electromagnetic performance. The various types of radomes that have been employed over the years to protect antennas are discussed and evaluated relative to the air traffic control radar application. The sandwich radome is selected as the best option and a detailed design analysis is presented which considers the vital characteristics of transmissivity, boresight error, and sidelobe perturbations. These characteristics must be practically negligible for accurate and dependable radar antenna performance as illustrated, for example, by the requirement for radome transmissivities of 97% or greater. Results of the analysis and experimental data show that transmissivity in excess of 97% is achievable along with minimal effects to both antenna sidelobe levels and tracking accuracy.

PREVIOUS PAGE  
IS BLANK



## I.

### INTRODUCTION

Many types of antennas have been covered by various radome designs over the past 30 years. The optimum radome extends operational capability to all environmental conditions, while providing minimal electromagnetic degradation. The critical performance criteria for each application varies considerably, requiring a radome design that is appropriate for each particular antenna system. No single radome design can fulfill all the requirements for every antenna type. The system designer must evaluate critical requirements of the antenna and select a radome design that closely matches those requirements. The modern secondary surveillance radar (SSR) antenna operates over a narrow frequency band, must have low sidelobe levels and must track accurately. The optimum radome to protect an SSR antenna must, therefore, have high transmissivity, 97% or greater, contribute very little to sidelobe levels and produce negligible boresight shift.

Consideration of various radome designs for SSR applications include several alternatives. The metal space frame radome is an excellent broad band design that is utilized for many applications ranging from less than 1 GHz to over 300 GHz and exhibits about .5 dB frame blockage over the broad frequency spectrum. The dielectric space frame radome performs best under 1 GHz where it exhibits less than .5 dB frame blockage and scatters moderately. The air supported radome is a reasonable match to the SSR application, but is dependent on a source of electrical power for inflation support. The solid laminate radome is electromagnetically sufficient but can only be produced in relatively small, discrete sizes because of structural loading considerations. A properly designed sandwich radome will exhibit high transmissivity over a selected frequency band and a low scatter characteristic. It can be constructed of individual panels over a range of sizes to meet structural requirements. It is the best choice for the modern SSR air traffic control antenna application.

The following analysis covers the important electromagnetic characteristics of transmissivity, boresight error and sidelobe perturbations for the ESSCO sandwich radome design. Other considerations such as noise temperature and performance under various forms of precipitation have been addressed and found to have minimal impact on antenna operation.

## II.

### DESIGN CONSIDERATIONS

Sandwich radomes are generally classified as type "A", "B", and "C". The "A" sandwich radome consists of two high-density, high-strength thin skins separated by a low-density, low-strength core. The distance between skins is normally a quarter-wavelength or odd multiples thereof in order to achieve the phase reversal necessary for cancellation of any skin reflections, and thereby minimize the power-reflection coefficient. The harmonic passbands then resulting can be useful in multiband applications. Reflection from a well designed sandwich wall, however, does not vary critically with the core thickness. Thus the production tolerance levels are practical and the radome can exhibit excellent performance over reasonable frequency passbands.

It should be noted that all sandwich radome constructions can be considered as special versions of the more general case of multi-layer laminate wall configurations. In the analysis to follow, formulations are given for the general case with which the electromagnetic performance requirements of all types of sandwich designs can be predicted. Although ESSCO has designed all types of sandwich radomes, by far the most popular is the ESSCO "A" type sandwich construction. This approach is chosen and analyzed because of the following factors:

1. The high-density outer skins provide a protective surface.
2. The strength to weight ratio is desirable.
3. The manufacturing tolerances on both laminate skin

- and core thicknesses are moderate.
4. The electromagnetic performance exhibits smaller losses over prescribed frequency passbands.
5. It is cost effective.

The design of the sandwich radome represents a balanced engineering approach derived from consideration of the structural and electromagnetic requirements of the application. Ideally, the radome would withstand the most severe environmental conditions encountered at the site and be essentially electromagnetically transparent at the specified operating frequency band so as to allow near perfect utilization of the enclosed antenna system. These capabilities are the goals of the design.

From a structural point of view, wind loading is the dominant criteria used to calculate shell or membrane stresses. These resultant stresses, in combination with ice and snow loads, are considered when calculating buckling pressure. For these determinations, the radome is modeled as a continuous, homogeneous shell with an effective modulus and thickness defined by the actual laminate and core used for the sandwich. The objectives are to obtain significant factors of safety for membrane tensile strength and stability, given the loading criteria.

In reality, the radome is not a continuous shell but is constructed from individual panels. The goal of the designer is to determine a method of panel interconnection that will transfer loads across the panel-to-panel interface so that continuous shell integrity is preserved. Herein lies one of the major compromises of sandwich radome design. The interconnection must not only provide a direct and stiff load path but must also maximize electromagnetic transmission efficiency. In addition, the interconnection technique must be configured so that it can be efficiently implemented during panel fabrication and utilized without complications during radome assembly.

## III.

### GENERAL ELECTROMAGNETIC ANALYSIS

The electromagnetic design of a sandwich radome is dependent on the size and configuration of the enclosed antenna system and the operating frequency. The physical size of the radome will determine the minimum thickness which can be used for the radome wall to insure adequate structural strength. Sandwich radomes may be designed with various core and skin thicknesses so that structural requirements are met.

The basic electromagnetic characteristics of the sandwich radome are: transmissivity, boresight error and antenna sidelobe perturbations. Methods which are used to compute these characteristics are presented along with the results for a typical radome/SSR antenna configuration.

### 1) TRANSMISSIVITY

The transmissivity through the radome depends not only upon the construction of the radome wall but also upon the antenna look angle, the field distribution over the antenna aperture, the location of the antenna inside the radome and the radome/antenna size ratio. Using ray-tracing methods, the transmissivity of the radome can be determined by summing the losses from all rays which have different weight functions and look angles. The basic method for computing the transmissivity of the radome is as follows:

$$L_w = 10 \log_{10} |T_d|^2$$

$$T_d = \frac{\sum_{n=1}^N f_n T_n}{\sum_{n=1}^N f_n}$$

where  $L_w$  = transmission loss of the antenna due to the radome (in dB)

- $T_a$  = field transmission coefficient of the antenna due to the radome
- $N$  = number of the rays combined as the antenna radiated field
- $f_n$  = weighting function for the  $n^{\text{th}}$  ray

Typical weighting function  $f_n$  for the  $n^{\text{th}}$  ray can be written as:

$$f_n = 1 - a(x_n - D_x)^2/r^2$$

- $a$  = illumination factor for antenna aperture = .75 for 12 dB taper

- $x_n$  = the position of the radiating element in the antenna aperture for the  $n^{\text{th}}$  ray

- $D_x$  = the displacement of the antenna on the  $x$  coordinate

$$\phi = \sin^{-1} \sqrt{x_o^2 + y_o^2} / R$$

$$\phi = \tan^{-1}(x_o / y_o) - \phi$$

- $x_o, y_o$  = the position of the antenna in the  $x'-y'$  radome coordinate

- $\phi$  = antenna look angle

As shown in Figure 1, the transmission coefficient  $T_n$  for the  $n^{\text{th}}$  ray is the function of the incident angle  $\theta_n$  of the  $n^{\text{th}}$  ray and its polarization, and is:

$$T_n = T_n(\theta_n, p)$$

$$\theta_n = \tan^{-1}(x_n / \sqrt{R^2 - x_n^2})$$

- $R$  = the radius of the radome

- $p$  = horizontal/vertical polarization

$$x_n = D_x + r \sin \phi - r$$

- $r$  = the radius of the effective antenna aperture

and using the transmission-line theory<sup>(1)</sup>, the transmission coefficient,  $T(\theta_n, p)$  for  $N$  homogeneous, air-backed layers is given by:

$$T = \frac{1}{e^{n+1}} \prod_{n=1}^N \frac{J_n(K_n \cos \theta_n) t_n}{(1+R) \prod_{n=1}^N \frac{1+\Gamma_n}{1+\Gamma_n e^{-2jK_n t_n}}}$$

where  $R = \frac{y_o - y_{in}}{y_o + y_{in}}$

$$\Gamma_{in}^{(n)} = \frac{1 - \Gamma_n e^{-2jK_n t_n}}{1 + \Gamma_n e^{-2jK_n t_n}} ; n = 1, 2, 3, \dots, N$$

$$\Gamma_n^{(n+1)} = \frac{y_n - y_{in}^{(n+1)}}{y_n + y_{in}^{(n+1)}} ; n = 1, 2, 3, \dots, N-1$$

$$\Gamma_N = \frac{y_N - y_o}{y_N + y_o}$$

$$y_n = \sqrt{\epsilon_n} \cos \theta_n \text{ for perpendicular polarization}$$

$$= \sqrt{\epsilon_n} / \cos \theta_n \text{ for parallel}$$

$$n = 1, 2, 3, \dots, N$$

$$\cos \theta_n = \sqrt{1 - \sin^2 \theta_o / \epsilon_n} ; n = 1, 2, 3, \dots, N$$

$$\theta_o = \text{Incident angle}$$

$$\epsilon_n = \epsilon_n' - j\epsilon_n'' \text{, the complex permittivity of the } n^{\text{th}} \text{ layer}$$

$$\epsilon_o = 1$$

$$K_n = K_o \sqrt{\epsilon_n} \cos \theta_n = \frac{\pi f}{5.9} \sqrt{\epsilon_n} \cos \theta_n ; f = \text{operating frequency (GHz)}$$

$$t_n = \text{thickness of the } n^{\text{th}} \text{ layer (inches)}$$

The absorbed power  $P_a$  in lossy dielectric layers is, therefore, given by:

$$P_a = 1 - |T|^2 - |R|^2$$

Using the above, the transmissivity of a homogeneous radome wall can be determined. However, large radomes must be fabricated using a panelized method of assembly. This will introduce discontinuities (panel interconnections) in the assembled radome which must be considered in order to determine the total loss of the radome. The approach used is as follows:

$$L_t = L_w + L_j^{(2)}$$

$L_t$  = total transmission loss of the sandwich radome in dB

$L_w$  = transmission loss due to the sandwich wall

$L_j$  = transmission loss due to the sandwich radome panel interconnections

$$= 10 \log |1 + p_s \text{IFR}|^2$$

The term  $L_j$  may, depending on the choice of the panel interconnection configuration, be determined by:

$$L_j = 10 \log |1 - p_s (1 - T_j e^{j\Delta\theta})|^2$$

where  $T_j$  = ratio of the transmission coefficient of the panel interconnections to that of the sandwich panel

and  $\Delta\theta$  = the insertion phase difference between the sandwich panel and its interconnections

$p_s$  = physical blockage of the interconnecting mechanism

IFR = the value of induced field ratio of the panel interconnection configuration

The physical blockage ( $p_s$ ) is obtained by projecting the antenna aperture onto the radome surface and computing the blockage due to the presence of the panel interconnections.

Richmond's method<sup>(3,4)</sup> represents the fields inside a dielectric cylinder by the equivalent current which defines the cylinder's induced field ratio (IFR). Based on this method, a computer program was developed by ESSCO for evaluating the IFR of a dielectric cylinder of arbitrary cross section, all angles of incidence and for parallel and perpendicular polarization.

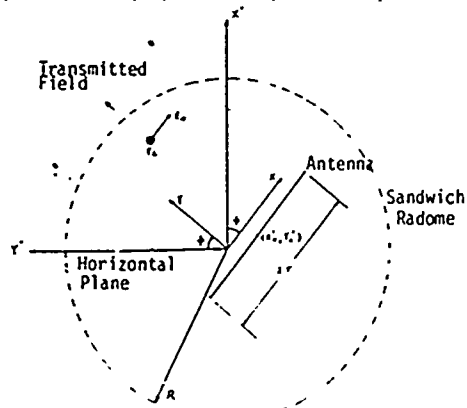


Figure 1 - SSR Antenna Enclosed In A Sandwich Radome

## 2) BORESIGHT ERROR

A spherical homogeneous sandwich radome will not introduce any boresight error if the enclosed antenna axis is coincident with the center of the radome. In large radomes which use a panelized method of assembly, some boresight error may be introduced by the panel edge configuration located in the aperture area of the antenna. The method (5) of computing this error is as follows:

$$BSE = \frac{0.27\lambda L W I_m (IFR_{ave.})}{A^2}$$

$\lambda$  = wavelength

$L$  = length of panel interconnection

$W$  = width of panel interconnection

$A$  = radius of antenna

$I_m (IFR_{ave.})$  = imaginary part of the  $IFR_{ave.}$

The phase perturbation thus introduced can influence the boresight error. Therefore, the average imaginary part of the IFR at the operating frequency is used in the above formulation.

## (3) SIDELobe PERTURBATIONS

The antenna sidelobe perturbations due to the radome are related to the amount of energy reflected and/or scattered by the radome. The energy absorbed by the radome wall will not affect antenna sidelobe levels. As the reflected energy is essentially omnidirectionally scattered, its level will be below the isotropic level and can be computed by:

$$dBi = 20 \log_{10} \frac{1}{|R|}$$

The maximum possible perturbation to a sidelobe can be determined by the following:

$$\text{Maximum Perturbation} = 20 \log_{10} \frac{VR_1 + VR_2}{VR_1}$$

$VR_1$  = voltage ratio of the antenna sidelobe

$VR_2$  = voltage ratio of the reflected and/or scattered energy in the direction of the perturbed sidelobe

It should be noted that for the maximum perturbation to occur, the sidelobe energy and the scattered energy must be additive or in phase. This condition does not occur frequently. The interaction between the sidelobe energy and the radome scattered energy is random in nature; therefore, more realistic predictions of sidelobe perturbations are generally significantly smaller than the maximum perturbation given in the above formulation and approximate an RMS value.

## IV. RADIATION PATTERN ANALYSIS

Presented thus far, analytical approaches have been applied for computing the effect of the radome on the primary characteristics of the enclosed antenna. These methods represent a general approach when specified data on the enclosed antenna subsystem is not available. However, if the antenna near-field electromagnetic data and physical configuration of the antenna/radome combination are known, a more rigorous analysis can be performed. The objective of this type of analysis is to determine the far-field antenna pattern, with and without the radome. This integrated approach focuses the designer on the antenna and radome as a combined unit or subsystem and provides insight into the inter-related characteristics of each. Generally, because this method of analysis is more rigorous than the methodology presented above, slightly smaller effects of the radome will result. The mathematical approach utilized by ESSCO and solved by one of our major computer programs is briefly presented below:

### 1) FORMULATION

The perturbed far-field of the antenna due to discontinuities introduced into the otherwise homogeneous

sandwich radome by the panel interconnections can be defined as the superposition of the unperturbed far-field of the antenna and the scattered field of the panel interconnections. In addition, the transmissivity can be determined by the ratio of the unperturbed far-field to the perturbed far-field in the direction of maximum antenna gain. Mathematically, this can be expressed as:

$F'(\phi, \theta)$  = perturbed far-field due to panel interconnections

$$= F(\phi, \theta) + \sum_{n=1}^M g_n I_n f_n^{(z)}$$

and transmission loss =  $L_s$

$$= 20 \log_{10} \left[ \frac{F'(\phi=0, \theta=\theta_{max})}{F(\phi=0, \theta=\theta_{max})} \right] \text{ (dB)}$$

where

$F(\phi, \theta)$  = unperturbed far-field of the antenna

$$= \int_S f(x, y) \exp[jk(y \sin \theta + x \cos \theta \sin \phi) + \psi(x, y)] dx dy$$

$\phi, \theta$  = azimuth and elevation angles respectively shown in Figure 2

$f(x, y) ; \psi(x, y)$  = amplitude and phase distribution of the near field of the antenna

$S$  = the area of the antenna

$\theta_{max}$  = elevation angle of the antenna main beam

$K$  = propagation constant of electromagnetic wave

$$= \frac{2\pi f}{11.8} ; f = \text{operating frequency (GHz)}$$

$M$  = number of the panel interconnections

$g_n$  = IFR (induced field ratio) of  $n^{\text{th}}$  panel interconnection

$$= g_{||} \cos^2 \delta_n + g_{\perp} \sin^2 \delta_n$$

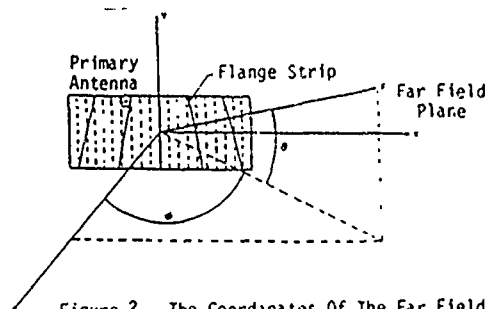


Figure 2 - The Coordinates Of The Far Field Of The Antenna

$g_{||}, g_{\perp}$  = IFR for electrical field parallel and perpendicular to the panel interconnection

$\delta_n$  = orientation angle of  $n^{\text{th}}$  panel interconnection to the electrical field

$f_n^{(z)}$  = average near field impinging onto the  $n^{\text{th}}$  panel interconnection

$I_n$  = radiation pattern of the  $n^{\text{th}}$  panel interconnection

$$= \frac{1}{A_n} \left( \frac{\sin A}{A} \right) \left( \frac{\sin B}{B} \right) \exp[jk(y_n' \sin \theta + x_n' \cos \theta \sin \phi)]$$



$W_n$  = width of nth panel interconnection

$l_n$  = length of nth panel interconnection

$$= \frac{l_n}{\cos \delta_n}$$

$$A_n = \frac{KW_n}{2} \sin \theta' \sin(\phi' - \delta_n)$$

$$B_n = \frac{Kl_n}{2} \sin \theta' \cos(\phi' - \delta_n)$$

$x_n, y_n$  = position of the nth panel interconnection center

$$\cos \theta' = \cos \theta \cos \phi$$

$$\sin \theta' = (\sin^2 \theta + \cos^2 \theta \sin^2 \phi)^{1/2}$$

$$\sin \phi' = \cos \theta \sin \phi / \sin \theta'$$

$$\cos \phi' = \sin \theta / \sin \theta'$$

The required inputs for the ESSCO computer program which solves the above formulation are as follows:

- System operating frequency
- Antenna aperture dimensions
- Antenna positioning data with respect to the radome
- Antenna near-field electromagnetic data, including the amplitude and phase distribution
- Appropriate physical characteristics of the radome configuration

Both methods of analysis described above may be utilized; namely (1) when the antenna electromagnetic data is unknown, and (2) when that data is available. The comparison of the results of both methods indicate excellent agreement, with the smaller effects of the radome determined from the more rigorous approach. Tests on full-scale sections of the radome wall and panel interconnections have verified these analytical techniques.

#### V. PERFORMANCE RESULTS

The electromagnetic performance of a typical SSR antenna when enclosed by a 35 foot diameter ESSCO sandwich radome is presented below as determined through use of the previous analysis methods. The SSR antenna (26.2 feet x 5.5 feet) is situated at the radome center and operates at 1.03 - 1.09 GHz. The antenna/radome configuration is shown in Figure 3 and the antenna parameters are given in Table 1.

##### 1) GENERAL ANALYSIS RESULTS

###### a) TRANSMISSION LOSS

The total transmission loss of the assembled radome is the sum of the radome wall loss and the panel interconnection loss. Using the formulations gives the transmission loss of the radome wall as 0.030 dB at 1.03 GHz and 0.033 dB at 1.09 GHz.

The physical blockage of the panel interconnections ( $p_c$ ) is obtained by projecting the antenna aperture (26.2 feet x 5.5 feet) onto the radome surface. This was found to be 3.19% using the configuration shown in Figure 3.

Tabulated below is the IFR for the panel interconnection configuration for both parallel and perpendicular polarizations and the resultant transmission loss (T.L.) at 1.03 GHz and 1.09 GHz.

Frequency GHz	IFR $\parallel$	IFR $\perp$	T.L. (dB)
1.03	-.143-j.58	-.010-j.168	.040
1.09	-.169-j.62	-.014-j.172	.047

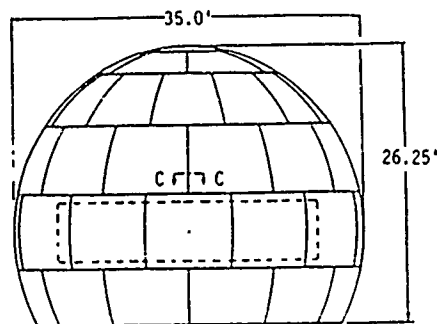


FIGURE 3 - TYPICAL SECTION C-C OF INTERCONNECTIONS

TABLE 1 - ANTENNA DESCRIPTION AND PARAMETERS

Transmit Frequency	1.03 GHz
Receive Frequency	1.09 GHz
Face Tilt	15 degrees up
Number Elements Azimuth	32
Number Elements Elevation	11
Spacing Between Elements Azimuth	10.125 inches
Spacing Between Elements Elevation	6.545 inches
Element Type	Vertically polarized dipole over ground plane

Combining the loss from the homogeneous wall and the associated panel interconnections results in the total loss tabulated below:

Frequency (GHz)	Transmission loss (dB)
1.03	.070
1.09	.080

###### b) BORESIGHT ERROR

The computed Peak and RMS value of boresight error in the azimuth plane due to the panel interconnections is as follows:

Frequency (GHz)	Boresight Error (milliradian)	RMS Boresight Error (milliradian)
1.03	.064	.026
1.09	.064	.026

###### c) SIDELobe PERTURBATION

The antenna sidelobe perturbations due to the radome are related to the amount of energy reflected and/or scattered by the radome. As noted above, the total transmission loss of the radome is 0.070 dB at 1.03 GHz and 0.080 dB at 1.09 GHz. The reflected energy is 0.060 dB and 0.070 dB respectively after subtracting 0.010 dB of energy that is absorbed in the radome wall. If this energy is omnidirectionally scattered, then its level will be about 18 dB below the isotropic level.

For the SSR antenna with a gain of 25 dB, the following maximum and RMS antenna sidelobe perturbations were computed:

Frequency (GHz)	Max. $\Delta$ @ -25 dB	Max. $\Delta$ @ -30 dB	RMS $\Delta$ @ -25 dB	RMS $\Delta$ @ -30 dB
1.03	0.96	1.64	0.38	0.66
1.09	1.03	1.76	0.41	0.70

##### 2) RADIATION PATTERN ANALYSIS RESULTS

As the near-field electromagnetic data of the SSR antenna was available, a more rigorous analysis of the

far-field antenna pattern, with and without the radome was performed.

The data for the SSR antenna is shown in Tables 2 through 4. Additional data is obtained from the antenna/radome configuration shown in Figure 3 and the computation of the I/R of the panel interconnections.

- $\theta_{max}$  = 4 above horizon
- $f$  = 1.06 GHz (mid band)
- $g_{||}$  = -.156-j.172
- $g_{\perp}$  = -.012-j.172
- $f_n, \psi_n$  = from Tables 2 through 3

TABLE 2 - TRANSMIT & RECEIVE ELEVATION DISTRIBUTION

NO.	POWER	AMP	PHASE	dB
1	5.6661	2.3804	-67.3	-12.47
2	5.6975	2.7869	-113.3	-12.44
3	5.3184	2.3062	-141.7	-12.74
4	8.3500	2.8896	162.1	-10.78
5	1.9196	1.3855	155.0	-17.17
6	20.7151	4.5514	42.0	-6.84
7	22.6571	4.7599	56.6	-6.45
8	8.2180	2.8667	.5	-10.85
9	9.2005	3.0332	-25.5	-10.36
10	6.6639	2.5815	-75.4	-11.76
11	5.5940	2.3652	-110.0	-12.52

TABLE 3 - TRANSMIT & RECEIVE AZIMUTH SUM DISTRIBUTION

PH(1)	.0102	.0108	.0114	.0146	.0184
	.0224	.0261	.0301	.0341	.0379
	.0414	.0444	.0471	.0492	.0505
	.0512	.0512	.0505	.0492	.0471
	.0444	.0414	.0379	.0341	.0301
	.0261	.0224	.0184	.0146	.0114
	.0108	.0102			

The resultant data are contained in Table 4.

RADIATION ANGLE ELEVATION AZIMUTH (DEGREES)	RELATIVE POWER TO BEAM PEAK UNPERTURBED (DB)	RELATIVE POWER TO BEAM PEAK PERTURBED (DB)
4 0	0000000773	023273441
4 2	0840292917	1074928874
4 4	3371923421	3407931138
4 6	7626303732	7863331601
4 8	13438633779	13896837329
4 1	2.1331184947	2.1790171371
4 1.2	3.1419443716	3.1439082402
4 1.4	4.3421830423	4.3442046711
4 1.6	5.7774610328	5.8013443980
4 1.8	7.4774713972	7.5019126374
4 2	9.4831343320	9.5096354873
4 2.2	11.8423016233	11.8872737434
4 2.4	14.7044633864	14.7325982114
4 2.6	18.1848825713	18.2126595073
4 2.8	22.4242103834	22.4358815641
4 3	28.847930842	28.8893373367
4 3.2	40.4477945319	40.7404196117
4 3.4	42.3837585324	42.3351321242
4 3.6	39.9146037424	39.9188375163
4 3.8	35.0323372248	35.0821833373
4 4	34.7831098239	34.8376047398
4 4.2	41.4323182310	41.8323942170
4 4.4	41.8834393202	43.9061373450
4 4.6	43.7502913337	43.1418910211
4 4.8	38.0009458994	37.4290749774
4 5	33.7228911459	33.2728492604
4 5.2	35.0023749401	34.4710011150
4 5.4	35.3484672311	34.8482334373
4 5.6	37.4543014711	34.4171031317
4 5.8	41.4784743133	39.6131828141
4 6	52.1154008315	46.2718145018
4 6.2	48.4307744084	54.1593348073
4 6.4	40.3370180039	43.3194205150
4 6.6	37.1347689183	39.2064092093
4 6.8	35.4942176792	37.2728747388
4 7	33.0046279233	34.7278236337
4 7.2	35.9000157239	37.3580138644
4 7.4	37.0968034212	39.3441313108
4 7.6	40.2991154343	43.4044603344
4 7.8	47.2294003328	39.3141882837
4 8	37.1384810402	47.4413924894
4 8.2	43.1344047994	40.4432692194
4 8.4	38.3784239904	37.0449002223
4 8.6	34.262220443	35.2285001298
4 8.8	35.1874248448	34.4034742211

4 9	35.0546252992	34.4169759609
4 9.2	35.8223419711	35.2648833341
4 9.4	37.6645983377	37.1329698881
4 9.6	41.1933969638	40.6011690368
4 9.8	49.0954617603	48.0682499162
4 10	53.8736648933	53.2734333932
4 10.2	42.6870633566	42.9141397302
4 10.4	39.4592819908	38.3368436211
4 10.6	34.2332650833	36.2804379821
4 10.8	35.2040392780	35.1982778086
4 11	35.0376777330	35.0034314571
4 11.2	35.7145338339	35.4398386134
4 11.4	37.3749010261	37.2278509390
4 11.6	40.3182900806	40.1929807198
4 11.8	47.0174036873	44.0688403298
4 12	40.9066846630	37.5037226328
4 12.2	44.1960393179	45.6248249273

The computed data derived from the more rigorous pattern analysis shows that the transmission loss due to the panel interconnections is 0.025 dB at 1.06 GHz which is less than the 0.040 and 0.047 dB values (1.03 and 1.09 GHz) arrived at by using the general analysis approach. The total radome loss is 0.057 dB obtained by adding the radome wall loss of 0.032 dB to the panel interconnection loss of 0.025 dB. Using the general analysis method, the total loss was ~0.075 dB.

Comparing the unperturbed data with the perturbed data shows that the maximum sidelobe and boresight error changes are also somewhat less than the changes calculated by the general analysis method.

VI. CONCLUSION

It can be seen that overall system application and performance requirements must be evaluated when considering alternative radome types. The capabilities to formulate, analyze and interpret the interactions of the system components must be utilized to optimize radome design. These capabilities, together with expertise in materials selection and manufacturing techniques, provide the opportunity to supply a radome which will enhance overall system performance. Modern radars, including state-of-the-art SSR's, demand an equally sophisticated radome. This type of radome is now available, and its performance can be readily and thoroughly evaluated.

REFERENCES

1. Microwave Engineering, by A.F. Harvey, Academic Press 1963, Chapters 1 & 2
2. K. C. Chang, "Laminate Radome Joint Study". ESSCO Memorandum, July 19, 1982
3. J. Richmond, "Scattering by a Dielectric Cylinder of Arbitrary Cross-Section Shape". IEEE AP-13, p. 334-341, May, 1965.
4. J. Richmond, "TE-Wave Scattering by a Dielectric Cylinder of Arbitrary Cross-Section Shape", IEEE AP-14, #4, p. 460-464, July, 1966.
5. A. Kay and D. Patterson, "Design of Metal Space Frame Radome", Report #RADC-TDR-64, Rome Air Development Center, Griffiss Air Force Base, New York, p. 36-55, June, 1964.

## DEVELOPMENT OF THE F-20 NOSE RADOME

E. L. Cain & P. Tulyathan

**AD-P004 374**

### INTRODUCTION

Northrop's newest fighter aircraft, the F-20 Tigershark, is based on the successful aerodynamic design and size of the F-5 Tiger II aircraft. It has a single engine providing 80 percent more thrust than that of the twin-engine Tiger II, digital avionics, and a newly designed AN/APG-67(V) X-band radar. This coherent pulse-doppler radar provides both look-up and look-down target detection and tracking. Successful operation of this radar necessitated an antenna/radome system which provides low RMS side-lobe levels to minimize false alarm rate in the look-down mode, and high antenna gain/low radome loss to maximize radar range. These system requirements prompted a redesign of the F-5 "Shark Shape" nose section which had been aerodynamically configured to improve the post-stall handling qualities of the Tiger II aircraft. The design change included (1) provisions for a larger radar antenna, (2) a "clean" radome, i.e., no pitot-static probe, air lines or heater wires, and (3) a blunted radome shape, designed to preserve aerodynamic handling qualities and provide the required electrical characteristics. Provisions for the increased radar antenna size were attained by moving the radome-to-aircraft attachment ring seven inches aft to a larger cross-sectional area. The F-20 radar antenna is an elliptically shaped (vertically polarized) flat-plate slotted array 21.4 inches by 14.4 inches (242 square inches); the Tiger II's shark nose antenna is 18.9 inches by 11.3 inches (168 square inches). The F-20 radome has an approximately elliptical cross-section attachment ring of 29 inches by 20 inches and a length of 45 inches. The shark nose base is 26 inches by 18 inches and its length is 49 inches. Figure 1 compares the F-20 radome geometry with its predecessor, the shark nose. To assure that the F-20 radome would meet or exceed electrical requirements, it was agreed early in the program to develop two identical radomes of different materials. The chosen materials were E-glass and quartz, and the common resin was polyester. This paper describes the shape studies and the testing effort expended to achieve a successful design for full electrical qualification.

## RADOME SHAPE STUDIES

Shape studies involved a close interaction between aerodynamic and radar requirements. Aerodynamic shaping of the forebody required a high (longitudinal) fineness ratio for low drag and a flattened (elliptical) cross section for directional stability at high angles of attack. A high fineness ratio increases the angle of incidence (defined below) for the radar signal and decreases transmissivity through the radome wall. A flattened cross section produces small radii of curvature in the forward section of the radome and flat top/bottom areas in the midsection. The small radius of curvature diffracts main beam energy, broadens the main beam and increases first and second side lobe levels. The flat top/bottom areas reflect the main beam energy and increase image lobes.

Several aerodynamic configurations to satisfy these two extreme requirements were chosen for investigation. Each shape was tested in the wind tunnel, and computer studies were performed to predict the range of incidence angles which could be expected. Figure 2 shows the mathematical representation of the F-20 radome. The radome shell was modelled by an analytic surface which was constructed from a series of parametric cubic (PC) patches[1]. Each PC-patch is bounded by four edges, and every point on the patch is defined by the  $(x,y,z)$  coordinates which are functions of two parameters  $(u,v)$  for each patch. These parameters are constrained for convenience to vary in value from 0 to 1 and so the entire patch is defined. This parametric representation of a patch can be considered as an extension to three dimensions of the parametric cubic spline approach to fitting two-dimensional curves. The incidence angle was obtained by finding the angles made from parallel rays emanating from a set of points on the antenna surface and the surface-normal at the intersection point. These incident angles were averaged with a weighting function representing the current distribution of the antenna.

Figure 3a compares cross-sections for the desirable aerodynamic shark nose radome and the F-20 radome which has been optimized for the coherent radar. Figure 3b shows the average incidence angles for these radomes. The elevation angles were used for the abscissa since it is in this plane that reflection lobes affect radar look-down capability. Identical effective radiating aperture, power distribution, and scan angles were used to represent the antenna. However, the gimbal (antenna face) was located 4.68 inches farther forward for the shark nose radome; this reflects actual antenna locations for the two radomes. As shown in Figure 3b, the F-20 radome has a lower overall angle of incidence. Other features include reduced forward edge discontinuities (chine areas) and increased curvature of the top/bottom midsection.

## RADOME MATERIAL EVALUATION

With the F-20 radome geometry fixed, the radome window anomalies removed (pitot, etc.), and the radar antenna size, placement, movement defined, it was next necessary to choose the most promising wall configuration and consider the material selection. The electrically homogeneous first order (half-wave) wall structure was selected based on its response level over a wide incidence angle range for the radar bandwidth -- a choice superior to other configurations such as an "A" sandwich. The solid wall construction offers low radome wall reflection levels at relatively high incidence angles, minimizes complexity in fabrication, and allows for accurate thickness control. The half-wave criterion for optimum transmission was maintained at different antenna scan angles by a longitudinal thickness-taper along the radome wall. To assure that the required minimum RMS sidelobe levels and maximum transmission were attained, two different materials were selected, and two radomes of each material were fabricated and tested. The first material was E-glass which has a relative dielectric constant of approximately 4.3, the second was quartz with a dielectric constant of about 3.3 which more nearly matches that of the polyester resin. All four radomes were made on the same mandrel; the thicker quartz radomes were allowed to exceed the outer mold line of the aircraft.

Initial tuning of each radome, to control "electrical thickness", was accomplished by the single horn interferometer method with the "bare" radome still on the mandrel. Final tuning was performed on an outdoor test range with a "flight ready" radome complete with a polyurethane rain erosion coating and segmented button lightning diverter strips. The electrical correction was accomplished by applying layers of silicon (adhesive) backed pressure sensitive E-glass tape to selected portions on the inside of the radome. The correction was made with the emphasis to minimize sidelobe levels. Boresight error was allowed to increase, provided (1) the error was within an acceptable repeatability between radomes and (2) the error rate was not excessive. Boresight error can be corrected in the radar processor provided the above criteria can be maintained.

Figure 4 compares transmission and boresight error for the two materials. Measurements were made at three frequencies within the primary band. Each curve summarizes data from two radomes of the same material. Any point on a selected curve represents an average, a minimum or a maximum value for a given azimuth position at several elevation angles. The average transmission efficiency for both E-glass and quartz is above 90%; the minimum is 87%. The maximum and average boresight error (vector sum beam deflection) for both materials are comparable.

Figure 5 shows the RMS sidelobe level of a typical E-plane scan with the antenna offset 30 degrees above the nose at 0 degrees azimuth. Note the reflection lobe at -55 degrees (below the nose). Figures 6a and 6b summarize and compare the maximum reflection lobe values for both E-glass and quartz. In these figures the maximum RMS reflection lobe levels for E-plane patterns at selected elevation antenna offset angles and 0 degree azimuth are plotted. The reflection lobes at both low and high frequencies within the primary band are shown in order to indicate the "worst case" condition.

The quartz polyester material exhibits a slightly higher transmissivity when compared with E-glass polyester. However, boresight error and reflection lobe magnitudes are comparable. Although the quartz material, with the lower dielectric constant, will have a broadband response which allows for an increased wall thickness tolerance, the electrical performance of the two materials compare favorably over the radar primary bandwidth. E-glass polyester is cost effective, readily available, and has been successfully used in the shark nose radome. Based on the above rationale, E-glass polyester was selected as the laminate for the F-20 radome.

#### SUMMARY

The F-20 Tigershark radome is fabricated from E-glass polyester and protected by a polyurethane rain erosion coating and segmented button lightning diverter strips. The radome wall design is a longitudinally tapered first order (half wave) solid laminate. The shape is a derivative of the F-5 shark nose radome, optimized to satisfy the electrical requirements of the AN/APG-67(V) multimode radar and preserve aerodynamic performance. Electrical qualification measurements have shown that the radome has met or exceeded all specification requirements.

#### ACKNOWLEDGEMENT

The authors would like to recognize the efforts of John Styron, Arthur Thompson, Carson Parker, Clyde Hoots and Harold Made of the Brunswick corporation, Defense Division, Marion, Virginia for their support of this project.

#### REFERENCE

- [1] S. A. Coons, "Surfaces for Computer Aided Design of Space Forms", Project MAC, Design Div., Dept. of Mech. Engineering, MIT, 1964. Revised to MAC-TR-41, 1967. Available from CFSTI, Sills Building, 5285 Port Royal Road, Springfield, Virginia 22151.

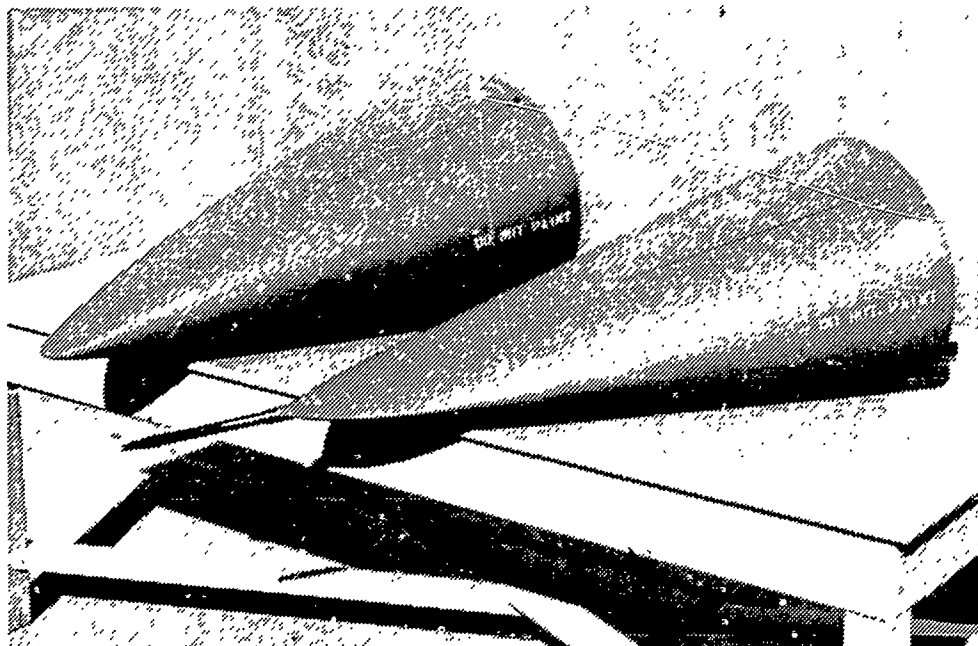


Figure 1. Shark Nose Radome (With Pitot Tube) and F-20 Radome.

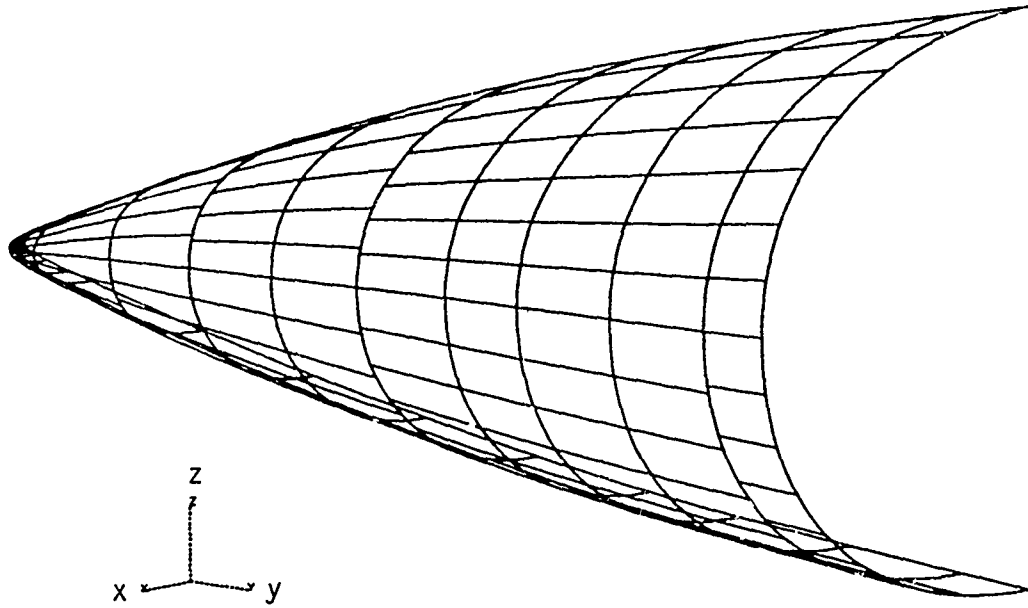
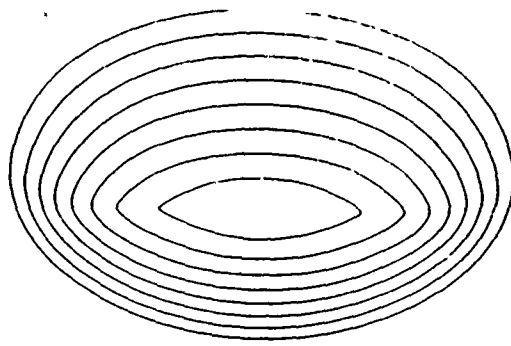
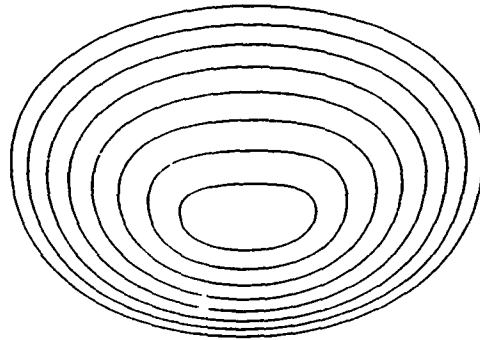


Figure 2. The analytic surface which models the outer mold line of the F-20 Radome.



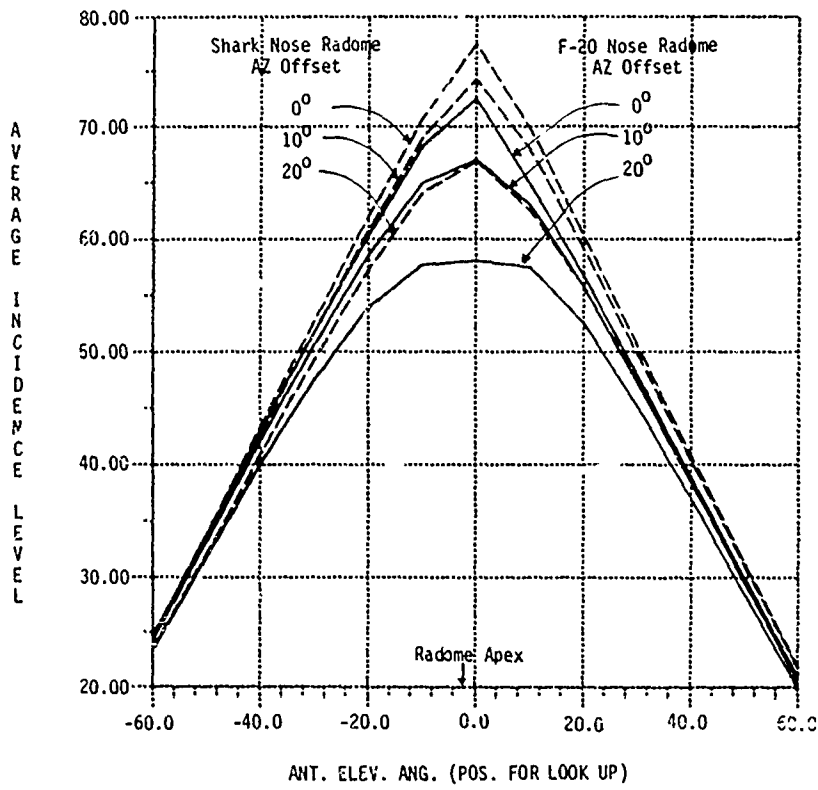


Shark Nose Radome



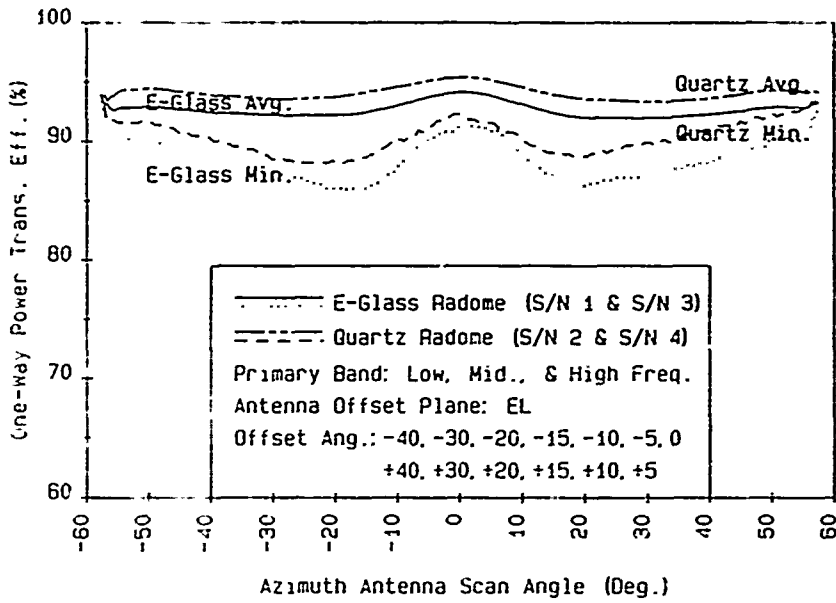
F-20 Radome

(a)

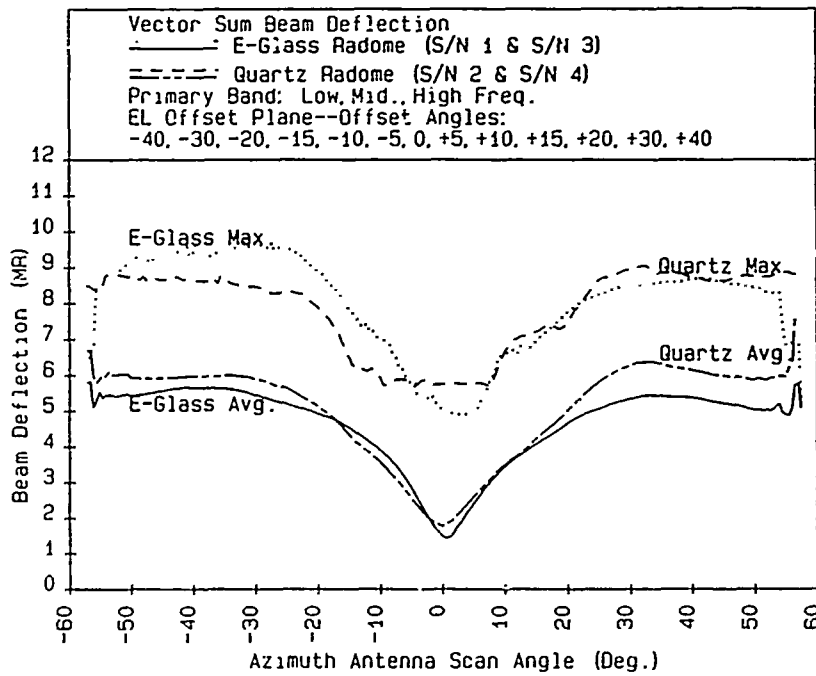


(b)

Figure 3. (a) Cross-sectional cuts of the Shark Nose and F-20 radomes in 5 inch intervals starting from the radome apex.  
 (b) Comparison of the incidence angles of the Shark Nose (---) and F-20 (—) Radomes.



(a)



(b)

Figure 4. Comparison of the transmission efficiency and vector sum beam deflection of the E-glass and Quartz radomes.

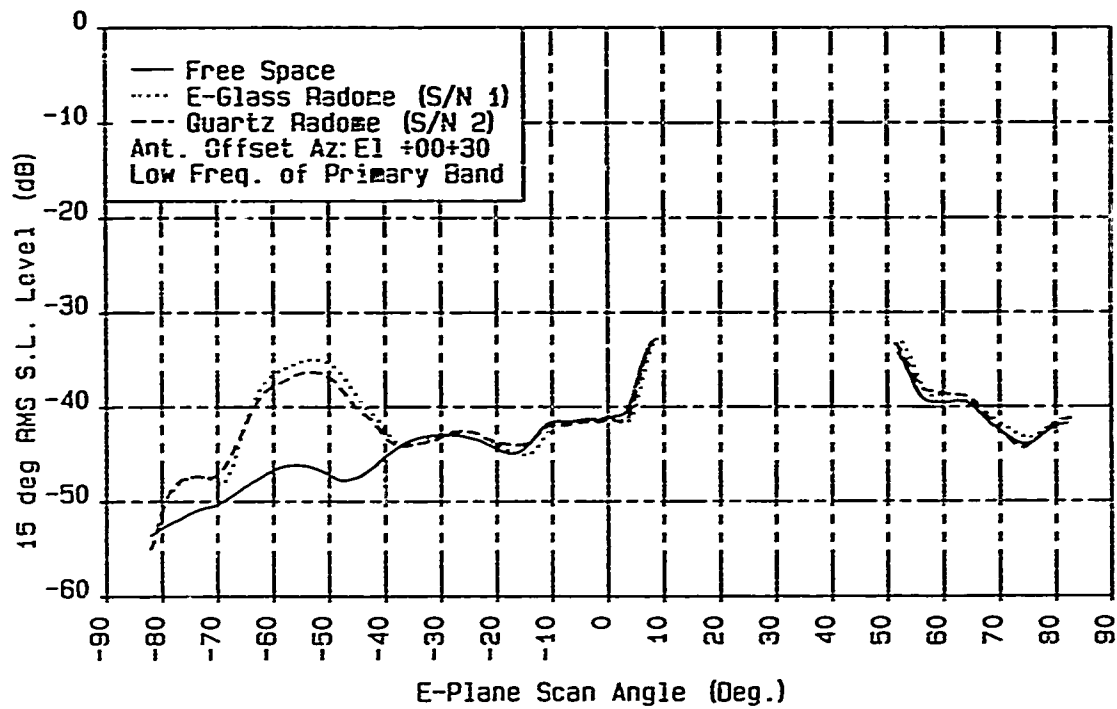
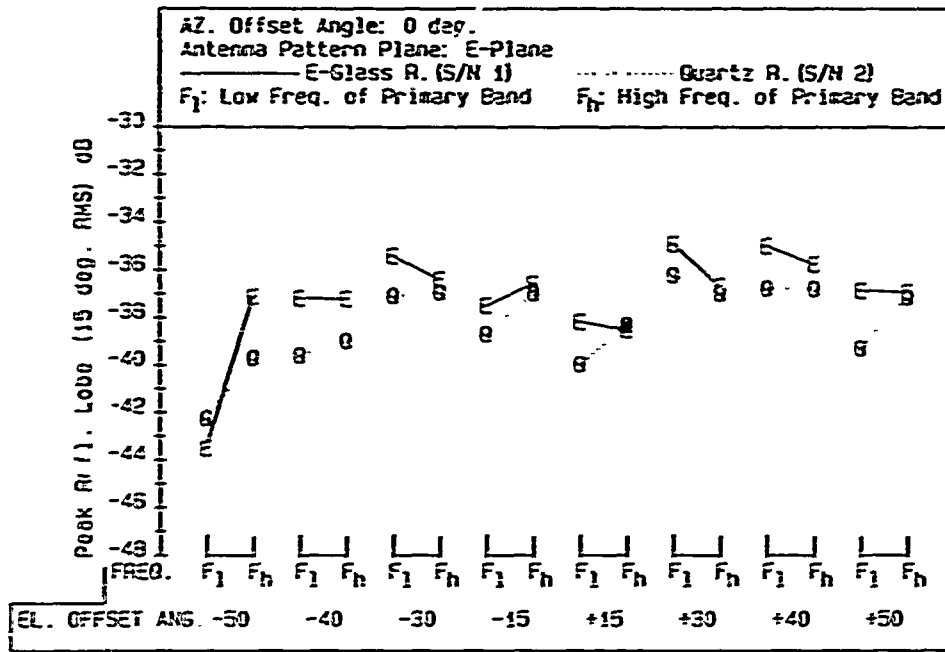
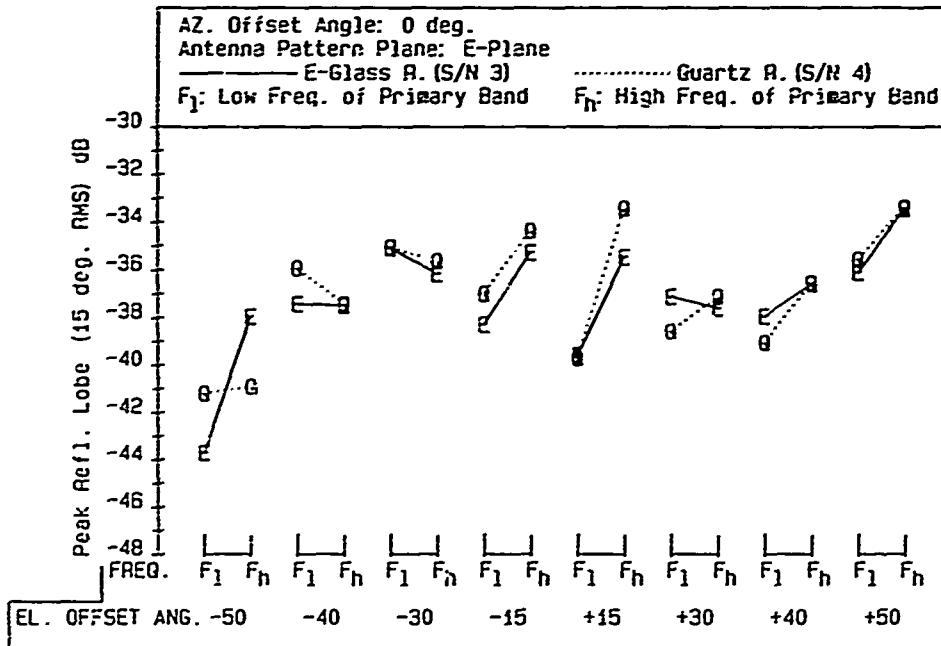


Figure 5. The antenna/radome pattern after a 15 degree sliding average window was performed on the raw data. Since the sidelobes are the quantity of interest, the mainbeam is not shown.



Radome S/N 1 and S/N 2

(a)



Radome S/N 3 and S/N 4

(b)

Figure 6. Maximum RMS reflection lobes in the E-Plane pattern.

**TITLE:** High Radiant Flux Thermal Testing of Ceramic and Ablative Coatings  
For Hardening EHF Radomes

**ABSTRACT:** Various ceramic and ablation thermal protection systems are evaluated for use over organic resin/glass composite radome shells. Test results are presented from a 1000 cal/cm<sup>2</sup>sec Xenon lamp flash facility include back face temperature response, transmitted flux, material loss, and post flash moisture absorption. Pre and post insertion loss data is also presented in the 18 to 26.5 and 33 to 50 GHz frequency ranges.

**AUTHORS:** K.A. Zimmerman (Harris Corp.)  
G.H. Briand (Harris Corp.)  
J.A. Fuller (GA. Tech.)

NOSE & INLET DUCT RADOMES FOR THE  
FIREBOLT AERIAL TARGET

by  
LEONARD C. HOOTS  
BRUNSWICK CORPORATION  
DEFENSE DIVISION  
MARION, VA 24354

AD-P004 375

Introduction

Radomes for the Firebolt Aerial Target (AQM-81A) facilitate an uncommon set of operational conditions. The target vehicle is first carried captively. Stones may be dislodged from the runway and impact the Nose or Inlet Duct Radomes with considerable force. The drone has various flight profiles after launch, encompassing levels of MACH 1.2 at 35,000 feet to MACH 4 at 100,000 feet. For flights of 10 minutes, attendant aerothermal loads produce temperature peaks of 680°F and 980°F for the Nose and Inlet Duct units, respectively. Firebolt is normally retrieved, by helicopter after its parachute deploys, for refurbishment and re-use. Occasionally, sea recovery is effected using flotation gear. Electrically, the Nose Radome accommodates an L-band antenna for the electronic scoring system, and a small circularly polarized X-band horn. The Inlet Duct Radome houses an identical broad-beamed horn.

The Radomes

The Nose Radome is a nearly conical body of revolution and is slightly more than 6.5 inches in base diameter and greater than 13 inches in length, plus pitot probe. It is a half-wave laminate at X-band and is re-useable. Thickness forward of the mounting provisions tapers from approximately 0.34 to 0.40 inches. It is sealed against sea water leakage and mounts over already in-place antennas, pitot probe, and base seal provisions.

The Inlet Duct Radome is an electrical thin-wall and is often re-useable but discarded after sea water exposure. This wall allows a close clearance around the horn antenna, permits a minimum drag frontal cross-section, and is relatively inexpensive to replace after sea water exposure. The frontal region is the antenna window portion and is 0.060" thick; the remaining length and flange attachment area is 0.080" thick.

Radome locations and shapes are illustrated in Figure 1. Both use BPI-373 quartz/polyimide materials for best electrical permittivity in temperature capable laminates. Fluoroelastomer coatings are used to accommodate the high temperatures.

PREVIOUS PAGE  
IS BLANK



## Foreign Object Impact

The radomes were designed to withstand impacts by 10 gram stones at 185 knots for nose-on and angles up to 20° from the longitudinal axis. No catastrophic failure or structural damage which would impair the ability to withstand design loads was allowable.

Foreign object impact testing was conducted by the Army Materials & Mechanics Research Center (AMMRC). Irregular shaped stones were selected from a driveway and fired by a pressure launch tube. Radomes were mounted on a fixture allowing setting the line of sight. Computer monitoring and computations gave projectile path information and an accurate velocity just before impact.

Each radome was impacted with three test shots as follows:

<u>Angle</u>	<u>Nose Radome Tests</u>		<u>Inlet Duct Dome Tests</u>	
	<u>Weight</u>	<u>Velocity</u>	<u>Weight</u>	<u>Velocity</u>
0°	10.73 gms	196 knots	10.11 gms	157 knots
10°	11.24	226	9.3	163
20°	11.02	270	9.3	244

The rugged Nose Radome is essentially impervious to such impacts. All hits were in the forward half-length and damage was restricted to coating tears and surface mars less than the depth of the outer laminate ply. The Inlet Duct radome's outer ply was locally fractured and the inside surface was crazed, however subsequent tests applying the applicable temperature profile and worst case aerodynamic loads were completed successfully, thus demonstrating that structural integrity was maintained.

## Protective Coatings, Temperature Shock Tests

Candidate protective coatings were screened to evaluate behavior under temperature exposure, and in particular to determine whether electrically lossy char materials were formed. Materials included proprietary paints, Teflon, and fluoroelastomer rain erosion protective coatings. Three colors of each material were tested, this to allow selection of a bi-color scheme on radomes as a maintenance inspection technique. Temperature exposure was to 980°F on panels 0.060 inches thick. The paints allowed panel blistering. White Teflon protected the panel, but color additives allowed panel blistering with a coating thickness of 0.003". The fluoroelastomer also allowed panel blistering with 0.003" of coating, but protected the panel well when used in a full 0.010" thickness as appropriate for rain erosion protection. Neither the Teflon nor the fluoroelastomer gave lossy chars, the electrical effects measuring tenths of a db. The fluoroelastomer was selected for its rain protection features after determining that it permitted the required electrical performance on the thin-wall Inlet Duct Radome.

The qualification Nose and Inlet Duct Radomes were tested to the total flight time-temperature profile. Figures 2 and 3 show the profiles for the Nose and Inlet Duct Radomes, respectively. The Nose Radome's outer surface is white, whereas the Inlet Duct uses black. Special test set-ups were made to impose the necessary temperatures. Quartz lamps were arranged in shaped shrouds and controlled by variac. Cool-down control was attained by shroud removal and blown air exposure. These means allowed temperature achievements virtually overlaying the desired profiles. Since the target Nose Radome life was at least 10 flights, one Nose Radome was subjected to 10 cycles of its temperature profile. The Inlet Duct Radome is counted-on for only a single flight at the extreme conditions, but re-use will occur if appropriate. Therefore an Inlet Duct Radome was tested for two cycles. All electrical and structural qualification tests were conducted using these units subsequent to temperature exposure and successfully met performance criteria.

### Sea Water Immersion

The Nose Radome is designed for re-use after a sea recovery of the Firebolt vehicle. After immersion in sea water to a depth of 12 feet for 8 hours, it is refurbished by fresh-water flushing. The radome body is sealed against leakage via the rain erosion coating. The base region has a controlled inner surface to fit a special seal, including one radome area machined to target inner diameter within a tolerance of  $+0.001$ ". After laminating directly to a metal pitot sleeve, resin is carefully added to prevent leakage in this region. Sealing around mounting bolts in the pitot and base attachment must be accomplished after the radome is installed to the vehicle.

Leakage and Sea Water Immersion Tests were conducted during radome qualification. First, the sealed unit was mounted on a test fixture and held to the equivalent of 100,000 feet altitude for an hour. Ten minutes of high temperature exposure (more than  $680^{\circ}\text{F}$ ) was then implemented. The radome temperatures and pressure were reduced to room ambient within 15 minutes and the radome was immersed in water within an additional minute. After one hour exposure, inspection revealed water within the radome interior due only to condensation of entrapped air. Sea water immersion testing was then effected by 40 hours exposure in a pressure vessel. No water was found and no damage detected after the test.

### Structural Loads

The radomes were analyzed and tested to verify their structural loads capabilities. The analyses included free flight dynamic pressures, free-flight pressures during maximum aerodynamic heating, and water impact loads. High structural margins of safety were predicted by analysis for both the Nose and Inlet Duct Radomes for all loading conditions.

Both the Nose and Inlet Duct Radomes were subjected to structural loads tests for the most severe flight loads and for the water impact loads. Both flight and water impact loads for the Nose Radome were applied using hydraulic cylinders and metal load straps while concurrently pressurizing



or evacuating the interior radome cavity. Flight loads for the Nose Radome were simulated using three strap locations and pressurizing the interior radome cavity to 30 psid bursting pressure while maintaining the radome temperature to 600°F. Water impact loads for the Nose Radome were applied in the same fashion at room temperature but with the interior radome cavity evacuated to produce a 3.4 psid collapsing pressure. The Inlet Duct Radome was tested at 400°F, first by evacuating the interior radome cavity to 20.1 psid crushing pressure, and then by pressurizing the interior radome cavity to 21 psi bursting pressure.

### Other Qualification Tests

The Nose Radome was also tested for vibration and shock. Vibration was along each of three orthogonal axes, and included four different durations and levels up to 13.38g RMS. A total of 18 shocks were applied with 11 millisecond duration and peak values up to 15g. The radome was unaffected by these tests.

### Electrical Performance

Antenna locations are indicated in Figures 4 and 5. The X-band horns are circularly polarized and provided beam widths of approximately 70° centered at -25° elevation over a frequency range of 8.5 to 10.25 GHz. A waveguide twist is used as the means to orient the horn and maintain the routing to the transmitter in a compact space. The L-band scoring system antenna operates over the 1.675 to 1.875 GHz band. A turnstile configuration provides the radiating structure in the Nose Radome location. All of the antennas are fixed with respect to the radomes.

The primary criteria for radome electrical performance are low loss and the maintenance of angular coverage. System radiation patterns were measured in comparison to the reference horn patterns. Within the 70° azimuth x 70° elevation half-power points, the requirement was that absorption and other effects cause deviation no worse than -2db for 90% of the coverage area. Further, pattern beamwidth narrowing could not exceed 15°, and the angular shift could not cause the midpoint between half-power points to shift more than 2°. Both radomes met this criteria. Measurements were made using the circularly polarized horn within the radomes and spinning linear polarization down range. The Nose Radome result is shown in Figure 6 for the center frequency azimuth pattern through beam peak.

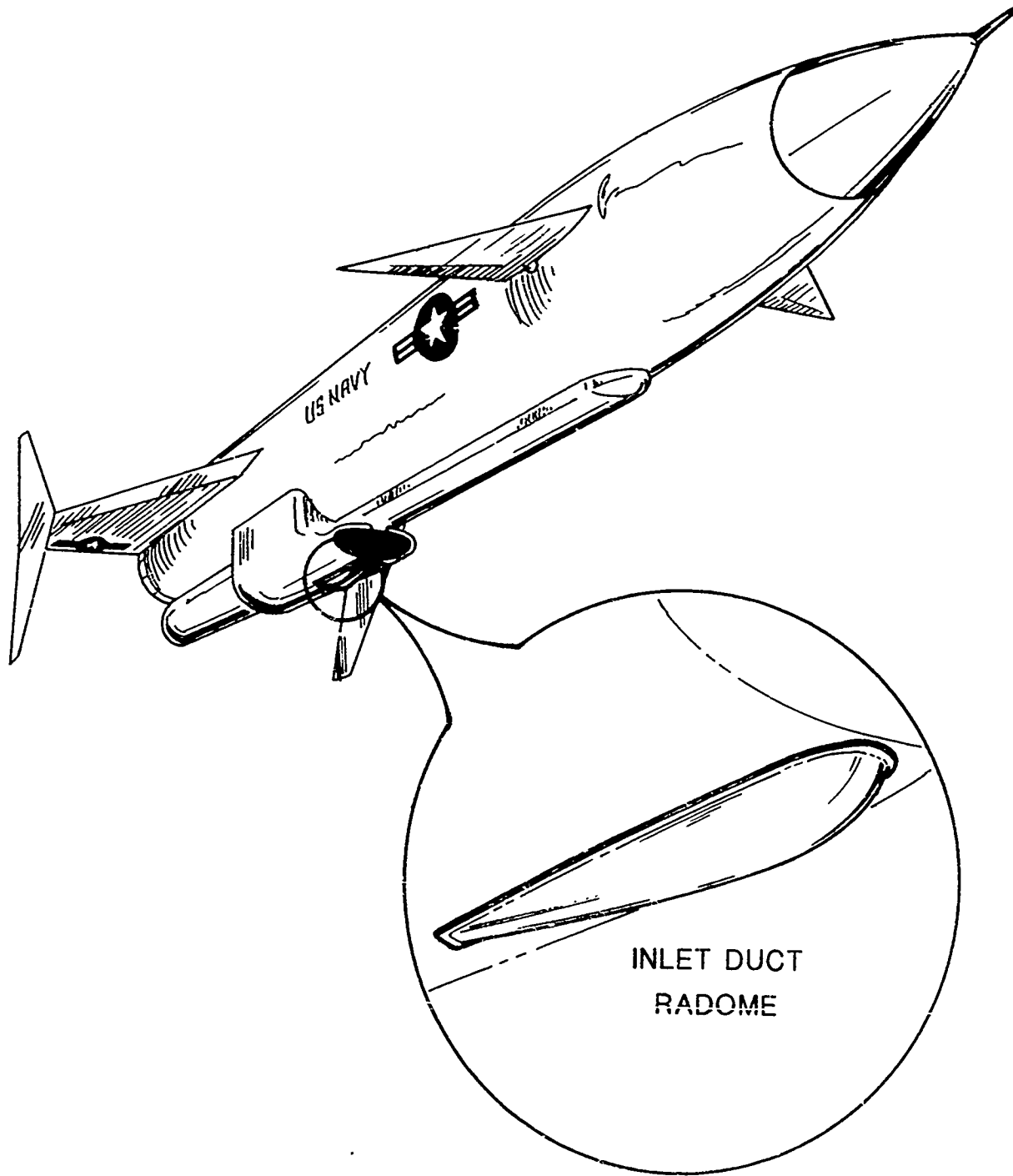


**FIGURE 1: RADOME LOCATIONS ON  
FIREBOLT AERIAL TARGET**

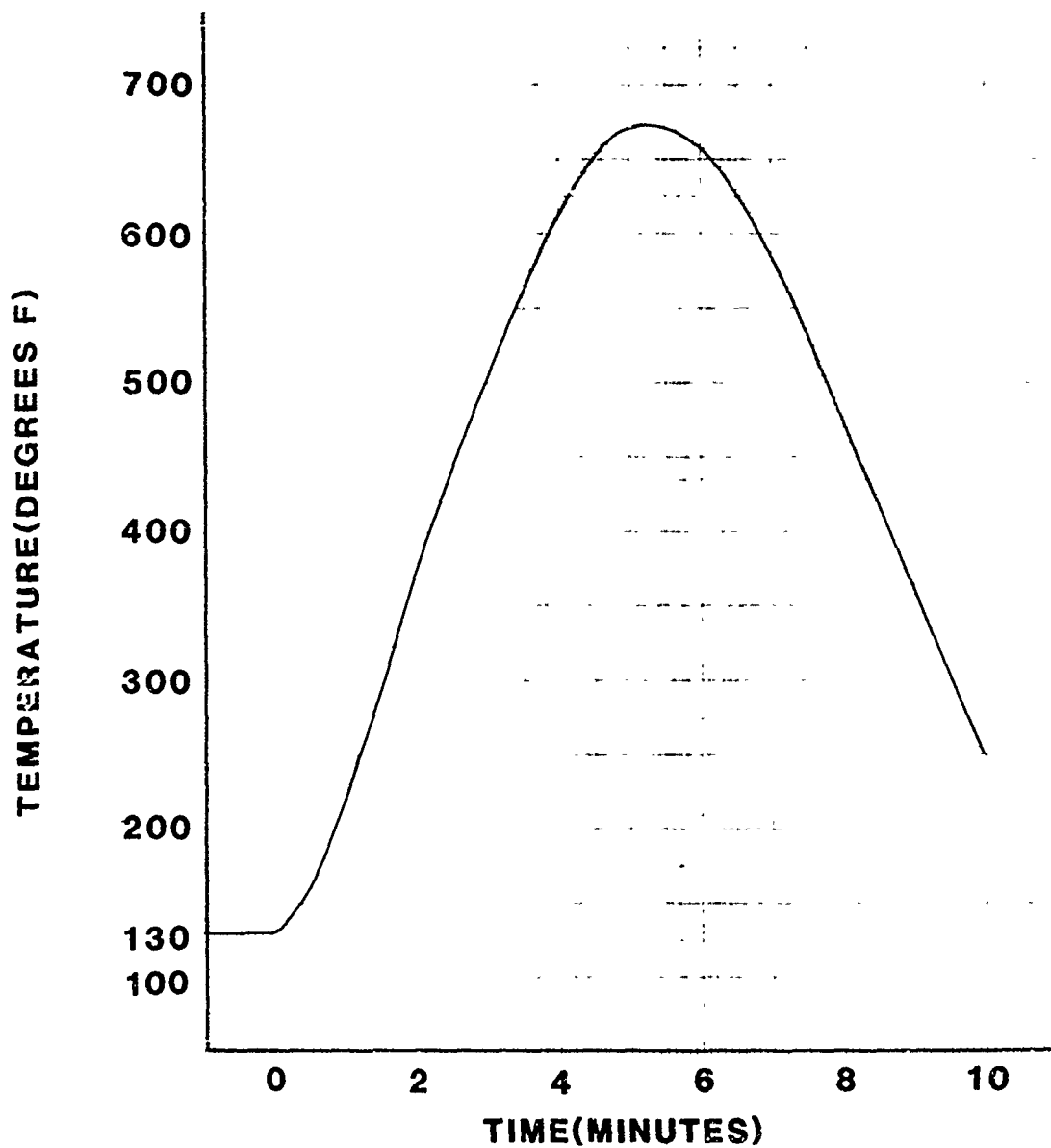


**FIGURE 2: NOSE RADOME SKIN  
TEMPERATURE PROFILE**

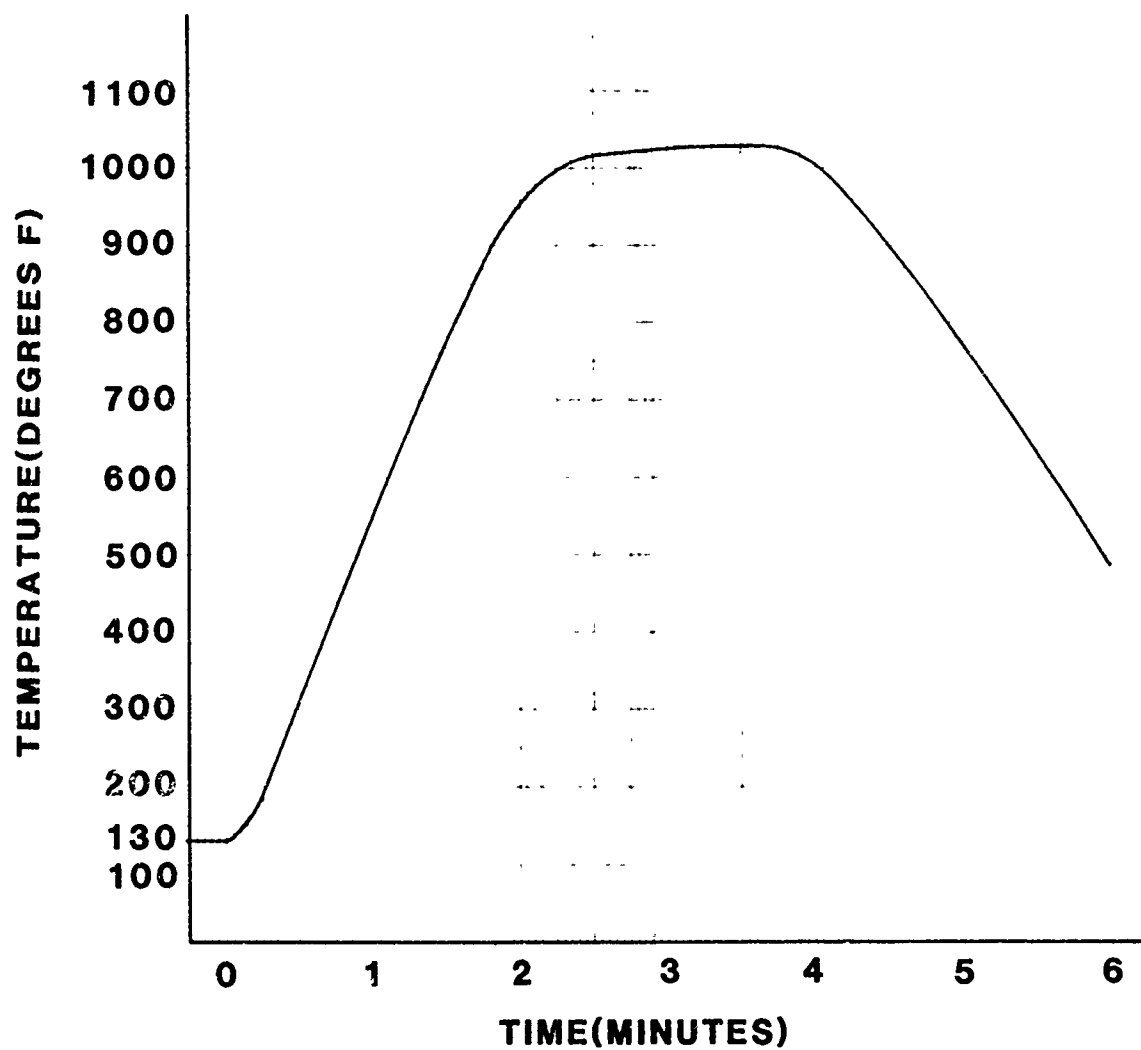


**FIGURE 3: INLET DUCT RADOME SKIN  
TEMPERATURE PROFILE  
(WORST REGION)**

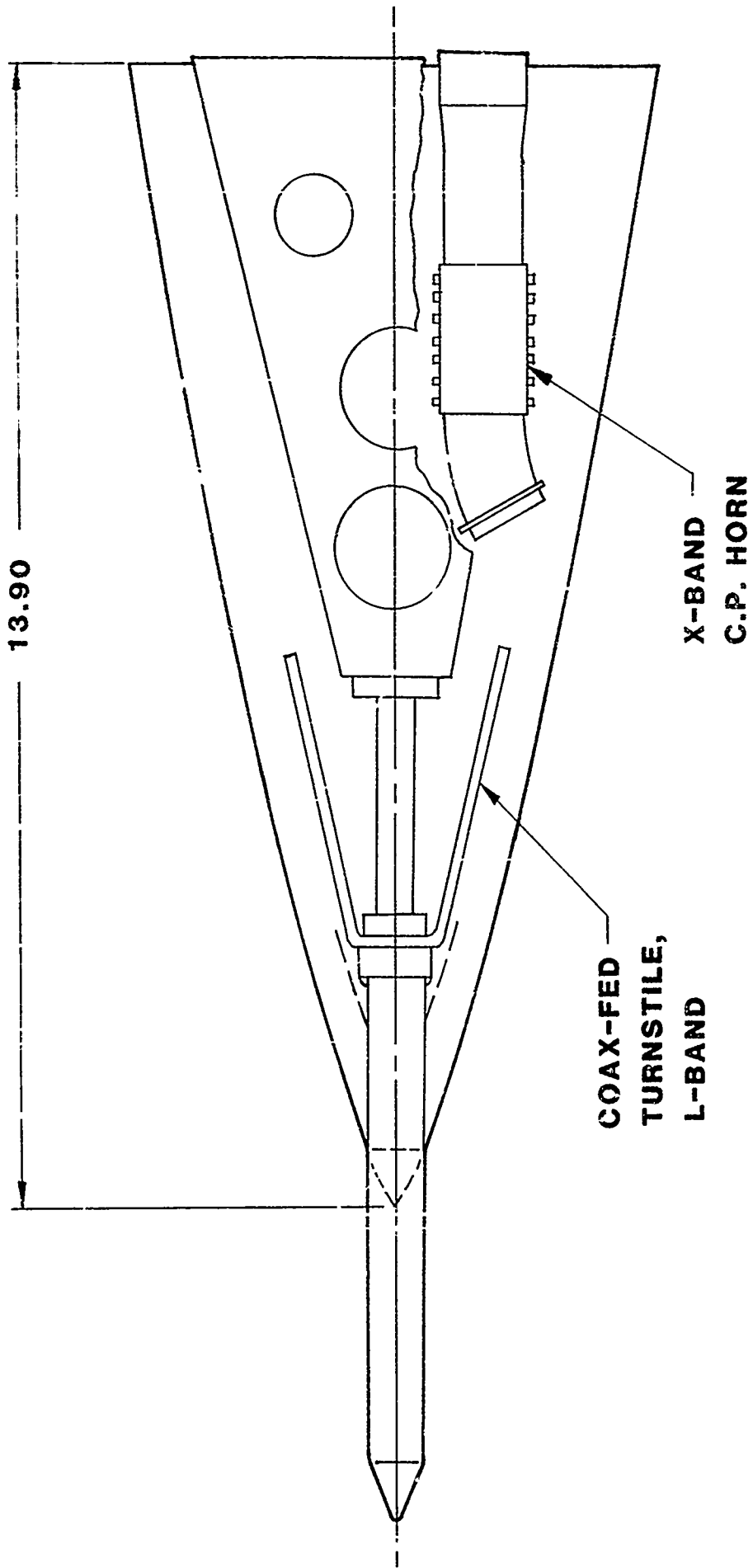


**FIGURE 4: ANTENNA LOCATIONS, NOSE RADOME**

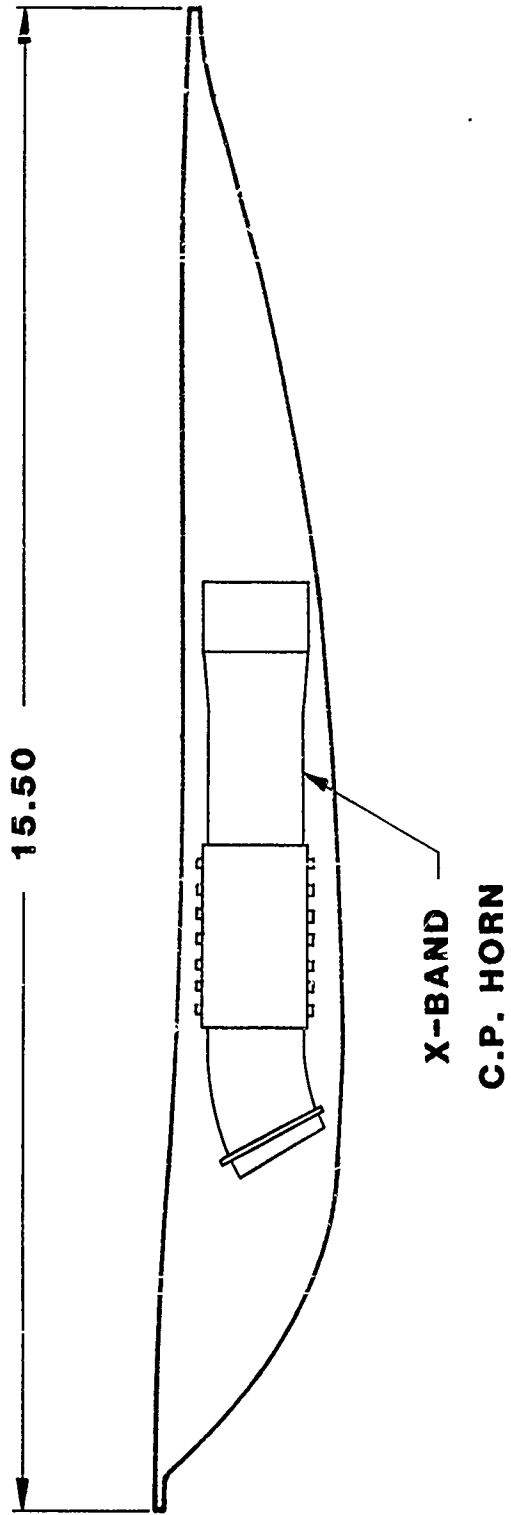


**FIGURE 5: HORN LOCATION, INLET DUCT RADOME**

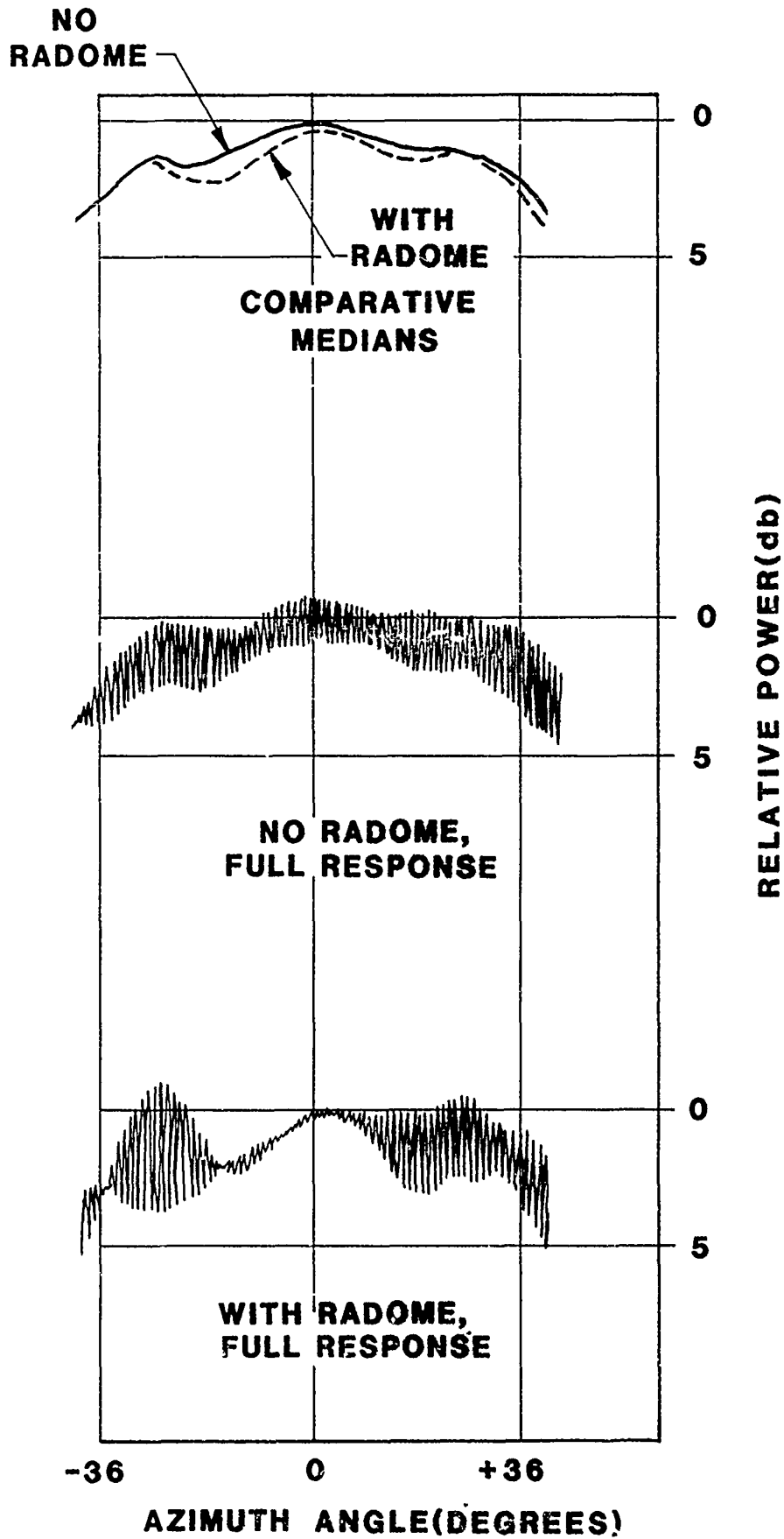


**FIGURE 6: HORN AND RADOME PATTERN AT CENTER FREQUENCY**

AUTHOR INDEX

Balageas, Daniel L.	207	Quinn, G. D	145
Ball, David E.	59	Rappaport, Harold L.	57
Bloom, D. A.	17	Rehrl, Matt	177
Brazel, J.	115	Rhodes, W. H.	187
Briand, G. M.	235	Risner, Steven P.	195
Burks, David G.	133	Rope, E. L.	1
Cain, E. L.	225	Schorsch, James F.	97
Cerullo, Michael	27,125	Smith, P. W.	159
Crowe, Bernard J.	61	Starobinets, S.	77
Cuthbertson, A.	33	Styron, John B.	105,135
Deom, Alain	207	Thompson, Arthur J.	87
Eastridge, G. Wayne	167	Tricoles, G.	1
Frazer, R. K.	215	Trickett, E. A.	187
Fuller, J. A.	235	Tulyathan, P	225
Gagnon, D. R.	99	Walck, J. C.	145
Gauffre, George	207	Ward, C. S.	125
Gordon, D.	77	White, D. J.	17,67,99
Hanson, J.	115	Zimmerman, K. A.	235
Hayward, R. A.	1		
Helmick, C. N.	67		
Hidahl, John W.	217		
Hollenbeck, Kurt	177		
Huddleston, G. K.	41		
Hizal, A.	33		
Hsieh, M. Y.	159		
Joachim, R. J.	85		
Joy, Edward B.	9,57,59		
Kessler, E. L.	217		
Letson, Kenneth N.	195		
Lyon, R. W.	33		
Meyer, F. P.	145		
Miller, Gary E.	97		
Mizuhara, H.	159		
Moore, Charles E.	105		
Overfelt, P. L.	17		
Plimpton, Glenn	27,125		
Punnett, Milton B.	9		
Pupko, B.	77		



## SOURCE INDEX

Aerofjet TechSystems Company Sacramento, California	217
Boeing Aerospace Company Seattle, Washington	97
Brunswick Corporation Marion, Virginia	87,105,135,167,237
CHEMFAB/Birdair Division Buffalo, New York	9
Electronic Space Systems Corporation Concord, Massachusetts	219
EKA Technology Ltd Leatherhead, Surrey, UK	33
ESSCO Collins Limited Kilkishen, Co. Clare, Ireland	219
Flight Systems, Inc. Newport Beach, California	61
General Dynamics Electronic Division San Diego, California	1
General Electric Company Philadelphia, Pennsylvania	115
Georgia Institute of Technology Atlanta, Georgia	9,41,57,59
GTE - WESGO Division Belmont, California	159,187
Harris Corporation Melbourne, Florida	59,235
Israel Aircraft Industries Israel	77
Johns Hopkins University Laurel, Maryland	215
Michelson Laboratory China Lake, California	17,67,99
Middle East Technical University Ankara, Turkey	33

Northrop Los Angeles, California	225
Office National d'Etudes et de Recherches Aerospatiales Chatillon (France)	207
Raytheon Company Bedford, Massachusetts	27,85,125
Texas Instruments Dallas, Texas	133,177
U. S. Army Materials and Mechanics Research Center Watertown, Massachusetts	145
U. S. Army Missile Command Huntsville, Alabama	195